Tidal currents on the continental shelf and slope off the west coast of India

A thesis submitted to Goa University for the award of the degree of

Doctor of Philosophy

in

Marine Sciences

by

M. P. Subeesh

Research guide

A. S. Unnikrishnan

Goa University

Taleigao, Goa 403206

June 2019

To

amma and achan,

for their love and struggles

Statement

As required under the University ordinance OB-9.9.(v-vi), I state that this thesis entitled *Tidal currents on the continental shelf and slope off the west coast of India* is my original contribution and it has not been submitted on any previous occasion.

The literature related to the problem investigated has been cited. Due acknowledgements have been made wherever facilities and suggestions have been availed of.

M. P. SUBEESH

CSIR-National Institute of Oceanography, Goa.
17 June 2019

Certificate

This is to certify that the thesis entitled *Tidal currents on the continental shelf and slope off the west coast of India*, submitted by M. P. Subeesh to the Goa University for the degree of Doctor of Philosophy, is based on his original studies carried out under my supervision. The thesis or any part thereof has not been previously submitted for any other degree or diploma in any university or institution.

A. S. UNNIKRISHNAN

Goa University, Talegao, Goa 403 206.
17 June 2019

Acknowledgements

It is indeed a tough task to acknowledge every person who paved my path towards the long journey of a fruitful research career. I was fortunate enough to join CSIR-NIO as a summer intern, which could be mentioned as the beginning of my career, followed by my dissertation, a project assistantship and subsequently to become a Research Scholar. As I look back, I can see many people who had a unique role to construct and refine me in so many ways, both academic and building my being. It is in fact rather impossible to mention everyone here, but I would say everyone is equally important. It is my pleasure to thank everyone.

I take this opportunity to express my sincere gratitude to my doctoral research supervisor, Dr. A.S. Unnikrishnan. He is truly a model for his approach towards students. His scientific wisdom and dedication to research always motivated me. He is a man of immense patience, care and critical advice. He always stood by me to overcome many difficulties during my Ph.D. I had the opportunity of learning many things from him, which I would follow throughout my life.

I extend my gratitude towards the Director, CSIR-NIO for providing the necessary facilities to carry out my research in the institute. I am grateful to the University Grants Commission (UGC), India, for providing a research fellowship to carry out this research.

My sincere gratitude to Dr. P. Vethamony (Vice Chancellors nominee) and my co-guide, Dr. S.G. Aparna for their constant support and encouragement. They evaluated my work and progress reports from time to time and came up with valuable suggestions.

I would like to thank Dr. D. Shankar, with whom I had an opportunity to work as a summer intern during my Masters degree. This made me to familiarise with research problems and also motivated me to learn Oceanography more seriously. I should also mention that I benefited from his lectures.

I am grateful to Dr. S.S.C. Shenoi, Director of INCOIS, for his constant support during my Ph.D., especially in the beginning phase. Despite his busy schedule, he spent time and patiently provided comments which helped me to improve my first paper.

Special thanks to Dr. P.A. Francis, who imparted his knowledge of ocean modelling to me without hesitation. He was very considerate to provide suggestions while setting up the ocean model.

I am grateful to Vice Chancellor, Goa University, faculty members of the Department of Marine Sciences, Prof. G. N. Nayak, Prof. H.B. Menon, Prof. C.U. Rivonker, Prof. Vishnu Murty Matta and the office staff, Mr. Yeshwant. They have always been approachable and helpful throughout my interactions.

I owe to the endeavours of mooring group of the Institute for obtaining ADCP data. I thank Mr. Fernando Vijayan, Mr. G.S. Michael, Mr. S.T. Khalap, Mr. Yogesh Agarwadekar, Mr. C. Santhosh, Mr. M.K Amey, Mr. Ashok Kankonkar and the seamen for their efforts behind the deployment and maintenance of the ADCPs on the continental shelf and slope off the Indian coasts. I also thank Mr. D. Sundar for his help. I thank Dr. A.K. Chaubey for providing the off Goa across-shelf bathymetry data.

I am deeply indebted to Nidheesh A.G., who has always stood by me throughout my life in CSIR-NIO. His comments and suggestions always refined my papers and thesis. I am thankful to my friend Jithin Abraham, for the discussions and suggestions which really helped me in improving the thesis. I thank Amol Prakash for being available for scientific and technical help. I would like to remember my beloved friend Gokul with whome I had good discussions.

I am thankful to Dr. Laurent Testut for his suggestions on using of satellite altimeter data. Thanks to Dr. A.L. New for the prompt reply through e-mails to my scientific queries and doubts. I am also thankful to Dr. Damien J. Allain for making a wonderful harmonic analysis toolbox TTTB available and helping me to install it.

I am grateful to the Director, IITM Pune, for allowing me to use HPC Aditya, where I installed the model and the supporting team, who helped me in various troubleshooting processes.

My love to Prajeesh A.G. for lending out a helping hand always, in cracking out any problem in Linux in crucial situations. Special thanks to Midhun Mohan for his suggestions in the preparation

of a schematic diagram used in the thesis.

I am immensely grateful to Dr. M. Ravichandran, Director NCPOR for encouragement. I would also like to thank my colleagues in NCPOR, Dr. Nuncio Murukesh, Mr. Sourav Chatterjee, Dr. Vidya P.J. and Ms. Divya David for their support.

I feel pleased to thank my colleagues in NIO, Manoj, Vijith, Amol, Abhishek, Arnab, Sarvesh, Mahesh, Remya, Byju, Gautham, Charles, Vineet, Somu, Vipin, Anil and Sreekanth who provided a good working and learning environment. The Oceanography classes followed by discussions in the lab were very informative.

I thank CTOH/LEGOS, France for providing the satellite altimeter data via AVISO website. I would also like to thank the HYCOM and ECMWF reanalysis group for providing their data. I extend my thanks to ROMS user community and ROMS AGRIF preprocessing toolbox. I am thankful to the Open source community for the software GMT, GFortran, Python, Ferret, CDO, NCO, LaTeX, etc. which were used extensively for the research.

I extend my love to my friends, Prajith, Teesha, Anoop, Tyson, Sherin, Aswini, Bijesh, Lathika, and Nikhil. No words to express the support rendered by Ponnu, my sister, who always remained for the needs of our parents whenever I was away. I thank Vrinda for being by my side throughout.

M. P. SUBEESH

CSIR-National Institute of Oceanography, Goa.

June 2019

Abstract

Internal tides (ITs) and near-inertial waves are two primary energy sources for mixing. While ITs are generated by barotropic tides (BTs) in the ocean, near-inertial waves are forced by surface winds. Though deep ocean ridges and seamounts are found to be the major generation sites for ITs, significant IT generation also occurs on the continental slope and shelf-break regions. ITs and BTs are important in shelf-slope mixing, and thereby playing an important role in controlling water mass distribution, circulation, and productivity in shallow waters. Though there have been many studies that described the characteristics of BTs and ITs on the continental shelves and slopes in many regions around the world, the eastern Arabian Sea has received little attention in this direction so far mainly due to the non-availability of sufficiently long measurements of ocean currents. This was overcome with the continuous measurements of currents using Acoustic Doppler Current Profilers (ADCPs) at several locations off the WCI by CSIR-NIO since 2006. This thesis provides a first comprehensive description of the physical characteristics of BTs and ITs on the shelf and slope off the WCI by mainly using long-term ADCP records, sea-surface height measurements from satellite altimetry, data from tide gauges and simulations using a regional ocean model.

Long-term observations of currents off the WCI showed the presence of strong BTs and ITs on the shelf and slope locations. Barotropic tidal currents on the continental shelf increase northward, in accordance with increasing continental shelf width. Barotropic tidal currents are oriented in a cross-isobath direction on the northern shelf regions (off Jaigarh and Mumbai at about 17° N and 20° N respectively). Maximum cross-isobath tidal currents are found at the northern shelf locations (20-30 cm s^{-1}) than those in the south (about 10 cm s^{-1}). Baroclinic current spectra of velocities show dominant peaks at IT frequencies of M_2, S_2, K_1 and O_1 and at inertial frequency (f). Most

of the IT energy is confined to first three baroclinic modes, which represent 70-90% of total IT variance. The IT on the shelf is found to be energetic, with a strong (weak) IT during southwest monsoon (pre-monsoon) owing to the high (weak) stratification on the shelf during this season. Both observations and model results show that one of the most important IT generation sites off the WCI is the shelf-slope region off Jaigarh where sea surface height data from satellite altimeter also revealed the presence of diurnal and semidiurnal ITs with surface amplitudes of about 2 cm. Based on the estimates of 'critical topography' (where the topographic slope is equal to the slope of characteristics of IT) and computed barotropic body force, the shelf break and mid-slope off Jaigarh are found to be the generation sites of ITs in the region.

A three-dimensional, high resolution (1/48°) model, Regional Ocean Modelling System (ROMS), was set up for the eastern Arabian Sea domain to simulate BTs and ITs and the model simulations were validated by comparing data from tide gauges, ADCP and hydrography. The model results were used to compute the IT energy flux, conversion of BT energy to ITs, dissipation rates and radiation. Large IT energy flux is found over the shelf and slope region between 16°-18.5° N and over the Lakshadweep ridge (northern part of Chagos-Laccadive ridge system extending from 8° N to 14° N). Offshore propagating ITs dominate in the northern shelf-slope region. Depth-integrated M_2 energy flux reaches up to 1-3 kW/m in the model domain. The shelf break region exhibits a clear positive conversion, indicating a local IT generation. Approximately 2.4 GW of energy is converted from M_2 BT to IT in the domain. Almost the entire IT energy is found to be dissipated inside the model domain. The depth-integrated K_1 energy flux ranges from 0.3-0.7 kW/m. The area integrated barotropic to baroclinic conversion for K_1 is about 0.6 GW, which is much less than that of M_2.

This thesis shows the characteristics and importance of BTs and ITs on the shelf and slope off the WCI, which were not known earlier. The thesis further points out the need for detailed study of small-scale mixing associated with ITs in the region, and the potential role of ITs in the redistribution of heat, salt and chlorophyll. This thesis also suggests the importance of Chagos-Laccadive ridge system as a potential IT generation source to understand its role in vertical mixing.

Contents

Acronyms

ADCP	Acoustic Doppler Current Profiler
BT	Barotropic Tide
CSIR	Council of Scientific and Industrial Research
CSIR-NIO	CSIR-National Institute of Oceanography
CTD	Conductivity Temperature Depth
EEZ	Exclusive Economic Zone
EOF	Empirical Orthogonal Function
FES	Finite Element Solution
HYCOM	Hybrid Coordinate Ocean Model
IT	Internal Tide
NIW	Near Inertial Wave
OTIS	Oregon State University Tidal Inversion Software
ROMS	Regional Ocean Modelling System
TASK	Tidal Analysis Software Kit
T/P	TOPEX/Poseidon
WCI	West Coast of India
WICC	West India Coastal Current
WOA	World Ocean Atlas

List of Tables

List of Figures

Chapter 1

Introduction

1.1 Barotropic and baroclinic tides

Tides are periodic oscillations of ocean surface caused by astronomical forcing. In general, these oscillations are dominant on daily (diurnal) and twice daily (semidiurnal) time scales, though oscillations also exist over fortnightly and longer timescales[1]. As a response to the astronomical "body force", these oscillations are depth independent, and are called barotropic tides (BT). BTs become large when they enter onto shelf and coastal regions (Fig. 1.1) and make strong mixing due to bottom friction. In Fig. 1.1, for example, tidal amplitudes are minimum in the tropical Indian ocean (20° S-20° N) and the amplitudes increase towards north (Along the rim of Bay of Bengal, off the Indian subcontinent and in the northern Arabian Sea). It is observed that semidiurnal tides get amplified on wide continental shelves, according to the theory developed by [Clarke and Battisti, 1981] for example, European shelf, the head of the Bay of Bengal, etc. In shelf regions, BTs can create residual circulations[2], by nonlinear interactions and dissipation, whose

[1]Tides are a combination of many waves with different frequencies, called tidal harmonics. They are classified according to their origin and frequency. For example, 'Lunar semidiurnal tides' represent tides with Lunar (moon) origin and semidiurnal (twice daily) frequency. The most important tides are semidiurnal tides (twice daily) and diurnal tides (once in a day). The relative importance of the above tides at a particular place can be identified by estimating 'form factor', the ratio of sum of amplitudes of two major diurnal to the sum of amplitudes of two major semidiurnal constituents ($F = \frac{K_1+O_1}{M_2+S_2}$). If F is less than value 0.25, tides are mainly semidiurnal in nature. If F is greater than value 3, tides are dominated with diurnal frequencies and if it falls in between these values tides are considered mixed tides. Fig. 1.2 gives the distribution of type of tides along the coast of world ocean.

[2]Tidal residual flow is computed as an average of tidal currents over a tidal period. It is generated by nonlinear interaction of tidal flow and bottom topography, and geometrical effect of horizontal boundary.

Figure 1.1 Amplitude of barotropic M_2 tide (The period of M_2 tide is 12.42 hours, i.e., approximately twice daily frequency), predicted from a global tide model, Finite Element Solution (FES). Blue colour indicates tide with small amplitudes, and red color indicates large tides. Amplitudes of BTs are large in coastal waters and small in deep waters. The black box indicates the region of present study.

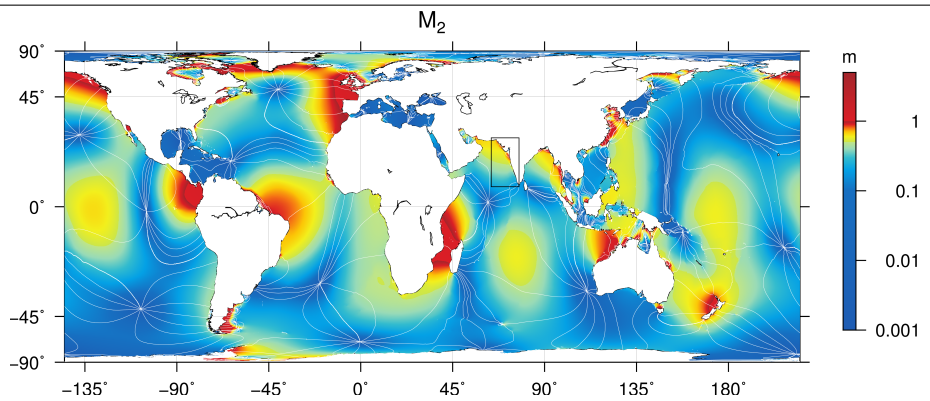

magnitudes can attain to those of wind-driven flow [Ganju et al., 2011] and can induce vertical mixing in sub-tidal time scales [Suanda et al., 2017]. Vertical mixing can destroy stratification of water column [Suanda et al., 2017]. Mixing can also create horizontal temperature variations and thermal fronts have been reported separating well-mixed water column and stratified water column [Simpson and Hunter, 1974]. As BTs interact with bottom topographic features such as ridges, seamounts, continental slopes and shelf breaks, the layers between different density fields in the interior ocean oscillate. These types of 'interior' tidal oscillations in a stratified ocean, which depend on density stratification and bottom topography, are called internal tides (ITs). ITs are also called baroclinic tides. ITs also have frequencies to those of BT and they cause oscillations in other ocean parameters such as salinity, temperature and currents. However, wavelengths of ITs are smaller ($<$ 300 km) than those of BT. Since ITs have a vertical structure (depth-dependence) owing to the ocean stratification, they break easily and usually dissipate either in the region of generation or far away from the generation sites.

The turbulence generated by BT and IT leads to the mixing of the oceanic water column. The ability of BTs and ITs in the mixing across the oceanic density layers makes these waves important in controlling various oceanic processes, such as, the transport of heat, freshwater and tracers, uptake and storage of heat and carbon [Bryan, 1987; Wunsch and Ferrari, 2004], productivity

Figure 1.2 Geographical distribution of semidiurnal, diurnal and mixed tides in the world oceans. While the east coast of India experiences semidiurnal tides, tides off WCI are semidiurnal mixed type. (Source: www.physicalgeography.net)

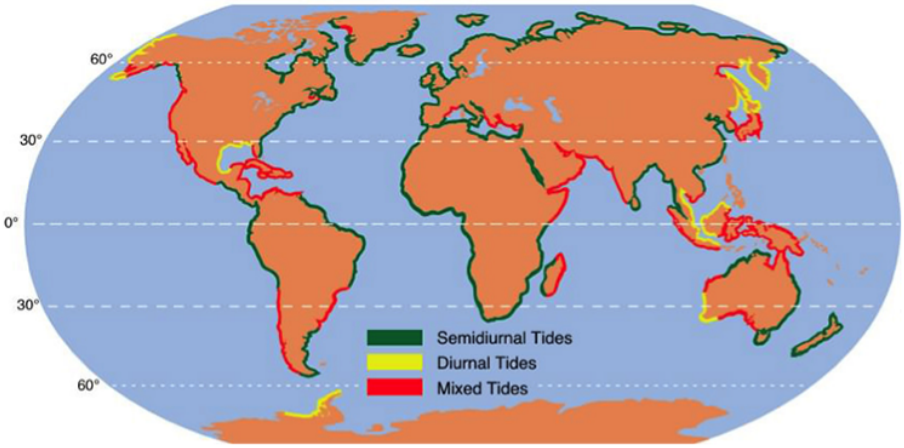

[Sharples et al., 2001], fisheries [Sharples et al., 2009] and climate change [Dalan et al., 2005; Schiermeier, 2007]. In fact, tides act as the major source of energy for the mixing of the interior as well as shallow (continental shelf and slope) oceanic regions. Dissipation of tidal energy occurs through a series of cascade processes, where large-scale barotropic tidal energy gets converted to small-scale ocean turbulence through the breaking and scattering of IT. Regions of varying topography are observed to be the hotspots for IT generation and dissipation. For example, Fig. 1.3 shows regions (blue boxes), where IT largely dissipates in the ocean and these regions are known for strong topographic features. As seen in Fig. 1.3, IT generate/dissipate over regions of large ridges in the deep ocean or on continental shelves, slopes, etc. While deep ocean ITs play an important role in the maintenance of meridional overturning circulation (MOC) and vertical stratification, shallow ITs are important in the local mixing of the water column.

1.2 Deep Ocean internal tides

Deep ocean ITs are mainly generated on the seamounts and ridges (see Fig. 1.3). In the deep ocean, they bring mechanical energy to the interior ocean via turbulent mixing and maintain a steady state abyssal ocean stratification, and hence driving MOC. If this mixing were absent, the interior ocean

Figure 1.3 Dissipation of M_2 ITs, estimated from the satellite altimeter data. The blue colour box shows some of major topographic features where large dissipation takes place (Madagaskar ridge, Andaman Islands, Palu ridge, Hawaii ridge, Tuomoto ridge, etc). The black box shows the eastern Arabian Sea. (Source: https://earthobservatory.nasa.gov).

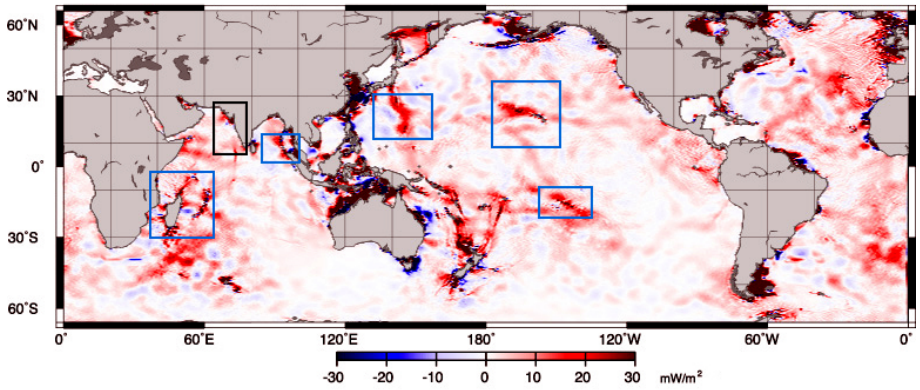

would have been filled with the cold water coming from high latitudes and a thin surface layer would remain warm due to the solar heating. However, in reality, the ocean has a gradual decrease in temperature in the interior ocean. It is shown that, the work done by surface winds and IT induced turbulent mixing (approximately 2.1 TW)[3] against ocean buoyancy is the main source of energy that maintains the current steady state condition of the interior oceans [Munk and Wunsch, 1998]. It is estimated that the Earth-Moon system and Earth-Sun system generate about 3.7 TW of energy via tides (Fig. 1.4). In this, after earth tide (.2 TW) and atmospheric tide (.02), 3.5 TW of energy is dissipated in the ocean. However, most of the tidal energy is dissipated in shallow waters ($\sim$ 2.5 TW) due to the bottom friction. Egbert and Ray [2000] suggested that approximately 1 TW of tidal power is converted from BTs to ITs in the deep ocean, which supplies half of the energy required for the maintenance of abyssal ocean stratification via energy cascading. The other half of energy is supplied by near-inertial waves excited by surface winds (See Fig. 1.4 for a schematic representation of this pathway of energy). Though the values given above are not exact, there is

[3][Munk, 1966] estimated the diffusivity value to maintain the steady-state of the interior ocean by assuming a one-dimensional balance between advection and diffusion and found eddy diffusivity to be of the order of $10^{-4} m^2/s$. The total work done by the turbulent mixing against buoyancy force was estimated and found that about 2.1 TW of energy is required to maintain the steady-state global stratification against 30 Sv bottom water formation.

Figure 1.4 The energy pathway in the ocean proposed by Munk and Wunsch (1998). Moon and Sun supply 3.7 TW to the ocean via tides. Winds supply 1.2 TW via near-inertial waves. 2.5 TW of energy gets dissipated through surface tides in shallow bottom boundary layer. The rest is converted to ITs and dissipated on shelf, slope and the Deep Ocean. Courtesy of Killworth [1998] for the figure (https://www.nature.com/articles/25444).

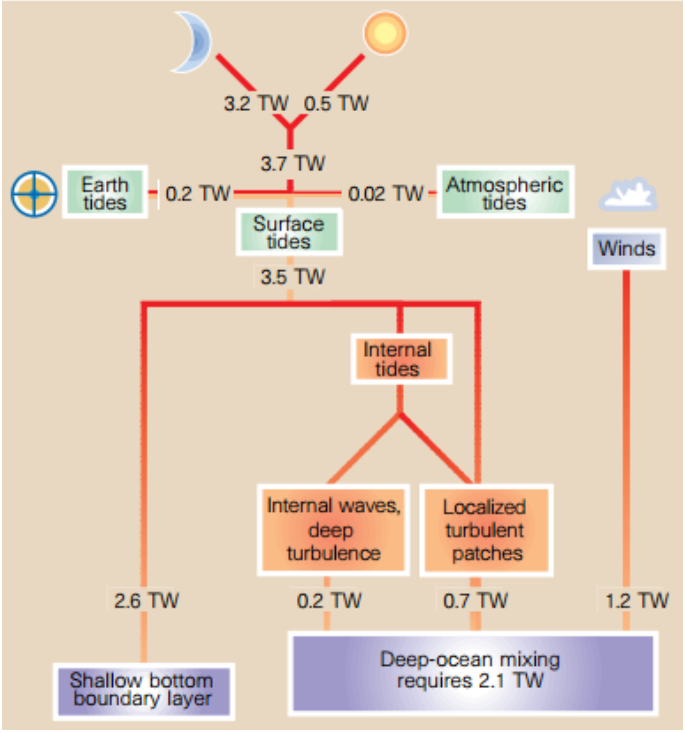

fairly good agreement among scientists that the ITs supply about 0.7-1.3 TW of energy into deep ocean mixing [Baines, 1982*a*; Sjöberg and Stigebrandt, 1992; Egbert and Ray, 2000; Nycander, 2005; Garrett and Kunze, 2007; Waterhouse et al., 2014], and near-inertial waves contribute to about 0.3-1.5 TW [Lueck and Reid, 1984] [D'Asaro, 1985; Large and Crawford, 1995; Watanabe and Hibiya, 2002; Alford, 2003; Jiang, 2005; Plueddemann and Farrar, 2006; Furuichi et al., 2008; Rimac et al., 2013].

1.3 Internal tides on the continental shelf and slope

Apart from deep ocean ridges and seamounts, the major IT generation occurs on the continental slope and shelf-break regions. The locally generated ITs either break there itself or propagate offshore (onshore) and dissipate in the deep (shallow) ocean. However, the contribution of ITs, generated on the shelf and slope, to the deep ocean mixing is very less. The rough estimation of the value is 15 GW [Ray, 2001], which is much smaller compared to the value for 1 TW of deep ocean IT. Apart from being generation sites, the continental shelves and slopes are also sinks for deep ocean IT, where ITs propagate thousands of kilometers from deep ocean and get dissipated in shallow waters by topographic scattering [Johnston, 2003]. Waterhouse et al. [2014] inferred based on microstructure datasets that a total of 1.8 TW of power input is dissipated in the ocean, where about 69% is dissipated in the interior ocean and the remaining 31% (.6 TW) is available for dissipation on either continental slope or shelf-slope canyons. Using a semi-analytical model, Kelly et al. [2013] showed that semidiurnal mode-1 ITs lose about 60% of energy on continental margins in which 20% is transmitted onto the shallow continental shelves and 40% is scattered to higher modes. The remaining 40% of IT energy in continental margin reflects back to the deep ocean. The low-mode ITs generated on the shelf breaks or slopes can also travel to the deep ocean, far from the source without significant energy loss.

Continental shelves and slopes are dynamically rich oceanic regions with the presence of eddies, low/high-frequency currents, waves and upwelling/downwelling. Besides, river discharges from the land also cause changes in stratification thereby in the ITs. This makes the variability of IT complex in these regions. Very often, ITs on the shelf and slope regions are not found to be coherent with local barotropic tides. The lack of coherence is caused by changes in the background stratification, presence of meso-scale eddies, low-frequency currents and remotely generated IT. ITs interact with background currents and mesoscale eddies, whose speeds are comparable to those of the ITs, resulting in the Doppler shifting [Gerkema et al., 2013] and refraction of ITs. The variability of IT can be considerably modified by background stratification [Aguirre et al., 2010; Bravo et al., 2013; Green et al., 2010; Rosenfeld, 1990] and bathymetry. Also, multiple generation sites make IT field complex at a location [Nash et al., 2004]. Any of these factors can make IT incoherent (uncoupled) with the local barotropic forcing.

IT mixing can control the ecosystem in the region. Many studies noted that ITs greatly help to bring nitrate from deep water to the euphotic zone by diapycnal mixing and play an important role in the biomass production [Sharples et al., 2001, 2009; Sandstrom and Elliott, 1984]. As the shelf and slope regions are important regions for fish catches [Pauly et al., 2002], studying ITs is very important to understand the potential fishing zones. Apart from the ecological impacts, studies on tidal mixing are important in modelling temperature and large-scale circulation. Incorporating tidal forcing in numerical models showed improved accuracies in simulated temperature, sub-tidal currents and water-masses due to the better representation of mixing by tides [Suanda et al., 2017]. However, tidal mixing process cannot be often resolved in coarse resolution general circulation models, hence needs to be parameterised [Laurent and Garrett, 2002; Polzin, 2004]. A number of studies in the past were dedicated to understand internal tide dynamics, especially to quantify the IT energy flux, mixing and dissipation, which pointed out the need for improving our observations and high-resolution regional models [for example, Nagai and Hibiya, 2015]. A prerequisite to any such detailed study is to know how important is the tidal mixing parameterisation in a given region.

1.4 Tides off the west coast of India

Co-tidal charts prepared using global tidal models indicate that tides in the Arabian Sea propagate from south to north [Lyard et al., 2006]. The amplitudes of major tidal constituents along the West coast of India (WCI) show that tidal amplitude is low in the south, which increases towards the north (see Fig. 1.1). The tides are found to be mixed semidiurnal (see Fig. 1.2). Large tidal range (about 3 m during spring tide), with semi-diurnal dominance, was reported on the mid-shelf off Mumbai, based on the measurements of water surface elevations made from a drilling platform for oil and natural gas [Joseph et al., 2009]. Many studies were made to study variations of tidal propagation in gulfs and estuaries along the WCI, for example, [Unnikrishnan et al., 1999; Shetye, 1999; Unnikrishnan and Luick, 2003; Sundar and Shetye, 2005; Testut and Unnikrishnan, 2016].

Tidal currents

The seasonal variability of hydrography and circulation off the eastern Arabian Sea were described

in earlier studies [Shetye et al., 1990, 1991]. However, a description of tidal currents in the Arabian Sea has received little attention so far. Shenoi et al. [1992] reported magnitudes of observed tidal currents at a mooring location in the mid-Arabian Sea (near 14° N and 64° E) based on the analysis of nearly one year-long current meter observations. Through harmonic analysis, they estimated M_2 tidal current to be varying between 1.2 cm s^{-1} and 1.6 cm s^{-1}. K_1 (the prominent diurnal constituent) tidal current in the location is found to have magnitudes of 0.89 cm s^{-1}. These magnitudes are consistent with those reported based on measurements in mid-Atlantic and mid-Pacific [Magaard and McKee, 1973; Weisberg et al., 1987].

Studies on tidal currents are very few even on the shelf of the eastern Arabian Sea due to the non-availability of sufficiently long measurements of currents. Though short records are available at some locations over the region, they are insufficient to describe the temporal variability of tidal currents. However, short-duration records provided information on high-frequency wind-driven currents in this region [Varkey, 1980; Shenoi et al., 1988; Unnikrishnan and Antony, 1990; Antony and Shenoi, 1993; Shetye et al., 2008] and limited information on major tidal constituents [Shenoi et al., 1988; Fernandes et al., 1993; Shenoi et al., 1994]. For example, Shenoi et al. [1988] found strong semidiurnal barotropic and baroclinic tidal signal off Goa (15° N) by using 8-day long current meter observations. Later, Shenoi et al. [1994] studied the variation of barotropic and baroclinic M_2 constituent off Goa in detail, using short-term (about 10 days) Rotor Current Meter (RCM) observations for different months (March, May and November). The study addressed seasonal variation of M_2 IT and found that M_2 baroclinic currents are dominated by the first mode and their values are equal to or higher than M_2 barotropic tidal currents. Fernandes et al. [1993] described the tidal currents on the mid-shelf in Mumbai High region (19.4° N, water depth 80 m) using a 10-day current meter record during winter and found that currents at different depths are nearly identical. Later, Unnikrishnan et al. [1999] simulated tidal currents off Mumbai, using a vertically integrated hydrodynamic model driven by tides, and showed that the circulation in the region is driven primarily by BTs. The short-period variability in observed temperature fields in shallow shelf locations caused by predominant ITs has also been reported in earlier works [Murthy and Kumar, 1991; Unnikrishnan and Antony, 1990; Kumar et al., 2006, 2010]. Shankar et al. [2005] reported the presence of ITs in the deep locations (about 2000 m) off Jaigarh (17°

N) and Goa (15° N) using continuous CTD measurements. Their study in fact showed significant isothermal fluctuations in tidal frequencies of M_2, S_2 and O_1 (amplitudes of 0.5°C, 0.45°C and 0.35°C respectively at 100 m depth off Goa). Though limited in number, all these studies pointed out the presence of ITs off the WCI, which can induce potential changes in hydrography and cause mixing in the shelves region.

1.5 Observational program of CSIR-NIO

The Indian peninsula encompasses a coastline of approximately 8100 km (Source: http://www.incois.gov.in/MarineFisheries/PfzAdvisory), with vast Exclusive Economic Zone (EEZ) about 2.1 million km^2. A large population, about 7 million, resides on the coasts and heavily depends upon fishing and other marine resources for their livelihood. Considering productivity, the WCI is more important, as approximately 70% of total fish production belongs to this region [George et al., 1977] and understanding the physics and biogeochemistry in shelf-slope region is essential to model the potential fishing zones. As mentioned earlier, the ITs and BTs are important in mixing in shelf and slope regions. Moreover, these waves have direct impact on the coastal ecosystem [Pingree, 1984; Sharples et al., 2001, 2009]. Even though there have been some efforts to understand the controlling factors of productivity off the WCI [Kumar et al., 2001; Vipin et al., 2015], changes in productivity caused by internal waves are practically not studied for this region, mainly due to the lack of sufficiently long observations of currents on the shelf and the slope. Though short records are available at some locations, they are insufficient to describe the seasonal variation of ITs and all the frequency bands associated with it. The data were also isolated so that a pan-west coast IT climate could not be described. A number of studies indeed pointed out the caveats posed by limited observations off the WCI and the importance of studying barotropic and ITs in detail.

The paucity of long-term current measurements has been overcome with the availability of data collected using continuous measurements of currents by Acoustic Doppler Current Profilers (ADCPs) by CSIR-National Institute of Oceanography by deploying a set of ADCPs at about 100 m and 1000 m on the shelf and slope respectively at several locations off the west and east coast of

Figure 1.5 The ADCP mooring locations along the shelf and slope off WCI. 100 m bathymetry contour is also shown. The triangles indicate shelf moorings and dark circles indicate slope moorings.

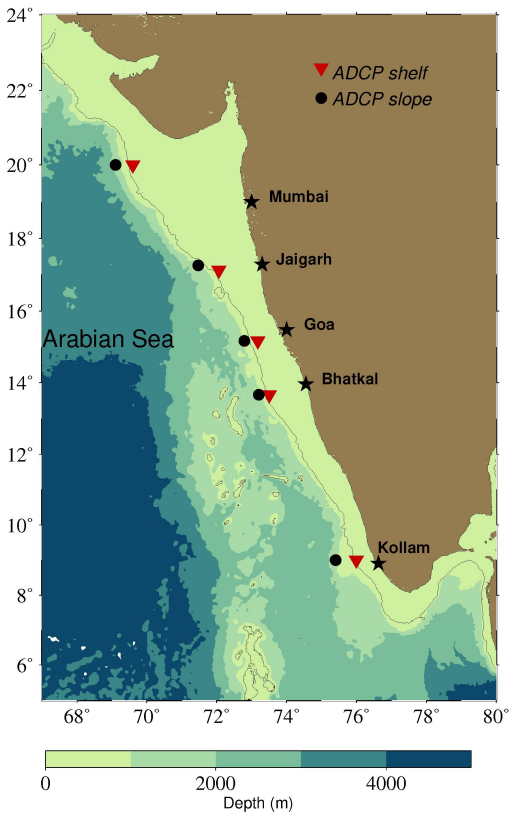

India since 2006. Off the west coast, five ADCPs (300 KHz) were deployed from the south (9° N) to north (20° N) on shelf and slope, where shelf-slope ADCP pairs were separated by a distance of about 50 km (Fig. 1.5). Observations are made at high frequency with 15-minute intervals on the shelf and one-hour interval on slope locations. Measurements were made at an interval of about 4-8 meters in the vertical, where shelf measurements covered almost the entire depth of water column and those on the slope covered the upper water column (300-450 m). The observations from these ADCP moorings provide a unique opportunity to look into tidal current variability in the region and to identify possible generation sites of ITs and to study their propagation characteristics. The present thesis extensively used the ADCP data to describe ITs and BTs off the WCI and aims to

fulfil the knowledge gap of tidal currents in the region.

1.6 Objectives

The present thesis examines the variability of tidal currents off the WCI. Besides, generation, propagation, and dissipation of internal tides on the continental shelf and slope in the region are studied by combining both observations and a numerical model. The main objectives of the present study are listed as follows:

i) To describe the characteristic features associated with both BTs and ITs by analysing ADCP data along the shelves and slopes off the WCI.

ii) To study the dynamics of tidal currents using a numerical model.

This involves setting up of a high resolution, three-dimensional numerical model to simulate BTs and ITs off the WCI. The thesis attempts to further investigate the energetics, generation, propagation and dissipation of ITs using this numerical model.

1.7 Thesis Layout

The present study describes the characteristics of BTs and ITs on the continental shelf and slope off the WCI using observations and a numerical model. The objective of the thesis is to understand BTs and ITs variability in the eastern Arabian Sea, their generation, propagation, and dissipation characteristics. The study first concentrated on the analysis of ADCP data on the shelf. The characteristics of BTs and ITs including their seasonal variations are discussed. Analysis of data on slope locations was carried out. A focus was made on the discussion of ITs off Jaigarh, using observations including ADCP, satellite altimeter data, and CTD. The altimeter data showed that ITs in the region are generated mainly from shelf break and continental slope, which propagate to the deep ocean. This motivated to develop a regional ocean model, which can simulate the IT characteristic over the shelf and slope regions, as the shelf-slope region hardly experiences any remotely generated ITs. A regional ocean model (ROMS), was set up for the eastern Arabian Sea by applying tidal forcing. The possible IT generation sites, their propagation characteristics, energetics, and dissipation were examined. The present thesis contains seven chapters. A brief

summary of each chapter is given below.

Chapter 2 describes the historical and recent developments in barotropic tide and internal tide studies.

Chapter 3 provides a description of the data used in present study, methods of analysis used and a brief description of the numerical model and its set up for the eastern Arabian Sea.

Chapter 4 describes the characteristics of barotropic tides and internal tides on the shelf using ADCP data. The results described in this chapter are reported in Subeesh et al. [2013]

Chapter 5 provides a description of the slope barotropic tides and internal tides. Main focus is given on variability of internal tides off Jaigarh (17° N). A small section is dedicated to describe the near-inertial waves. The results on internal tides and near-inertial waves off Jaigarh are described in Subeesh and Unnikrishnan [2016].

Chapter 6 focuses on the results of numerical simulation of barotropic tides and internal tides. Here I compared the model results with observation and validated. The energy flux, conversion rate and dissipation of internal tides are estimated and the generation, propagation and dissipation of internal tides are discussed in this chapter.

Important findings are summarised and the scope of further research about internal tides on the shelf and slope off the WCI is briefly described in **Chapter 7**.

Chapter 2

Literature Review

This chapter describes the evolution of studies on tides from historical to modern oceanographic era. I attempt to describe the studies in the past, measurements of tides, various theories on tide and recent work on numerical modelling of tides and tidal currents.

2.1 Barotropic tides

Tides are ubiquitous phenomena on the earth. They are observed not only in the ocean, but they occur on the earth's surface and in atmosphere with relatively lower magnitudes than those found in oceans. Tidal oscillations were known to many scientists historically. Most of the theoretical studies of tides have been carried out in the era before the 'oceanographic discipline' came into existence. Tide was considered as an 'explained phenomenon' in the beginning of modern oceanography. From the very beginning of tidal studies, each major finding on tidal studies was considered as the ultimate to explain this phenomenon. The study of tides progressed with the progression of humankind in history. The primitive understanding of tides and its usage for the practical life was spread in all major human civilisations including Indus Valleys, Arabic, Greek, Babylonian, Roman and Chinese. For instance, the design of a dockyard (spanning 37 x 22 m area) excavated from Harappa [Cartwright, 1999], a part of Indus Valley Civilisation (2000 BC) site, shows that the people had a good understanding of tides. Though the interactions of humans with tides and efforts to understand the phenomenon date back to ancient civilisations, an

in-depth inquiry had only started during the European Renaissance period (15-17th century) and well emerged during 'scientific revolution' time (Age of enlightenment, 17th century). This period witnessed the sweeping out of old paradigms of science and concentrated on the understanding of fundamental mechanism of natural phenomenon within a rational framework. Galileo's "*Dialogue Concerning the Two Chief World Systems, Ptolemaic and Copernican*" (1632 AD) is generally considered as the final work of this period, and by Newton's "*Philosophiae Naturalis Principia Mathematica*", the era of scientific revolution ended and gave opening for modern science. Tide was an exciting subject for physicists and philosophers in that period, mainly because of its relation with the movements of celestial bodies, the moon and the sun. Moreover, tide is an observable phenomenon every day by most of the people, who live near the coast. This led them to think tides to be a 'fascinating subject'. Galileo tried to explain tides in his '*Day four*' chapter of the aforementioned book. He believed that the sea experienced tide due to the alteration of sea surface speed caused by combination of the earth's rotation on its axis and its rotation with respect to the sun, where the explanation did not include any kind of attractive force.

The very first description of the tide was given by [Newton, 1687] in the *Principia*, in which he described that the cause of tides is the gravitational force of attraction (Astronomical Tide-Generating force[1]) of the sun and the moon on the ocean. Euler [1740] realised that the tide is driven by horizontal component of tide-generating force and not by the vertical component. Daniel Bernoulli made into practise the tidal theory by predicting High Waters in many ports [Bernoulli, 1740]. After about 90 years of Newton's theory, Laplace [1776] made a leap in tidal studies by introducing the dynamic theory, which replaced Newton's classical equilibrium theory. Newton's theory considered that the response of the ocean to the tide-generating force is quasi-static, whereas, Laplace identified that the response is dynamic and rectified Newton's theory. Laplace considered ocean geometry and the force due to earth's rotation (later known as Coriolis force) in his famous Laplace Tidal Equations (LTEs). Solving LTE is difficult without assumptions and simplifications. Analytical solutions to LTEs cannot be attained for ocean tides due to the complex bathymetry, ocean boundary and importance of friction in tidal dynamics. It took nearly two

[1]Tide-generating force is the resultant of gravitational and centrifugal force. The Earth-Moon system (or Earth-Sun) is revolving around the common center of mass, where gravitational force is balanced by centrifugal force. As the gravitational force varies with distance (centrifugal force does not) at each point at the surface of the earth, the resultant force also varies.

hundred years to solve LTE by incorporating realistic bathymetry and boundaries using numerical modelling [Bogdanov and Magarik, 1967; Pekeris and Accad, 1969].

2.1.1 Tidal observations and analysis

Parallel to the theoretical studies on tides, there were many efforts to collect tidal observations from the middle of 17^{th} century. In the beginning, the observations were made visually by human observers using tide staffs, which are graduated tide poles. The observations were confined to recording high and low waters and the time of their occurrence. The automatic and continuous tide measuring was started after the invention of recording tide-gauges in 1831 by Henry Palmer. By 1850, the installation of automatic tide-gauges spread around the world. The availability of long time-series of sea-level records eventually made scientists to analyse tides in more detail. The major progress of tidal studies in the 19^{th} century is the development of harmonic analysis for tidal prediction by William Thomson (Lord Kelvin). This technique allowed extracting tidal constituents (Table 2.1) from a long continuous time series of sea level by using information on known periods of tidal constituents. The constituents estimated by harmonic analysis could further be used for predicting future tides, based on the fact that the amplitude and phase of a particular tidal constituent do not vary in time at a particular location. The technique was improved by G. H. Darwin and W. E. Ferrel. Later, Arthur T. Doodson substantially improved the method by introducing Tidal potential theory [Doodson, 1921] that became the strong base for modern tidal analysis. The tidal analysis and prediction were later improved by many researchers [Godin, 1972; Foreman, 2004; Cartwright, 1967].

All of the tidal studies were confined to the coastal regions or islands, as it was practically impossible to take measurements in the deep sea. The development of bottom-pressure recorders in the 1960s helped to overcome this problem, and enabled researcher to take long-term measurements of sea level from the deep regions. These measurements greatly made progress on the knowledge of BTs in the deep sea.

Table 2.1 Primary tidal constituents, their period and origin. Among the constituents listed, M_2 and S_2 are the major semi-diurnal tidal constituents, while K_1 and O_1 are the major diurnal constituents.

Constituents	Origin	Period
Semidiurnal		(Hour)
M_2	Principal Lunar	12.421
S_2	Principal Solar	12.000
N_2	Elliptical Lunar	12.658
K_2	Declination Luni-Solar	11.967
Diurnal		(Hour)
K_1	Declination Luni-Solar	23.93
O_1	Principal Lunar	25.82
P_1	Principal Solar	24.07
Q_1	Elliptical Lunar	26.87
Long-Period		(Day)
M_f	Fortnightly Lunar	13.661
M_m	Monthly Lunar	27.555
S_{sa}	Semiannual Solar	182.621

2.1.2 Numerical Models

The advent of computers revolutionised physical oceanography by allowing storage of large volumes of data and in developing numerical models to simulate processes in realistic oceans. Many attempts were made to solve LTE numerically by taking advantage of this [Bogdanov and Magarik, 1967; Pekeris and Accad, 1969; Zahel, 1977; Parke and Hendershott, 1980]. Though the models did not meet the accuracy for geophysical applications, they greatly helped to understand the tidal regimes around the world and sensitivity of tidal models to friction, bathymetry, tidal-loading and self-attraction [Le Provost, 2001]. Schwiderski [1980*b*,*a*] developed a hydrodynamic interpolation scheme to incorporate coastal, island, and deep ocean tidal data into Global Tidal Model (GTM). He developed global tidal charts of 1-degree resolution for eleven tidal constituents (M_2, S_2, N_2, K_2, K_1, O_1, P_1, Q_1, M_f, M_m, and S_{sa}).

The potential of using altimeter data for tidal studies was recognized since the launch of GEOSAT in March 1985. Cartwright and Ray [1990, 1991] constructed diurnal and semidiurnal ocean tides by tidal analysis of Geosat altimetry data. As the construction does not depend upon any dynamical assumption, the global fields of tidal constituents became useful for validating other tidal solutions. Topex/POSEIDON (T/P), launched in 1992, led to a breakthrough in measuring sea level owing to its orbital accuracy in conjunction with its repeat period. The

availability of spatial seal-level data enabled tidal researchers to undertake efforts to improve or develop new tidal models with centimetre level of accuracy [Le Provost et al., 1994]. Since the availability of altimeter data from T/P, many GTMs were developed by assimilation of altimeter data. In 1994, twelve GTMs were released [Andersen et al., 1995]. All the above GTMs are much improved compared to the models of Schwiderski [1980*b*,*a*] and Cartwright and Ray [1990, 1991].

The premier GTM was developed based on fully nonlinear shallow water equations [Le Provost et al., 1994]. The model is based on the finite element formulation. Le Provost's model covered the entire global ocean including the Arctic Ocean. Later, a number of GTMs also were developed [Eanes and Bettadpur, 1996; Lyard et al., 2006; Egbert and Erofeeva, 2002] by assimilating multi-mission satellite altimeter data (T/P, ERS-2, Envisat, Jason-1) and coastal tide gauge data. For instance, FES2004 GTM [Lyard et al., 2006] used a hydrodynamic model to simulate tides and assimilated with 671 tide gauges and altimeter data from T/P and ERS satellites to improve the results. TPXO7.2 global tide model used an inverse tide model [Egbert and Erofeeva, 2002], which also assimilated different satellite altimeter data and tide gauge data. The focus of the recent GTMs shifted from deep sea to shallow shelf and coastal regions, where errors of GTMs are large due to inaccuracies in the altimeter data near the coast. For example, FES2012 and FES2014, the improved versions of FES2004 incorporated many shallow water constituents and increased the horizontal resolution to simulate shallow water tides. However, there are a number of factors including complex bathymetry, which still make accurate modelling of the BTs in the shallow seas difficult. The need for accurate bottom topography, the parameterisation of dissipation of energy in the tidal equations, and the effects of ocean stratification on the BTs still make difficulties to reproduce BTs accurately. This demands development of regional models with a high-resolution bathymetry. Regional models make use of results from GTM for prescribing open boundary conditions.

2.2 Internal tides

'Internal tides' were not observed unlike 'surface tides' until the invention of Oceanographic instruments, such as Nansen bottle and reversing thermometer, which are capable of measuring

subsurface phenomenon. Nansen [1902] made the first observation of internal waves in his *Fram expedition* (1893-1896) using hydrographic measurements in the Arctic Ocean. He noted "oscillations of some kind on the interface between cold polar water and the Gulf Stream", however, could not recognise them as ITs. It was Otto Pettersson, a Swedish scientist, who first discovered oscillations in the stratified water column in a Swedish fjord and understood that these oscillations have tidal frequencies [Ekman, 1945]. The instruments such as Nansen bottles and bathythermographs made it possible for the scientific community to observe ITs in many regions around the world including deep ocean, continental shelf and slope [Fjeldstad, 1933; Rudnick and Cochrane, 1951; LaFond and Rao, 1954; Emery, 1956; Reid, 1956; LaFond, 1961; Lee and Cox, 1966; Weston and Reay, 1969; Rooth and Düing, 1971]. Further, temperature and current observations from moored instruments like current meter and thermistor chains made it possible to understand ITs in more detail.

All observations showed the presence of ITs with varying magnitudes in different depths in which most of the energy is confined to the semidiurnal frequencies followed by diurnal frequencies [Cairns and LaFond, 1966; Halpern, 1971; Schott, 1971; Wunsch and Hendry, 1972; Wunsch and Dahlen, 1974]. In the vertical, most of the IT energy is found to be concentrated in lowest baroclinic modes [Hendry, 1975]. Generally, the observations showed that unlike BTs, the presence of ITs is intermittent [Magaard and McKee, 1973]. These studies also found that the topographic features and water column stratification are important in IT generation. Wunsch [1975] contributed a review article, which described all the important studies on IT. An important finding that was made during that period is the discovery of Garrett and Munk spectra (Generally known as GM spectra) of internal waves. Garrett and Munk [1972] constructed a universal internal wave energy spectrum (GM spectra) from a number of diverse observations from the deep ocean. The energy level of GM model is surprisingly found to be unvarying throughout the world ocean [Wunsch and Webb, 1979; Briscoe, 1975]. The GM spectrum is widely used as a reference spectrum for internal wave field in the deep ocean, where the departure from the observed spectra can be considered as an indication of either sink or source of IT energy [Garrett and Munk, 1975; Cairns and Williams, 1976; Garrett and Munk, 1979].

2.2.1 Internal tides on continental shelves and slopes

There have been many efforts to study ITs on shelf and slope regions in the world ocean (Holloway [1984], off the northwest Australia; Sherwin [1988], off the northern Ireland; Pingree and New [1989], Bay of Biscay; Huthnance [1989], off the North America west coast; Rosenfeld [1990], off the northern California; Shenoi et al. [1994], off the west coast of India; Lerczak et al. [2001], off the southern California; Rao et al. [2011], Mohanty et al. [2017], Jithin et al. [2017a], off the east coast of India; Nash et al. [2004], continental slope off Virginia; Klymak et al. [2011], slope off South China Sea, etc.). A detailed review of observational studies of ITs on the shelves and shelf breaks in many regions of the world ocean is summarised in the paper by Huthnance [1989]. Main findings from the studies indicate that amplification of ITs occur in regions, where the characteristic slope[2] of ITs matches with the slope of bottom topography. Bottom intensification and enlarged shear were observed in many observations, in regions where the topographic slope matches with that of IT slope [Horn and Meincke, 1976; Schott, 1977]. Many studies showed the lack of coherence between BTs and ITs [Wunsch, 1975] in a given region and a few studies showed strong coherence between them (Sherwin [1988], shelf off Malin; Schott [1977], shelf break off Norway). The seasonality of ITs due to the background stratifications changes is also noted in many studies [Hayes and Helpern, 1976; Leaman, 1980; Huthnance and Baines, 1982; Holloway, 1984; Bratkovich, 1985]. IT energy flux across the shelf estimated from observation is found to be typically of the order of 100-300 W/m [Sherwin, 1988; Holloway, 1984].

Theoretical studies on internal waves go back to the middle of 19$^{\text{th}}$ century. Stokes [1847] gave the first theoretical description of internal waves, where he treated internal waves as the waves occurring at the interface of a two-layer fluid. Later, Rayleigh [1882] considered continuous stratification and extended the theory. Zeilon [1912] developed internal wave theory further, in which he demonstrated the generation of internal tide as a result of isopycnal oscillations when BT passes through varying depth in a stratified fluid. It was referred to as tidal boundary waves, i.e.,

[2]When the IT reflects from a topographic feature the IT energy (Internal tidal characteristics) propagates at an angle to the horizontal determined by its frequency, background stratification and the Coriolis frequency. The characteristic slope of IT, $C = (\frac{\omega^2 - f^2}{N^2 - \omega^2})^{\frac{1}{2}}$; where N is the buoyancy frequency, ω is the frequency of ITs and f is the Coriolis frequency. Based on the ratio of topographic slope($\gamma = \frac{\Delta H}{\Delta X}$ in x direction) and slope of characteristics, the topography can be divided into three categories. i) Critical($\gamma = c$) ii) Subcritical ($\gamma < c$) iii) Supercritical ($\gamma > c$). Critical topography experience large shear and bottom intensification of velocities. Subcritical topography allows IT to further propagate onshore and supercritical topography reflects IT back from topography in an offshore direction.

the waves originating at the boundaries of two density layer in the ocean. The detailed description of physics of internal wave generation is given in many books [Eckart, 1960; Phillips, 1966; Turner, 1973]. Some of the basic theory of internal wave dynamics is given in Appendix A. Using simplified approach, several attempts were made to solve the equation to study IT propagation when BTs hit topographic region like shelf break and slope. Rattray [1960] and Weigand et al. [1969] used a step topography with two-layer stratification. Later, Rattray et al. [1969] improved the model by incorporating uniform stratification. Prinsenberg et al. [1974] considered wedge-like topography in the presence of uniform stratification. Prinsenberg and Rattray [1975] considered flat-slope topography in the presence of uniform stratification. New [1988] considered the same but with varying stratification.

2.2.2 Internal tide models

Numerical modelling of ITs in global scale started only in the beginning of the 21^{st} century [Arbic et al., 2004, 2010; Simmons et al., 2004; Niwa and Hibiya, 2011]. The earlier attempt to model ITs was mainly using simplified analytical models with idealised topography and stratification [Rattray et al., 1969; Prinsenberg and Rattray, 1975; Baines, 1982*a*, 1973, 1974]. Later, numerical models using finite difference scheme were used to study ITs across the shelf [Chuang and Wang, 1981; Sherwin and Taylor, 1990; Serpette and Mazé, 1989]. Holloway [1996] used three-dimensional Princeton Ocean Model (POM) to the Australian North West Shelf to study the generation and propagation of ITs. However, the model developed by Holloway neglected the alongshore variation of ITs. Three-dimensional model with barotropic forcing, realistic bathymetry and stratification to simulate ITs was started towards the end of 20^{th} century [Cummins and Oey, 1997; Xing and Davies, 1998; Holloway and Merrifield, 1999; Merrifield and Holloway, 2002; Holloway et al., 2001]. Till now, there have been a number of regional models used to understand IT's generation, propagation, dissipation, and their interactions with other ocean processes. Regional models are found to be useful tools to understand the generation source of ITs [Jachec et al., 2006; Carter, 2010], to study their energetics [Martini et al., 2007; Buijsman et al., 2012; Mohanty et al., 2018], to understand interference pattern [Rainville et al., 2010], etc. Carter [2010] showed that changes in pressure gradient associated with IT could even alter barotropic tidal currents. Many studies

combining observations and model greatly helped to understand the potential IT generation sites and accordingly to identify the regions suitable for observations to study mixing characteristics [Rudnick, 2003; Alford et al., 2006; Lee et al., 2006; Klymak et al., 2006; Nash et al., 2006; Rainville and Pinkel, 2006].

2.2.3 Internal tide mixing and parameterisation

Egbert and Ray [2000] inferred from satellite data that 1 TW of tidal energy, that is 20-30% of total tidal energy is dissipated in the deep ocean, which is the half of the energy needed to maintain abyssal stratification [Munk and Wunsch, 1998]. The dissipation of turbulent energy due to IT breaking results in mixing of tracers across density layers (diapycnal mixing). The spatial and temporal variations of diapycnal mixing can play an important role in climate time scale (decadal to centennial) processes in ocean. This makes incorporating mixing due to IT in ocean general circulation models (OGCM) important. However, the parameterisation of IT driven mixing is still a challenge in oceanography, owing to the chaotic behaviour of mixing [MacKinnon et al., 2017]. Laurent and Garrett [2002] proposed a formulation for additional vertical diffusivity term due to breaking of ITs in deep ocean. The eddy diffusivity term due to IT mixing is represented by, $A_{Tides} = q\Gamma\frac{E(x,y)F(z)}{\rho N^2}$ where $E(x,y)$ is the IT energy flux, Γ is the mixing efficiency, q is the tidal dissipation efficiency ($q = \frac{\text{Baroclinic energy dissipation}}{\text{Baroclinic energy conversion}}$) and $F(z)$ is the vertical structure function. q represents part of IT that dissipates locally (near-field dissipation). The value is taken as 1/3 [Laurent and Garrett, 2002]. It means that one-third of IT gets dissipated locally and remaining part is radiated away from the source. This parameterisation scheme is used in climate models, such as Coupled Model Inter-Comparison Project (CMIP5) [Dunne et al., 2012], Hallberg Isopycnal Model [Simmons et al., 2004], etc. Koch-Larrouy et al. [2007] showed that model simulation with the above parameterisation improved the simulation of distribution of water masses in the Indonesian Archipelago. They considered q as unity, by assuming all ITs dissipating inside the domain and not radiating out. Nagai and Hibiya [2015] estimated the mixing efficiency using high-resolution numerical model in the Indonesian Archipelago and pointed out the danger of using constant mixing efficiency parameter in parameterisation, which has significant spatiotemporal variations. Active research is going on IT driven mixing parameterisations [Melet et al., 2016], es-

timation of appropriate mixing efficiency values in parameterisations [Gregg et al., 2018], by making use of observations, numerical model and theoretical frameworks. MacKinnon et al. [2017] reviewed the recent progress of IT driven mixing parameterisation schemes and their impact in climate models.

Chapter 3

Data and Methods

3.1 Introduction

This chapter describes the data used in the present study, methods of analysis and a description of the numerical model, developed for the eastern Arabian Sea. The study used the current data from ADCP (Acoustic Doppler Current Profiler). A long time-series of ADCPs current data available on the shelf and slope off the WCI for different years were used in the present study. The study also used the hydrographic data from CTD (Conductivity Temperature Depth) measurements available for a cross-shelf section off Jaigarh (17° N), to study stratification. A deep ocean CTD time series was used to study isopycnal oscillations associated with ITs. The spatial distribution of ITs and BTs was analysed by making use of satellite altimeter data. Argo data were used for the comparison with the model output. A three-dimensional numerical model, Regional Ocean Modeling System (ROMS), was used to simulate tidal currents in the eastern Arabian Sea. A brief introduction to regional ocean models and the challenges of numerical modelling of ITs are described in section 3.4. A brief description of ROMS and the model set up for the eastern Arabian is also given in this section.

Figure 3.1 A Schematic diagram, showing the instruments used for the data collection. Data collected from various instruments were used in the present study. The instruments, tide gauge, ADCP, CTD, Argo, and satellite are shown respectively from the right-hand side of the diagram. A brief description of instruments and data collection is given in the following sections. The cross-section of ocean from shore to deep ocean shows the continental shelf, shelf break, continental slope and abyssal plain. The observations used in the present study spread from the coast to deep ocean. Sea level measured by tide gauges, installed at the coast were used to compare with the simulated sea level. Measurements of currents from ADCPs, moored on the shelf and slope regions, were used in this study for describing the characteristics of BTs and ITs. ADCPs were placed above the bottom using a short taut mooring so that the ADCP looks upward over the entire water column. Measurements of temperature and salinity using CTD made from ship, were used to understand the stratification and isopycnal oscillations. Satellite altimeter data were used to examine the spatial distribution of ITs and BTs in deep ocean and also used to compare simulated sea level in deep ocean. Argo floats measure temperature and salinity from deep ocean in regular time intervals. The data were used for the comparison of model simulated temperature and salinity.

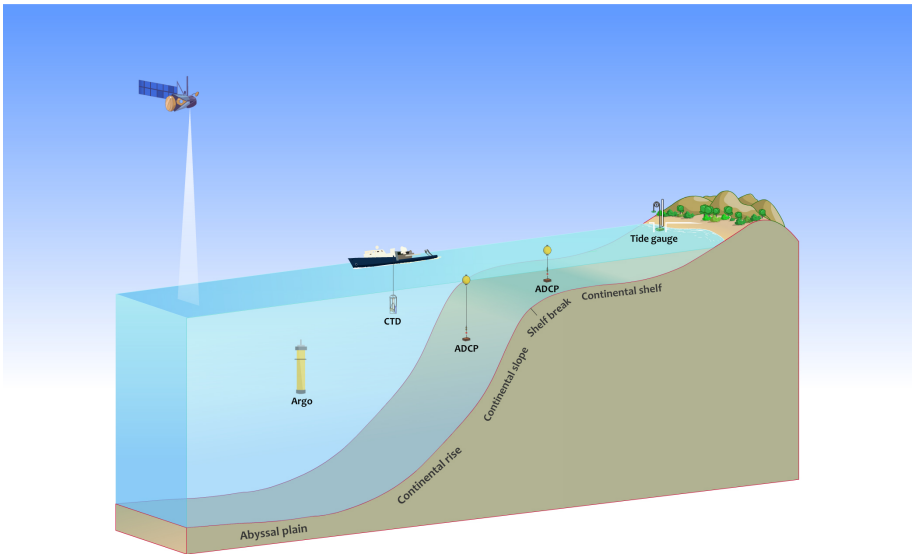

3.2 Data

3.2.1 Acoustic Doppler Current Profiler (ADCP)

ADCP is an instrument used to measure water velocity. ADCP measures the flow speed and direction of water. The working principle is based on the '*Doppler effect*', in which a change in

frequency of a wave occurs due to the motion of a source or listener. In this case, the source is ADCP and the listener is the small suspended particles in the ocean like fine silt, planktons, etc. ADCP releases high-frequency sound signal at a particular frequency either upward or downward according to instrument's orientation. When the released signals hit any moving particle in the ocean, they eventually come back and are received by a hydrophone. The velocity of the particle, thereby water velocity, can be calculated from the frequency change of the sound wave received. A single instrument can measure currents in different depth layers, where the depth resolution can be fixed.

The measurements were made off the WCI using upward-looking Teledyne RDI ADCP (300 kHz/150 kHz), which were deployed on the shelf (near 100/150 m isobaths) and slope (about 1000 m) regions (Fig. 3.1 and 3.2) respectively.

Shelf moorings

Five ADCP moorings were deployed (Table 3.1) on the shelf off the WCI, with the adjacent ones separated by a distance of about 150-200 km. Off Kollam (9° N), two ADCP deployments were made, one at about 100 m depth and the other at 150 m depth. The dataset from the former mooring was not included in the present analysis, since more than 40% of water column near the surface had missing values. Hence, the data from the ADCP mooring at 150 m were used, since it had good values of about 80% of the water column after removing all contaminated data. Missing values of data from the moorings off Bhatkal and Goa are 18% and 19% respectively, while those at Jaigarh and Mumbai are 34% and 40% respectively. ADCPs were placed just above the bottom using a short taut mooring so that the ADCP looked upward over the entire water column. The sampling was done at every 4 m level in vertical and the temporal sampling interval was 15 min, except off Kollam, where sampling interval was done at 30 min interval. The accuracy of velocity measurements is better than 1.55 cm s^{-1} [Amol et al., 2012]. Table 3.1 provides the duration of the available data. Data were not available close to the surface owing to the contamination due to echoes. All data were available mostly downward of 15 m from the surface. United States Geological Survey (USGS) ADCP Processing System (ADCP Toolbox) was used for processing of ADCP data. The velocity data from ADCP records, after careful quality checks, were used to

Figure 3.2 Model domain (black dashed rectangle) and locations of shelf (red triangle) and slope (dark circles) ADCP moorings. Tide gauge at the coastal locations used for model comparison are shown (Circled star). The black and white slanted lines are satellite tracks across shelf. The white lines indicate interleaved tracks. 100 m and 1000 m depth contours are also shown.

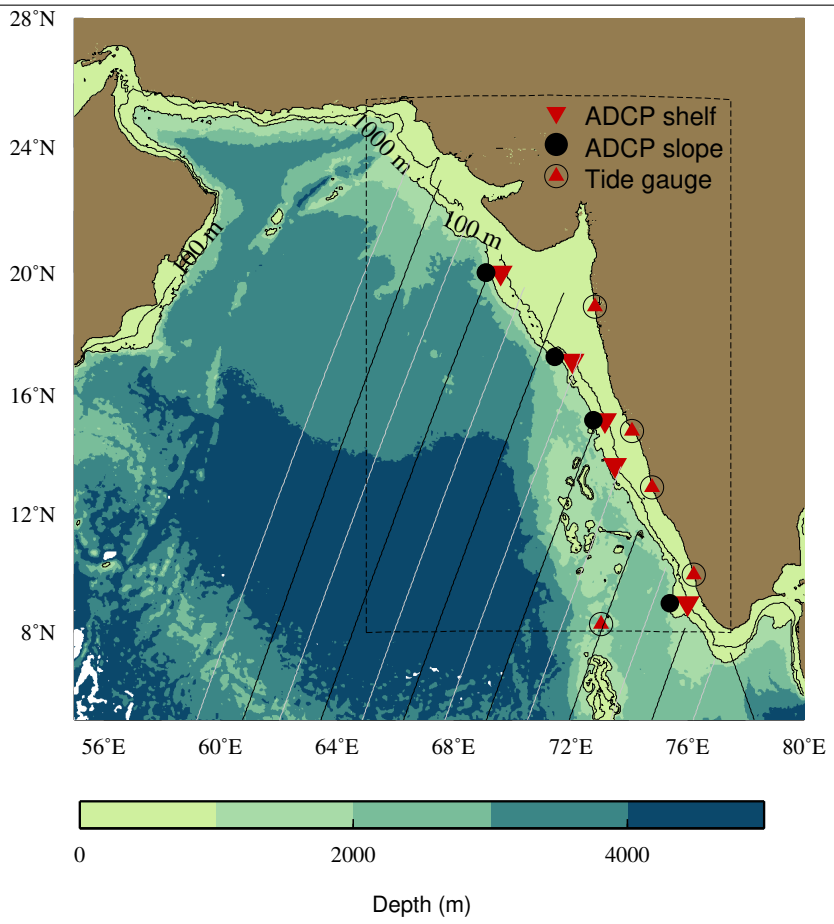

analyse tidal currents along the shelf. The results are described in Chapters 4 and 5.

Slope moorings

Slope data off Mumbai, Goa and Kollam available for the period 2013-2014, and the data off Jaigarh for 2008, were used to describe the ITs (See Table 3.1) on the continental slope off WCI. Off Mumbai, three ADCPs were deployed at 180, 350, and 856 m depths. However, ADCP data obtained from the mooring at 856 m were not used for the present study due to data gaps. The

Table 3.1 Details of ADCP Moorings. The fourth column shows the depth range of water column where data are available. The coastal angle is also given, which is the angle of isobath anticlockwise from true north.

Mooring Location	Latitude (^{0})	Longitude (^{0})	Depth Range of data availability	Water Depth (m)	Coastal Angle (^{0})	Starting Date	Ending Date
Shelf							
Mumbai	20	69.56	15-79	112	20.91	21/Oct/08	12/Sep/09
Jaigarh	17.15	72.08	12-92	108	36.00	04/Mar/08	18/Oct/08
Goa	15.17	73.19	12-92	98	21.40	02/Mar/08	22/Oct/08
	15.20	72.98	17-153	169		08/Nov/13	20/Nov/14
Bhatkal	13.67	73.51	12-96	104	16.94	05/Mar/08	07/Sep/08
Kollam	09.00	75.96	15-151	177	30.57	20/Sep/10	25/Oct/11
Slope							
Mumbai	20	69.25	39-351	1100	17	21/Oct/08	02/Nov/09
	20	69.2	20-172 260-356	1134		18/Nov/14	30/Oct/14
Jaigarh	17.2	71.5	55-438	1100	43	03/Mar/08	20/Oct/08
Goa	15.16	72.75	18-150 145-227 336-842	958	16	11/Nov/13	18/Oct/14
Kollam	9	75.4	23-143 231-623	1118	23	23/Nov/13	24/Sep/14

sampling interval of these ADCPs was 1 h in time with a bin size of 8 m. Three ADCPs were deployed on the slope location off Goa at different depths covering almost the full water column (Table 3.1). Two ADCPs (150 kHz) were placed at 175 m and 350 m, and one 75 kHz ADCP was placed at about 850 m depth. Two ADCPs were deployed at 152 and 631 m depths on the slope off Kollam.

Off Jaigarh, the upward looking 75 kHz ADCP mooring was deployed at about 438 m of water depth on the slope (17.2° N and 71.5° E; Fig. 3.2) on 03rd March 2008, and it was recovered on 20th October of the same year. Water depth of the location is about 1100 m. Measurements were made at an interval of 1 h in time and 8 m in vertical. The ADCP data analysed in this study ranged between 55 m to 438 m depths, as the measurements over the upper 55 m depth were removed due to contamination of data. The ADCP measurements on the shelf off Jaigarh (Fig. 5.10) were also used to describe the shelf-slope variation of IT. In Chapter 5, the data corresponding to the shelf and slope off Jaigarh were used to investigate the IT activity over the region.

ADCP data on the slope off Mumbai for the year 2009 were also used in Chapter 6 for comparison with model output. The data availablity off Mumbai was within 39-351 m depth range.

The ADCP was deployed on 21st October 2008 and was recovered on 01st November 2009. The water depth of the location is 1000 m. The data interval in depth is 8 m and time interval is 1 hour.

Apart from the above data sets, the study used the data off Goa available at a location near the shelf break at a depth of 169 m during the period of 2013-2014 (Table 3.1) in Chapter 5 along with the slope datasets. The same data were also used in Chapter 6 to compare with the model output.

3.2.2 Satellite altimetry

Altimeter onboard satellites measure sea-surface height (SSH) along their paths in regular intervals with an accuracy of about 2 cm. However, if there are sufficient number of measurements, altimetry can resolve tidal signals with 1-2 mm accuracy [Zhao et al., 2012]. ITs are mostly confined to the subsurface depths, they leave small signatures on the sea surface, which can be detected in the altimeter measurements [Ray and Cartwright, 2001; Merrifield et al., 2001]. Harmonic analysis of the sea-level time series gives the amplitude of each constituent, which is a combination of both barotropic and phase-locked baroclinic tides. The application of a high-pass filter ($<$ 1000 km) in the space domain will remove the long-wavelength BT leaving out the IT signals [Zhao et al., 2012].

Fig. 3.2 shows that the ascending tracks of the satellites nearly cross the shelf break at right angles. The tracks stand for the TOPEX/Poseidon (T/P) satellite (black lines in 3.2), which was started in 1992 and shifted to the next orbit (interleaved orbit) in 2002. Further measurements were maintained by the two satellites, Jason-1 (J1) (2002-2009) and Jason-2 (J2) (2008-till now) along the same track. The other track is called interleaved track (white lines in 3.2), which is the track of shifted T/P after the starting of J1. J1 was also shifted to the same orbit after the arrival of J2. The derived constituents from combined altimetry records of T/P-J1-J2 and T/PN-J1N (interleaved track) are available in the Archiving, Validation and Interpretation of Satellite Oceanographic data (AVISO) website (www.aviso.org). The time period considered for the harmonic analysis is 23 November 1993 to 19 May 2011 (T/P-J1-J2) and 20 September 2002 to 14 May 2011 (T/PN-J1N), which consist of 17.4 and 8.6 years respectively. The repeat period of satellites is 9.9156 days. The time series of both combined missions are enough to resolve major tidal constituents (M_2, S_2, K_1 and O_1). We used a high pass filter ($<$ 1000 km) in space to remove the barotropic part

of the tide from the SSH measured by satellite. Satellite measurements over the shallow region (water depth $<$ 500 m) were discarded from the present analysis, as they could be contaminated by land effects. The track data were also used for comparing with model-simulated BTs (Chapter 6).

3.2.3 Conductivity-Temperature-Depth (CTD)

CTD is an instrument to measure conductivity and temperature with respect to depth. Conductivity is a measure of salinity, i.e., conductivity measures how well a water parcel conducts electricity which depends upon the concentration of salt and other inorganic matters in the water. From salinity and temperature data, water density can be estimated using the equation of state. CTD data used in this study are mainly used for understanding stratification of the water column and for computing buoyancy frequency. The density difference between two layers gives the stratification of water column (Buoyancy frequency $N^2 = -\frac{g}{\rho_0}\frac{\partial \rho}{\partial z}$; where ρ is the density, ρ_0 is the average density between two layers). In the present study, the study also used CTD time series to estimate the amplitude of isopycnal oscillations. A 9-day long 2-hourly time series data were available in a deep location off Jaigarh (16.94° N, 71.19° E, water depth 2250 m), 43 km away from the ADCP mooring. The data were collected in July 2002 [Shankar et al., 2005]. Thirteen CTD casts across the shelf off Jaigarh were used to estimate the stratification across the ADCP mooring. The casts were made in February and April 2008 cruise. Five CTD casts taken at depths of 100, 200, 300, 800 and 1000 m depths across the shelf break off Goa on 19 and 20 September 2014 were also used in the thesis.

3.2.4 Argo Floats

Argo floats are the array of free-drifting profiling instruments, which measure temperature, salinity and pressure in the upper 2000 m water column at regular intervals. Once they are deployed at the surface, they start to sink down up to 1000 m depth and float around there for 10 days. The depth where an Argo float rests is called “parking depth” (Fig. 3.1), where the density of instrument being the ambient density. Every 10 days, Argo floats sink down to 2000 m and return to the surface. While moving, the float measures temperature and salinity, and the data is transmitted

to satellites once they reach the surface. The study used about 1200 Argo profiles in the model domain to compare with the simulated temperature and salinity.

3.2.5 Tide gauges

Tide gauge data were used to evaluate the accuracy of model-simulated tides in the coastal regions. Towards coastal regions, satellite altimeter measurements get contaminated by land effects and hence a comparison was not done in this region. ESSO-Indian National Centre for Ocean Information Services (INCOIS) maintains a number of coastal tide gauges along the east and west coasts of India. In the present thesis, the study used four of them (Fig. 3.2) to assess the accuracy of model simulated tidal variations. Apollo Bandar (18.91^0N) data were obtained from Admiralty Tide Tables. The tidal constituents were extracted from the tide gauge sea level data and model output. Data are available in different years, from 2010-2014 and the model run was for the year 2008. As the amplitude and phase of a particular constituent in a given location do not vary with time the data availability for different periods does not affect the comparisons. The harmonic analysis was performed, if a full month data are available without gaps.

3.3 Methods of analysis

An upward looking ADCP measures horizontal currents in the east-west and north-south directions. In the present study, observed currents are rotated with respect to the orientation of isobaths at the mooring point, and along isobath and cross isobath velocity components were extracted, which allows tidal currents to be interpreted in relation to the shelf-slope topography. The terms 'along-isobath/alongshore' and 'cross-isobath/cross-shore' currents in the thesis indicate the rotated currents.

$$U_r = U cos(\theta) + V sin(\theta) \tag{3.1}$$

$$V_r = -U sin(\theta) + V cos(\theta) \tag{3.2}$$

Where U_r and V_r are the rotated currents and θ is the angle of isobaths (Table 3.1).

The direction of tidal propagation is not always across the isobaths. To infer the direction of tidal propagation, I separated tidal currents from the total currents and constructed tidal ellipses. The method of the separation of tidal currents from the raw currents is described below.

3.3.1 Separating barotropic and baroclinic currents

As described in Chapter 1, barotropic currents are depth independent, though they are significantly affected by the bottom friction. Hence, when the horizontal currents are averaged over depth, the depth-dependent components (baroclinic) will be removed and the remainder can be considered as depth-independent barotropic flow. The baroclinic part can be obtained by subtracting barotropic flow from the raw current.

Accordingly, baroclinic currents can be defined as,

$$(u', v') = (U, V) - \int_{-h}^{0} (U, V) \tag{3.3}$$

Where (u', v') are the x and y components of the baroclinic currents, and (U, V) are the same components of raw currents.

However, the difficulty is that this approach demands data to be available over the entire water column. On the shelf locations, data are available over the entire water column. The barotropic currents were obtained by vertically averaging the raw velocity field, by excluding the top and bottom boundary layers. The bottom boundary layer was anyway not included, as the ADCP is positioned at least 10 m above the bottom and the data from 8 m above the ADCP-position are non-usable due to blanking. The surface data (about 10-15 m) were also removed due to contamination. Subsequently, the baroclinic currents were obtained by subtracting the barotropic currents from the raw currents. On the slope, measurements do not cover the full water column. Off Jaigarh, the data covered almost half of the water column. Here, the barotropic tidal currents, extracted from vertically averaged currents, show a good comparison with the tidal currents from OTIS (Oregon State University Tidal Inversion Software, version 7.2) global tidal model results. However, in other slope locations, barotropic tidal currents were not removed from raw currents due to the insufficient data in the vertical.

3.3.2 Harmonic analysis

Observed sea level and current data contain tidal signals and their residuals, which encompass all other signals mostly attributed from atmospheric forcings. Harmonic analysis is a method to separate tides from observed sea level. The method can also be applied separately for velocity components. Two software were used to perform harmonic analysis on the observed signals, (i) TASK (POL/PSMSL Tidal Analysis Software Kit-2000; Bell et al. [1999]) and (ii) TUGOm Tidal Tool Box (TTTB; Allain [2016]), developed by CNRS, LEGOS France. TTTB is designed to analyse high resolution gridded data. While harmonic analysis of model output was carried out by TTTB, TASK was used for point observations of ADCP and tide gauges. The two methods were intercompared by performing harmonic analysis on the same data and found no significant difference in results. The time series of both barotropic and baroclinic currents were subjected to harmonic analysis to extract the tidal constituents. The ellipse parameters (Fig. 3.3) for different constituents of both barotropic and baroclinic tides were estimated and tidal ellipses were constructed.

3.3.3 Spectral analysis and bandpass filtering

Rotary spectra and power spectra were used for assessing the energy associated with dominant frequencies in tidal currents. The horizontal components of currents can be separated into clockwise and counter-clockwise spectra using rotary spectral analysis [Gonella, 1972]. The baroclinic currents were bandpassed between 0.8 cpd and 4 cpd, using a third-order Butterworth filter. Besides, a third order band pass filter was used to separate semidiurnal (1.8-2.2 cpd) and diurnal (0.8-1.2 cpd) ITs from baroclinic currents. Currents over near-inertial frequencies were derived by a third order filtering (0.85-1.15f, where f is the local inertial frequency) of the observed currents.

3.3.4 EOF analysis

EOF (Empirical Orthogonal Function) analysis is a statistical technique to determine dominant variability of a time series distributed in a spatial domain [Kundu et al., 1975]. The method does not need dynamical assumptions. ITs are distributed over a depth as a sum of different vertical modes. As a result, EOF becomes a useful method to separate the ITs into vertical modes

Figure 3.3 A schematic diagram showing the tidal ellipse of a given tidal constituent. Semi-major axis (R/2) represents the magnitude of maximum current. θ represents angle of tidal propagation. (Source: www.oc.nps.edu)

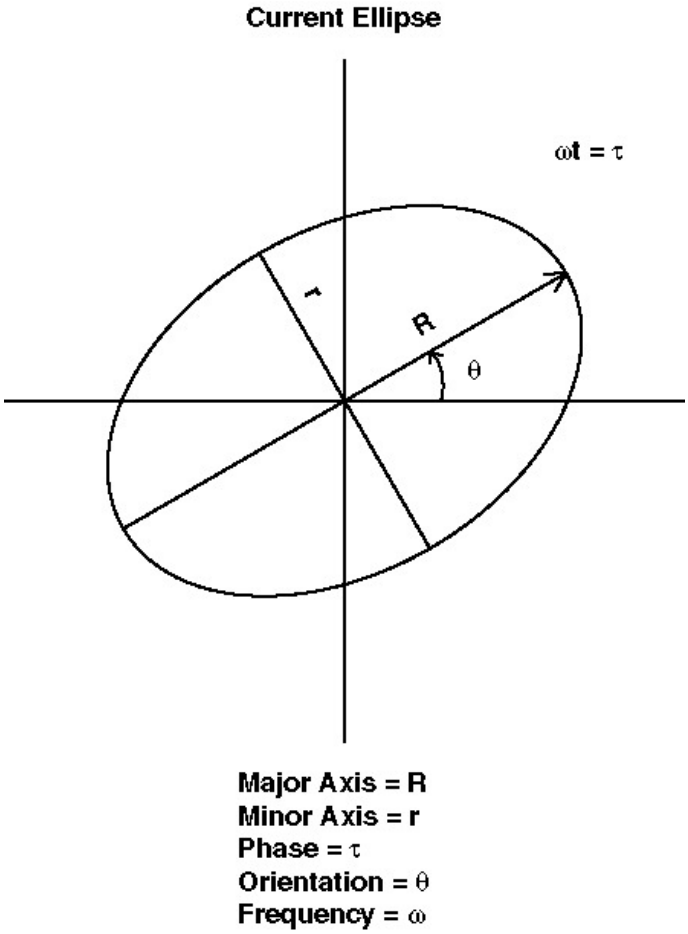

and for constructing corresponding time series for each mode. EOF analysis was carried out for bandpassed semidiurnal and diurnal ITs to determine their vertical modes.

3.3.5 Computation of internal tide energetics terms

Generation and propagation of ITs off the WCI are discussed in terms of IT energetics. Baroclinic tidal flux was calculated from the correlation between baroclinic tidal velocity (u') and pressure (p'), obtained from model output, by considering hydrostatic assumption [Alford and Zhao, 2007]. Semidiurnal and diurnal IT frequencies are much lower than buoyancy frequency so that the hy-

drostatic assumption is generally valid. Baroclinic velocity can be directly estimated from the velocity components by removing depth and time averaged velocity components. Harmonic analysis of baroclinic currents will give the perturbation of each tidal constituent. However, baroclinic pressure cannot be obtained directly, instead it has to be estimated from the density perturbations using hydrostatic equation. Density can be derived from temperature, salinity and pressure values using the equation of state.

Depth-integrated IT energy flux can be estimated from the following relation [Alford and Zhao, 2007],

$$\mathbf{F} = \int_{-H}^{0} < \mathbf{u}'(z)\, p'(z) > dz \tag{3.4}$$

$$\mathbf{u}' = \mathbf{u} - \frac{1}{H}\int_{0}^{H} \mathbf{u} dz \tag{3.5}$$

Where u' is the baroclinic part of each tidal constituents and p' is the baroclinic pressure anomaly for the same. Angled bracket indicates the average over a tidal period. Baroclinic pressure is determined by following equation,

$$p'(z) = \rho\Big(\int_{-z}^{0} N^2(z')\, \eta(z') dz' - \frac{1}{H}\int_{-H}^{0}\int_{-z}^{0} N^2(z')\, \eta(z') dz' dz\Big) \tag{3.6}$$

Where ρ is the density, N is the buoyancy frequency, η is the isopycnal displacement. The vertically averaged pressure is removed from the total pressure to satisfy baroclinicity condition.

The isopycnal displacement is obtained from following equation,

$$\eta(t,z) = \frac{\rho'(t,z)}{d\overline{\rho}/dz} \tag{3.7}$$

where,

$$\rho'(t,z) = \rho(t,z) - \overline{\rho}(z) \tag{3.8}$$

Barotropic to baroclinic energy conversion is estimated using the equation [Kelly and Nash, 2010],

$$C = < \nabla H \cdot \mathbf{U}_{bt}\ p'_b > \tag{3.9}$$

Where $\mathbf{U}_{bt}$ is the x and y components of barotropic tidal currents, p'_b is the baroclinic pressure at bottom and, ∇H = ($\frac{\partial H}{\partial x}$, $\frac{\partial H}{\partial y}$) is the topographic slopes in x and y directions.

Baroclinic energy dissipation is estimated as [Niwa and Hibiya, 2004],

$$D = C - \nabla \cdot \mathbf{F} \tag{3.10}$$

Where C is the conversion and F is the depth-integrated energy flux.

Depth-integrated horizontal kinetic energy (HKE) and available potential energy (APE) are computed using following equations,

$$HKE = \frac{\rho_0}{2} \int_{-H}^{0} < \mathbf{u}'^2(z) > dz \tag{3.11}$$

$$APE = \frac{\rho_0}{2} \int_{-H}^{0} < N^2(z)\ \eta^2(z) > dz \tag{3.12}$$

Where ρ_0 is the vertically averaged density and η is the isopycnal displacement.

The model simulations give full depth water column information of velocity and density. The study used ROMS output to compute energy flux over the domain. Baroclinic energy flux was computed for March and July separately, which represent the pre-monsoon and SW monsoon seasons respectively.

3.4 Numerical Model

3.4.1 Modelling of internal tides

The purpose of numerical modelling of BTs and ITs is twofold i) to understand generation, propagation and their dissipation characteristics and ii) to understand effect of BTs and ITs on other oceanic variables (e.g., Temperature, Salinity, Chlorophyll, etc.). The present thesis primarily focuses on the first aspect. There are strong IT variations over both spatial and temporal scales

owing to their high dependency on bottom topography and ocean density stratification. This makes mapping of ITs using observations difficult and calls for numerical model simulations. The spatial scale of IT is less than 300 km in the open ocean, and it can be even less than 50 km on shelf regions. The time scale varying from a few hours to days, which is same as the barotropic counterpart. The temporal scales are relatively small compared to other oceanic processes (for instance, mesoscale eddies having a spatial scales of about 100 km, have a time scale varies from 10 to100 days). The small spatial scale of ITs demands high horizontal grid resolution in their modelling. In general, ITs are generated by the interaction of BTs with bottom topography. Hence, the model should incorporate high-resolution bathymetry to simulate ITs accurately. In the vertical, ITs can vary over a few tens of meters due to the presence of higher vertical modes. As a result, we need high vertical resolution over the entire water column for an accurate representation of ITs in models. ITs propagate thousands of kilometers away from the source, once they are generated. As we cannot give realistic IT boundary forcings in models, the model domain needs to cover all the IT generation sites to capture even those remotely generated ITs. The seasonal variations of IT at the place of observation are not necessary to be linked with the local variability of stratification alone but can be controlled by the stratification in the IT generation region as well. So, the selection of model domain is crucial that should necessarily take into account all the possible generation sites of ITs to be simulated. The interaction of ITs with other ocean waves over similar frequencies (for example, near-inertial waves), mesoscale eddies and topographic scattering further modulates the characteristics of ITs and makes their simulation more challenging. Low-frequency currents are also found to modulate ITs [Mitchum and Chiswell, 2000]. The interaction of coherent ITs with the mesoscale eddies can lead to transferring their energy into incoherent IT [Rainville and Pinkel, 2006]. Hence, to understand ITs, the model simulation should consider all these oceanic processes. The grid resolution is not only important to rightly pick the topographic features, but it will also help the model to resolve the eddies, which can modulate the ITs [Park and Watts, 2006]. The output files have to be stored at least in hourly intervals for a period of one month to extract all tidal constituents and to study the spring-neap variability. This makes simulation of ITs challenging and demands high-performance computers and large data storage. In the present thesis, the study used Regional Ocean Modelling System (ROMS) to simulate BTs and ITs. ROMS

has widely been used to simulate BTs and ITs [Merrifield and Holloway, 2002; Niwa and Hibiya, 2004; Simmons et al., 2004; Carter et al., 2008; Arbic et al., 2010; Powell et al., 2012]. A brief description of the model and its set up for the eastern Arabian Sea is given below.

3.4.2 Regional Ocean Modelling System (ROMS)

ROMS is a three-dimensional, free-surface ocean model [Shchepetkin and McWilliams, 2003, 2005, 2009] that solves the primitive equations which are discretised in fixed orthogonal curvilinear horizontal coordinates and topography following vertical coordinates (sigma-coordinates). A number of ROMS versions had been developed [Haidvogel et al., 1991; Haidvogel and Beckmann, 1999; Song and Haidvogel, 1994], and the version used in the present thesis was developed in Rutgers university [Haidvogel et al., 2008]. ROMS is based on hydrostatic approximation; therefore the model cannot simulate non-hydrostatic motions. If the horizontal scale of the fluid motion is lower than the vertical scale, the non-hydrostatic pressure becomes important and the motion becomes nonhydrostatic [Vitousek and Fringer, 2011]. An example of this kind of motion is solitary waves, which occur on continental margins, where IT steepen while interacting with continental shelf [Holloway et al., 1997; Ramp et al., 2004; Scotti et al., 2007]. However, horizontal scale of low-frequency ITs is much larger than the depth and the hydrostatic approximation is valid. ROMS uses Arakawa C grid for horizontal discretisation of the state variables u, v, w, p and η [Arakawa and Lamb, 1977], where tracer variables are placed at the centre of the grid and the velocity variables are at the edges of the cells. ROMS uses a split-explicit time stepping scheme [Shchepetkin and McWilliams, 2005, 2009; Killworth et al., 1991], in which 2D and 3D horizontal momentum equations are solved separately. Integration of 3D momentum equations are performed with a larger time step and 2D equations with smaller time steps. This allows solving faster barotropic mode separately from slower baroclinic modes, thereby satisfying CFL criteria for both modes. The model computation involves 30 barotropic time steps between each baroclinic time step. The main advantage of split-explicit time stepping scheme is the better numerical stability and computational efficiency [Shchepetkin and McWilliams, 2005].

The vertical coordinates are the stretched terrain following sigma coordinates, where $\sigma = \frac{(z-\eta)}{h}$ in which η is the sea surface elevation and h is the total water depth. Sigma coordinate ranges

from σ = 0 (Surface) to -1 (Bottom). The advantage of the terrain following coordinate system compared to other coordinates like z-coordinate and isopycnal coordinate is that it can represent the bathymetry variations better than other systems. In terrain-following coordinates, the vertical resolution increases when the ocean gets shallow. Terrain-following vertical coordinate system is suitable for coastal ocean modelling, where topography change is significant. As ITs are largely topographically generated, the terrain following coordinates are a good option to simulate them. However, the coordinates get stretched in upper water column, when ocean gets deep. Hence in the model, the representation of deep ocean upper water column, which is more dynamic, is a challenge. ROMS uses vertical stretching functions to deal this up to a certain limit, where it is possible to adjust the vertical resolution by adjusting the stretching parameters [Haidvogel and Beckmann, 1999; Haidvogel et al., 2000; Shchepetkin and McWilliams, 2003]. Stretching parameters allow us to control the vertical resolution according to our interest. For instance, to capture the bottom generated ITs on deep slope region, we can add high vertical resolution in the bottom, and coarse resolution in the middle.

As mentioned in Chapter 1, small-scale motions are very important in the ocean which allow mixing of the tracers across the isopycnals and thereby redistribute heat. Vertical mixing scale varies from a few centimeters (For instance, salt fingers) to a few kilometers (Convective mixing). As most of the mixing process happens in less than the model grid size (sub-grid scale mixing), model cannot resolve associated turbulent exchange of momentum, heat and salt, and these effects are often parameterised. There are many parameterisation schemes in ROMS to obtain the viscous and diffusive coefficients. Details of mixing schemes available in ROMS are given in Robertson [2006]. The present configuration uses Large-McWilliams-Doney (LMD) vertical mixing parameterisation [Large and Gent, 1999], in which the mixing process is represented by the product of vertical gradient of the momentum (tracers) and the eddy viscosity (diffusivity) coefficients. LMD scheme involves two distinct parameterisations to obtain surface boundary layer diffusivity and interior diffusivity. Internal wave-induced mixing is represented by constant eddy viscosity (10^{-4} m^2 s^{-1}) and eddy diffusivity (10^{-5} m^2 s^{-1}) when Richardson number ($R_i = N^2/(\frac{\partial u}{\partial z})^2 + (\frac{\partial v}{\partial z})^2$; where N is the buoyancy frequency and the denominator is the vertical shear of horizontal currents) is greater than the critical value of 0.7. The basic equations used in ROMS are given below.

Model equations

Momentum equations in zonal directions,

$$\frac{\partial u}{\partial t}+u\frac{\partial u}{\partial x}+v\frac{\partial u}{\partial y}+w\frac{\partial u}{\partial z}-fv=\frac{-1}{\rho_0}\frac{\partial p}{\partial x}+\frac{\partial}{\partial z}[K_v(\frac{\partial u}{\partial z})]+\frac{\partial}{\partial x}[K_h(\frac{\partial u}{\partial x})]+\frac{\partial}{\partial y}[K_h(\frac{\partial u}{\partial y})]+F_u \tag{3.13}$$

$$\frac{\partial v}{\partial t}+u\frac{\partial v}{\partial x}+v\frac{\partial v}{\partial y}+w\frac{\partial v}{\partial z}+fu=\frac{-1}{\rho_0}\frac{\partial p}{\partial y}+\frac{\partial}{\partial z}[K_v(\frac{\partial v}{\partial z})]+\frac{\partial}{\partial x}[K_h(\frac{\partial v}{\partial x})]+\frac{\partial}{\partial y}[K_h(\frac{\partial v}{\partial y})]+F_v \tag{3.14}$$

Continuity equation for incompressible fluid,

$$\frac{\partial u}{\partial x}+\frac{\partial v}{\partial y}+\frac{\partial w}{\partial z}=0 \tag{3.15}$$

Hydrostatic pressure,

$$p(z)=\int_z^\eta g\rho dz \tag{3.16}$$

$$\frac{\partial T}{\partial t}+u\frac{\partial T}{\partial x}+v\frac{\partial T}{\partial y}+w\frac{\partial T}{\partial z}=\frac{1}{\rho_0 C_p}\frac{\partial I}{\partial z}+\frac{\partial}{\partial z}[K_v(\frac{\partial T}{\partial z})] \tag{3.17}$$

$$\frac{\partial S}{\partial t}+u\frac{\partial S}{\partial x}+v\frac{\partial S}{\partial y}+w\frac{\partial S}{\partial z}=\frac{\partial}{\partial z}[K_v(\frac{\partial S}{\partial z})] \tag{3.18}$$

Equations for free surface elevation,

$$\frac{\partial \eta}{\partial t}+\frac{\partial (h+\eta)\overline{u}}{\partial x}+\frac{\partial (h+\eta)\overline{v}}{\partial y}=0 \tag{3.19}$$

Where, u and v are horizontal components of current, w is vertical component of current. f is Coriolis frequency ($f=2\omega sin(\Phi)$, where Φ is the latitude and ω is earth's angular frequency). p is the pressure, ρ is the density, g is acceleration due to gravity (9.8 m s^{-2}), h is the water depth, T is the potential temperature, I is the solar irradiance, C_p is the specific heat capacity, S is the salinity, η is the sea level, F_u, F_v are forcing terms, K_v, K_h are the vertical and horizontal eddy diffusivity.

3.4.3 A regional ocean model for the eastern Arabian Sea

The model domain covers the entire shelf and slope regions off the WCI and the open boundaries are extended to deep ocean (Fig. 3.2). The model domain extends from 65° E to 77.5° E and 8° N to 25.5° N. The model grid used is rectilinear coordinates in x and y. The horizontal resolution of model is 1/48° (about 2.3 km) degree, which is kept constant over the entire domain. 40 vertical sigma layers were used, and the stretching parameters were chosen in such a way that the vertical resolution was finer near the sea surface. The grid was generated using the gridding package 'roms pre-processing toolbox' provided by ROMS AGRIF. Bathymetry for the model grid was taken from SRTM30_PLUS, which is developed by merging satellite-derived and ship acoustic sounding bathymetry [Becker et al., 2009]. Initially, the study used Sindhu et al. [2007] bathymetry in the model, which is the bathymetry data developed for Indian Ocean by incorporating all available coastal bathymetry observations in ETOPO2 data. However, it is found that this bathymetry misses small topographic features present on the shelf break, mid-slope and deep region in the domain, which are important in IT simulations. For example, a section across the shelf off Goa (15° N) [Rao et al., 2010] shows that SRTM30_PLUS compares better with bathymetric data collected by the ship than other products (Fig. 3.4). This prompted us using the state-of-art bathymetry data SRTM30_PLUS, with a resolution 30 arc seconds.

Open boundary

We kept southern and western lateral boundaries open. As ITs are not included as open boundary conditions, fixing the seaward extent of the open boundary is important where open boundary needs to be kept away from all the IT generation sources. Kelly and Nash [2010] showed that the remotely generated shoaling ITs significantly change ITs on a shelf. The simulations of both barotropic and baroclinic boundary forcings are found to significantly vary from simulations of barotropic forcing. Observations from satellite altimeter clearly show that ITs are generated on the continental margins and propagate offshore off the WCI. This information has been useful to make a decision to fix the open boundary quite away from the shelf-slope regions. Satellite data also indicate that there is no deep ocean generation source from where ITs are travelling towards the WCI.

Figure 3.4 Topography across 15° N off the WCI from different bathymetry products and observations from the ship.

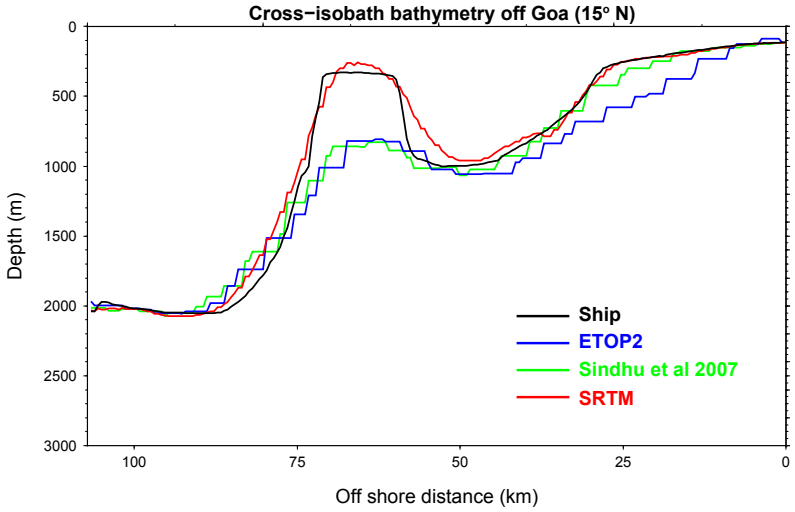

Numerical experiments

i) *Tidal forcing in the presence of monthly climatology temperature and salinity fields*

Tidal forcing was applied along the open boundary of the model, for which tidal elevation and barotropic currents were provided using 10 tidal constituents (M_2, S_2, N_2, K_2, K_1, O_1, P_1, Q_1, M_f and M_m) obtained from TPXOv7.1 global tidal model [Egbert and Erofeeva, 2002]. Flather [Flather, 1976] and Chapman [Chapman, 1985] open boundary conditions were used for the barotropic momentum and free surface open boundaries, and a passive active radiation condition was used for the baroclinic velocity and tracer boundary conditions [Marchesiello et al., 2001]. The model used the KPP mixing scheme [Large et al., 1994] to parameterise the vertical mixing. Smagorinsky type viscosity and diffusion schemes [Muschinski, 1996; Griffies et al., 2000] were chosen for horizontal mixing. The model run was carried out for the year of 2008. The model starts from the state of rest. Stratification in model was restored for every month from climatology of World Ocean Atlas (WOA09) so that model stratification is constant for each month.

ii) *Tidal forcing in the presence of monthly averaged temperature and salinity fields from HYCOM reanalysis*

The same model set up as above was maintained and the stratification was given from monthly

averaged HYCOM (Hybrid Coordinate Ocean Model) and NCODA (Navy Coupled Ocean Data Assimilation) global 1/12° reanalysis product (https://hycom.org/data/glbu0pt08/expt-19pt1). Major limitation of WOA climatology is that it does not cover the shallow shelf region. Most of the data ends in mid-slope or shelf break region. Interpolating this to model grid loses the information of stratification on the shelf. The shelf-slope variation of stratification is found to be important in our study area. This is noted particularly true off Jaigarh, where shelf and slope IT dynamics greatly varies due to the spatial variation in stratification. To address this, we used monthly temperature and salinity data from high resolution (1/12°) HYCOM, which covers the shelf-slope region better than that in climatology.

iii) *Tidal forcing combined with atmospheric forcing*

In this experiment, the model is additionally incorporated with atmospheric forcing along with tidal forcings, and boundary and initial conditions were given from a low-resolution Indian Ocean model. The model domain, resolution and bathymetry are exactly same as in the previous experiments. Model boundary forcing was obtained from the coarse resolution (1/12°) Indian Ocean model output, forced with winds, atmospheric fluxes and tides. In an earlier study, the results from the Indian Ocean model were compared and validated with observations [Francis et al., 2013]. The temperature, salinity and sub-tidal velocities from the above model were interpolated to the present high-resolution model grid and given at the boundaries in each day. Initial conditions were also given from the same model. Wind forcings and other atmosphere parameters (air temperature, pressure, relative humidity, solar radiation and precipitation) were obtained from NCMRWF Global Forecast System (GFS) ($http://www.ncmrwf.gov.in/t254-model/t254\_des.pdf$). Bulk flux formulations [Fairall, Bradley, Godfrey, Wick, Edson and Young, 1996; Fairall, Bradley, Rogers, Edson and Young, 1996] were used to compute atmospheric momentum and heat fluxes. The horizontal resolution of atmospheric fields was 1/4° and time interval was 6 hours. Improved WOA climatology for the north Indian Ocean [Chatterjee et al., 2012] was used to relax surface salinity in the model. KPP mixing scheme [Large et al., 1994] is applied for parameterising subgrid scale vertical mixing. Horizontal mixing is parameterised by Smagorinsky type viscosity and diffusion schemes [Muschinski, 1996]. The model run was carried out for the period of 2013-2014 and the model output for 2014 was taken for the validation. The model run in this experiment was

done for the year 2014, as the boundary conditions were available from Indian Ocean model run for that period.

Chapter 4

Tidal currents on the continental shelf

4.1 Introduction

This chapter provides a description of tidal currents on the shelf off the west coast of India (WCI) based on the data obtained through long-term measurements of currents using self-recording ADCPs, moored at five locations along the shelf (Fig. 3.2). The WCI experiences tides having small ranges in the south, which increase gradually towards the north. Table 4.1 shows the amplitude and phase of the major tidal constituents along the coast of WCI (Admiralty Tide Tables, Vol. 3, NP 203-11 (2011), 324-325). In general, amplitudes increase northward. For instance, amplitude of M_2, the principal semi-diurnal constituent, varies from 20 cm in Cochin to 120 cm in Mumbai. The last column of the table shows the form factor, which is the ratio of amplitudes of two major diurnal tidal constituents to those of two major semi-diurnal ($F = \frac{K_1+O_1}{M_2+S_2}$) constituents. The values of form factor varying between 0.25 and 3 indicate that tides are mixed type. Along the west coast, tides are mixed semidiurnal in northern part of the coast, while they are mixed diurnal type in the south. This shows that both semidiurnal and diurnal constituents are important along the WCI and should be considered for analysis. Also, spring-neap variability is also important along the WCI, as both M_2 and S_2 are significant.

The continental shelf region off the WCI exhibits strong seasonal variations in stratification. This will result in large variability in internal tidal currents in the region with seasons. Arabian Sea experiences mainly two seasons, the South West (SW) monsoon (May-September) and the North

Table 4.1 Amplitude (A) and Phase (g) of five major tidal constituents. The last column gives the form factor F=($\frac{K_1+O_1}{M_2+S_2}$) of the tide. (Source: Admiralty Tide Tables, Vol. 3, NP 203-11 (2011), 324-325).

Location	Latitude (^{0} N)	Longitude (^{0} E)	M_2 A	g (^{0})	S_2 A	g (^{0})	N_2 A	g (^{0})	K_1 A	g (^{0})	O_1 A	g (^{0})	F
Mumbai	18.92	69.97	123	345	048	025	029	326	042	055	020	052	0.36
Ratnagiri	16.98	73.30	066	317	026	355	015	297	034	054	016	057	0.55
Marmagao	15.41	73.80	056	312	020	350	013	292	031	054	016	051	0.62
Bhatkal	13.96	74.53	035	325	026	016	006	309	024	058	007	049	0.52
Cochin	09.97	76.26	020	346	007	047	004	319	017	064	009	065	0.96

East (NE) monsoon (November-January). The ADCP data used in the present analysis covered the period from March to August (Table 3.1), that is, the period of pre-monsoon (March-April) and most of the SW monsoon (May-August) respectively. Hydrography on the shelf shows distinct patterns during NE and SW monsoons, which are associated with downwelling and upwelling respectively. On the shelf, no significant signal of coastal upwelling has been reported during March. Weak upwelling is developed in early April off Kochi (9° N) and off Mangalore (about 12° N) [Shenoi et al., 2005] and it gets strengthened during May onwards and becomes well developed during June to September. An equatorward upwelling gradient is present in the northeastern Arabian Sea [Shetye et al., 1990]. This occurs because upwelling starts first in the south and the signal progressively propagates to the north of the shelf [Shankar and Shetye, 1997]. Upwelling causes shallowing of the mixed layer and increases the vertical gradient of density of water column. The highly stratified layer may enhance the internal wave activity on the shelf [Kumar et al., 2010]. However, strong upwelling may cause vertical mixing of the water column and may decay the internal waves [Aguirre et al., 2010; Rosenfeld, 1990]. The present study provides a description of characteristic features associated with both BTs and ITs along the shelf off the WCI, for the two seasons, the pre-monsoon (March-April) and the SW monsoon (May-August).

4.2 Data and methods

The data were collected using upward looking RDI Acoustic Doppler Current Profilers (ADCP, 300 kHz/150 kHz), which were deployed on the shelf, off the WCI (Fig. 3.2). In addition to those on the shelf, the ADCPs were also moored on the slope. The depths of deployment on the shelf and slope are about 100 and 1000 m respectively. However, the data from the shelf were only used

in the present chapter. The analysis of data on slope locations is provided in Chapter 5. Table 3.1 provides the duration of the available data. Data were not available close to the surface owing to contamination due to echoes. All data were available mostly downward of 15 m from the surface. The velocity data from ADCP records, after careful quality checks, were used to analyse the tidal currents along the shelf. A 6-month period of observation (March-August) was picked from different years (2008, 2009 and 2011) for the analysis, as it provides an opportunity to look at the seasonal variation of tidal currents. The period includes two seasons, pre-monsoon (March-April) and SW monsoon (May-August). I divided the raw data into three subsections of 2 months each, March-April, May-June and July-August, based on the density structure on the shelf. Vertical density structure obtained from climatology does not show considerable difference between these 2-month periods (Details of density structure are given in the next section). Various analyses were carried out for three subsections. The barotropic currents were obtained through vertically averaging the raw velocity field. By excluding the top and bottom boundary layers, depth averaging the measured velocity provides a good estimate of barotropic velocity. The bottom boundary layer is anyway excluded, as the ADCP is positioned at least 10 m above the bottom and the data from 8 m above the position of ADCP are non-usable due to blanking. The surface data (about 10-15 m) was also removed due to contamination. The rest of the velocities were averaged vertically for each subsection separately and considered as barotropic currents. Subsequently, baroclinic currents were obtained by subtracting the barotropic currents from raw currents. The time series of both barotropic and baroclinic currents (U and V components) thus obtained were then subjected to harmonic analysis using TASK (Tidal analysis and Software Kit) software package [Bell et al., 1999] to extract the tidal constituents. The ellipse parameters for different constituents of both barotropic and baroclinic tides were estimated and tidal ellipses were constructed. The current vectors were rotated with respect to the orientation of isobaths for all analysis carried out subsequently (Table 3.1 gives the angle of rotation at each location). Hence, the terms 'along-isobath' and 'cross-isobath' currents indicate the rotated tidal currents. Rotary spectra of baroclinic currents were calculated to obtain clockwise and anticlockwise components. The baroclinic currents were bandpassed between 0.8 cpd and 4 cpd, using a third-order Butterworth filter, to retain baroclinic tidal currents and also bandpassed them for semidiurnal (1.8-2.2 cpd) and diurnal (0.8-1.2

cpd) ITs. Empirical Orthogonal Function (EOF) analysis was carried out for semidiurnal and diurnal ITs separately to determine the vertical modes. Vertical shear was calculated for above bands to further characterize ITs.

4.3 Results

4.3.1 Current spectra

To describe the characteristics of high-frequency currents on the shelf, the study computed variance spectra of cross-isobath and along-isobath raw currents at near surface, mid-depth and bottom over the entire 6-month period (Figs. 4.1 and 4.2). The current spectra show prominent peaks at near-inertial frequency and tidal frequencies. Off Kollam, at the southernmost shelf location, tidal energy is predominant in the along-isobath direction (Fig. 4.2). Tidal energy tends to be more oriented in the cross-isobath direction further north off Bhatkal. At Bhatkal, both peaks in cross-isobath and along-isobath at tidal frequencies have nearly the same energy. Further north, cross-isobath tidal energy is stronger than that of along-isobath. The maximum difference between the cross- isobath and along-isobath energy is found on the shelf off Jaigarh (Figs. 4.1 and 4.2). In tidal spectra, significant peaks are found at frequencies of M_2, S_2 and N_2 (semidiurnal) and K_1 and O_1 (diurnal). The energy of each constituent varies along the shelf. Generally, M_2 is found to be the most prominent peak in all locations. Off Bhatkal, M_2 has less energy at near surface and at bottom it has high energy, where significant bottom amplification of M_2 is apparent. Though O_1 is weak compared to other constituents, off Mumbai, it has a significant peak (Fig. 4.1). No substantial difference in diurnal energy peaks is found at surface, mid-depth and bottom, except off Goa, where diurnal energy is weak at bottom. Compared to other locations, semidiurnal energy is strong in the northern shelf locations (off Jaigarh and Mumbai). Apart from tidal frequencies, near-inertial wave (NIW) energy is also significant on the shelf. NIW is mainly forced by surface winds, when strong winds blowing over the ocean surface create a current and when winds stop, currents undergo 'Rossby adjustment' and waves with frequency near to the Coriolis frequency are generated. Unlike precise frequency for tidal constituents, near-inertial spectrum is distributed in a broad frequency band. Off Kollam, surface enhanced NIW is clearly present. Off Jaigarh,

both near-surface spectral energy and bottom energy show nearly same level. This indicates that NIW in the location is mainly dominated by the first baroclinic structure. The observed frequency of NIW is slightly higher than the theoretical frequency, consistent with freely propagating NIW [Garrett, 2001]. In the present thesis, my focus is mainly on the variability in the tidal frequency bands.

4.3.2 Stratification on the shelf

The vertical section of sigma-t across each mooring point on the shelf is shown (Fig. 4.3). Density was calculated from the revised climatology of temperature and salinity atlas of the North Indian Ocean [Chatterjee et al., 2012]. During SW monsoon, high discharge from various rivers and excess precipitation cause increased stratification on the shelf region. Moreover, coastal upwelling occurring off the WCI during the SW monsoon [Shetye and Shenoi, 1988; Shetye et al., 1990] also determines the density structure of water column. Upwelling is discernible from May onwards off the southwest coast of India, and extends northward along the coast with the progress of monsoon [Rao et al., 2008]. Upwelling signal off Goa (15° N) has been reported in July but as a weak signal and it was observed to be intense during September [Antony and Unnikrishnan, 1993]. During March and April, the isopycnals are quasi-horizontal or slightly bending down towards the coast, which shows weak stratification over the shelf during this period (Fig. 4.3). From May onwards, the water column becomes stratified. During June, at the southern location (off Kollam), isopycnals are found to be bending upwards. The upward tilt of isopycnals is visible off Goa and Bhatkal from July onwards only. During August and September, upwelling is found to be maximum in the above three locations. No significant upwelling signal is noticeable on the shelf off Jaigarh and Mumbai during the period of deployment (Fig. 4.3). With the progress of upwelling towards north, stratification of water column gradually increases.

Fig. 4.4 shows the difference in stratification on the shelf from pre-monsoon to SW monsoon. The buoyancy frequency was calculated from HYCOM (Hybrid Coordinate Ocean Model) temperature and salinity reanalysis data for the year 2008. Buoyancy frequency was calculated for each depth and it was averaged over the vertical. An increase in buoyancy frequency of about 3-7 cph is observed on the shelf during July when compared to that of March (Fig. 4.4).

Figure 4.1 Variance-preserving spectra of tidal and inertial currents from cross-isobath observed currents at near surface (about 20 m), middle, and bottom depths. 20 m was chosen as near-surface data,which is the depth at which data were available at all locations. Vertical lines indicate the different frequencies. Theoretical inertial frequency ($f = 2\omega sin(\Phi)$, where ω is the angular frequency of rotation of the earth and Φ is the latitude) is also shown.

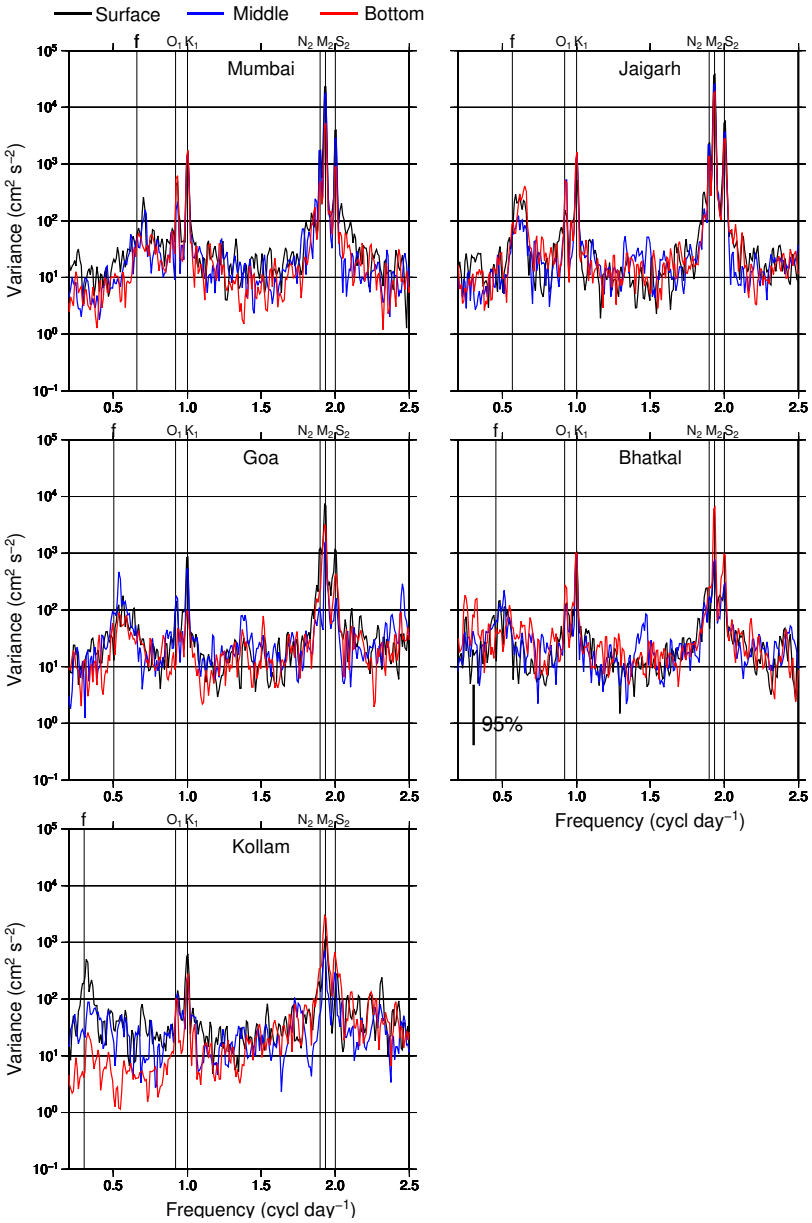

Figure 4.2 Same as Fig. 4.1 but for along-isobath currents

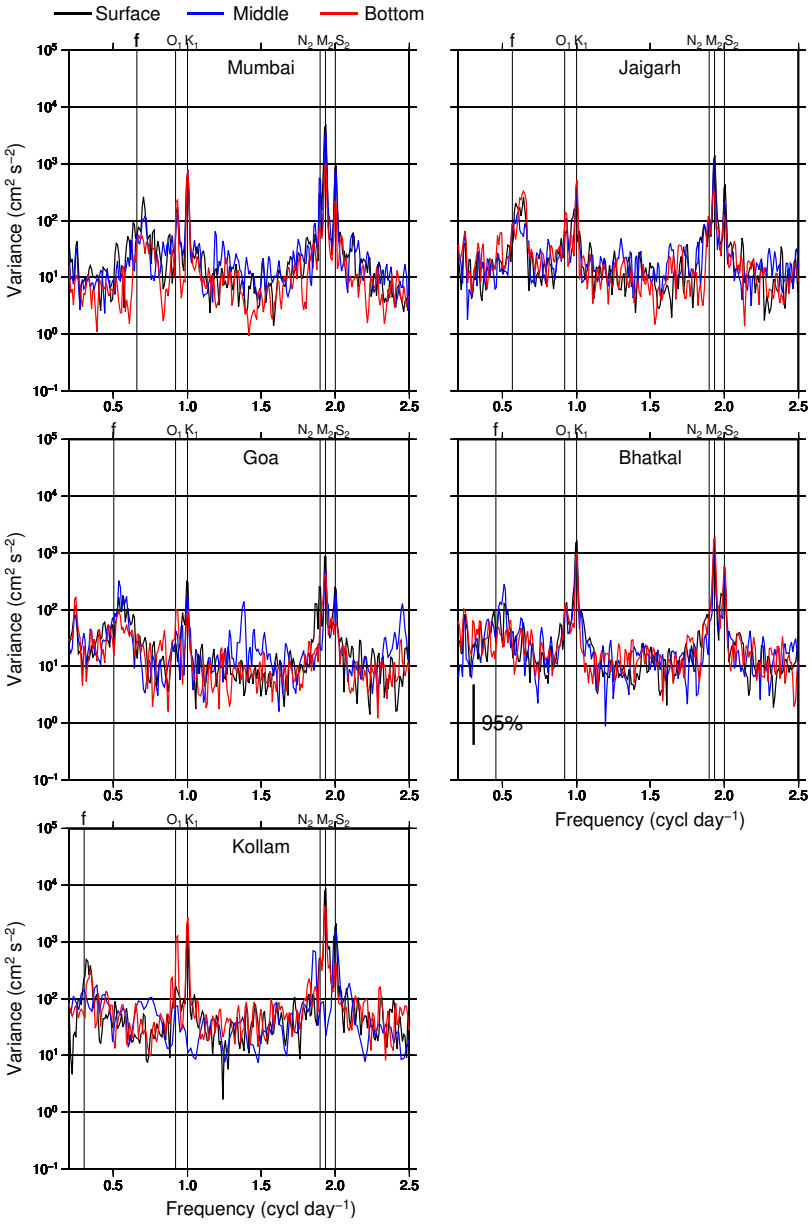

4.3.3 Barotropic tidal currents

The amplitudes of major tidal constituents obtained through the harmonic analysis applied to the full records of cross-isobath and along-isobath barotropic currents are shown in Fig. 4.5. In the

Figure 4.3 The vertical structure of sigma-t across the ADCP mooring locations for March, May and July. The density data were calculated from the revised climatology data of North Indian Ocean [Chatterjee et al., 2012]. Triangle indicates the location of moorings on the shelf. Contour interval is 0.5.

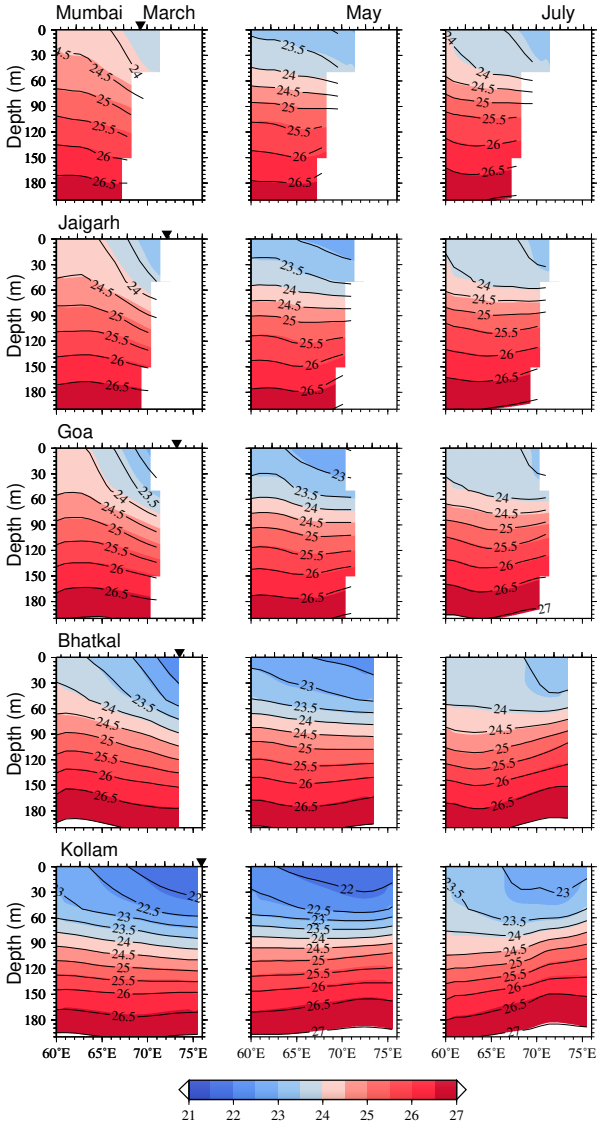

hierarchy of tidal constituents driving the barotropic tidal currents over the shelf off the WCI, the M_2 constituent is the largest, followed by K_1, S_2, N_2 and O_1. K_1 and S_2 have nearly comparable amplitudes while O_1 is the weakest among them (off Kollam, N_2 is the weakest constituent). Off

Figure 4.4 Vertically averaged buoyancy frequency for March and July. Buoyancy frequency was calculated using temperature and salinity data obtained from HYCOM reanalysis monthly averaged data for 2008. March and July represent premonsoon, SW monsoon seasons respectively. 100 m bathymetry contour is also shown.

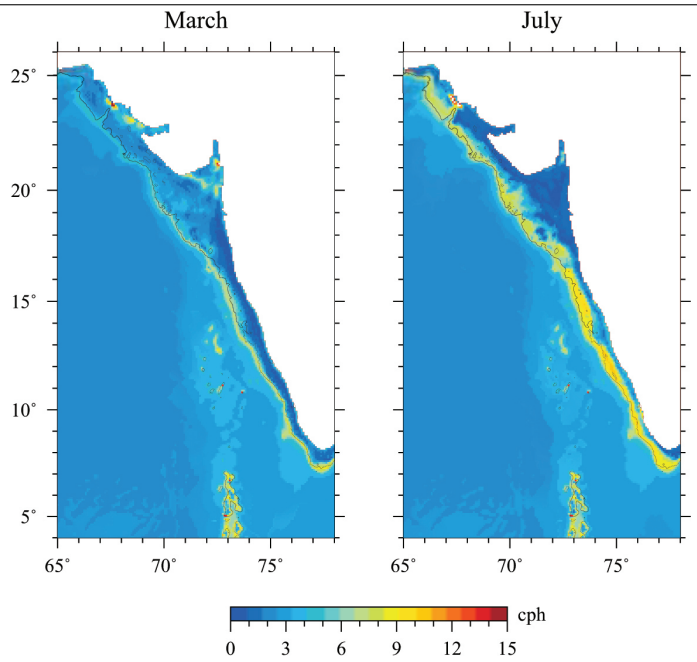

Jaigarh, S_2 is the second largest constituent. The amplitudes of semidiurnal constituents are found to be large off Jaigarh and Mumbai compared to those in the southern locations (Fig. 4.5). A comparison between the amplitudes of cross-isobath and along-isobath components of major tidal constituents shows that the cross-isobath component of BTs tend to increase towards north. Off Kollam, near the southern tip of the shelf, the tidal currents are oriented clearly in an along-isobath direction. But, off Bhatkal, both components have more or less same magnitudes. Further north, off Goa, Jaigarh and Mumbai, the cross- isobath component is stronger than the along-isobath component.

The relationship between eastward (U) and northward (V) components of barotropic currents is described in terms of ellipses. I determined the ellipses of M_2 and S_2 for semidiurnal (Fig. 4.6a) and K_1 and $O_1$for diurnal constituents (Fig. 4.6b). Ellipses were constructed for different 2-month periods of data to check the temporal stability of barotropic tidal currents. As seen

in Fig. 4.6, amplitudes of semidiurnal constituents do not vary appreciably with time, except off Kollam, where M_2 ellipse gets slight amplification in July-August period. Off Mumbai and Bhatkal, K_1 ellipses vary from March-April to those in May-August. The study also computed barotropic tidal constituents using entire velocity records (not shown). The study compared the values of semimajor axis obtained from successive 2-month data segments and the values obtained from the entire observation period. Most of M_2 and S_2 amplitudes obtained from former analysis vary within 10% from those obtained from the latter analysis. In March-April, ellipses of diurnal constituents off Mumbai and Bhatkal show 20-40% of variation of amplitude between the two analyses. Semimajor axes of K_1 and S_2 ellipses have about 40-60% of those of M_2. It is found that S_2/M_2 ratio is 0.4 to 0.6 on the shelf, which shows a pronounced spring-neap cycle. Velocity vector consistently rotates in clockwise direction, as expected in the Northern Hemisphere. At the southernmost location, off Kollam, the major axis of the ellipses of all the major constituents is oriented quasi-parallel to the isobaths. Off Bhatkal, the orientation of ellipses differs for different constituents. For example, the K_1 ellipse is inclined north-south (quasi-parallel to isobaths) while those of M_2 and S_2 are oriented east-west (quasi-perpendicular to isobaths). Further north, off Jaigarh and Mumbai, where shelf widths are larger than in the south, the ellipses are oriented more or less perpendicular to the isobaths. The semidiurnal tidal ellipses in these locations are much larger than those in the south.

4.3.4 Internal tidal currents

Internal tides time series

Fig. 4.7 shows the time evolution of cross-isobath internal tidal currents during a 15 day period in March and July. Variance profile for March and July is also shown (Fig. 4.7c). Baroclinic currents, bandpassed between 6 and 30 h are considered as internal tidal currents. This frequency band excludes inertial energy (The inertial period is 76.7 h and 35.0 h at 9° N and at 20° N, respectively), which is present substantially along the shelf (See Fig. 4.1 and 4.2). ITs on the shelf are intermittent in nature with irregular temporal variability. Figs. 4.7a and 4.7b show considerable difference between the amplitudes of IT from March to July. From the right panel of Fig. 4.7, it is clear that IT variance exhibits seasonal variability. ITs are found to be weak

Figure 4.5 The amplitude of different barotropic tidal constituents, obtained from the harmonic analysis of entire period of records of cross-isobath and along-isobath barotropic current. All constituents larger than 1 cm s^{-1} are shown in the figure. The red colour represents cross-isobath and green shows along-isobath barotropic velocity.

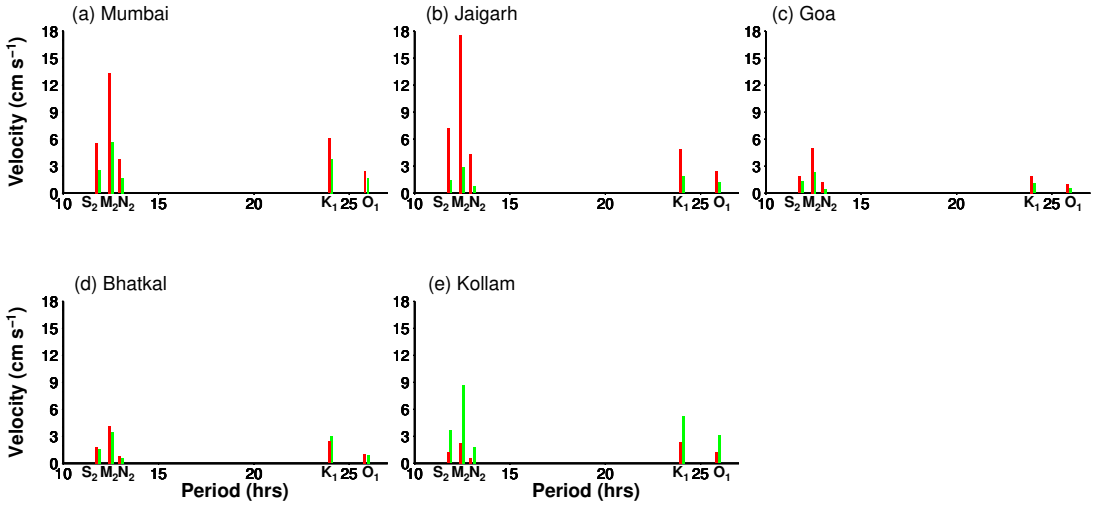

during March when the stratification is weak over the shelf. During July, when the stratification is high, ITs are found to be strong. Current-reversal always occurred at mid-depths (40-60 m, except off Kollam, where it occurred at 70-100 m depth) suggesting that current velocity is dominated by the first baroclinic mode motion in all the locations. Off Kollam, especially in March, the vertical structure is complex, where higher mode motions are also significant. I performed the EOF analysis for a detailed description of the vertical structure of baroclinic tidal currents on the shelf.

Rotary spectra

Fig. 4.8 shows the result of rotary spectra analysis of baroclinic currents at about 20 m depth during March to April and July to August. Clockwise (CW) spectrum dominated anticlockwise (ACW) spectrum in all IT and near-inertial frequencies, consistent with the propagation in Northern Hemisphere. This shows the presence of strong internal and near-inertial current on the shelf.

Figure 4.6 The spatial distribution of (a) semidiurnal (black circle is M_2 and dotted circle is S_2); (b) diurnal (black circle is K_1 and dotted circle is O_1) barotropic tidal ellipses along the shelf. Ellipses are obtained from the two month subsection analysis as indicated in figure label. Locations A (Mumbai), B (Jaigarh), C (Goa), D (Bhatkal) and E (Kollam) are shown. The sense of rotation of all ellipses is clockwise. The 100 m and 50 m depth contours are also shown.

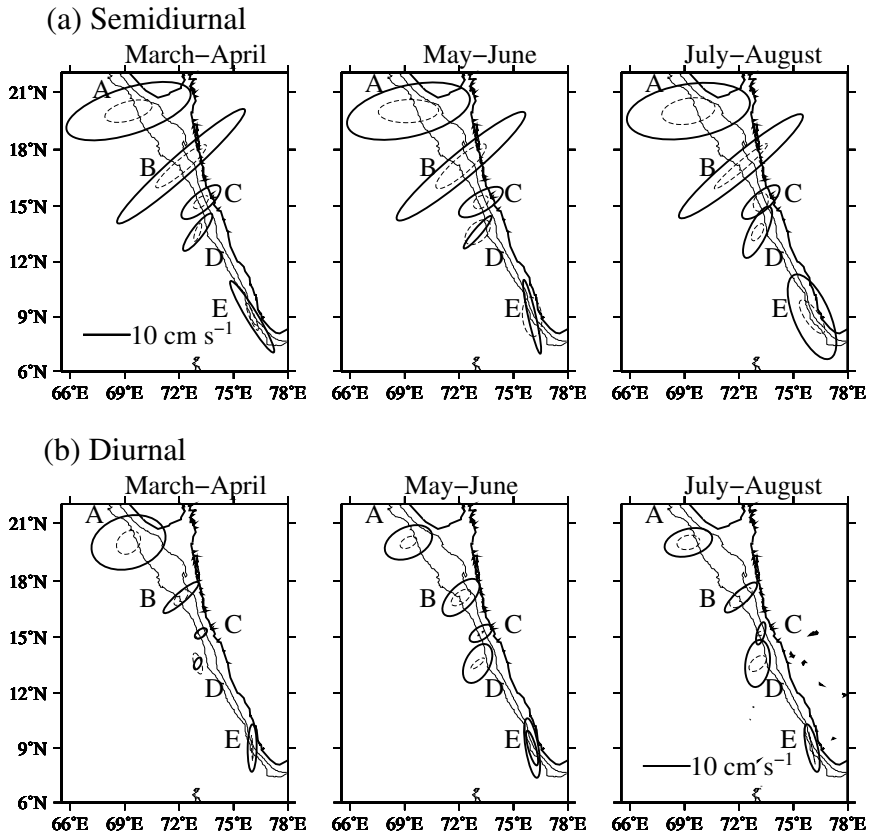

Large and broad peaks appear in the spectra of inertial currents with significant difference between CW and ACW energy (polarity, which is the ratio of CW and ACW, is greater than one). Though near-inertial currents are significant on the shelf, I restricted our discussion to tidal currents in the present chapter. In the tidal band, an energetic peak occurs at M_2 frequency with apparent clockwise rotation. Other than M_2, prominent peaks observed in semidiurnal are those of S_2 and N_2. Spectra show prominent peaks at diurnal frequencies, K_1 and O_1. Off Jaigarh and Kollam, diurnal band contributes to significant energy. Off Kollam, the difference between CW and ACW spectra

Figure 4.7 Band-pass filtered (6-30 hrs) cross-isobath internal tidal band during March and July. The observation period chosen for the analysis comprises first spring and neap cycle of barotropic tidal current. Varianceof IT in March and July($< u^2 + v^2 >$, where bracket indicates 1-month average) is also shown on the right panel.

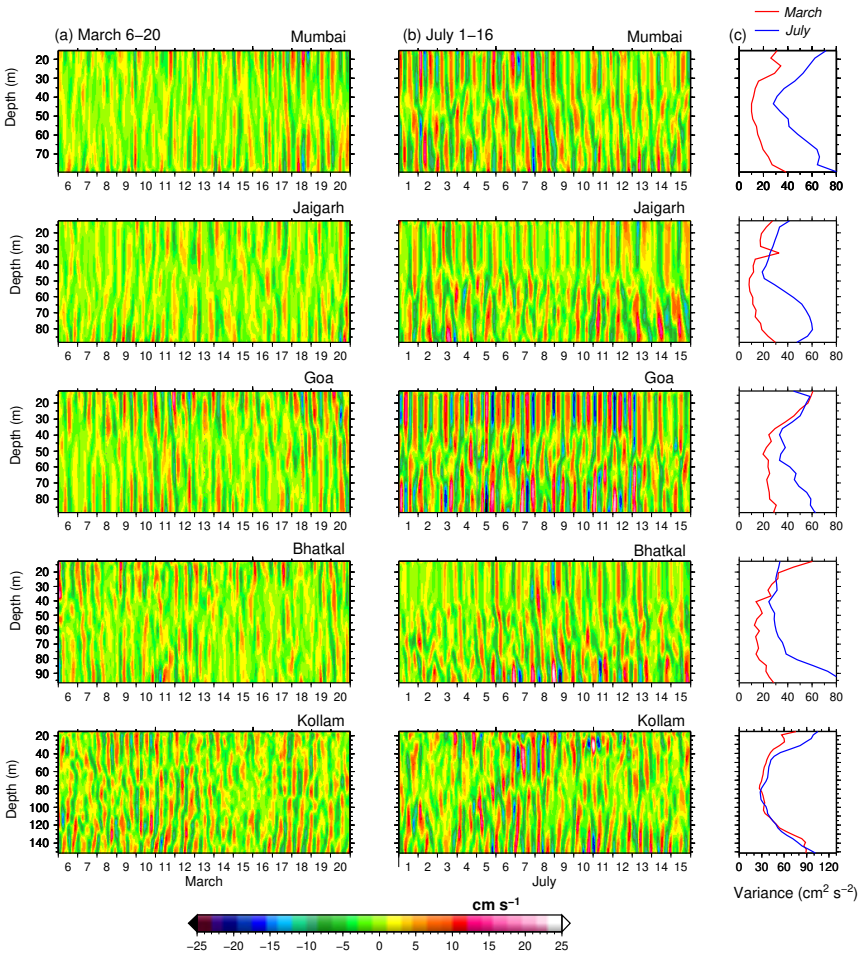

is small in K_1 (polarity is less than one). Off Goa and Bhatkal, CW component of diurnal IT energy is weaker compared to those in other locations. Other peaks emerge at higher harmonics like, M_4 and M_2+O_1 but comparatively with less energy. M_2+O_1 peaks are caused by the combination of semidiurnal and diurnal tides because of nonlinear interaction and advection of major diurnal and semidiurnal tides [Xu et al., 2013]. Figs. 4.8a and 4.8b indicate seasonal variation of M_2. Generally, during pre-monsoon period, CW component of M_2 energy is found to be weak and its

energy strengthens in SW monsoon period (Fig. 4.8). During pre-monsoon, its energy is found to be weaker than those in near-inertial (at all locations) and diurnal (Off Mumbai, Jaigarh and Kollam) frequencies. However, off Goa, M_2 energy is found to be stronger during pre-monsoon and there is no substantial strengthening of energy between spectra of March to April and July to August (Fig. 4.8). There is no considerable strengthening of energy in the diurnal spectra from pre-monsoon to the SW monsoon.

M_2 ellipses

To determine the vertical structure of semidiurnal ITs and their seasonal variations, I constructed M_2 baroclinic ellipses for different depths at different seasons. Fig. 4.9 shows the ellipses of M_2 IT obtained through harmonic analysis on baroclinic velocity for each 2-month period (March-April, May-June, and July-August). As seen from the previous section (Fig. 4.8), semidiurnal and diurnal IT spectra are broad, which include M_2, N_2, and S_2 (semidiurnal) and K_1 and O_1 (diurnal) frequencies. In semidiurnal frequencies, M_2 is the largest constituent in all locations, followed by S_2 and N_2. For example, during SW monsoon, S_2 contributes 40-60% of M_2 IT to the total for all the locations (except off Kollam, where S_2 is found to be very small). In this section, the study used M_2 ellipses to describe semidiurnal variability on the shelf.

Maximum value of semi-major axis of M_2 is found on the shelf off Mumbai (about 8 cm s^{-1}). Velocity maxima are always found in either near surface or near bottom depths (Fig. 4.9). Seasonal variation of M_2 IT is apparent on the shelf. For example, semi-major axis of M_2 off Mumbai varies from 1 cm s^{-1} to 8 cm s^{-1} during pre-monsoon to SW monsoon (Fig. 4.9a). It is interesting that, during most of the period of observations, M_2 IT is strong on the shelf off Goa. Even in the pre-monsoon season, M_2 IT is found to be strong (Maximum value of semi-major axis is about 5 cm s^{-1}) on the shelf off Goa. Here, M_2 IT strengthened during May-June and it weakened in July-August (Fig. 4.9c). To find out the month at which M_2 IT is really weakening, I conducted a running 1-month harmonic analysis (not shown) of baroclinic currents off Goa. This analysis shows that the M_2 ITs are strong in July and weak in August. Maximum value of semi-major axis off Goa during August is 2 cm s^{-1} which is much smaller than those during July when the corresponding value is 6 cm s^{-1}.

Figure 4.8 Clockwise and anticlockwise spectra of baroclinic currents at near surface (about 20 m) for all locations. Red color represents clockwise part and blue color represents anticlockwise part. Left panel (a) is for the pre-monsoon months (March-April). Right panel (b) is SW monsoon months (July-August). Theoretical inertial frequency ($f = 2\omega sin(\Phi)$) is also shown in figure.

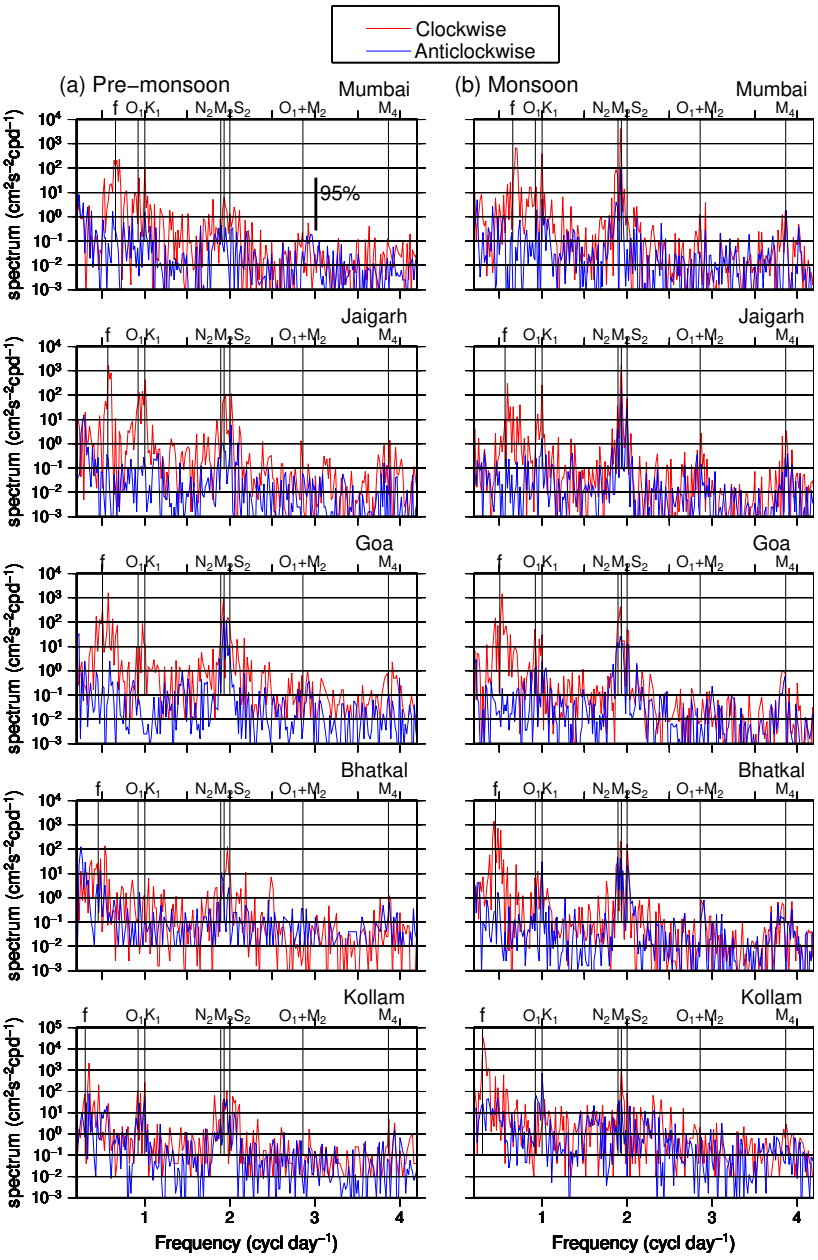

Figure 4.9 Baroclinic M_2 current ellipses at different depths from running 2-month harmonic analysis for the different moorings. MA indicates March-April, which is representative pre-monsoon month. MJ, JA indicate May-June and July-August which are the representative SW monsoon months. All ellipses, except those gray colored, rotate clockwise. Gray color indicates anticlockwise rotation. (a) Mumbai, (b) Jaigarh, (c) Goa, (d) Bhatkal and (e) Kollam.

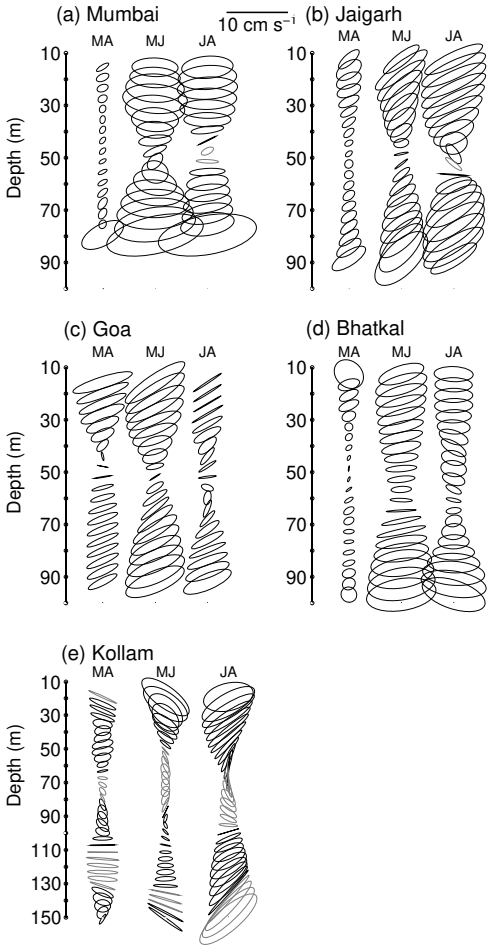

Most of the M_2 baroclinic ellipses are aligned in a cross-isobath direction. The baroclinic M_2 ellipses off Mumbai and Jaigarh (Figs. 4.9a and b) are aligned in the same direction of their barotropic ellipses (Fig. 4.6). The internal tidal ellipses are oriented in the same direction of energetic barotropic ellipses here. Off Goa, M_2 ellipses are oriented more in cross-isobath direction than their barotropic counterpart (Fig. 4.9c). Off Bhatkal also, M_2 ellipses are well aligned across

the isobaths, where ellipses are slightly inclined to the south of the barotropic ellipses. In both locations, during the time of strong IT, M_2 IT exceeded the barotropic M_2 currents. For instance, at near surface, semi-major axis of M_2 IT off Goa (Bhatkal) during May-June is 5.73 cm s^{-1} (5.71 cm s^{-1}) which is higher than those of barotropic ellipses, which are 5.3 cm s^{-1} (4.52 cm s^{-1}). This is more or less true for other semidiurnal constituents such as S_2 and N_2, and not evident in diurnal constituents. For example, off Goa, at near surface, semidiurnal S_2 (about 3 cm s^{-1}) and N_2 (about 4 cm s^{-1}) show larger amplitude than their barotropic counterpart (1.5 cm s^{-1} and 1.8 cm s^{-1}).

The length of semi-major axis is always found to be minimum at about 50 m depth (Fig. 4.9), except off Kollam, where they are found to be around 70 m (Fig. 4.9e), i.e., the minimum amplitudes of ellipses are always found at mid-depth of water column. Fig. 4.10b-d shows that the depth of minimum amplitude of M_2 ellipses varies slightly between 2-month periods, probably with the seasonal variation of pycnocline. Most of the M_2 ellipses rotate in clockwise direction, as expected for the internal tidal currents in the Northern Hemisphere. However, off Kollam, tidal ellipses tend to rotate anticlockwise in different depths (Fig. 4.9e).

K_1 ellipses

In diurnal internal tidal constituents, the largest is K_1 followed by O_1. K_1 ellipses are weakest off Goa and Bhatkal and strongest off Kollam. Off Kollam, K_1 has comparable magnitude to that of M_2 (Maximum velocity of K_1 is found about 6 cm s^{-1}, for M_2 it is about 5.9 cm s^{-1}) (Fig. 4.9e). Here ellipses are oriented mostly in an along-isobath direction. The sense of rotation is predominantly anticlockwise here during the time of SW monsoon. Off Mumbai and Jaigarh, during pre-monsoon, ITs are found to be stronger in K_1 than in M_2 (Figs. 4.9 and 4.10). Diurnal constituents also show variations in vertical structure of ellipses in different seasons, though not as prominent as in semidiurnal. The details of seasonal variation of diurnal internal current will be described in the following section. The absence of velocity minima at mid-depths suggests that the vertical structure of K_1 (Fig. 4.10) is more complex than that of M_2 (Fig. 4.9). O_1 is not shown since it is found to be small and the semi-major axis never exceeded 3.0 cm s^{-1} at any depths and for any other location, except off Kollam.

Figure 4.10 Same as Fig. 4.9 but for K_1

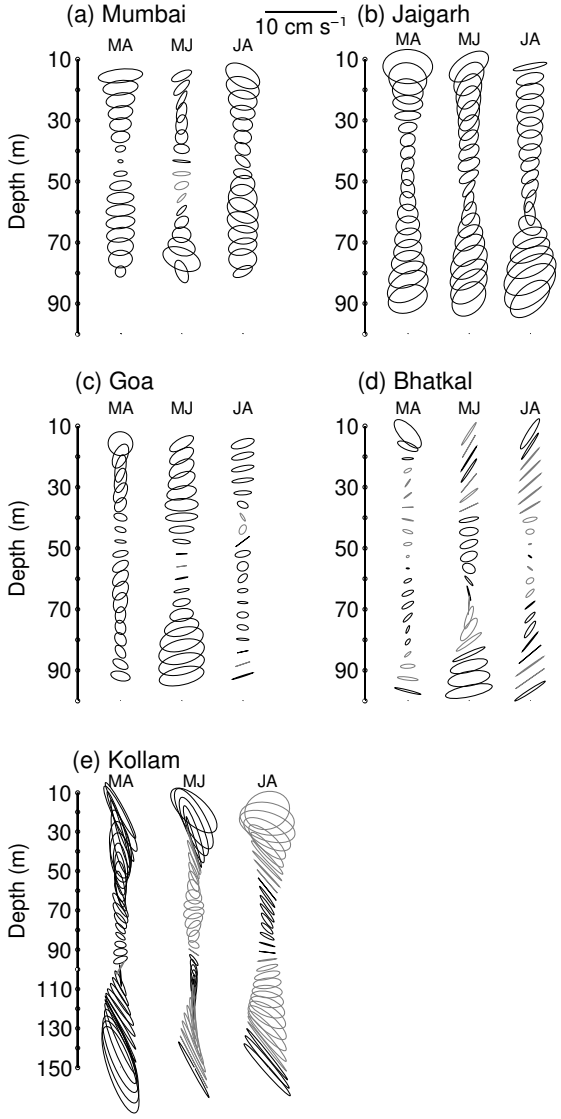

Temporal variation

To further address temporal variation of IT, I calculated depth-averaged variance ($u^2 + v^2$) for both semidiurnal (1.8-2.2 cpd) and diurnal bands (0.8-1.2 cpd) separately, which is shown in Fig. 4.11. I also calculated 2-month averaged (March-April and July-August) semidiurnal and diurnal baroclinic current variance with depth (Fig. 4.12). Prior to the analysis, a third order Butterworth filter was used to extract the semidiurnal and diurnal bands from rotated baroclinic currents.

Figure 4.11 Time series of baroclinic current variances ($u^2 + v^2$) at semidiurnal (1.8-2.2 cpd) and diurnal (0.8-1.2 cpd) frequency bands. (a) Mumbai, (b) Jaigarh, (c) Goa, (d) Bhatkal and (e) Kollam.

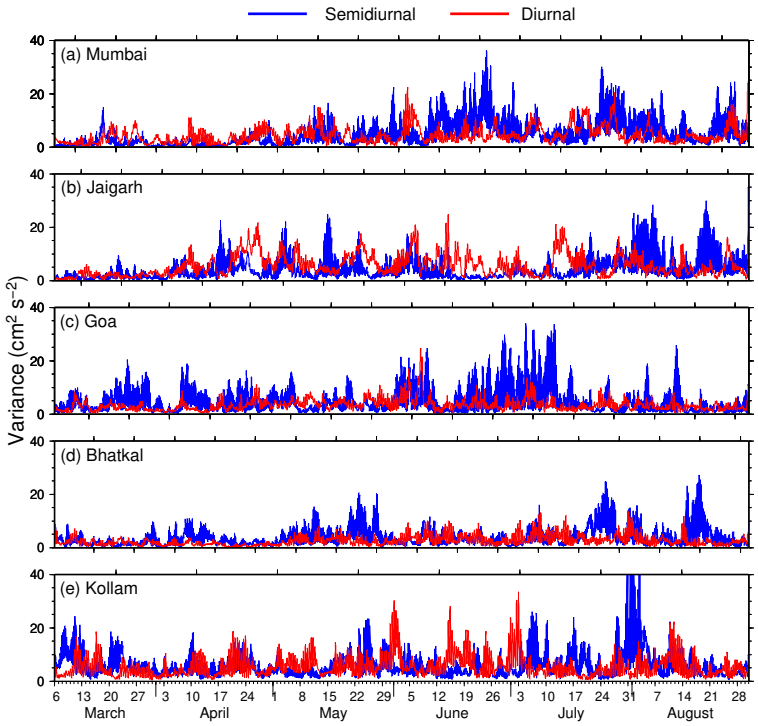

Semidiurnal and diurnal ITs exhibit spring-neap modulations (Fig. 4.11) and seasonal variations. Semidiurnal ITs are stronger in SW monsoon than those during pre-monsoon, which is consistent with the previous analysis. The shelf exhibits monthly and seasonal variations in diurnal ITs also. Off Goa and Bhatkal, diurnal kinetic energy is weak during the observation period. The strengthening of IT is not consistent during all the months of SW monsoon. The semidiurnal and diurnal variance tends to weaken from mid-July to August off Goa and from June to mid-July off Bhatkal. Minimum variance of IT is always found at mid-depths (Fig. 4.12). Off Mumbai, during March-April, ITs are stronger in diurnal band than in semidiurnal. Diurnal wind is well developed along the Indian west coast during February-April [Aparna et al., 2005]. However, there is no near-surface amplification of diurnal IT during these months (March-April) (Fig. 4.12), when land-sea breeze are present, indicating that the role of diurnal wind on the generation of IT may not be significant.

Figure 4.12 Average semidiurnal (1.8-2.2 cpd) and diurnal (0.8-1.2 cpd) bands variance $(u^2 + v^2)$ versus depth for pre-monsoon (March-April) and SW monsoon (July-August). Dotted (Thick) line indicates the variance for March-April (July-August).

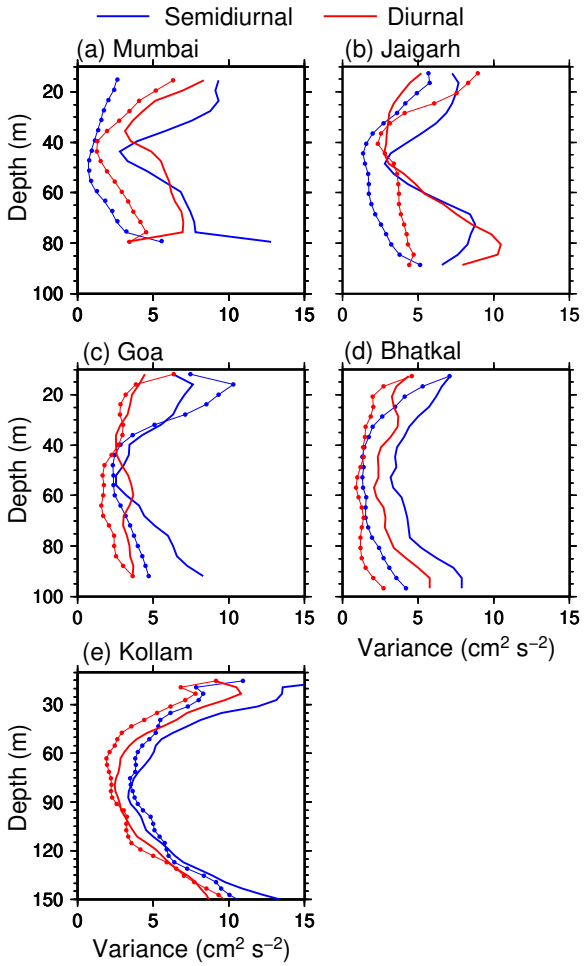

EOF analysis

EOF analysis was used to decompose the baroclinic tidal currents into vertical modes of variance. Prior to this, the cross-isobath component (U') and along-isobath component (V') of baroclinic currents for different 2-month periods were bandpassed for semidiurnal (1.8-2.2 cpd) and diurnal (0.8-1.2 cpd) ITs. The time series obtained were decomposed into various vertical modes (Figs.

4.13 and 4.14). To explain the seasonal variability of vertical structure of ITs, the study shows the results of EOF analysis for representative pre-monsoon (March-April) and SW monsoon (July-August) periods separately.

The analysis showed that the first three modes are sufficient to describe most of the variability in both semidiurnal and diurnal IT on the shelf, as they represent about 70-90% of total variance. The contribution from higher modes is much small and not shown. On the shelf, both semidiurnal and diurnal ITs are dominated by the first mode (Figs. 4.13 and 4.14). Mostly the vertical pattern of first mode velocity of V′ is similar to that of U′ but with weaker amplitudes. The variance of each mode varies from pre-monsoon to SW monsoon and also with locations. Variances of first mode semidiurnal IT increase from pre-monsoon to SW monsoon in all locations. On the northern shelf, off Mumbai, the first mode accounts for nearly 80% of cross-isobath semidiurnal internal tide during SW monsoon, which is only about 69% during pre-monsoon. Off Kollam, variance of the first mode semidiurnal (diurnal) is only about 58% (48%) during SW monsoon and the second mode explains 15% (23%) of the total variance (Fig. 4.13). This shows that the vertical pattern of IT is complex on the shelf off Kollam. Variance of the second mode cross-isobath diurnal ITs is slightly higher than that of semidiurnal. This indicates that diurnal IT has more complex vertical structure than that of semidiurnal. The zero-crossing of the first mode lies between 40 and 60 m. However, off Kollam, first mode zero-crossing lies between 70 and 100 m. Off Jaigarh, zero-crossing point of first mode diurnal IT changes from 40 m to 60 m from pre-monsoon to SW monsoon, which is more or less consistent with vertical pattern of K_1 ellipses (Fig. 4.10). The modal structure of the first mode obtained from EOF analysis more or less agrees with the vertical pattern of ellipses determined from the harmonic analysis for all locations.

Shear analysis

Fig. 4.15 shows the computed vertical shear $((\frac{\partial u}{\partial z})^2 + (\frac{\partial v}{\partial z})^2)$ field, caused by the semidiurnal and diurnal band of internal tidal currents. The baroclinic tides induced small-scale vertical shear in the velocity fields on the shelf. The intermittent vertical shear is noticed at all locations in semidiurnal and diurnal bands. Shear induced by semidiurnal baroclinic tidal current is relatively weaker than that due to diurnal. Semidiurnal shear is found to be large at mid-depths of the water

Figure 4.13 EOF analysis of cross-isobath semidiurnal and diurnal baroclinic tidal currents for different locations for 2-month periods: pre-monsoon (March-April) and SW monsoon (July-August)are shown. The vertical structure of first three modes for semidiurnal IT is shown in left panels (a) and same for diurnal internal tide is shown in right panels (b).

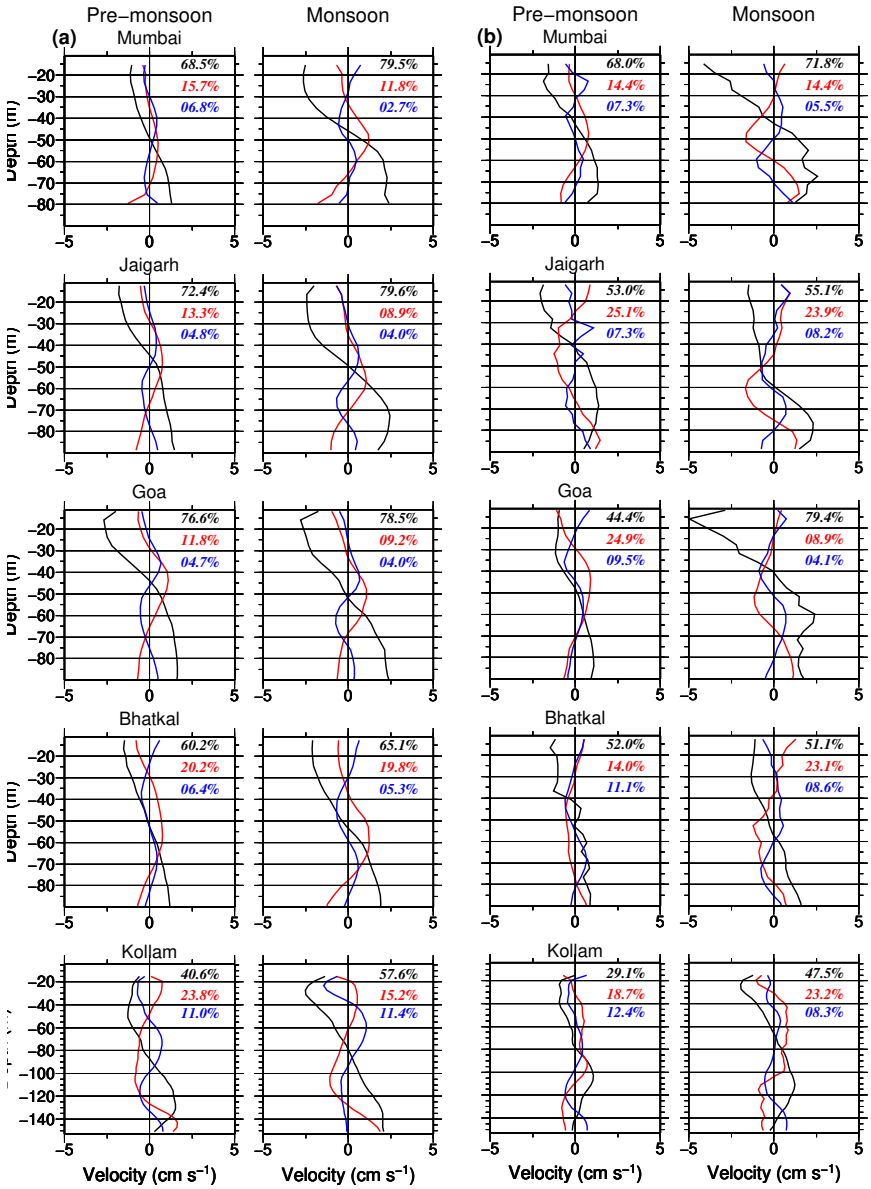

column (40-60 m), where the current reversal occurs. Diurnal shear spreads at different levels of water column. As seen in the previous section (Figs. 4.13 and 4.14), semidiurnal and diurnal IT is dominated by the first mode, where the zero crossing is found at mid-depths. This is consistent with shear maxima, which are also found at mid-depths. However, vertical structure of diurnal IT is more complex (Figs. 4.13 and 4.14), where higher mode motions are also substantial, and they induce shear at different levels of water Column.

Coherent and incoherent internal tides

To understand the intermittency of ITs on the shelf off WCI, the coherent and incoherent ITs were separated out for ITs. Here the coherent signal implies the predictable component that can retain a constant phase and amplitude over a given time period [Nash et al., 2012], so that it can be resolved by harmonic analysis. The incoherent IT greatly varies in time so that it cannot be resolved by the harmonic fits over a given time span. Incoherent IT can be obtained by subtracting harmonic fits from the band-passed signals. The capability of harmonic analysis to resolve ITs varies in different time windows due to the intermittency of ITs associated with background variability such as stratification, mesoscale eddies, currents, etc., which vary in different timescales. The analysis was carried out on both semidiurnal and diurnal bandpassed ITs. Coherent ITs are defined as the ITs, which retain constant phase and amplitude during the entire time period of observation. First, a third order Butterworth filter was applied to baroclinic currents to obtain broadband semidiurnal and diurnal IT time series. Harmonic analysis was done on both semidiurnal and diurnal bands and the result was considered as coherent signal. Three major semidiurnal constituents (M_2, S_2, and N_2) were kept in the control file to do the harmonic analysis of semidiurnal band. For harmonic analysis of diurnal internal tide, two major diurnal constituents (K_1 and O_1) were used. The harmonic analysis output was subtracted from bandpassed time series and the remainder was considered as incoherent signal. The capability of harmonic analysis to resolve the internal tides from the broadband signal was estimated by applying skill score test [Murphy, 1988; Nash et al., 2012].

$$SS_T = 100\% \times \left[1 - \frac{\langle (u\prime - H_T(u\prime))^2 \rangle}{\langle u\prime^2 \rangle}\right] \tag{4.1}$$

Where u' is the band-passed cross-isobath internal tide, which includes either semidiurnal or

Figure 4.14 Same as Fig. 4.13 but for along-isobath baroclinic tidal currents.

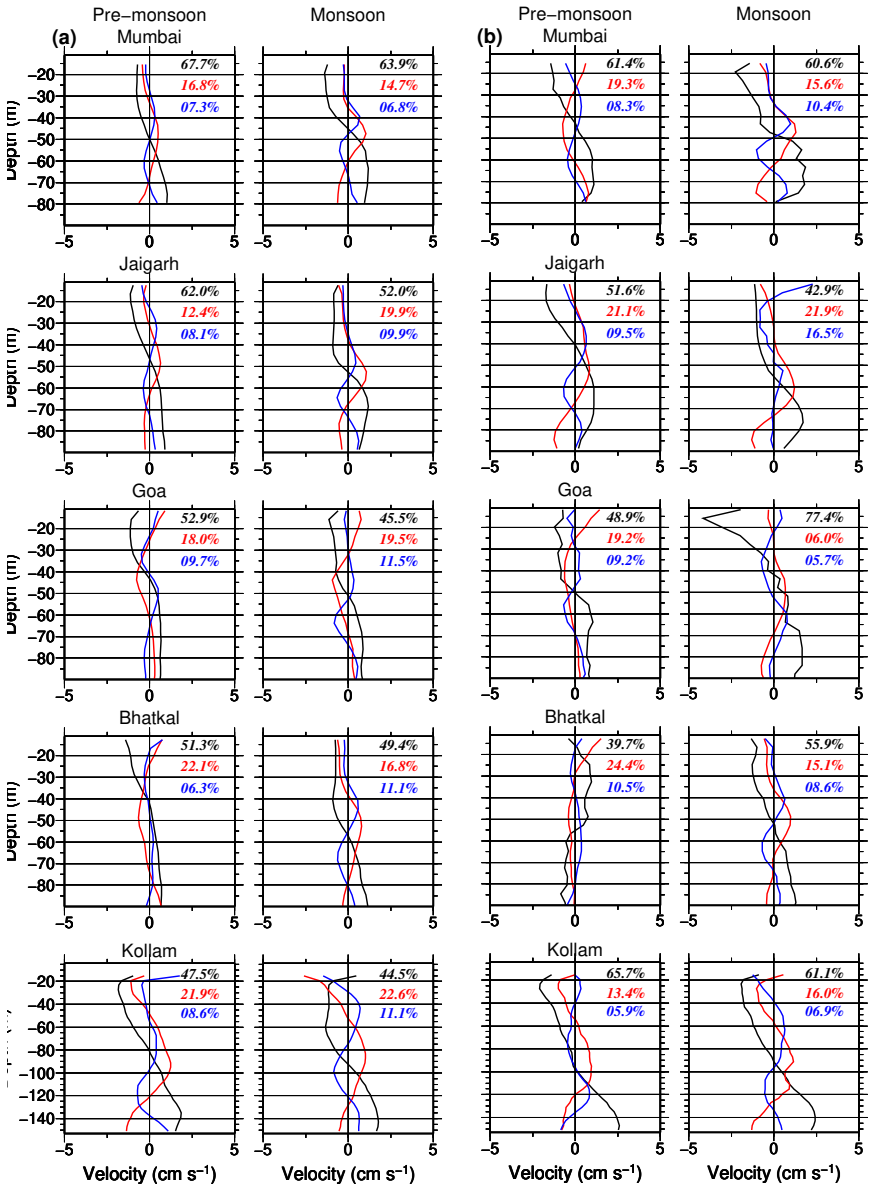

diurnal bandpassed signals. $H_T(u')$ is the output from harmonic analysis. After subtracting the coherent IT from the band-passed signal, all the values were squared and averaged over time and depth. The value was then divided by the averaged band-passed signal over time and depth for the

Figure 4.15 Time evolution of the vertical shear (s^{-1}) of semidiurnal and diurnal baroclinic tidal currents. I chose the first 15 day period starting from July 1^{st} to estimate the variations in shear field. Shear was calculated over 4 m interval.

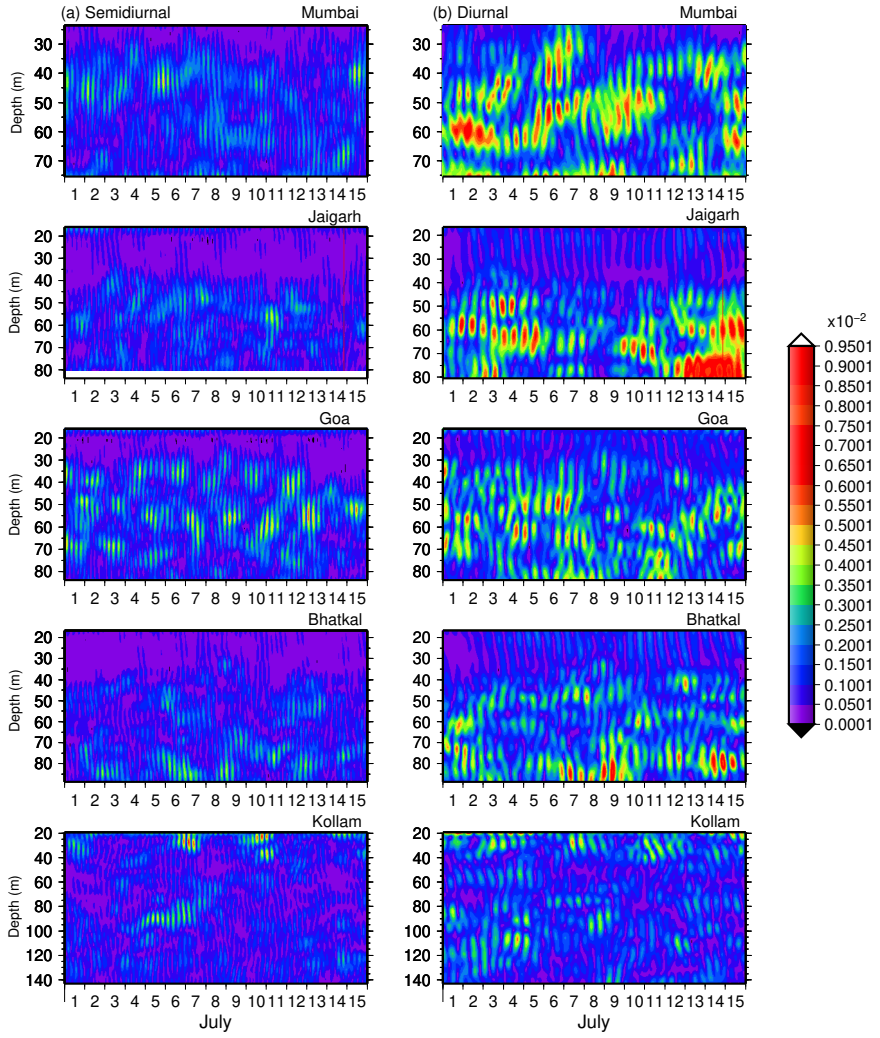

same period. 100% SST implies that the harmonic analysis captures all the observed variance. The capability of harmonic analysis to resolve internal tides varies from location to location (Table 4.2). The skill score values show that shelf experiences large incoherent internal tides, that is the part unresolved by harmonic analysis.This indicates the background variability such as stratification, mesoscale eddies and currents play an important role in determining IT variability on the shelf.

Compared to semidiurnal IT, diurnal IT is more intermittent in all locations, except off Kollam. Off Kollam, cross-isobath diurnal IT shows a relatively strong coherent nature.

Table 4.2 The percentage of predictability. Skill score (Eq. 4.1) was calculated and the predictability was determined. Observations for the period March to August (Table 3.1), were taken for the harmonic analysis.

Location	Semidiurnal		Diurnal	
	U (%)	V (%)	U (%)	V (%)
Mumbai	20	14	9	7
Jaigarh	26	10	20	15
Goa	10	6	7	5
Bhatkal	22	12	5	5
Kollam	6	7	5	28

4.4 Discussion and Conclusions

Observations from five ADCP moorings along the shelf off the WCI revealed the presence of significant barotropic tidal currents on the shelf associated with varying internal tidal current in different frequencies. Current spectra show narrowband signals at four tidal frequencies (M_2, S_2, K_1 and O_1), and a broad frequency band signal at near-inertial frequencies.

4.4.1 Barotropic tidal current

In the southernmost location (Kollam), tidal currents propagate clearly in an along-isobath direction. Further north, tidal currents tend to be oriented in a cross-isobath direction. On the northern part of the shelf (off Mumbai and Jaigarh) barotropic tidal currents are strong. Semidiurnal tidal currents are found to be stronger on the northern part of the shelf (off Mumbai and Jaigarh) and they contribute to most of the energy of barotropic currents. It is found that, off Jaigarh, semi-major axis of semidiurnal barotropic tidal ellipses are larger by about three times than those off Goa. This shows that the semidiurnal barotropic tidal currents considerably increase towards the north, from a narrow shelf to a wider shelf (Fig. 4.6a). But, there are no significant variations noticed in the diurnal tidal currents from south to north (Fig. 4.6b). Shelf width plays an important role in the amplification of semidiurnal tidal currents off Mumbai and Jaigarh.

4.4.2 Internal tidal current

The detailed analysis of the tidal currents off the WCI, using data from long-term mooring revealed the presence of strong ITs on the shelf, which are confined mostly to semidiurnal and diurnal periods. The baroclinic tidal currents on the shelf show variations in amplitude and in their vertical structure from pre-monsoon to monsoon periods. Formation or generation of IT requires density stratification as a prerequisite. During May, isopycnals are quasi-horizontal and the surface density is low. A strong thermocline, sandwiched between upper and bottom homogenous layer (Tri-layer structure) is common in Indian coastal waters off the west coast during SW monsoon [Kumar et al., 2005, 2006]. This may enhance the IT generation on the shelf. Kumar et al. [2010] showed that the degree of vertical stratification and the amplitude of high-frequency IT are directly related on the shelf of the northeast coast off WCI (22.13° N and 68.62° E). This may be true for all the locations discussed in this study, where IT amplitudes are directly related to the seasonal density variations on the shelf. In general, the amplitude of ITs shows a tendency to increase with increasing stratification, as noted elsewhere on the shelf region of the world ocean (for instance, Holloway [1984]; Huthnance and Baines [1982]).

Though the amplification of M_2 IT from March-April to May-June is observed off Goa, there is a dampening of M_2 observed during July-August. Off Goa, upwelling becomes stronger from August onwards [Antony and Unnikrishnan, 1993], which may tend to cause the water column to be homogenous and inhibit the generation of IT to some extent. This feature had been reported in other regions, especially in upwelling regions [Aguirre et al., 2010; Rosenfeld, 1990]. This cannot be fully confirmed, as there was no real time temperature and salinity measurements during the time of ADCP observations.

During the presence of strong IT off Goa, Bhatkal and Kollam, cross-isobath M_2 ITs are found to be larger in magnitude than their barotropic counterparts. But at the same time, for the along-isobath component, the barotropic component is prominent. This is found in other semidiurnal constituents (S_2 and N_2) and not in diurnal constituents. This lack of coherence in the cross-isobath and along-isobath component could be due to the difference in the generation mechanisms of internal tidal currents. The cross-isobath component of semidiurnal internal tidal current might have been generated due to the incidence of BT at the slope region and then directed towards the

shore. On the other hand, the along-isobath component of internal current might be generated due to the direct local forcing. These results are consistent with the results reported earlier [Shenoi et al., 1988]. Off Jaigarh and Mumbai, barotropic tidal currents are found to be more energetic than IT.

The first mode of baroclinic current is dominated by M_2, which contributes significant energy to IT. Our study shows that baroclinic tidal currents in most of the locations on the shelf off the WCI are dominated by the cross-shelf propagating first mode M_2, as reported on many other shelf regions [Holloway, 1983, 1984; Sherwin, 1988]. However, off Kollam, internal tidal currents are weaker in cross-isobath direction compared to along-isobath direction. Relatively weak cross-isobath barotropic forcing component could be one reason for the presence of weak cross-isobath IT. Higher mode internal tidal currents are also significant in different locations. The exact generation site of these internal currents is unknown and rather difficult to explain using the available data. I shall address this issue in Chapter 6 using numerical simulations. Higher modes of internal tidal currents present in semidiurnal and diurnal ITs are probably generated on the shelf or from nearby regions since small vertical scale waves cannot propagate far from the source of generation [Laurent and Garrett, 2002].

During the occurrence of strong internal tidal currents, shear is evolving at different depth levels intermittently (Fig. 4.15). Small-scale vertical shear is present at different depth levels due to semidiurnal and diurnal internal tidal currents, with a maximum found at mid-depth. In surrounding depth levels, shear is possibly generated by the superposition of different vertical modes of IT. In fact, the barotropic and baroclinic currents over the shelf off the WCI are complex in nature. Results from numerical modelling will be used to explain the observed characteristics of tidal currents in this region.

Chapter 5

Tidal currents on the continental slope

5.1 Introduction

In the present chapter, the characteristics of tidal currents on the continental slope off the WCI is discussed. The locations on the slope include Mumbai (20° N), Jaigarh (17.2° N), Goa (15.1° N) and Kollam (9° N). Though the analyses were carried in above locations, emphasis was given on the IT characteristics on the slope off Jaigarh, as this region is characterized by the presence of strong ITs. Off Jaigarh, the presence of strong cross-shore barotropic forcing is favorable for the generation of IT. The chapter deals with an analysis of the ADCP, CTD and satellite altimeter data off Jaigarh to describe the characteristics of ITs in a region, where the ITs are very large. The characteristics of ITs in other three slope locations of ADCP measurements are also discussed. The mechanism of generation of ITs is addressed in detail using numerical model simulations, which will be discussed in Chapter 6.

Oceanography off the WCI varies mainly in two seasons; southwest (SW) monsoon (May-September) and northeast (NE) monsoon (October-December). The ADCP data used in the present analysis covers three periods, the pre-monsoon (March-April), SW monsoon, and the first 20 days in October (October is the transition period between SW monsoon and NE monsoon). The west coast experiences the low-frequency seasonally reversing coastal current, known as the West India Coastal Current (WICC). The WICC flows equatorward during SW monsoon and reverses and flows poleward during NE monsoon [Shetye et al., 1990, 1991]. Another characteristic feature is

Figure 5.1 Clockwise rotary spectra of horizontal currents. Data for the month of January 2014 were taken for the analysis. The spectra were estimated at each layer of the water column and averaged over vertical. For the location on the shelf break (c), the spectra were averaged over the entire water column. For the locations on the slope (a, b, d), spectra were averaged for upper water column. The depths taken for averaging are given on the top of each panel. The vertical dotted lines indicate the dominant frequencies. The black dashed line is $\omega^{-1.5}$, where ω is the frequency given in x-axis. The slope of the spectra is consistent with the slope of GM spectra which varies from $\omega^{-1.5}$ to ω^{2} (Ref Fig. 5.14). f is the Coriolis frequency.

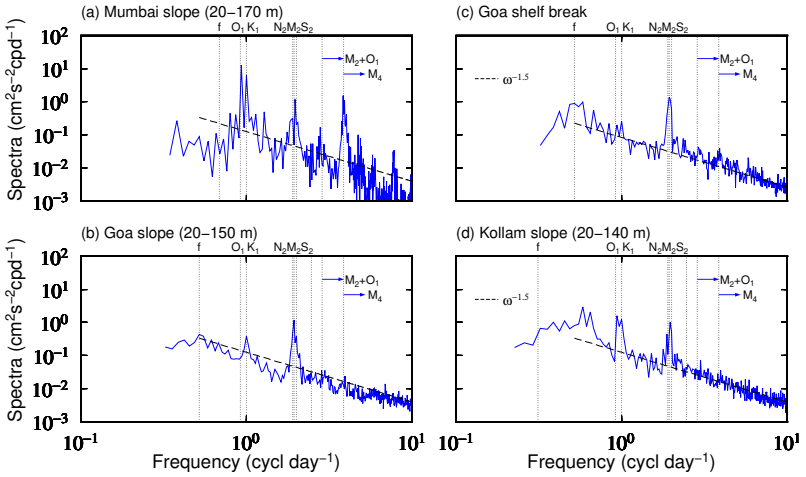

the seasonal upwelling present during SW monsoon [Shankar et al., 2005; Shenoi et al., 2005; Rao et al., 2008].

The chapter is organized as follows: Section 5.2 describes the characteristic features of tidal currents on the slope off Mumbai, Goa and Kollam. Section 5.3 gives a detailed description of ITs off Jaigarh. Section 5.4 discusses the possible causes of generation of IT in terms of criticality parameter and barotropic forcing off Jaigarh. Section 5.5 deals with the near-inertial waves (NIWs) off Jaigarh. Section 5.6 summarises and concludes the findings of the Chapter.

5.2 Tidal currents on the slope off Mumbai, Goa and Kollam

In this section, the characteristic features of IT on three slope locations, Mumbai, Goa and Kollam, off the WCI is described using data from ADCP records for the year 2014 (Table 3.1). The

Figure 5.2 Same as 5.1, but for counterclockwise (CCW) spectra.

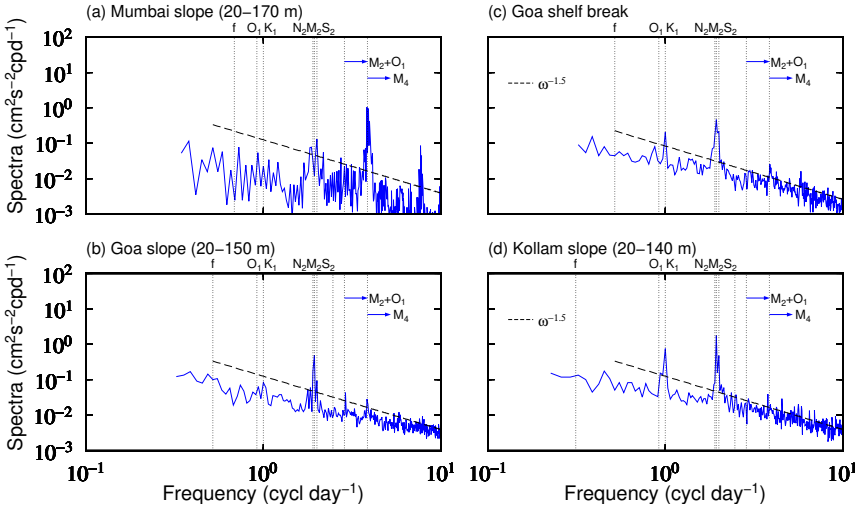

dominant frequencies and temporal variations of ITs on the slopes are described. During this period, simultaneous data were available for three locations. The same data will be used for model validation in Chapter 6 (Section 6.4). Besides, ADCP data available at a location on the shelf break off Goa during the same period were also used to study the shelf-slope variability of ITs and characteristics of propagation. Measurements on shelf break were not made for the other two locations.

5.2.1 Current spectra

Clockwise and counterclockwise rotary spectra of currents are shown in Figs. 5.1 and 5.2 respectively. For the data on the shelf break, the rotary spectrum was calculated on baroclinic currents and for data on slope locations, the calculation was carried out on the raw data. As the barotropic tidal currents could not be removed from observations on the slope, all the analyses were carried out on the total currents at these locations. Rotary spectra were computed using the data for the month of January 2014. IT energy peaks at semidiurnal, diurnal and higher harmonics like quarter-diurnal frequencies. On the shelf and slope off Goa, diurnal ITs are found to be weak. Diurnal IT is strong on the slope off Mumbai and Kollam. Off Mumbai, clockwise spectrum shows energetic peaks at diurnal frequencies, however, the counterclockwise spectrum does not. Off Kollam, both

Figure 5.3 M_2 tidal ellipses for three slope locations (a) Mumbai, (b) Goa, and (c) Kollam. The black (gray) color represents ellipse with clockwise (anticlockwise) rotation. Harmonic analysis was carried out on the data for the period January, 2014. The scale of ellipse is given below. The depths at the three locations are 1134, 958, and 1118 m respectively.

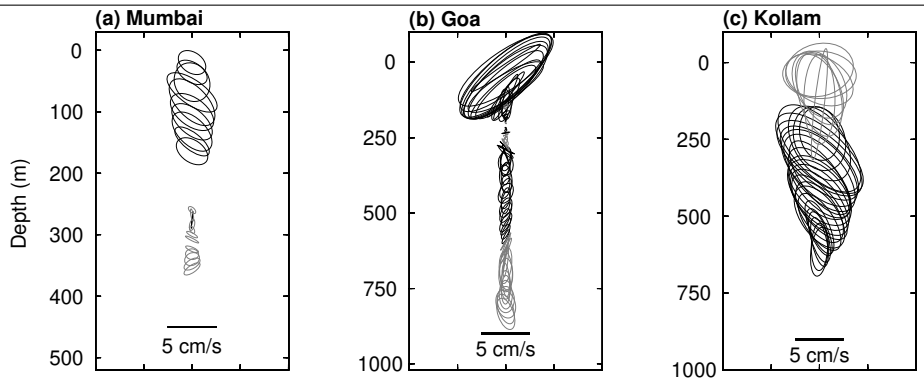

clockwise and counterclockwise spectra show strong peaks at diurnal frequencies. The slopes of spectrum are smooth ($\omega^{-1.5}$), which is less steep than the GM spectra (ω^{-2}).

5.2.2 Tidal ellipses

Figs. 5.3 and 5.4 show the tidal ellipses for M_2 and K_1 respectively in three slope locations Mumbai, Goa and Kollam. Harmonic analysis was carried out on the raw data for January 2014. Barotropic currents were not removed from the raw data. As there were no full depth water column data available, removing barotropic part is not possible. However, barotropic global model (OTIS) output extracted for these locations shows that barotropic tidal currents are weak (maximum rms value of 2 cm s^{-1}) compared to the total tidal currents (maximum rms value of 16 cm s^{-1}). This shows that the variability of tidal currents is dominated by ITs.

In general, M_2 ITs are stronger compared to the other constituents. For instance, semimajor axis of M_2 ellipse in Goa at 23 m depth is 6 cm s^{-1} and that of K_1 ellipse is 1 cm s^{-1}. However, slope off Mumbai experiences strong K_1 ITs. The magnitude is even higher than that of M_2. For example, the magnitude of K_1 at 20 m depth is 5 cm s^{-1} (Fig. 5.4), whereas that of M_2 is 1.5 cm s^{-1}. Off Goa, M_2 ITs are strong in upper water column. The vertical structure of M_2 ellipses off Goa (Fig. 5.3b) shows that the ITs are dominated by the first baroclinic mode. However, vertical

Figure 5.4 Same as in Fig. 5.3, but for K_1.

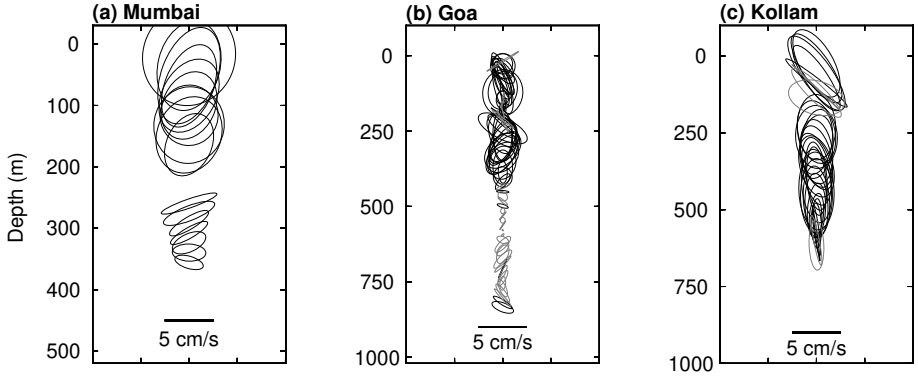

structures of K_1 ITs off Goa are found to be complex with multiple zero crossings. This shows the importance of higher modes in diurnal ITs in the region. Off Kollam, M_2 ITs and K_1 ITs show comparable magnitudes. Off Kollam, M_2 ITs are found to be intensified in middle depths (Fig. 5.3c).

5.2.3 Time series

Fig. 5.5 shows time series of M_2 and K_1 tidal currents constructed from harmonic analysis of U component of velocity. Figs. 5.6 and 5.7 show the bandpassed tidal currents for semidiurnal and diurnal bands respectively. To understand the shelf slope variation of ITs off Goa, the data available for a location on the shelf break was also analysed. On the shelf break off Goa, semidiurnal ITs are found to be bottom intensified (Figs. 5.5 and 5.6). The amplitude of semidiurnal IT reaches up to 10-15 cm s^{-1} at the bottom of the water column. Semidiurnal barotropic velocity on the shelf break is moderate (4-5 cm s^{-1}), however, velocity of IT exceeds BT on the shelf break. This indicates that the shelf break off Goa is a potential IT generation site. A clear upward energy propagation of IT at the bottom on the shelf break (Figs. 5.5b and 5.6b) also indicates the local IT generation. Semidiurnal IT on the slope off Goa is relatively weak compared to those on the shelf. Strong downward propagating IT packets are found near 700-800 m depth on the slope off Goa during 02^{nd} to 4^{th} January (Fig. 5.6c), coinciding with the presence of strong IT on the shelf break (Fig. 5.6b). This may be the ITs originating from the shelf break and propagating down the slope. Off Kollam, the semidiurnal ITs are found to be intensified at mid depths (300-600 m,

Figure 5.5 M_2 and K_1 tidal currents during January, 2014. Amplitude and phase of M_2 and K_1 obtained from harmonic analysis of U currents were used for constructing the tidal currents. Depths of the mooring locations are given in Table 3.1

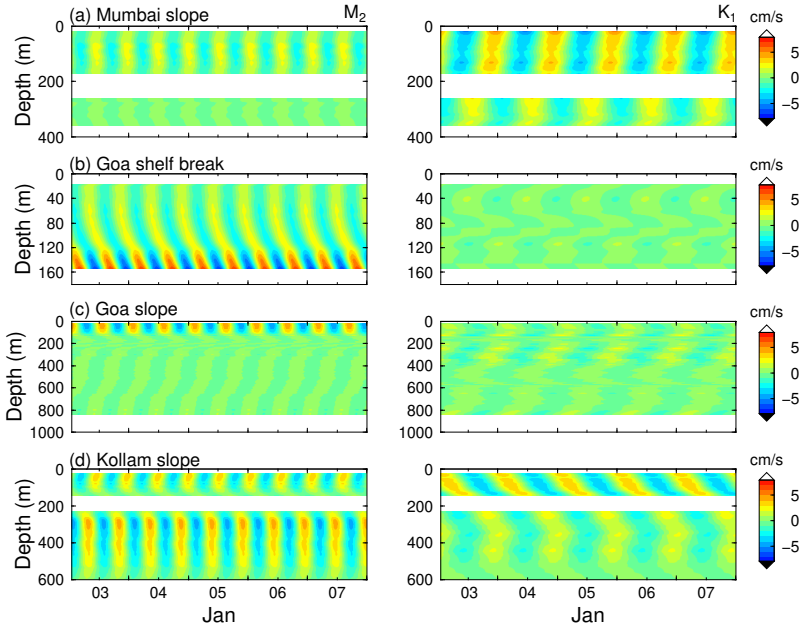

where the depth of water column is 1100 m). Diurnal ITs are weak on the slope and shelf off Goa, but strong off Mumbai and Kollam (Figs. 5.5 and 5.7). Diurnal ITs show complex vertical structure with intermittent patches (Figs. 5.7).

Fig. 5.8 and 5.9 show the vertically averaged rms values ($< \sqrt{u^2+v^2} >$, where brackets indicate averaging over vertical) of semidiurnal and diurnal IT for January to August. On the slope off Goa, the surface water column data (18-150 m, see Table 3.1 for more details) was not taken for averaging due to their bad quality from month of May onwards. Semidiurnal ITs on the shelf off Goa experience spring-neap variability (Fig. 5.8a). Though temporal variations are present, ITs are found to be strong during the entire period of observations. Unlike on the shelf off WCI, seasonality in IT is not apparent in the slope locations. However, it cannot be confirmed whether this argument is true on the surface water column on the slope off Goa, as ADCP mooring data were not available in 18-150 m depth, restricting the seasonal analysis. On the shelf break off Goa, maximum IT activity is found during August.

Figure 5.6 Semidiurnal bandpassed tidal currents on the slope. (a) Mumbai, (b) Goa (shelf break), (c) Goa and (d) Kollam.

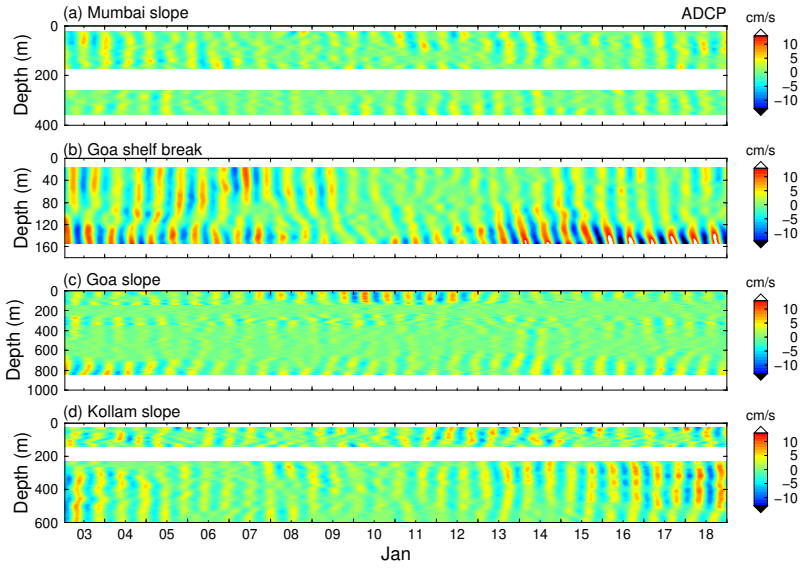

Figure 5.7 Same as 5.6 but for diurnal tidal currents.

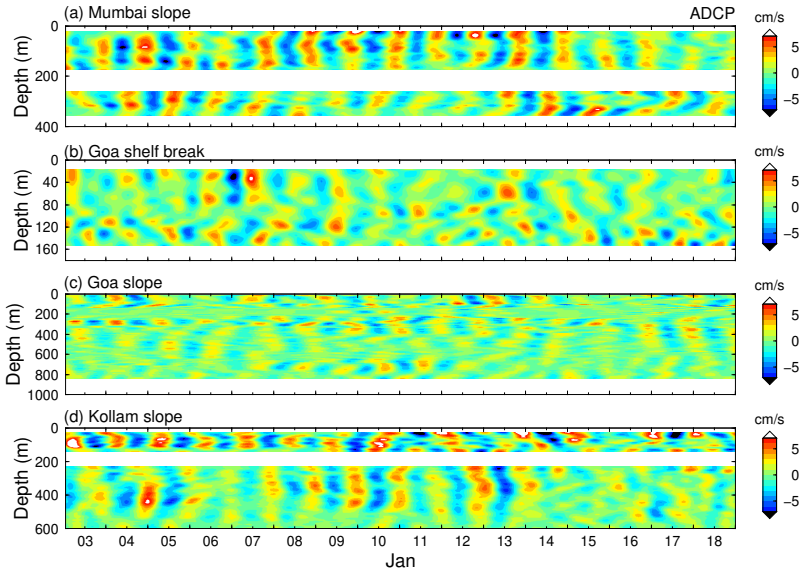

5.3 Internal tides on the shelf and slope off Jaigarh

The shelf region off Jaigarh is particularly significant from an IT point of view due to the presence of large amplitudes of M_2, S_2, K_1 and O_1, where all four major tidal constituents have significant

Figure 5.8 Vertically averaged RMS ($< \sqrt{u^2 + v^2} >$, where brackets indicate averaging over vertical) value of semidiurnal tidal currents. The surface water column data off Goa (18-150 m: See Table 3.1 for more details) was not taken for averaging due to their bad quality. The blue line overlaid is the 14 day low passed tidal signal.

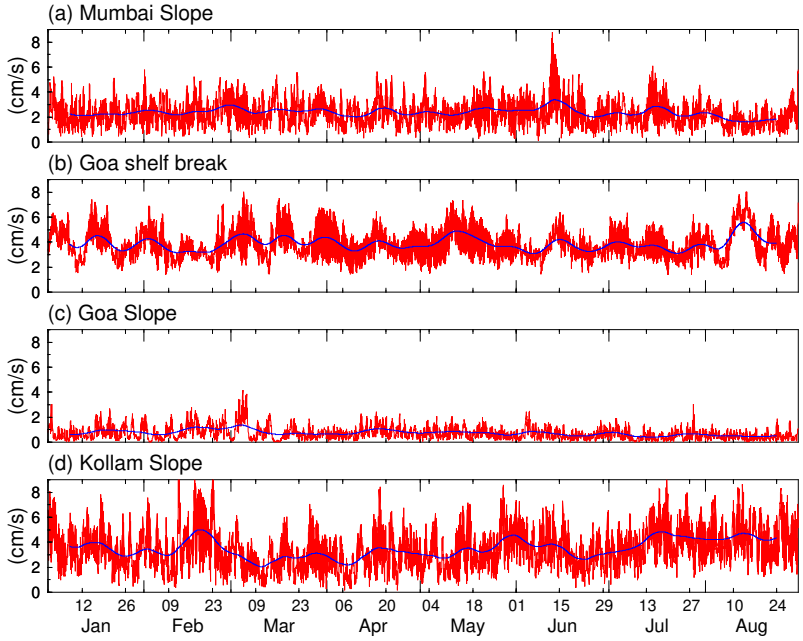

amplitudes and a prominent spring-neap cycle. The continental shelf in the southern part of the Indian west coast is narrow (about 85 km at 9° N) which broadens gradually towards the north, reaching to about 140 km at Jaigarh (17° N). The central WCI is characterized by the presence of large semidiurnal tides [Unnikrishnan et al., 1999]. The wide continental shelf in the northern part is believed to generate strong barotropic tides and thereby expected to be one of the strong generation sites for baroclinic tides. Moreover, the ellipses of all major tidal constituents are aligned in a cross-shore direction. Off Jaigarh, M_2 barotropic tidal currents are about three times larger than those off Goa (15° N). It is found that the variations in seasonal stratification strongly influence the IT on the shelf region; especially ITs are found to be weak during pre-monsoon when the stratification is weak, and it is strong during SW monsoon when the stratification increases. Baines [1982*b*] estimated the internal tidal energy fluxes of semidiurnal components (M_2, S_2) at different continental shelf-slope regions of the world, including the northern part of the shelf off

Figure 5.9 Same as 5.8 but for diurnal ITs.

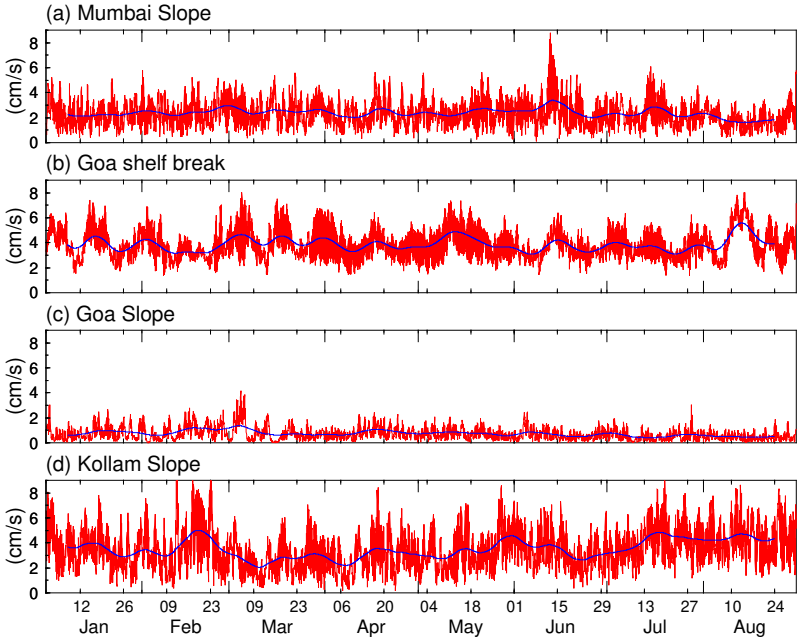

WCI (Porbandar-Goa, 21°-16° N), and showed large conversion of barotropic to baroclinic energy taking place in the region. Their study showed that the regions having wide continental shelves make a substantial contribution to the global internal tidal energy flux.

In this context, I analysed the data off Jaigarh to describe the IT characteristics in detail. Apart from this, there was also some additional supporting data available off Jaigarh. For instance, a deep ocean CTD time series was available, which enabled to understand IT activity away from shelf and slope region. Moreover, a CTD transect across the shelf-slope was used to understand possible generation sites and characteristics of propagation of ITs. A brief description of NIW observed on the shelf and slope is also given.

5.3.1 Surface signatures of internal tides from satellite altimetry

Before going into the detailed analysis of the ADCP data, I show the presence of M_2 and K_1 ITs in the region as observed in satellite altimeter data. The aim of this section is to describe the broad characteristics of ITs on the slope and deep regions (water depth $>$ 500 m) off the WCI. Fig. 5.11 shows that the two ascending tracks of the satellites nearly cross the shelf break at right angles.

Figure 5.10 Locations of ADCP moorings. The two triangles are the locations of the shelf and slope ADCP moorings. Two lines are the satellite tracks, TOPEX/Poseidon-Jason-1-Jason-2 (T/P-J1-J2) and TOPEX/Poseidon-Jason-1 (T/PN-J1N), across the shelf-slope. Distance scale of satellite track is given at the top middle of the figure. The locations of 13 CTD casts across the slope-shelf region are shown. The green dots are the CTD casts along the shelf made during the February 2008 cruise and blue are the same made during April cruise. Barotrpic M_2 (black bold line) and K_1 (red dotted line) ellipses for both shelf [Subeesh et al., 2013] and slope locations are shown. The amplitude scale bar for the ellipse is given in upper right. Two hourly CTD profiles were conducted from the deep location off Jaigarh (pentagram in red color) from 30th June to 10th July as a part of Arabian Sea Monsoon Experiment (ARMEX) which was carried out during summer monsoon 2002 [Shankar et al., 2005]. The water depth of the location is 2250 m. Right inset map shows the WCI where the red box is the study area.

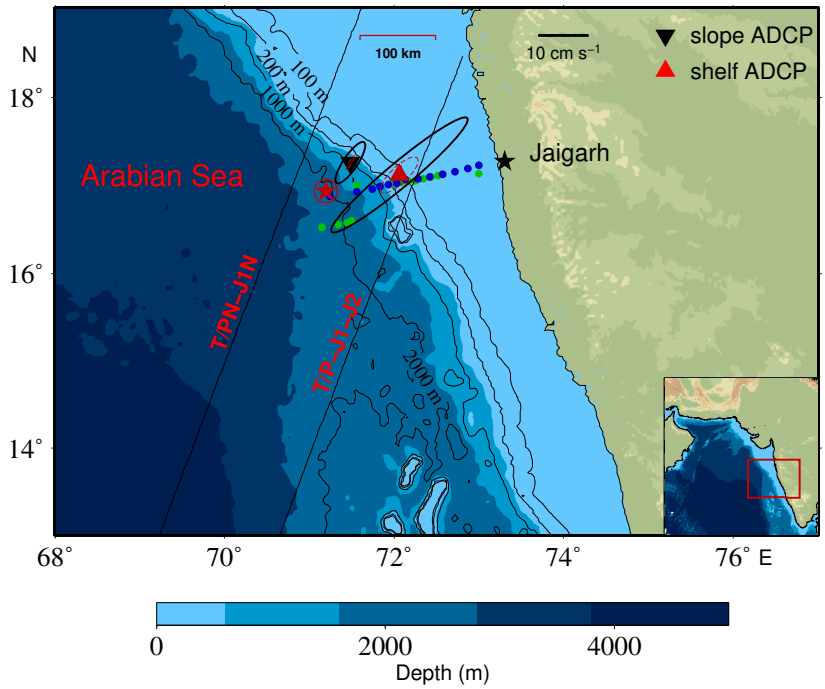

The barotropic ellipses on the shelf in this region are also oriented nearly perpendicular to the shelf (Fig. 5.10) so that I can expect the altimeter to capture the IT signal. The study used a high pass filter ($<$ 1000 km) in space to remove the barotropic part from the satellite-derived tide. Satellite measurements over the shallow region (water depth $<$ 500 m) were discarded from the analysis. I also used a global tidal model, FES2012 [Carrère et al., 2012], to remove the barotropic signal

Figure 5.11 (a-d) M_2 and K_1 ITs along the two ascending tracks, TOPEX/Poseidon-Jason-1-Jason-2 (T/P-J1-J2) and TOPEX/Poseidon-Jason-1 (T/PN-J1N) tracks. The black lines denote the IT obtained by the high-pass filtering (<1000 km) of along-track amplitude of the tidal constituents and blue lines denote the IT obtained by subtracting barotropic tidal constituents from along-track amplitude of tidal constituents. The barotropic tidal constituents were extracted from the global tidal model, FES 2012 output, for the two tracks. (e) Topography along the two tracks is shown. The black filled curve denotes the bottom topography along the T/P-J1-J2 track and red line is the topography along T/PN-J1N track. Along-track wavenumber spectra of the (f) M_2 and (g) K_1 are shown in the right panel. The two arrow marks in f and g denote the peaks in wavelengths at 125 km and 270 km respectively.

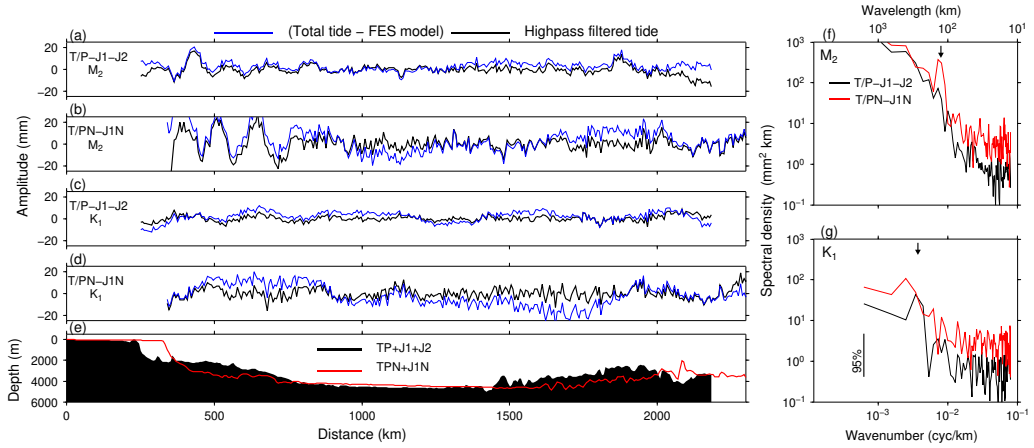

from the total tide. The amplitude of barotropic tide for each constituent, M_2 and K_1, at every satellite measurement point was extracted from the model output and subtracted from the total signal. Fig. 5.11 shows the along track amplitudes of M_2 and K_1 ITs obtained from the above two methods. The pattern of outputs from both methods visibly matches well. The RMS error between the two methods lies in 2-6 mm. Fig. 5.11 shows oscillation of M_2 and K_1 ITs along the two tracks. Towards the shelf region, the amplitude of oscillation is found to be high and it reduces towards the deep water. This is true in both tracks. This suggests that the shelf-slope region off Jaigarh could be a possible generation site of ITs, with IT propagating away from the region of generation. Spectral analysis of the M_2 and K_1 ITs reveals peaks at wavelengths near about 125 km and 270 km (Fig. 5.11f and g) respectively. The M_2 peak is more clearly visible in T/PN-J1N track than that in T/P-J1-J2 track. Theoretical wavelengths of M_2 and K_1 in the deep ocean were calculated from the phase-speed of the first mode baroclinic wave, which is about 2.4

m/s [Chelton et al., 1998]. The wavelengths of M_2 and K_1 for these values are 112 km and 250 km respectively. The spectral peaks occur close to the theoretical values (Figs. 5.11f and g). Spectral energy mainly peaks at first mode IT and higher mode peaks are relatively small.

5.3.2 Ocean stratification

In this section, I describe the hydrographic observations at a location close to the slope mooring location. Fig. 5.10 shows the CTD observations from three cruises, which were carried out in February, April and June. The CTD measurements during February and April were taken in the same year as that of ADCP observations while measurements in June were taken in 2002. The available hydrographic data cover three seasons. (1) February represents winter, (2) April falls in the pre-monsoon and (3) June represents SW monsoon period. In February, the mixed layer depth is found to be shallow (15 m) even in the presence of 30 m isothermal depth. In February, salinity values are found to be low (about 34.7) in the surface layers as compared to those in other months (35.8 and 36 in April and June respectively). The plausible reason for salinity decrease at the northern region is the advection of low saline waters from the southern region during NE monsoon by the WICC [Naqvi, 1991]. The low saline waters might have a role in determining the shallow mixed layer depth in February. This indicates that salinity has an important role in the stratification of the region. During the pre-monsoon period, upper ocean layers start to warm due to the increased intensity of short-wave radiation. During the starting period of the SW monsoon May and June), sea surface temperature becomes maximum, which decreases gradually with the progress of the SW monsoon. The mixed layer in April and July is found to be relatively deep (36 and 25 m respectively) compared to that in February. The values of buoyancy frequency (N) are almost similar in all the above three months, where the depth-averaged N is about 3 cph in all the three months.

5.3.3 Normal mode decomposition

In a continuously stratified ocean, internal waves can be represented by the vertical normal modes [Kundu and Cohen, 1990]. For a flat bottom, the baroclinic modes for vertical displacement $\Phi(z)$ can be estimated by solving the equation (5.1), an eigenvalue problem, under hydrostatic, inviscid

Figure 5.12 Hydrography profiles and the baroclinic normal modes for February, April and June at the slope location. (a) Temperature and salinity profiles (b) Density and buoyancy frequency (c) Normalised baroclinic modes for vertical displacement (d) Normalised baroclinic modes for horizontal velocity. Speed of each mode (m s^{-1}) is given in the figure.

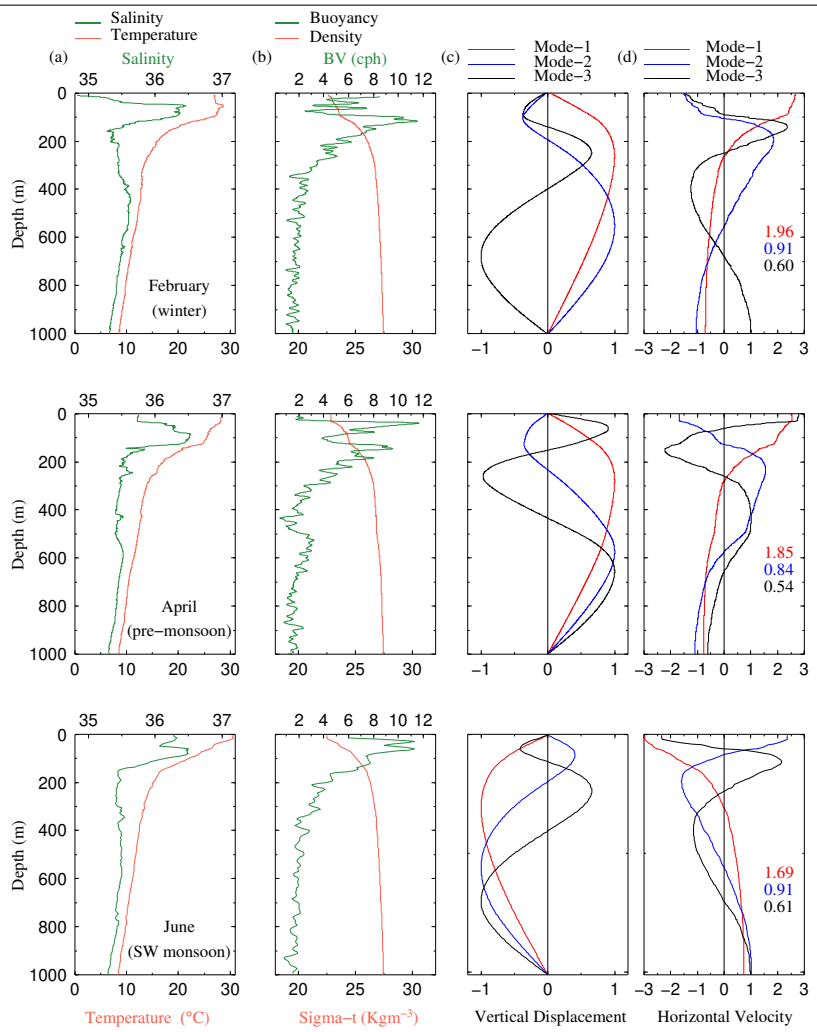

and the Boussinesq approximations.

$$\frac{d^2\Phi(z)}{dz^2} + \frac{N^2(z)}{c_n^2}\Phi(z) = 0 \tag{5.1}$$

For the horizontal velocity, the equation is,

$$\Pi(z) = \rho_0 c_n^2 \frac{d\Phi(z)}{dz} \tag{5.2}$$

Where $\Phi(z)$ is the eigenfunction, c_n is the eigenvalue for n^{th} mode, and ρ_0= 1028 kg/m^3 is the reference density. The displacement, $\Phi(z)$ depends only on the buoyancy frequency $N(z)$ and the water depth. For a constant stratification, the equation can be solved analytically. For varying stratification, the equation must be solved numerically by setting a boundary condition at the sea floor and sea surface ($\Phi(0) = \Phi(-H) = 0$ at $z = 0$, $z = -H$ respectively). All the motions are confined into these boundaries so that the waves are reflected from boundaries and propagate horizontally. $\Phi(z)$ and $\Pi(z)$ describe the modal structures for vertical and horizontal velocity of internal waves respectively. Strictly, the normal mode decomposition is valid for a flat horizontal topography for vertically standing waves. However, several studies [Klymak et al., 2011; Lee et al., 2012] show that the normal mode decomposition is useful on the slope regions. Once a solution is obtained, the phase speed (c_p), group speed (c_g) and horizontal wavenumber (k_x) of ITs with frequency ω can be derived from the dispersion relation as follows

$$c_p = \frac{\omega}{(\omega^2 - f^2)^{\frac{1}{2}}} c_n \tag{5.3}$$

$$c_g = \frac{(\omega^2 - f^2)^{\frac{1}{2}}}{\omega} c_n \tag{5.4}$$

$$k_x = \frac{(\omega^2 - f^2)^{\frac{1}{2}}}{c_n} \tag{5.5}$$

Fig. 5.12 shows buoyancy frequency profiles near the slope mooring and the first three baroclinic modes for vertical displacement and horizontal velocity in three representative months of different seasons. Mode-1 of the horizontal velocity has a node at 250 m; mode 2 has two nodes at 100 m and 600 m. The speed of the first mode internal wave is about 1.6-1.9 m/s on the slope. The linear first mode speed is 2.4 m/s in deep water off the slope [Chelton et al., 1998]. The phase speed, group speed and the wavelength of major tidal constituents were calculated from equations 5.3-5.5 (Table 5.1). Though the variation of stratification is small in the three different months, the phase speed and wavelength of the IT for each constituent are found to vary from month to month. The largest values are found in February and the smallest in June (Fig. 5.12, Table 5.1). This reveals that even a small change in stratification influences the propagation of ITs in the region.

Table 5.1 Phase speed (C_p), Group speed (C_g) and Wavelength (λ) of the first three modes of M_2, S_2, K_1 and O_1 ITs on the slope location. Normal modes were computed from the CTD data of February, April and June.

		M_2			S_2			K_1			O_1		
	Mode	C_p m/s	C_g m/s	λ km	C_p m/s	C_g m/s	λ km	C_p m/s	C_g m/s	λ km	C_p m/s	C_g m/s	λ km
Feb	1	2.0	1.8	91.1	2.0	1.8	87.8	2.3	1.6	203.5	2.4	1.5	228.4
	2	0.9	0.9	43.0	0.9	0.8	41.4	1.1	0.7	096.0	1.1	0.7	107.7
	3	0.6	0.5	28.0	0.6	0.5	27.0	0.7	0.4	062.6	0.7	0.4	070.3
Apr	1	1.9	1.7	86.9	1.9	1.7	83.7	2.2	1.5	194.1	2.3	1.4	217.9
	2	0.8	0.8	39.2	0.8	0.8	37.8	1.0	0.6	087.6	1.0	0.6	098.4
	3	0.5	0.5	25.2	0.5	0.5	24.3	0.6	0.4	056.3	0.6	0.4	063.2
Jun	1	1.8	1.6	79.0	1.8	1.6	76.1	2.0	1.4	176.4	2.1	1.3	198.0
	2	1.0	0.9	42.5	0.9	0.9	50.0	1.1	0.8	095.0	1.1	0.7	106.6
	3	0.6	0.6	28.5	0.6	0.6	27.4	0.7	0.5	063.6	0.8	0.5	071.4

5.3.4 Isopycnal displacement

I estimated the isopycnal displacements determined from a 9-day 2 hourly time series CTD data [Shankar et al., 2005], made in July 2002 at a deep slope location (Fig. 5.10) (16.94° N, 71.19° E, water depth 2250 m) about 43 km away from the slope ADCP mooring. The isopycnal displacements were calculated from the density anomaly as follows.

$$\rho'(t,z) = \rho(t,z) - \bar{\rho}(z) \tag{5.6}$$

Where $\bar{\rho}(z)$ is the time-mean density

$$\eta(t,z) = \frac{\rho'(t,z)}{d\bar{\rho}/dz} \tag{5.7}$$

Where $\eta(t,z)$ is the amplitude of IT oscillation. The large isopycnal oscillation in diurnal and semidiurnal periods (Fig. 5.13) shows a significant IT activity in the water column. The magnitude of observed η varies between 5 m and 30 m, with maximum values found at about 100 m depth. Barotropic tidal currents for the same observation period obtained from OTIS output are also shown (Fig. 5.13a). Internal tides follow the barotropic tide indicating that a large fraction of ITs in the region is phase locked with the barotropic tides. This is consistent with the previous results from the satellite altimetry (Fig. 5.11), where significant coherent IT is present in the deep region off the slope. The spectral analysis shows oscillations at tidal frequencies M_2 and K_1 and at higher frequencies (Fig. 5.13c).

Figure 5.13 (a) Barotropic tidal current (BT) from OTIS output. (b) First 9-day density record in July 2002 computed from the temperature and salinity time series observation over the deep location off Jaigarh (shown in Fig. 1). (c) Power spectra of isopycnal displacement at 100 m. The dotted curve denotes the Garrett-Munk spectrum for the vertical displacement based on N=2 cph.

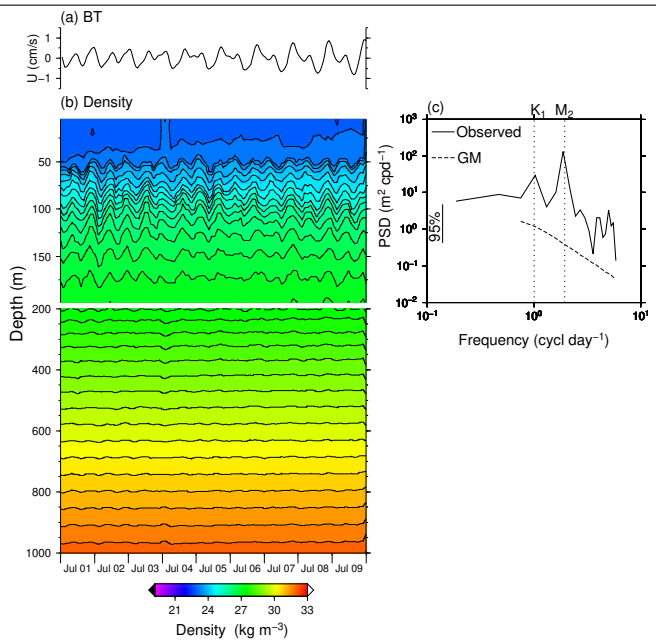

The Garrett-Munk internal wave spectra (Equation 5.8) for vertical displacement [Munk, 1981] was computed as

$$F_\zeta(\omega) = \frac{2}{\pi}\frac{f}{N}E_0 b^2 N_0 \frac{(\omega^2 - f^2)^{1/2}}{\omega^3} \tag{5.8}$$

using the canonical values for E_0 = 6.3 $\times$ 10^{-5}, N_0=3 cph and b=1300 m, f is the Coriolis frequency for the location. N is the local buoyancy frequency. The GM spectrum based on 2 cph buoyancy frequency is shown (Fig. 5.13c). Observed spectra show high energies than those in Garrett-Munk reference spectra at all the depths. The observed spectra follows ω^{-2} slope, consistent with the slope of GM spectrum.

5.3.5 Rotary spectra of baroclinic currents

To determine the distribution of energy in different frequency bands, rotary spectra of baroclinic horizontal currents from slope ADCP mooring were computed. Rotary spectra decompose a complex velocity ($u+iv$) into clockwise and counterclockwise rotating components [Gonella, 1972]. The computations were done for different depths and spectral energy obtained was averaged over the upper 50 m and the lower 50 m water columns. Spectra were computed for the entire period of observation. For the deep ocean, i.e., away from boundaries, GM spectrum represents internal wave continuum, a continuous spectrum of waves between Coriolis frequency (f) and buoyancy frequency (N). The clockwise and counterclockwise GM spectra [Levine et al., 1997] for the upper (N=10 cph) and lower water columns (N=1 cph) were computed separately. Clockwise (CW) and counterclockwise (CCW) spectra of cross-isobath component of velocity along with the smooth Garrett-Munk (GM) spectrum are shown in Figs. 5.14a and b. The energy of internal waves is not distributed as smoothly in the observed spectra as that in the GM spectra. Observed spectra lie above the curve of the GM spectra with multiple peaks at different frequencies. In the observed current spectra, the dominant spectral lines are located at M_2, S_2, N_2, K_1 and O_1 frequencies and at Coriolis frequency (f). Another significant peak is observed at harmonics of M_2+O_1 and M_4. The former peak arises from the non-linear interaction and advection of semidiurnal and diurnal ITs [Xu et al., 2013]. Observed spectra also show a peak at M_2+f. Alford et al. [2012] suggested that the peak at M_2+f is generally associated with the heaving of the NIW motion by the oscillation of the IT. The slope of current spectra is more or less consistent with the slope of GM which varies from $\omega^{-1.5}$ to ω^{-2}.

The level of energy over the NIW period is relatively low, and it is distributed in a broader band compared to those of IT frequencies, for which the energy distribution is confined to narrow bands with well-resolved peaks. Near-inertial energy is strong in the top layer of the water column which gets reduced downwards. The CCW component of near-inertial current is almost negligible (Fig. 5.14a), that is, polarization (ratio of CW and CCW) is maximum at NIW frequency and decreases with increasing frequency [Gonella, 1972]. CW spectrum dominates CCW spectrum in internal wave spectra (Figs. 5.14a and b), which is found to be consistent with the internal wave theory for the northern hemisphere. I calculated the vertically averaged CW to CCW ratio, and

Figure 5.14 Rotary spectra of baroclinic currents. (a) Vertically averaged spectra for the upper water column (54-102 m). (b) same as (a) but for the water column of 390-438 m depth. The curves represent Garrett-Munk clockwise (blue) and counterclockwise (red) spectra. The GM spectra was calculated using N=10 cph for upper water column and 1 cph for the water column at 390-438 m depth. The dotted lines indicate ω^{-2} and $\omega^{-1.5}$, where ω is the frequency. The 95% confidence level is also shown. (c) ratio of vertically averaged clockwise and counterclockwise spectra (blue dots). The black line is the theoretical ratio [Müller et al., 1978].

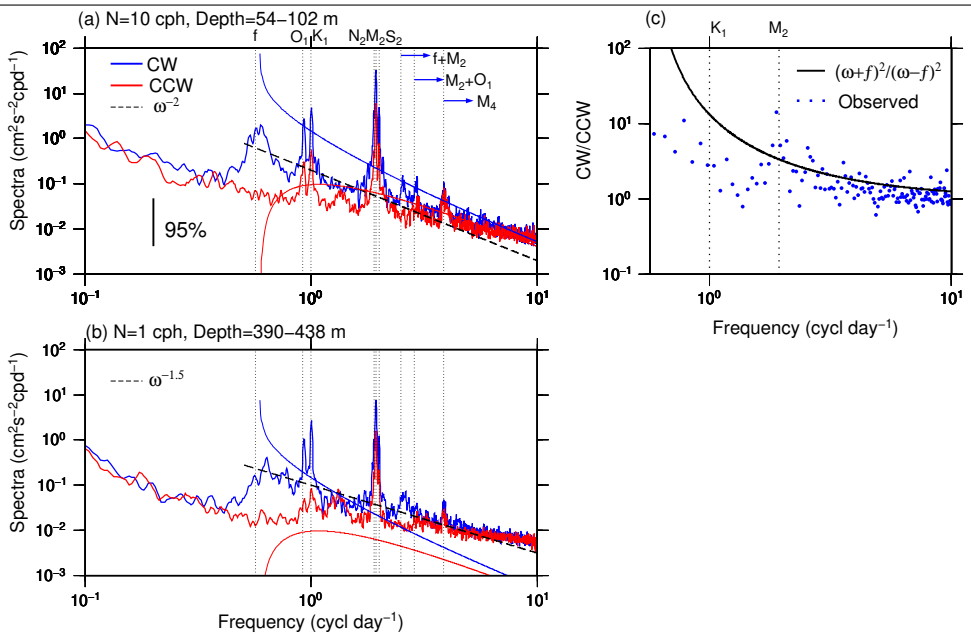

those were compared with the theoretical ratio ($\frac{(\omega+f)^2}{(\omega-f)^2}$) for the random superposition of free linear internal waves [Müller et al., 1978; Lien et al., 2013]. Theoretical ratio is found to be closer to the observed ratio for frequencies greater than tidal frequencies (Fig. 5.14c). However, for the tidal frequencies, the values deviate from the theoretical curve, which might be due to the nonlinearity associated with the semidiurnal and diurnal tides.

5.3.6 Tidal currents

The U and V components of the measured velocity vectors were rotated with respect to the orientation of isobath (about 44° with respect to the true north) to get the cross and along-isobath components of velocities. Strictly, separation of barotropic and baroclinic currents on the slope is

not possible since the data were available only up to the upper half of the water column. However, I considered the vertically averaged current in the available water column as barotropic current at the mooring location. Harmonic analysis was performed for this vertically averaged current to obtain the barotropic tidal current (BT). I also extracted BT from 1/12 degree OTIS regional tidal solution for the Indian Ocean (Egbert and Erofeeva, 2002) and found an agreement between the two which allowed me to consider vertically averaged currents as BT with a good level of confidence. The difference between observed and barotropic current was taken as baroclinic currents. Baroclinic currents were subjected to harmonic analysis to obtain baroclinic tidal currents. Baroclinic currents were analysed for the period of three months March-May, June-August and a period covering September and October. Harmonic analysis, was done for the baroclinic currents separately for these three periods, and tidal ellipses were constructed. Besides, a third order band-pass filter was used to separate semidiurnal (1.8-2.2 cpd) and diurnal (0.8-1.2 cpd) ITs from the baroclinic currents.

I show both cross and along-isobath sub-inertial currents (Figs. 5.15a and b) along with the band-passed IT (Fig. 5.15d) on the slope off Jaigarh. Cross-isobath sub-inertial currents (Fig. 5.15a) are found to be weak during the entire period of observation. Cross-isobath raw currents are tidally dominant, where 64% of the total variance is explained by barotropic and baroclinic tides. In the along-isobath direction, tidal currents account for only 13% of the total variance. Barotropic tidal current obtained by the harmonic analysis of cross-isobath barotropic current for March is also shown in Fig. 5.15c. I compared the barotropic velocity with the predictions from a global tidal model (OTIS) (Fig. 5.15c). The observed barotropic tidal currents show good agreement with OTIS output with an RMS error of about 1 cm s^{-1}. Thus, the method of removing barotropic signals from the total currents by vertically averaging current is found to be valid for slope location. Cross-isobath baroclinic currents were band-passed for total (0.5-6.0 cpd), semidiurnal (1.8-2.2 cpd) and diurnal (0.8-1.2 cpd) ITs (Figs. 5.15d, g and h). Barotropic tidal currents show an apparent fortnightly cycle. Internal tides on the slope are strong, with the maximum speed attaining to about 32 cm s^{-1} in the upper layer of the water column. Strongest IT is always observed during the period of spring tide, indicating the coherency of ITs with local barotropic tides. This is true in band-passed semidiurnal and diurnal IT, where they also followed the spring-neap cycle of their

Figure 5.15 Time series of (a) Cross-isobath sub-inertial currents (b) Along-isobath sub-inertial currents. (c) Result of harmonic analysis of cross-isobath barotropic current along with the OTIS output for March (d) the corresponding band passed IT. The harmonic analysis was carried out on the cross-isobath barotropic currents by keeping semidiurnal and diurnal constituents separately. (e-j) A two-day BT and IT are zoomed for both semidiurnal and diurnal bands and the time evolution of 8 m vertical shear (s^{-1}) corresponding to both bands are shown.

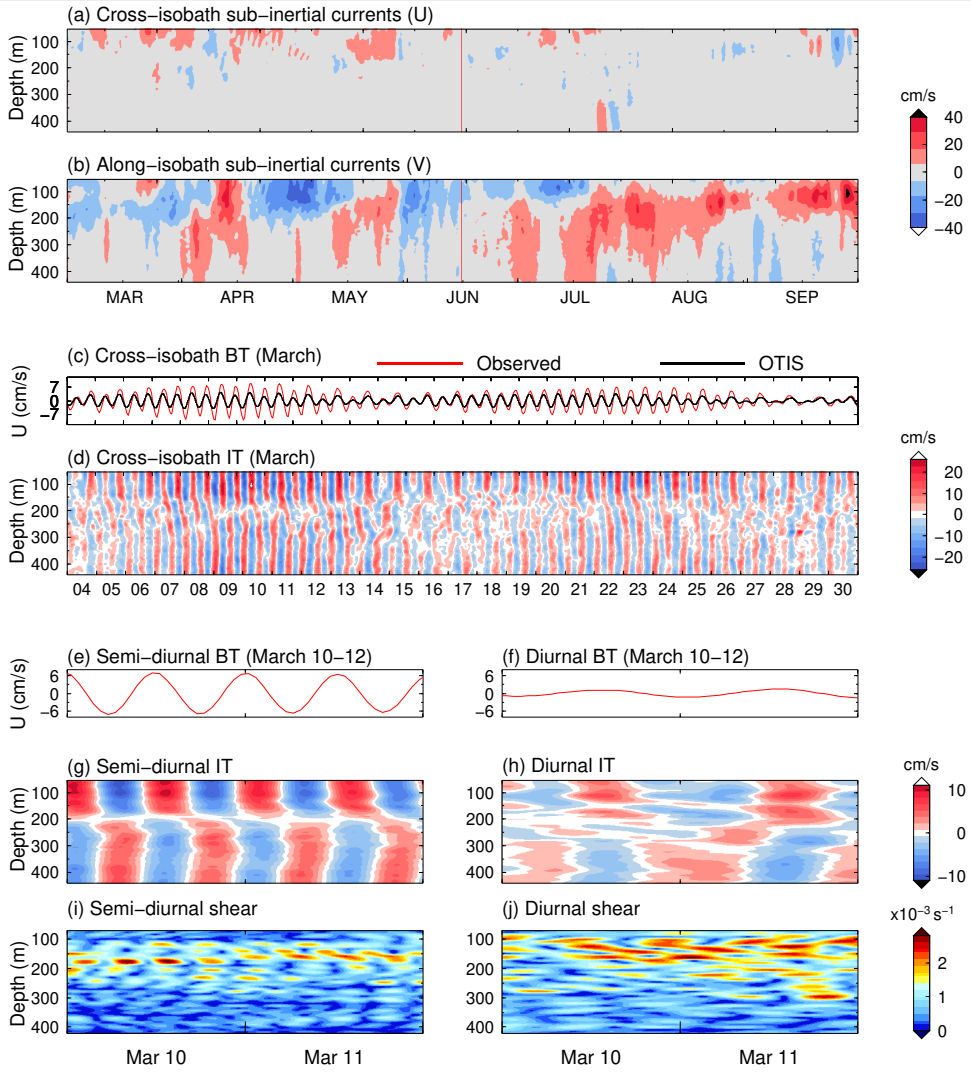

barotropic counterpart (not shown). Internal tides are found to be strong in the upper water column (55-100 m), where the stratification is high. Figs. 5.15g and 5.15h show a two-day time series of band-pass filtered semidiurnal and diurnal IT along with their barotropic tides (Figs. 5.15e and f). The currents in the upper layer are clearly out of phase with those in the lower layer. The semidiurnal IT shows low vertical mode standing wave structure (Fig. 5.15g). In diurnal IT, higher modes are also significant (Fig. 5.15j). During many other periods, the downward propagation of diurnal IT is also found to be strong with higher mode vertical structure (For instance during April and June). Figs. 5.15i and 5.15j show the vertical shear (S=$((\partial u/\partial z)^2, (\partial v/\partial z)^2)$) computed at 8 m interval for both semidiurnal and diurnal IT. Shear depends on the vertical structure of IT. Semidiurnal shear is strongest at about 200 m depth, which indicates the dominance of first mode. Diurnal IT shear is found to be significant in different layers indicating multiple modal structures.

5.3.7 Tidal ellipses

Both barotropic and baroclinic currents were subjected to harmonic analysis and tidal ellipses were constructed. I also examined the temporal stability of barotropic tidal currents by doing the harmonic analysis for different periods. I divided barotropic currents into four periods of two months and harmonic analysis was carried out in each period. Results obtained from full-month harmonic analysis of barotropic currents were compared with those obtained from the two-month harmonic analyses. The difference in magnitudes from two analyses lies in the limit of 1 cm s^{-1}. Thus the seasonal variation of barotropic currents is found to be negligible. Barotropic tidal ellipses of M_2, S_2, K_1 and O_1 on the slope location are shown in Fig. 5.16. Ellipses consistently rotate in a clockwise direction and appeared more or less in the same shape with the semimajor axis oriented across the bathymetric contours. The cross-isobath barotropic M_2 tidal current (4.8 cm s^{-1}) is found to be three times stronger than that of along-isobath current (1.6 cm s^{-1}).

Baroclinic tidal ellipse parameters for every depth were calculated by harmonic analysis of baroclinic currents. To study the seasonal variation of IT, I divided baroclinic currents into two periods of three months March-May, June-August and a period consisting of September and October. Harmonic analysis was carried out for each period and the results are shown in Fig. 5.16. Tidal ellipses computed for the September-October period show similar patterns of those in June-

Figure 5.16 Baroclinic (bold line) and barotropic (dotted line) tidal ellipses of (a) M_2, (b) K_1, (c) S_2, and (d) O_1. Baroclinic tidal ellipses were constructed for March-May (black line) and June-August (red line) periods. Barotropic ellipses were constructed for the entire period of observation. The scale is shown on the top. All ellipses rotate in clockwise direction.

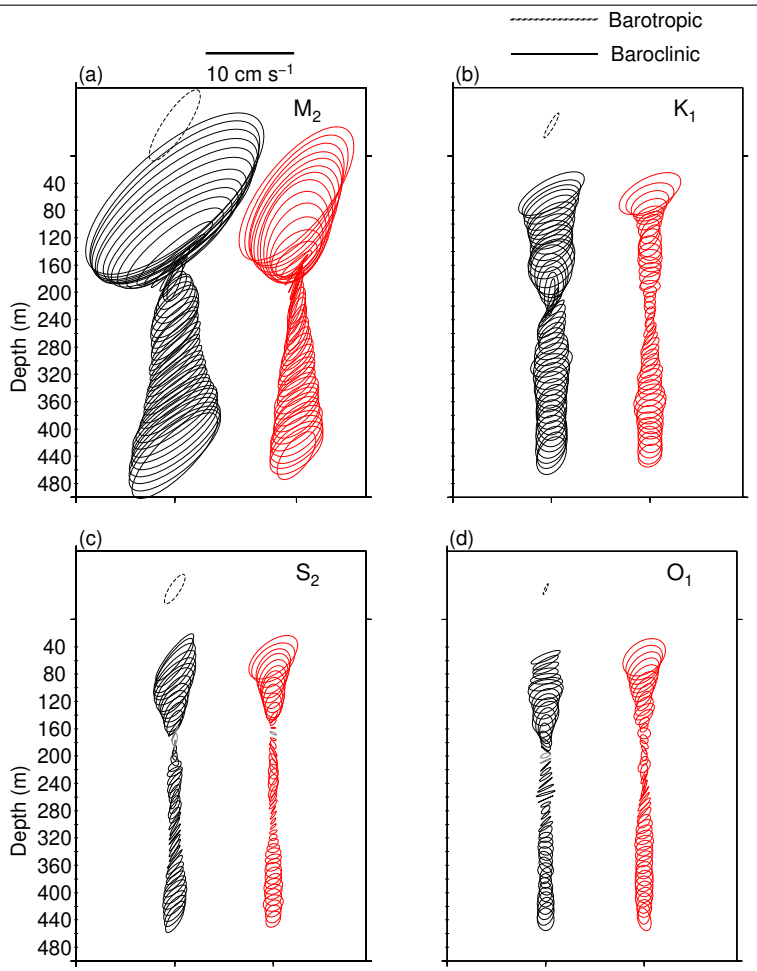

August and hence not shown. Internal tides greatly vary in time by the background changes in currents and stratification. These variations cannot fully be resolved through the harmonic analysis, which gives only an average pattern of each IT constituent. The present analysis shows that M_2, S_2, K_1 and O_1 are the most significant constituents for the region. For M_2, the semimajor axis is about 12 cm s^{-1} at the surface, and it gradually decreases with the depth reaching a minimum of 2 cm s^{-1} at 200 m depth. The tidal ellipses show seasonal variations with M_2 and K_1, IT being

the strongest in March-May period (semimajor axis at the upper layer is 12 cm s^{-1} and 4 cm s^{-1} respectively) when compared to June-August period (9 cm s^{-1} and 3.7 cm s^{-1} respectively). Even though magnitudes of tidal ellipses vary from season to season, their vertical structure is found to be similar throughout the period (Fig. 5.16). This may be due to the small variations in pycnocline depth during the observational period. The vertical structure of the ellipses (Fig. 5.16) shows that ITs are dominated by first baroclinic mode motion with a minimum occurring in the middle depth. However, the vertical structure of S_2 is complex with two minima, where the second mode vertical structure seems to be dominant (Fig. 5.16c). All the baroclinic ellipses are oriented in the same direction as those of barotropic ellipses in both seasons indicating that ITs are coherent with the local barotropic tides. Semimajor axes of both barotropic and baroclinic ellipses are oriented across the isobaths. For freely propagating IT, the ratio of semiminor to semimajor axis can be obtained as f/ω, where f is the Coriolis frequency and ω is the frequency of the wave [Petruncio et al., 1998]. The theoretical value of this ratio is found to be 0.29 and 0.56 for M_2 and K_1 respectively. The observed values (varies between 0.1 to 0.5 for M_2 and 0.2 to 0.8 for K_1) are found to be consistent with the theoretical ratios.

5.3.8 Vertical structure of internal tides

EOF analysis was done to the cross-isobath and along-isobath components of band-passed (0.5-6 cpd) baroclinic IT on the slope location. Figs. 5.17a, b and c show the first three spatial modes of the horizontal components (shown as red-colored vectors) along with the power spectra estimated for its time function (Fig. 5.17d). The results show that the first mode of cross-isobath IT explains about 65% of the total variance while the second and third modes, the variance accounts for about 11% and 4% respectively. These three modes together represent 80% of the total IT variance in the region. However, in the along-isobath component, the first mode explains 40% of total variance and the second and third mode variances are 14% and 8% respectively. First mode variability in the cross and along-isobath IT exhibits a two-layer structure with zero crossing at about 200 m. To examine the kinetic energy distribution over frequencies in the first three modes, power spectra of the principal components are plotted (Fig. 5.17d). The semidiurnal and diurnal ITs are dominated by the first mode. I also carried out EOF analysis of baroclinic currents for both semidiurnal and

Figure 5.17 The vectors (red color) are derived from the cross-isobath (U) and along-isobath (V) EOF modes. First three EOF modes are shown here. The black color vectors indicate the least square fits (LSF) (equation 9) for the first three EOF modes. (d) power spectra of the principal component of each EOF mode of U (black) and V (red). The percentage of variance contributed by each mode is shown.

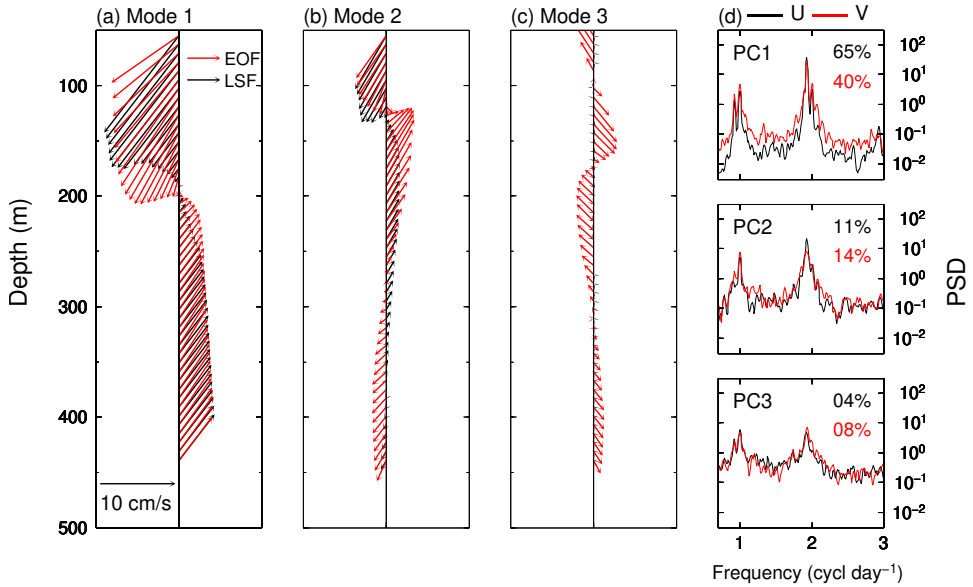

diurnal bands on the slope location (Table 5.2). For the semidiurnal band, first and second EOF mode of the cross-isobath component represents 77% and 10% of total semidiurnal IT variance respectively. Higher modes are found to be weak. In the along-isobath semidiurnal IT, the first mode explains 55% of the total semidiurnal variance. Second and third modes explain 14% and 7% of the variance respectively. Though the diurnal IT is dominated by first mode, higher modes are also found to be significant (Table 5.2). This is consistent with the shear analysis, where the shear for diurnal IT is found to be large in different layers of water column (Fig. 5.15j), which might be due to the presence of the higher modes.

I found that the vertical structure of first and second EOF modes resembles the corresponding baroclinic normal modes for the horizontal velocity. Using a linear regression method [Lee et al., 2012] I fitted the EOF modes to the corresponding theoretical normal modes and the regression result is plotted as black colored vectors in Figs. 5.17a, b and c. The normal modes were calculated by using computed buoyancy frequencies for February (Fig. 5.12). The normal modes were

Table 5.2 The percentage EOF variance for the semidiurnal and diurnal IT on the slope location.

	Semidiurnal		diurnal	
	Cross-isobath (%)	Along-isobath (%)	Cross-isobath (%)	Along-isobath (%)
Mode 1	78	55	45	37
Mode 2	10	14	13	11
Mode 3	02	07	08	10
Mode 4	01	05	06	06

normalized to have unit variance before doing the least square fits. The first EOF mode (both U and V components) on to the first mode of the normal mode and the regression coefficient for U and V components are plotted as black-colored vectors over the first EOF mode structure in Fig. 5.17a. Similarly, a best matching regression model for second and third mode U, V components are shown in Figs. 5.17b and c respectively. The U and V components of each EOF mode are regressed to corresponding normal modes as,

$$U_{e(k)} = \alpha_k + \beta_k U_{n(k)} \tag{5.9}$$

Where k=1, 2 and 3 represent different modes; α_k and β_k are the regression constants for each mode, $U_{e(k)}$ and $U_{n(k)}$ are the corresponding EOF and normal modes. The first mode structure of U (V) shows an r^2 value of 0.97 (0.87) to the normal mode; for the second mode it reduces to 0.57 (0.72) and it further reduces to 0.1 (0.004) for the third. This suggests that the first and second mode variability of the observed currents is largely explained by the corresponding baroclinic normal mode structure. The third mode does not show any obvious relationship with its corresponding normal mode structure as seen in the Fig. 5.17c. I repeated the experiment for different months and found that the results are nearly identical (not shown).

5.3.9 Seasonal and cross-shelf variations

In this section, I show the seasonality of IT over slope and shelf regions and slope-shelf variation of IT amplitudes. Figs. 5.18a and b show the band-passed barotropic and IT variance ($u^2 + v^2$) running averaged over three days for the shelf and slope regions respectively. Internal tide variance was also averaged over the depth. The barotropic tidal currents do not vary with seasons on both slope and shelf locations. However, ITs show seasonality in their magnitudes. On the slope, ITs

are found to be strong during March to the first week of April, and they are less strong during June. This continues up to the third week of September, and they intensify later. This pattern is found in semidiurnal and diurnal IT (Fig. 5.18c). The study used shelf ADCP data to see whether this pattern is consistent on the shelf and found that IT are weak during March and the first two weeks of April, and they slowly start picking up strength. I analysed the evolution of buoyancy frequency (Figs. 5.18d and e) on the shelf and slope during the same period computed from the simulated temperature and salinity from MOM4p1 ocean model [Chatterjee et al., 2013]. The slope was stratified during the entire period of observations with minimum variability in time. However, the shelf shows significant seasonal variations in stratification, with low stratification found during March-April and high stratification observed during SW monsoon (May-September). Available CTD observations on the shelf and slope during the same year show a similar pattern, where the slope stratification does not appreciably vary from February to April, but that of the shelf does change. On the shelf (at about 100 m), in February the temperature difference between upper and bottom water column, indicative of stratification, is about 0.5-3°C and it increases to about 2-4°C in April. However, towards the slope (500 m, 1000 m) region, the water column is well stratified in the above two months, where the temperature difference is about 15°C and 20°C respectively (Figure not shown). The well-mixed condition of shelf during the pre-monsoon could be one reason of comparatively weak IT during March and April. Other possible mechanisms that affect the IT generation on the shelf will be discussed in section 5.4.3. The slope stratification is strong during the entire period, and the IT retains their strength over the period of observation.

5.3.10 Coherent and incoherent internal tides

In this section, I discuss the relative contribution of coherent and incoherent IT on the slope and shelf regions. The broadband ITs were extracted by 6-30 hrs bandpass filtering of the baroclinic currents. This band excludes the NIW and encompasses only the coherent and incoherent IT signals. I performed running harmonic analysis for periods ranging from 3 days to 8 months and separated the coherent and incoherent IT for each time window (Fig. 5.19). The intermittency of ITs and the capability of harmonic analysis to represent the ITs was examined for different time windows in the shelf and slope regions.

Figure 5.18 (a) Time series of variance of barotropic tidal currents ($u^2 + v^2$) for shelf and slope locations. A running 3-day averaging was applied on the variance. The scale for shelf BT is given on the right axis and that of slope BT is given on the left axis. (b) Time series of IT variance. Variance was vertically averaged and a running average over 3 days applied before plotting. (c) Time series of semidiurnal and diurnal IT variance on the slope location. The variance was vertically averaged but not smoothed in time. (d-e) The buoyancy frequency distribution during the ADCP observation period near the mooring locations, on the shelf and slope, computed using hydrography from MOM4p1 model output [Chatterjee et al., 2013]. For the slope location, only upper 300 m values are shown.

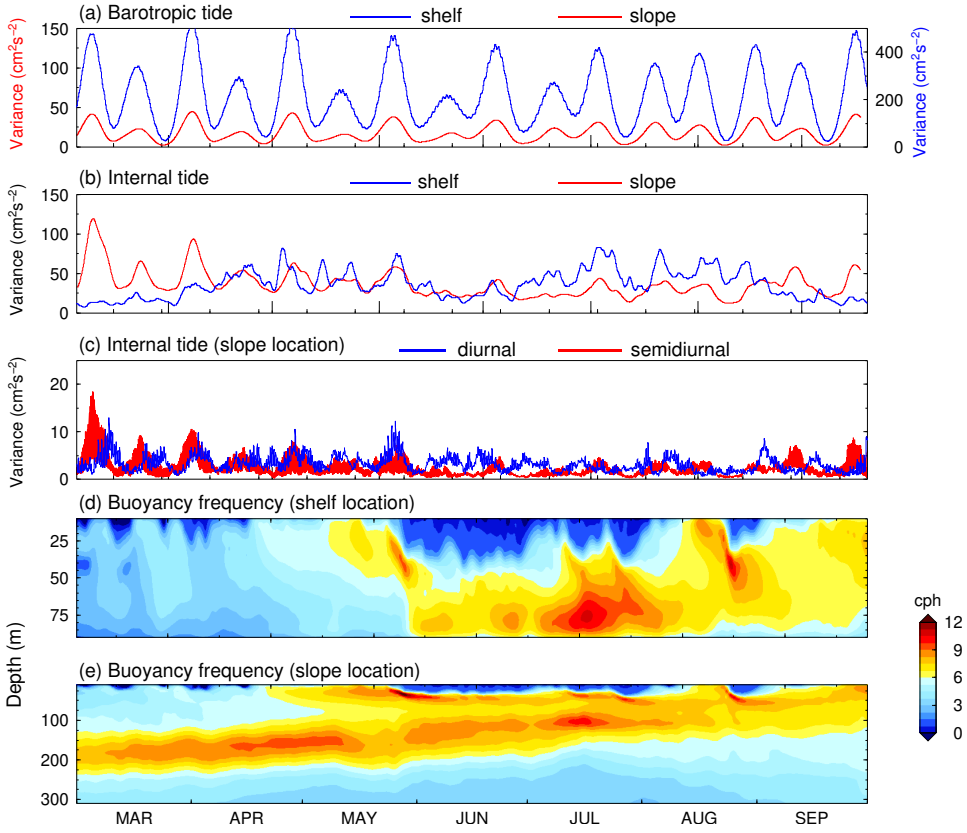

I calculated the predictive capability of a harmonic fit for each time window by using a skill score test [Murphy, 1988; Nash et al., 2012]

$$SS_T = 100\% \times \left[1 - \frac{\langle (u' - H_T(u'))^2 \rangle}{\langle u'^2 \rangle}\right] \tag{5.10}$$

where u' is the bandpassed cross-isobath IT, which includes all the signals of the period from 6 to

Figure 5.19 Time series of coherent and incoherent IT variance ($u^2 + v^2$) for the (a) slope and (b) shelf locations. Harmonic analysis over different time span was carried out on the broad band (6-30 hrs) IT and the time series were generated. The variance of the regenerated harmonic analysis ($U_H^2 + V_H^2$) (red) and that of the residual ($U_R^2 + V_R^2$) (blue) are shown. The variance was averaged over depth. The time span taken for harmonic analysis is indicated in each panel. Skill score (equation 10) was calculated for each harmonic analysis and predictability was determined. The percentage of predictability is also shown in each panel.

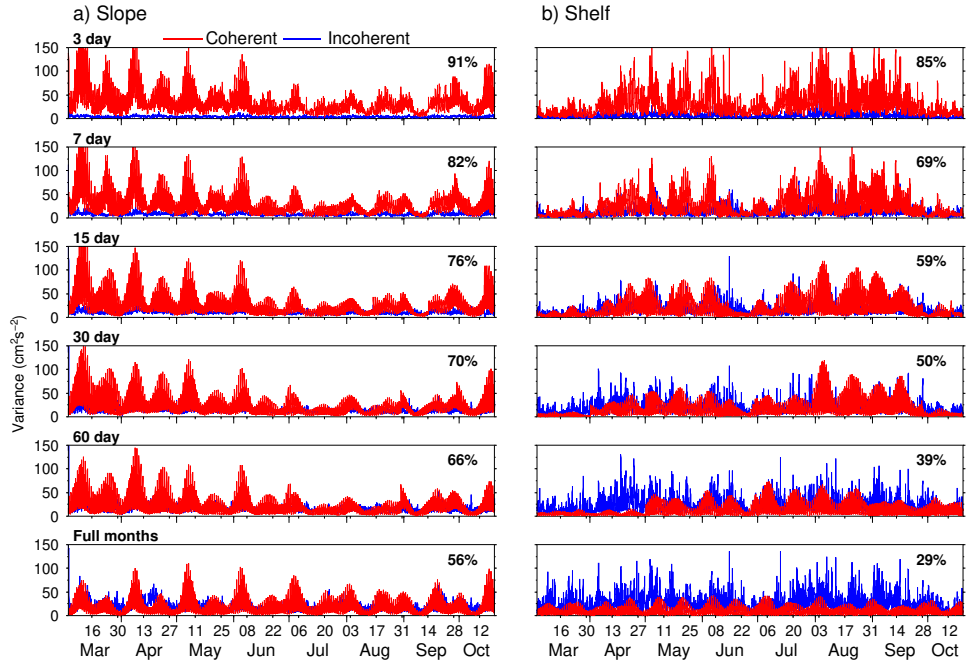

30 hrs. H_T is the regenerated coherent IT from harmonic analysis, where T is the time window (3 days-full months) used for the analysis. The term $(u' - H_T(u'))$ gives the incoherent part of IT. After subtracting the coherent IT from the band-passed signal, all the values were squared and averaged over time and depth. The value was then divided by the averaged bandpassed signal over time and depth for the same period. 100% SS_T implies that the harmonic analysis captures all the observed variance. The tests show that the capability of harmonic analysis to capture the IT over different time windows varies over the shelf-slope region significantly. For example, on the slope, harmonic analysis of 15-day window could represent 76% of IT. When the time window was increased, the capability was found decreasing. 30-day window could only represent 66% and 90-day window represented 52% of total IT (Fig. 5.19). On the shelf off Jaigarh, the ITs are

found to be more incoherent where even 7-day harmonic fits could only represent 69% of total IT. During March, shelf IT is found to be weak in broadband IT (Fig. 5.18b). 30-day and 60-day running harmonic analysis show that during March-April, the coherent ITs are weak on the shelf and dominated by the incoherent part. The well-mixed state of shelf water might have restricted the local generation of IT there. A part of shelf IT during March-April may be shoaling from the slope, where slope IT is strong during these periods. The results from harmonic analysis over the entire period of observations show that (Fig. 5.19) the variance of coherent ITs is dominant on the slope region with skill score of 56% where the IT retains its amplitude and phase over a long period of time. However, on the shelf, IT variance is high in the incoherent part with a skill score of only 29%. The slope ITs are comparatively more predictable than those over the shelf.

5.4 Possible generation sites of internal tides

5.4.1 Criticality

From the generation source, IT travels as a beam with a slope c to the horizontal where the slope depends upon the frequency of IT, the stratification and the latitude. The slope c, can be estimated as,

$$c = tan(\alpha) = \left(\frac{\omega^2 - f^2}{N^2 - \omega^2} \right)^{1/2} \tag{5.11}$$

Where ω is the frequency of the corresponding IT (for M_2 (K_1) it is .081 cph (.04 cph)), f the Coriolis frequency (.024 cph at 17.2° N) and N is the buoyancy frequency. Baines [1986] suggested that generation of IT would be efficient if the slope of bottom topography ($\Delta H/\Delta X$) matches the characteristic slope of IT (c), where even weak barotropic tides can generate ITs.

The shelf bathymetry off Jaigarh gradually changes by a few meters from the coast and reaches shelf break after 140 km where the depth is about 100-120 m. From shelf break to continental rise, slope of topography varies gently where 20 km from the shelf break, the depth reaches 1000 m. The slope of the continental slope in the region varies between 1 to 4 degrees. In the deep part (3600 m), a seamount of about 800 m tall is present, where the bottom slope reaches up to 4-6 degrees. I estimated the topographic slope from the fine resolution SRTM30_PLUS [Becker et al.,

2009] bathymetry with a grid resolution about 1 km, prepared by merging satellite-derived and ship acoustic sounding bathymetry (ftp://edcsgs9.cr.usgs.gov/pub/data/srtm/SRTM30). The buoyancy frequencies across the shelf-slope were calculated from the 13 CTD observations available in April (Fig. 5.20a). The 13 CTD data were averaged spatially and considered as horizontally homogeneous. The criticality parameter, which is the ratio of bottom slope and characteristic slope ($\gamma = \frac{\Delta H}{\Delta X}/c$), across the shelf-slope was also calculated (Fig. 5.20b). Towards the shelf break, at 100-180 m, the bottom buoyancy frequency is about 8-10 cph. The high buoyancy frequency observed at the bottom is because the pycnocline is found near the shelf break where the stratification is highest. The characteristic slope of M_2 IT for these values is 0.009-0.006. For K_1, the characteristic slope will be nearly half of that of M_2. Near shelf break, the water depth varies 1-10 m over a horizontal distance of 1 km. The average topographic slope value is found to be 0.004. There are several critical regions, where the bottom slope matches the characteristic slope of both M_2 and K_1 frequencies (Fig. 5.20b). From 200 m to deeper depths, buoyancy values range between 1-3 cph. The value of the characteristic slope is reduced by a factor of ten for these frequencies. However, due to the large topographic slopes, the continental slope is found to be critical for semidiurnal and diurnal frequencies. At the mooring point, the topographic slope is about 0.04. I also estimated the criticality parameter by using the buoyancy frequency information from the MOM4p1 ocean model simulation and found that the mooring location is near critical for M_2 and K_1, where the ratio between bottom slope and characteristic slope for M_2 is about 0.9, and that of K_1 is about 2 respectively. Bottom intensification and upward energy propagation are expected in the region. However, this cannot be substantiated in this work as we do not have the information of bottom velocity. The deep part of the slope (about 2800-3200 m) is also found to be near critical at both frequencies (not shown in Fig. 5.20).

5.4.2 Baines forcing

Baines [1982*a*] barotropic forcing term is often used to identify the regions of IT generation [Da Silva et al., 2009; Merrifield and Holloway, 2002].

$$F = zN^2(z)\int Qdt.\Delta(1/h) \tag{5.12}$$

Figure 5.20 (a) Buoyancy frequency from 13 CTD casts during April 2008 (the transect shown by green dots in Fig. 5.10), across the moorings. The triangles are the locations of CTD measurements across the shelf. Bottom topography along the cruise observations is also marked in blue line. The inset map shows the spatially averaged buoyancy frequency. (b) The black circles denote the criticality parameter (the ratio between bottom slope and characteristic slope) of M_2 and K_1 along the cruise track. Characteristic slopes were computed using the buoyancy frequency values near the bottom. Bottom slope was calculated using SRTM30_PLUS bathymetry. M_2 and K_1 internal wave characteristics emanating from shelf break, where the bottom slope is nearly equal to the characteristic slope, are shown. Distance from the location of CTD cast nearest to the coast is shown in the north axis.

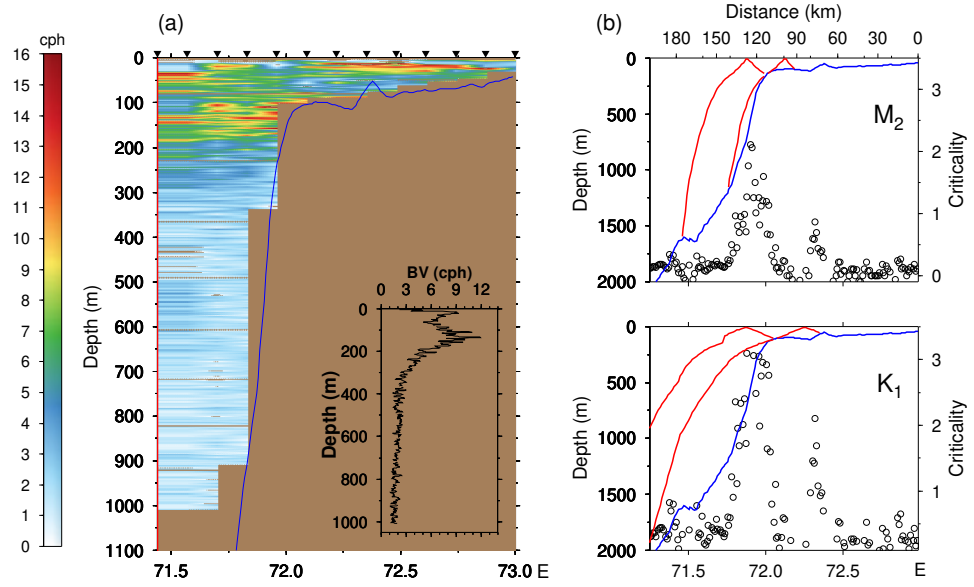

where N represents buoyancy frequency. $Q = (uh, vh)$, Q is the barotropic mass flux vector, u and v are the velocities of zonal and meridional components of barotropic tidal-currents, and h is the water depth. $\Delta(1/h) = (dx/dh, dy/dh)$ are the topographic slopes in zonal and meridional directions respectively. The semidiurnal and diurnal barotropic mass fluxes were obtained from 1/12 degree OTIS regional tidal solution for the Indian Ocean. The fluxes for 15 days including a spring-neap cycle were interpolated to SRTM30_PLUS bathymetry, and slope of topography was determined at every grid points. Buoyancy frequency was computed using temperature and salinity monthly mean climatology (http://www.esrl.noaa.gov/psd/data/gridded/data.godas.html). The buoyancy values were averaged out spatially (between 69.8°-74.7° E and 13.8°-18.2° N) and

considered as horizontally homogeneous. Spatially averaged buoyancy frequency matches well with the monthly mean climatology and CTD observations near the slope gave confidence us to use the spatially averaged buoyancy frequency for the calculation (Fig. 5.21b). The body force was calculated at every grid point using stratification for each month. The maximum absolute value of depth-integrated body force for both semidiurnal and diurnal frequencies are shown in the Figs. 5.21a and b. Fig. 5.21 shows that the body force is strong along the shelf break (near 200 m), and it enhances towards the north. The average value of semidiurnal (diurnal) body force on the shelf break off Jaigarh is about 1 $m^2\ s^{-2}$ (0.59 $m^2\ s^{-2}$) in January, and it increases to about 1.2 $m^2\ s^{-2}$ (0.66 $m^2\ s^{-2}$) in June. Seasonal variation of the body force is attributed to the increase in stratification during SW monsoon. The northward intensification of body force is mainly attributed to the increase in velocity of both semidiurnal and diurnal tidal currents towards north (Figs. 5.21a and b). On the shelf-slope region off Jaigarh, barotropic velocities are found to be large compared to those in the southern part of the coast. The variation in the topographic slope in cross-shore direction was also noticed from the south to northern region, where the topographic gradient is found to be high in the study region and north of it. This also enhances the body force in the northern regions. The body force values on the shelf off Jaigarh are comparable to the values for other known major hotspots in the world's oceans like southern and central Bay of Biscay [Azevedo et al., 2006; Muacho et al., 2014], west Iberian coast [Magalhaes and da Silva, 2012] and Hawaiian Ridge [Merrifield and Holloway, 2002]. Further north, in 19°N, the body force values are found to be significantly higher (For instance 3 $m^2\ s^{-2}$ and 2.8 $m^2\ s^{-2}$ for semidiurnal and diurnal body force respectively) than that on the shelf off Jaigarh.

5.4.3 Bottom intensification of internal tides on the shelf

In the sections 5.4, I discussed the possible generation sites of ITs based on criticality and barotropic body forcing on the continental slope region off Jaigarh. In this section, I analyse the role of stratification and the topography slope in the generation of ITs on the shelf region. In generation sites, the topography slope is expected to be comparable with the characteristic slope of internal tidal frequency. I also expect the high bottom velocities, strong vertical shear in the bottom and upward energy propagation in the generation sites. The shelf ADCP covered almost the entire water

Figure 5.21 Spatial distribution of maximum depth-integrated (a) semidiurnal and (b) diurnal barotropic body force (equation 12) for April. The vertical profile of spatially-averaged monthly climatology of buoyancy frequency for April, used for the body force calculation, is shown in the inset map (black bold line). The vertical profile of buoyancy frequency from monthly climatology (red line) and CTD observation (blue line) on the slope for April are also shown. The blue line denotes the stratification on the slope obtained from the in situ CTD observation. M_2 and K_1 tidal ellipses are shown with the semidiurnal and diurnal body force. The red star denotes the location of slope ADCP mooring. 100, 200, 1000 and 1500 m depth contours are also shown.

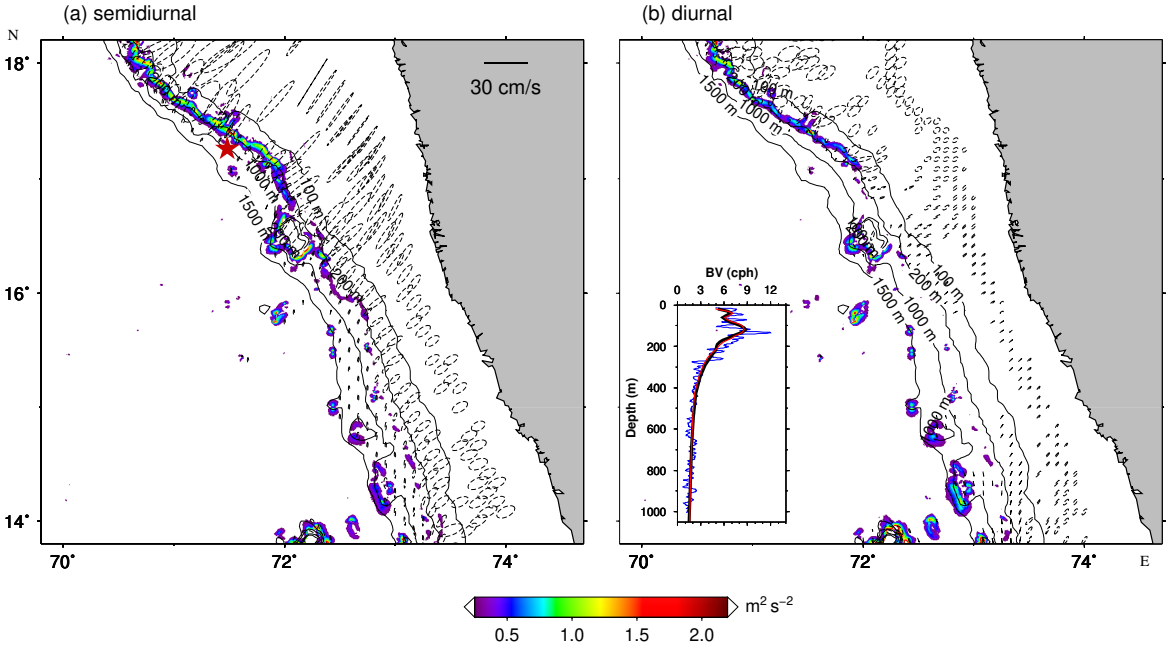

column that enabled us to study the bottom variation of ITs in different periods of stratification. Most of the time, ITs show low mode vertical standing wave structure. However, in June, July, and August, the internal tidal energy is found to be high in the bottom water column in both semidiurnal and diurnal frequencies. The characteristic slope of semidiurnal and diurnal IT was calculated from the equation (5.11) based on the buoyancy frequency at bottom obtained from the MOM4p1 model output of temperature and salinity, and the ratio of bottom slope and the characteristic slope was estimated (Fig. 5.22a). Fig. 5.22 shows the band-passed semidiurnal and diurnal IT in July, one of the above months, along with its barotropic tidal currents. Internal tides do not follow the

spring-neap cycle of the barotropic tide in July. During one neap tidal phase, (July 11-12) a strong IT event is observed. In diurnal also, the maximum IT event does not coincide with the barotropic spring time. Towards 26 to 29 July, semidiurnal IT shows bottom intensification with clear upward energy propagation. This can also be seen in diurnal IT during July 12-17. The ITs during these periods are zoomed in Figs. 5.22e and 5.22g along with its shear evolution (Figs. 5.22f and h). The shear is also found to be strong in bottom layers during these periods. The shelf ADCP mooring was located in the region where the bottom topography is nearly flat. The depth variation near the mooring location is about 7 m over one-kilometer distance. The slope of the topography is thereby about 0.007. There are several events, in which the topographic slope is comparable to the characteristic slope (Fig. 5.22a). The bottom stratification is found to be maximum during July (Fig. 5.18). Due to the high stratification, the mooring location turns to be a favorable site for the IT generation. Strong shear at bottom and the upward energy propagation confirm this hypothesis. Though barotropic tides are weak in the diurnal compared to the semidiurnal band, ITs are found to be stronger in diurnal frequency. This suggests that the topography is more favorable for the generation of diurnal IT for the given bottom stratification.

5.5 Near-inertial Waves

In this section, I describe the characteristics of NIW on the slope and the shelf regions off Jaigarh. As a first step, baroclinic currents were band-passed for 0.85-1.15f band, and the NIW signals were extracted for both shelf and slope locations. Since the information of slope currents in upper water column (up to 50 m) is missing due to the contamination of ADCP data, we can only study those NIWs, which have penetrated from the mixed layer into the thermocline. However, the shelf ADCP covered almost the entire water column, except the near surface (12 m depth). Wind stress was calculated from the 4-day high passed QuikSCAT daily winds (Figs. 5.23a and b). To show the energy distribution of NIWs over the period of observation, I performed a wavelet analysis of baroclinic currents, which provides the temporal distribution of energy in the frequency domain. The wavelet power was then averaged over the NIW band (0.85-1.15f) at each depth level and plotted as depth-time series (Figs. 5.23c and d).

Figure 5.22 (a) The criticality parameter for M_2 and K_1 for the entire observation period. The characteristic slopes were estimated using the bottom buoyancy frequency obtained from the temperature and salinity values of MOM4p1 model output [Chatterjee et al., 2013]. (b-d) The BT and IT for semidiurnal and diurnal band are zoomed for July. I further zoomed semidiurnal and diurnal IT (The marked portion of (c) and (d)) in (e) and (g) and the evolution of 8 m vertical shear (s^{-1}) for the same period is shown in (f) and (h).

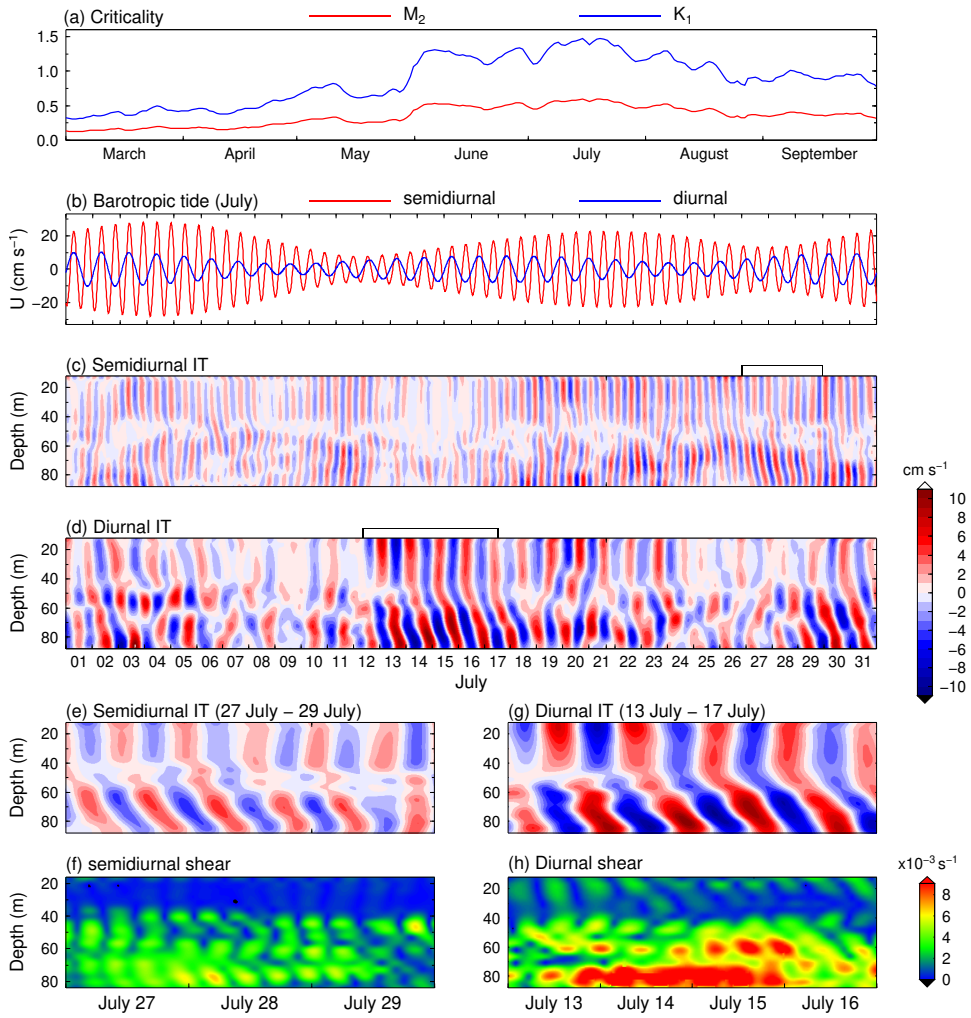

5.5.1 Near-inertial waves on the slope

On the slope, a strong NIW event is observed from April 21 to May 3 and another event is observed shortly after 3rd May which ended on May 15. The wavelet power shows that the energy maximum is present near 100 m depth. Towards the upper layers, energy is found to be weak.

Figure 5.23 (a-b) 4-day high pass wind stress (QuikSCAT) over the slope and shelf locations is shown during the period of observation. (c-d) The band averaged (0.85-1.15f, where f is the Coriolis frequency) wavelet spectra of NIW. (e-f) Time series of cross-isobath component of NIW. (g-h) 8 m vertical shear evolution of NIW for the same period. Two strong NIW events observed during 15 April-15 May (at slope) and 01 June- 30 June (at shelf) are considered for figures e, f, g and h.

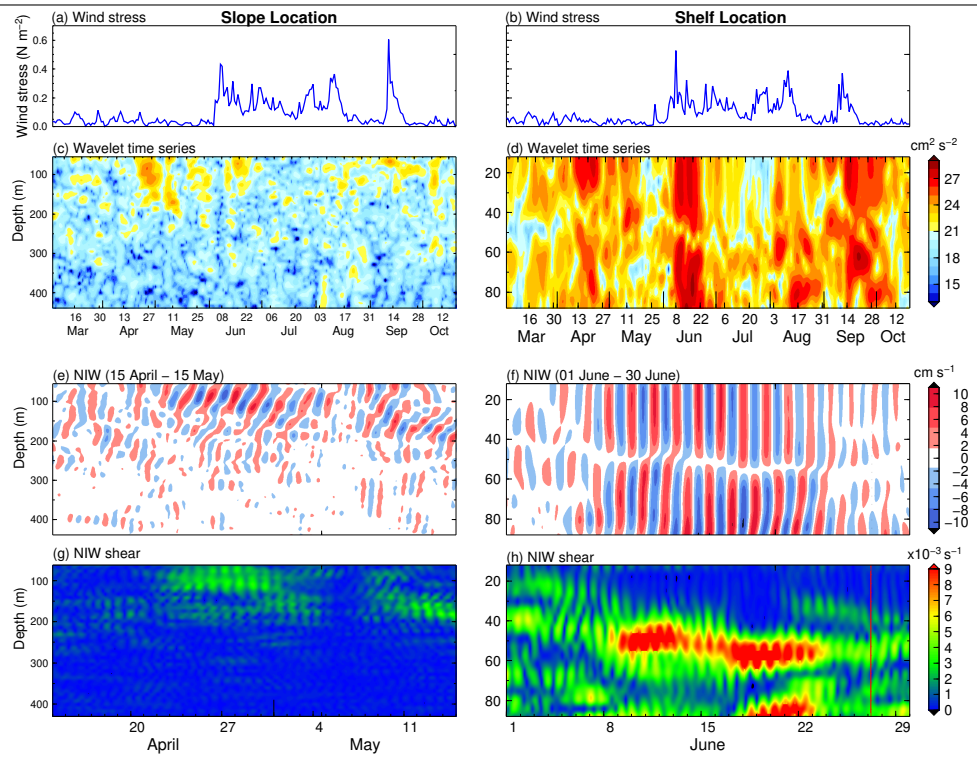

Fig. 5.23e shows a clear downward energy propagation (upward phase propagation) which indicates the possibility of remote generation of NIW. One more feature of NIW during this period is that the frequency of NIW is shifted to below the local inertial frequency where NIW peak is observed at 0.91f. It is not observed in any other NIW events. The effective frequency of NIW is $f_e = f + \zeta_g$ where ζ_g is the relative vorticity of background geostrophic currents [Kunze, 1985]. Cyclonic background current (positive vorticity) can cause the blue shift of the NIW, and anti-cyclonic (negative vorticity) flow can cause the redshift. The daily geostrophic currents were calculated from the altimeter sea level (http://www.aviso.oceanobs.com/en/data.html). Cyclonic and anticyclonic eddies are found to be common in the central Arabian Sea during the observa-

tional period. Vorticity (ζ=$\partial v/\partial x$ - $\partial u/\partial y$) was estimated from the geostrophic velocities. The vorticity is found to be negative (roughly about -3.01 $\times$ 10^{-6} s^{-1}) in the mooring location during April. The negative vorticity at the observation site might be the reason for observed frequency shifting of NIW. The estimated f_e is $0.96f$ from the above value.

5.5.2 Near-inertial waves on the shelf

There are three main NIW events observed on the shelf, during 10-24 April, 14-23 July and 13-24 September. The decay time scale is more than a week for all the events. During all these three events, NIW shows a vertical standing wave structure (Fig. 5.23f) most of the time. The vertical modal structure of NIW was determined by an EOF analysis, carried out on the band-passed (0.85-1.15f) NIW for three events separately. For all the events, the first mode EOF is dominant with a two-layer structure, where zero crossings are found at 40-50 m depth. In April, 78% (12%) of total variance is explained by the first mode (second mode). From September 13-24, the first mode EOF shows a clear two-layer structure and after that the higher modes become important. The second EOF mode shows three-layer structure from September 26-October 3. Shear (S=$((\partial u/\partial z)^2, (\partial v/\partial z)^2)$) structure is consistent with the vertical structure of NIW, where most of the time shear is concentrated near zero-crossing depth (Fig. 5.23h). At the time when the higher modes become important, shear is found to be concentrated at corresponding zero-crossing depths. For instance, on September 13-24, when the first mode vertical structure is dominant, the maximum shear is seen near 45 m. After 24th September, shear occurs at 40 m, 60 m and 70 m depth. This is due to the presence of higher mode vertical structure of NIW during the period.

The wind effect on NIW was studied by using the QuikSCAT daily wind data with a spatial resolution of 0.25° (http://www.ifremer.fr/cersat/en/data/download/download.htm). The wind forcing is critical to the generation of NIW [D'Asaro, 1985; Mukherjee et al., 2013]. The wind pattern is similar in both shelf and slope regions. Several depressions are observed during the period of observations. No cyclone was reported in the year 2008 in the Arabian Sea. As expected, the NIW is found to be associated with the strong wind events. However, NIW in the month of April is found to be strong (about 7-10 cm s^{-1}) when the wind stress is found to be weak. I calculated the wind stress from another available wind product (ECMWF, European Centre for Medium Range

Weather Forecasting) and found identical results. One possible reason is that the above coarse resolution wind products may not capture some short wind burst events that cause the generation of NIW. However, this statement is not conclusive and numerical modelling studies are needed to understand the generation and propagation of NIW on the slope and shelf off Jaigarh.

5.6 Summary and Conclusions

In this chapter, I report the characteristics of ITs on the continental slope off WCI using ADCP data. First, ADCP data on the slope off Mumbai, Goa and Kollam were analysed to describe the ITs on the slope. The study provides estimates of amplitude of ITs, their vertical structure and seasonal variations. The IT activity is found to be significant in all three locations with varying magnitudes. The rms value of ITs on the slope of three locations reaches up to 16 cm s^{-1}. Spring-neap cycle is clearly found in IT. The vertical structure of ITs show that they are dominant by the first baroclinic mode. Unlike the ITs on the shelf, the seasonal variation of IT is not apparent in slope locations. This could be due the seasonal variation in stratification on the slope is much less compared to that on the shelf. The generation and propagation of IT on the slope off the above three locations is not addressed in detail in the present Chapter due to the limitation of data. Some part of ITs on the slope region can be explained by IT generating from the shelf break. The downward propagating IT seen on the slope off Goa gives indication of shelf-break generating ITs. The detailed description of generation and propagation of ITs are addressed using numerical model simulations in Chapter 6.

Second, ITs on the continental slope off Jaigarh are described in detail, using observations from satellite altimeters, besides the ADCP current measurements. Strong ITs are observed on the continental slope off Jaigarh (17.2 N), where they are highly coherent with the barotropic tides. On the shelf, ITs are found to be less coherent with their barotropic counterparts. Observed near-inertial waves are found to be comparatively weak on the slope and strong on the shelf. As the north Indian Ocean is well known for its strong seasonal variability associated with the NE/SW monsoon, seasonal variations of observed IT are discussed in relation to the changes in ocean stratification.

The satellite altimeter data captured the surface signature of coherent IT present on the shelf-slope region. Time series of computed density, at the deeper part of the continental slope (depth 2250 m) also revealed the presence of strong coherent ITs, where the pycnocline oscillation is in phase with the barotropic tides. The presence of ITs is more clearly visible along the T/PN-J1N track (interleaved track) than that in T/P-J1-J2 track. The T/PN-J1N track is oriented north of the shelf, where the barotropic tidal currents are found to be stronger than those on the southern shelf (Fig 5.21). Moreover, the T/PN-J1N track is aligned more perpendicular to the shelf, in the same direction of semimajor axis of M_2 and K_1, than that of T/P-J1-J2 track, so that satellites along T/PN-J1N track is expected to capture the internal tidal signal well.

The ADCP observations were used for the detailed analysis of slope ITs. The data showed fairly strong internal wave continuum where the energy spectra of the ITs are higher than those in the GM reference spectra by roughly about 2-3 times. Significant spectral peaks are observed at semidiurnal (M_2, S_2) and diurnal frequencies (K_1, O_1). The vertical structure of tidal ellipses for different constituents and EOF modes reveals the dominance of first mode vertical structure for semidiurnal and diurnal bands. The higher modes are also found to be significant in diurnal IT. A number of possible generation sites of ITs across the mooring location are identified, including the deep region and the shelf break. The slope mooring location is found to be more favorable for the generation of diurnal IT than semidiurnal. Strong diurnal IT is triggered even by weak diurnal barotropic forcing in the location (Fig. 5.15). The significant higher mode diurnal IT (Table 5.2) also shows that the mooring location might be favorable for the generation of diurnal IT.

Slope and shelf ITs off Jaigarh show seasonality but not in a similar way. On the shelf, ITs are weak during March and April, which is attributed to the weak stratification on the shelf during pre-monsoon time. However, on the slope, during the same period, the water column is well stratified (Fig. 5.18) and IT is also found to be strong. Even though the barotropic forcing over the shelf is three times larger than that on the slope, ITs are weak on the shelf during this period. The generation of IT on the shelf is greatly controlled by the background stratification. During SW monsoon time, stratification on the shelf increases considerably. This causes occasional intensification ITs on the seabed with a clear upward energy propagation. On the slope region, the stratification remains more or less consistent over the period of observation. Thereby, IT on the slope remains

strong during all seasons of the observation period. The deep permanent pycnocline also may be important in the generation of ITs in the region, which persists all through the year without any seasonal variation [Gerkema et al., 2004]. Another aspect is the part of ITs propagating shoreward from the slope. The present observations show that the energy of ITs is weak on the shelf and strong on the slope during the March and April, which is consistent with the stratification in these regions during this period. This is possible if a part of IT propagating from the slope towards the shore gets dissipated before reaching the location of shelf mooring due to the well-mixed state of shelf water, probably inhibiting their propagation. The present work is not conclusive on this aspect.

In Chapter 6, I address the generation and propagation of ITs on the shelf and slope off WCI using a numerical model.

Chapter 6

Numerical modelling of barotropic and baroclinic tides

6.1 Introduction

In the present chapter, I describe the generation, propagation, and energetics of BTs and ITs on the continental shelf, slope and deep regions off the west coast of India (WCI) using simulations from a hydrostatic, finite-difference, high-resolution (1/48°) numerical model, Regional Ocean Modelling Systems (ROMS), configured for the eastern Arabian Sea. Different numerical experiments were carried out to examine the IT energetics in different background conditions. The three experiments carried out considered the effect of tides along the open ocean boundaries using the output from global tidal model. i) In the first experiment, temperature and salinity fields were given from monthly climatology values ii) In the second experiment, temperature and salinity fields were given from monthly averaged HYCOM reanalysis data iii) In third experiment, atmospheric forcing (wind and atmospheric fluxes) was given additionally, and boundary and initial conditions of temperature and salinity were given from the coarse-resolution Indian Ocean model. The stratification obtained from the model was compared with that computed using Argo data and CTD observations. Simulated fields of currents, sea level, and temperature were compared with available observations and validated.

The chapter is organised in two main sections. The first section deals with to a description of

the simulations of BT and IT using temperature and salinity fields from climatology and reanalysis respectively (First and second experiments). The second section is dedicated to describe IT simulations using realistic forcing (Third experiment).

6.2 Simulations using climatology and reanalysis temperature and salinity fields

6.2.1 Validation of barotropic tides and tidal currents

Satellite altimeter data

The amplitude and phase of simulated M_2 and K_1 were compared with those obtained T/P-J1-J2 and T/PN-J1N satellite altimeter tracks data. M_2 and K_1 were chosen for comparison, as they are the largest tidal constituents among the semi-diurnal and diurnal tides respectively. The details of satellite data are given in section 3.2.2. The model sea level for one month (July) was extracted and harmonic analysis was carried out at each point along the tracks using TUGOm Tidal Tool Box (TTTB) (see section 3.3.2 for the details of TTTB). One month data is sufficient to separate M_2 and K_1. Fig. 6.1 shows the difference between simulated sea level amplitude and phase for M_2 and K_1 constituents with those obtained from satellite data. In deep regions, the differences between model and observations are small while, towards the coast it is found to be increasing. On the shelf, the difference in amplitude for M_2 is less than 3-7 cm, and towards the coast the differences exceed 10 cm, mainly inside the Gulf of Khambhat. The differences found very near the coast could be resulting from the inaccuracies of constituents derived from satellite altimeter data near the coast. Previous studies in other regions have also reported that shallow water tides may distort the semidiurnal and diurnal tides extracted from the altimetry track data near the coast [Andersen, 1999; Andersen et al., 2006]. Hence, in coastal regions, the tide gauge data were used to compare with the model results.

Tide gauge data

The study used four tide gauge data along the WCI (Fig. 3.2) maintained by ESSO-Indian National Centre for Ocean Information Services (INCOIS) to further evaluate the accuracy of model-simulated tides along the coast (Table 6.1). The tidal constituents were extracted from the

Figure 6.1 The difference in amplitude and phase between model and satellite altimeter observations for M_2 and K_1 constituents. Observations are subtracted from model results.

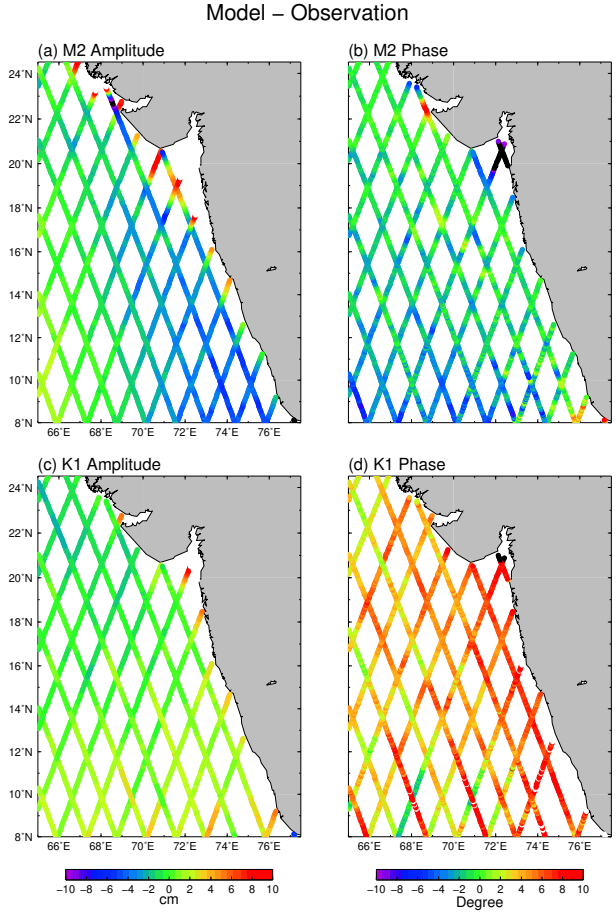

sea level measured by tide gauges. The model output at the nearest grid point to the tide gauge was used for comparison. Data were available for different years, from 2010-2014 and model run was for the year 2008. As amplitude and phase of a particular constituent in a given location do not vary with time, analysis can be made using data of different years. I chose the observations only when a full month record was available and the model data for the corresponding month was used to carry out harmonic analysis. Harmonic analysis results show that the model could reproduce tides well. The accuracy of model simulations was determined by estimating root mean square (RMS) values. The amplitude error for M_2 is found to be less than 6 cm. The phase error is less than 20 minutes and 40 minutes for semidiurnal and diurnal constituents respectively. As the main

objective of the present work is to study the tidal propagation on the shelf and slope regions, where model gives a good comparison with observation, the fine-tuning was not attempted to improve the simulation in nearshore regions.

Table 6.1 Comparison of amplitude (m) and phase with respect to Greenwich (G), of five constituents obtained from model and observations. Apollo Bandar data are obtained from Admiralty Tide Tables. Root Mean Square (RMS) was calculated using Equation 6.1. Phase g obtained from the tide gauge data is converted to G for comparing with model ($G_n = g_n + j\sigma_n$, where σ_n is the angular speed of a particular constituent, j is the difference between local time and Greenwich Mean Time, g is the phase in local time zone and G_n is Greenwich phase.).

	Observation		Model		RMS
Constituents	Amplitude (m)	Phase	Amplitude (m)	Phase	
Minicoy (8.28° N, 73.05° E)					
M_2	0.2654	179.0	0.2091	177.6	4x10^{-2}
S_2	0.0997	225.3	0.0929	229.3	6x10^{-3}
N_2	0.0584	136.7	0.0515	121.5	1x10^{-2}
K_1	0.1833	344.9	0.2286	341.7	3x10^{-2}
O_1	0.0832	343.7	0.1124	337.8	2x10^{-2}
Cochin (9.96° N, 76.26° E)					
M_2	0.2594	183.3	0.2179	172.1	4x10^{-2}
S_2	0.0750	234.1	0.0944	229.2	1x10^{-2}
N_2	0.0491	146.2	0.0560	113.8	2x10^{-2}
K_1	0.1634	321.1	0.2405	335.9	6x10^{-2}
O_1	0.0552	331.3	0.1166	330.4	4x10^{-2}
Mangalore (12.91° N, 74.8° E)					
M_2	0.4177	144.5	0.3638	154.6	6x10^{-2}
S_2	0.1240	169.4	0.1299	193.9	3x10^{-2}
N_2	0.0933	112.8	0.0984	106.5	8x10^{-3}
K_1	0.2347	312.7	0.2881	336.8	8x10^{-2}
O_1	0.0933	112.8	0.0984	106.5	8x10^{-3}
Karwar (14.8° N, 74.11° E)					
M_2	0.5415	135.8	0.4941	151.0	10x10^{-2}
S_2	0.1795	168.3	0.1785	183.1	3x10^{-2}
N_2	0.1150	113.4	0.1342	106.1	1x10^{-2}
K_1	0.2931	323.1	0.3220	337.5	5x10^{-2}
O_1	0.1788	334.7	0.1529	332.5	1x10^{-2}
Apollo Bandar (18.91° N, 72.83° E)					
M_2	1.23	185.3	1.201	175.3	15x10^{-2}
S_2	0.48	218.3	0.473	232.0	08x10^{-2}
N_2	0.29	169.3	0.275	141.4	09x10^{-2}
K_1	0.42	333.2	0.486	347.0	09x10^{-2}
O_1	0.20	336.2	0.194	330.8	01x10^{-2}

ADCP data

The study used ADCP data from five locations on the shelf and two on the slope (Table 3.1) for comparison of model-simulated tidal currents. The data on the shelf used for comparison are the

same as described in Chapter 4. The data on the slope off Jaigarh used for comparison is discussed in Chapter 5. The data on the slope off Mumbai available during 2008-2009 was additionally used for comparison. The water depth of the shelf ADCP mooring is nearly 100 m, and the data covered almost the entire water column (Table 3.1). The water depth of the slope ADCP mooring is 1100 m. However, ADCP data on the slope covered only the upper water column (Table 3.1). The model was run for the year 2008 and the results for the month of March and July, which represent the pre-monsoon and SW monsoon seasons respectively were taken for the analysis. Simulated and observed currents were rotated with respect to the angle of isobath (Table 3.1). Harmonic analysis was carried out on the vertically averaged current for each location using the software TASK [Bell et al., 1999] and tidal signals were separated out. Tidal constituents were estimated from the model output and the results were compared with those obtained from observations. Off Mumbai and Kollam, the data were available for the years 2009 and 2011 respectively (Table 3.1). In these two locations, predicted tidal currents, by making use of tidal constituents obtained from the 2008 run were used for comparison. 24 tidal constituents obtained from the harmonic analysis of model results were used to predict the barotropic tidal currents for other years. Amplitude and phase of a barotropic tidal constituent do not vary significantly with time, so that predicted tides for different years can be taken for comparison with observations. Also, the seasonal variation of major barotropic tidal currents is found to be negligible off the WCI, as described in section 4.3.

Time series of observed and modeled cross-isobath tidal currents are shown in Fig. 6.2. To estimate the predictive skill quantitatively, the study used statistical analysis to estimate RMS and correlation coefficient. The correlation coefficient is above 0.9 for all the locations. The predictive capability of the model for each constituent was also estimated. To do this, tidal ellipse parameters were calculated from the eastward and northward velocity components. I determined ellipse parameters for M_2 and K_1 for each grid point and compared at the points, where observations were made. All calculations were carried out for the month of March. The model skill was assessed quantitatively by calculating the RMS error including both amplitude and phase values of each constituent [Cummins and Oey, 1997].

$$RMSE = \sqrt{0.5(A_o^2 + A_m^2) - A_o A_m cos(G_o - G_m)} \tag{6.1}$$

Where A_o and A_m are observed and modelled amplitudes of a given constituent, and G_o and G_m are the corresponding phase values respectively. The amplitude of barotropic tidal currents simulated by the model matches well with observations (Table 6.2).

Table 6.2 The amplitude and phase (G) of cross-shore barotropic tidal currents from observations and model. Phase g obtained from the ADCP data is converted to G for comparing with model. RMSE values (Eq.6.1) are also given in the last column.

	Model		Observation		RMS
Constituents	Amplitude (m)	Phase	Amplitude	Phase	
Mumbai					
M_2	16.18	124.33	13.79	150.27	5.04
S_2	7.44	345.88	6.10	352.16	1.08
N_2	3.82	110.95	3.24	132.81	1.03
K_1	7.75	271.77	5.08	271.54	1.89
O_1	3.36	261.96	2.51	284.5	1.01
Jaigarh					
M_2	23.08	76.15	16.7	81.12	4.63
S_2	11.09	111.08	7.06	106.82	2.88
N_2	5.02	52.04	4.56	66.06	0.89
K_1	4.9	39.35	4.5	29.87	0.62
O_1	1.7	43.85	3	33.43	0.97
Goa					
M_2	4.86	65.72	5.1	61.1	0.33
S_2	2.29	86.61	1.9	85.16	0.28
N_2	1.26	28.61	1.37	44.1	0.26
K_1	2.18	29.6	2.14	58.65	0.77
O_1	0.77	347.43	1.26	228.64	1.25
Bhatkal					
M_2	5.82	68.25	5.98	38.72	2.13
S_2	3.58	112.61	2.19	57.32	2.09
N_2	1.32	43.27	0.69	61.77	0.49
K_1	4.47	256.67	5.34	69.47	6.92
O_1	2.68	53.08	2.28	46.57	0.35
Kollam					
M_2	9.11	359.56	10.59	42.65	5.14
S_2	4.77	31.89	4.59	249.95	6.25
N_2	1.75	351.63	3.6	346.27	1.32
K_1	3.34	44.04	4.88	47.96	1.11
O_1	2.51	63.05	4.08	43.29	1.35

6.2.2 Barotropic tides and tidal currents off west coast off India

Figs. 6.4 and 6.5 show the spatial distribution of amplitude and phase of both M_2 and K_1 respectively along with the barotropic tidal ellipses. Spatial distribution of amplitude and phase of semidiurnal and diurnal constituents is found to be consistent with the very fine resolution coastal model, devoloped for the off WCI region [Testut and Unnikrishnan, 2016]. The amplitudes of M_2 and K_1 get enhanced in the northern region, as reported in the previous studies. Barotropic tidal

Figure 6.2 Comparison between model and observed cross-isobath component of barotropic tidal currents for the shelf mooring locations. Barotropic tidal currents were rotated with respect to the coastal angle. Refer Table 3.1 to see the year of observations for each location.

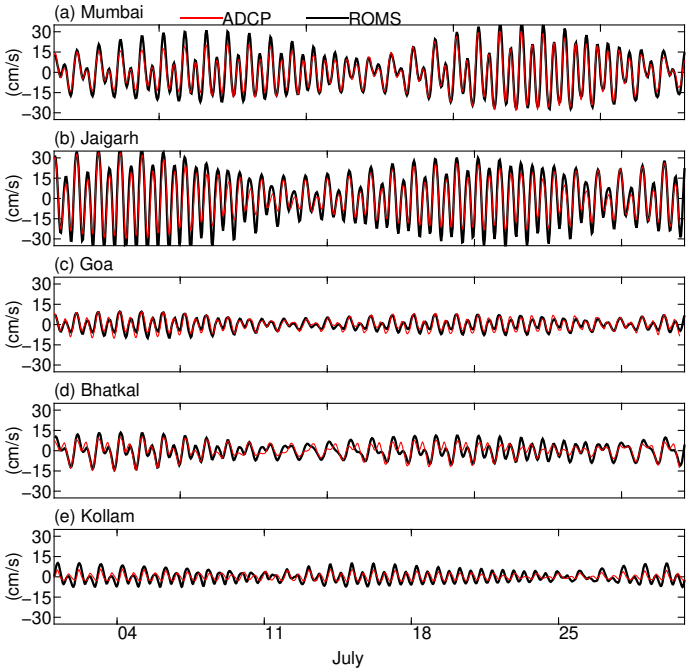

currents are strong on the shelf north of 17° N with strong cross-isobath components. The shelf experiences smaller K_1 tide compared to those of M_2. However, in the southern locations, diurnal tidal currents have comparable magnitudes with those of semidiurnal (Fig. 6.5b). In the deep regions, simulated tidal currents are small. Both semidiurnal and diurnal barotropic ellipses show more or less similar structures off WCI. The phase of M_2 varies considerably from south to north, but the phase for K_1 does not vary much spatially. As reported in earlier papers, the northward increase in amplitudes of semidiurnal tides could be explained by the theory of Clarke and Battisti [1981], in which semi-diurnal tides amplify on wide shelves, while diurnal tides do not.

6.2.3 Barotropic tidal energetics off the west coast of India

I examined the propagation characteristics of BTs by estimating tidal energy flux associated with M_2 and K_1 constituents. In the deep ocean, tides are largely progressive in nature and they bring energy to shallow shelf and coastal regions, where they get dissipated due to bottom friction. Some

Figure 6.3 Same as in Fig 6.2 but for along-isobath component of barotropic tidal currents.

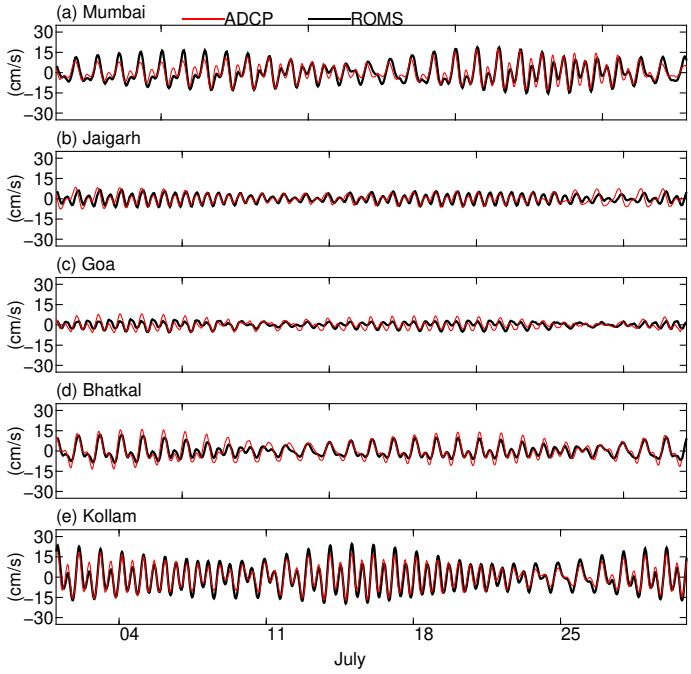

part of the energy gets dissipated through ITs mostly on shelf breaks and slope regions. The energy balance of tide,

$$W - \epsilon = \nabla.F \tag{6.2}$$

Where W is the local work rate, ϵ is the dissipation rate and $\nabla.F$ is the divergence of barotropic energy flux. The local work rate W is negligible in shallow coastal oceans and semi-enclosed seas where most of the dissipation rate is balanced by the divergence of flux [Kantha et al., 1995]. The flux of BTs can be computed using the following equation.

$$F = (\rho g h \zeta U, \rho g h \zeta V) \tag{6.3}$$

Where F is the energy flux vector, h is the water depth, ρ is the reference density (1024 kg/m3), ζ is the sea level fluctuation , U and V are the eastward and northward velocities of barotropic tidal currents. In the present work, flux computations were carried out for two constituents, M_2 and K_1. The mean energy flux [Blanton et al., 2004] in x and y directions can be estimated by,

Figure 6.4 (a) M_2 barotropic tidal ellipses from model output. Harmonic analysis is carried out for March result. Ellipses near the coast (< 40 m depth) are not shown. M_2 sea level is shaded and the phase values (G) are contoured. Scale of ellipses is shown. b) Barotropic M_2 energy flux vector. Baines barotropic forcing (Equation 5.9) is shaded. M_2 ellipses estimated from model output (black) and observation (red) are also shown. The scales of ellipses and the barotropic energy flux are given at the top right corner.

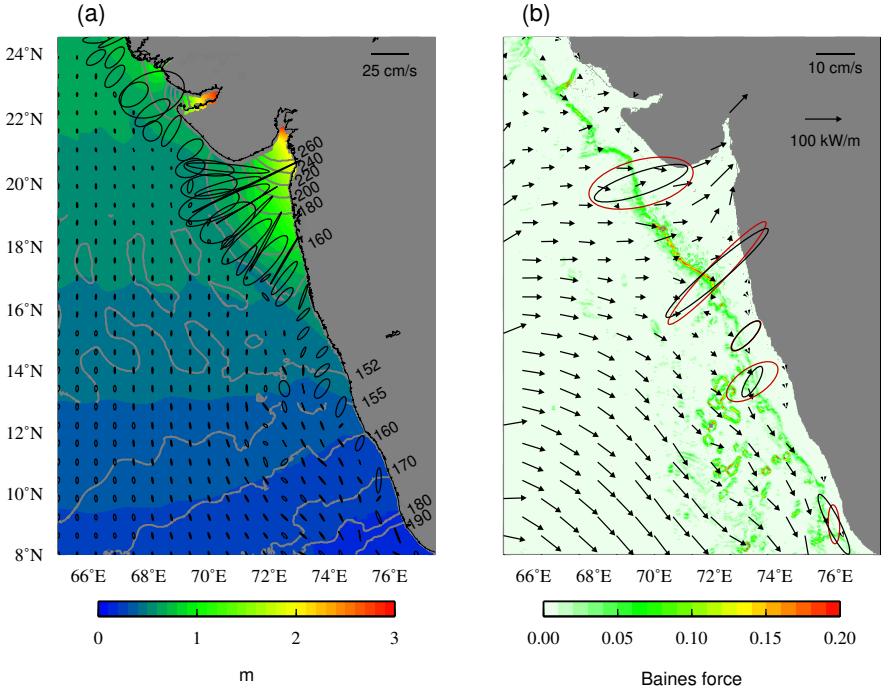

$$F_x = \frac{1}{2}(\rho g h \zeta U cos(\Phi_\zeta - \Phi_u)) \tag{6.4}$$

$$F_y = \frac{1}{2}(\rho g h \zeta V cos(\Phi_\zeta - \Phi_v)) \tag{6.5}$$

Where Φ_ζ and $\Phi(u,v)$ are the phases of sea level and tidal currents respectively for a tidal constituent. $\Phi_\zeta - \Phi(u,v)$ is the phase difference between sea level elevation and currents. Barotropic flux values depend upon the phase difference between sea level and current, where flux will be maximum when there is no phase difference between the two and it is zero when the phase difference is 90 degree. In the shallow regions, the dissipation of BTs occurs mainly due to bottom friction. The dissipation rate due to friction can be calculated from the equation [Blanton et al.,

Figure 6.5 Same as Fig. 6.4 but for K_1.

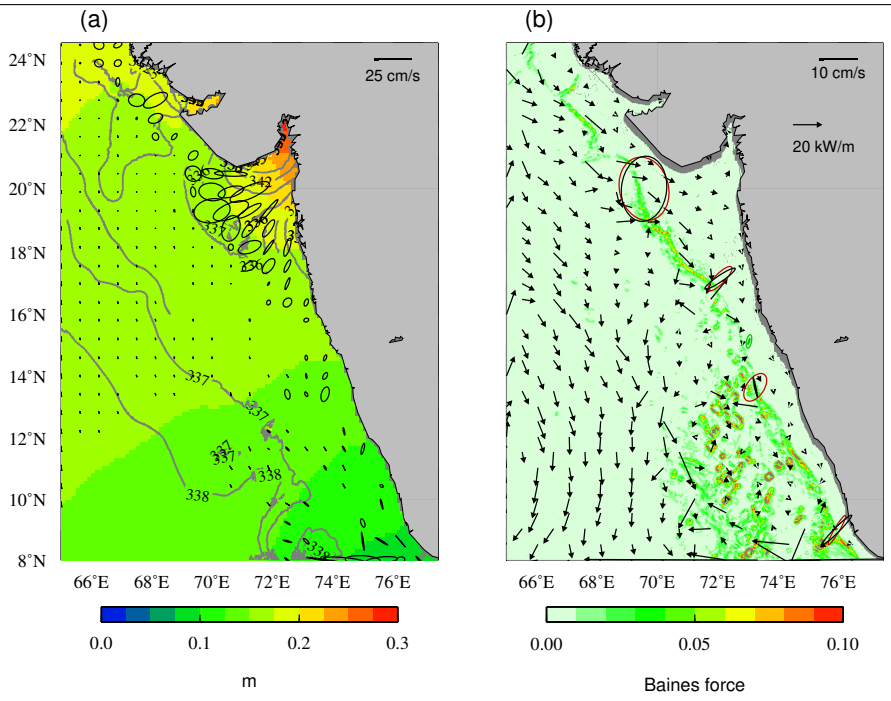

2004],

$$\epsilon = \frac{K\rho}{T}\int_0^T (U^2(t)+V^2(t))^{\frac{3}{2}}dt \tag{6.6}$$

Where T is the tidal period (Table 2.1), K is the bottom friction coefficient used in the model (.001), ρ is the reference density (1024 kg/m3), and $U(t)$ and $V(t)$ are the depth-averaged velocities [Taylor, 1919].

Figs. 6.4b and 6.5b show BT flux for M_2 and K_1 constituents respectively. Barotropic energy flux is large in the domain with values varying between 50-80 kW/m for M_2 and 20-30 kW/m for K_1 respectively. M_2 energy flux propagates from the western boundary and one branch goes straight onto the shelf and other branch propagates southward. The computed energy is found to be small in the central part of the shelf. The source of M_2 flux is the amphidromic point located in the south-west region of the Arabian Sea. Maximum tidal energy flux is found to be on the northern part of the shelf and in the surroundings of the Gulf of Khambhat region. This is due to the large barotropic tidal currents in the region. Except in the Gulf of Khambhat region, flux decreases towards shallow regions. Large dissipation takes place in the Gulf of Khambhat, where

M_2 velocity is found to be very large (1-2 m/s). The area integrated barotropic flux divergence for M_2 and the dissipative rates are 29.8 GW and 27.6 GW respectively. The remainder (about 2.2 GW) is converted to ITs. The independent calculation of IT conversion (Eq. 3.9 in section 3.3.5) provides consistent values. This is given in details in the section 6.3.

6.2.4 Validation of internal tides

Since I got confidence in the simulation of BTs, which are the forcing of ITs, I further analysed the capability of the model to simulate ITs. Two types of numerical experiments were performed. In the first run, monthly temperature and salinity fields were used and restored (Referred as ROMS-CLM hereafter). In the second run, temperature and salinity values were taken from monthly averaged HYCOM reanalysis data (ROMS-HYC). It is rather difficult to get the precise IT variations using the simplified model set up forced with the tide in the presence of monthly averaged stratification. ITs on the shelf are highly sensitive to the stratification, low-frequency currents, mesoscale eddies etc. However, the aim of the present study is to understand the capability of model to resolve ITs in simplified model set up, and to study this variability on fortnightly (spring-neap cycle) and seasonal timescales, for which the present approach can be followed. The approach of using constant stratification over a time with tidal forcing to simulate IT has been also employed elsewhere [Rayson et al., 2011; Jan and Chen, 2009; Merrifield and Holloway, 2002]. Prior to the detailed comparison of model output with ADCP data, the stratification obtained from climatology and reanalysis was compared with the stratification obtained from CTD data available on the shelf-slope transect at 17° N. Comparison of computed buoyancy frequency along 17° N shows that the latter compares better with the values determined from observations (Fig. 6.6). The model was run for the year 2008. These results were compared with observations from shelf (Chapter 4) and slope locations. Data from the slope off Jaigarh and Mumbai locations were used for comparison with model. A description of the currents on the slope off Jaigarh is given in detail in Chapter 5. The model output was compared with the observations made in other years also. This was done by reconstructing ITs for the observation period using harmonic constituents derived from the model output for the year 2008. The monthly averaged reanalysis stratification in other years shows no significant changes from that in 2008 (not shown), hence it will not affect

Figure 6.6 Buoyancy frequency across 17° N from 13 CTD casts during April 2008 (Refer Fig. 5.10 for details of CTD data.). (b) HYCOM reanalysis monthly averaged buoyancy frequency (c) Buoyancy frequency from WOA 2008 climatology. The black triangles shown along the x-axis in (a) represent the locations of CTD casts.

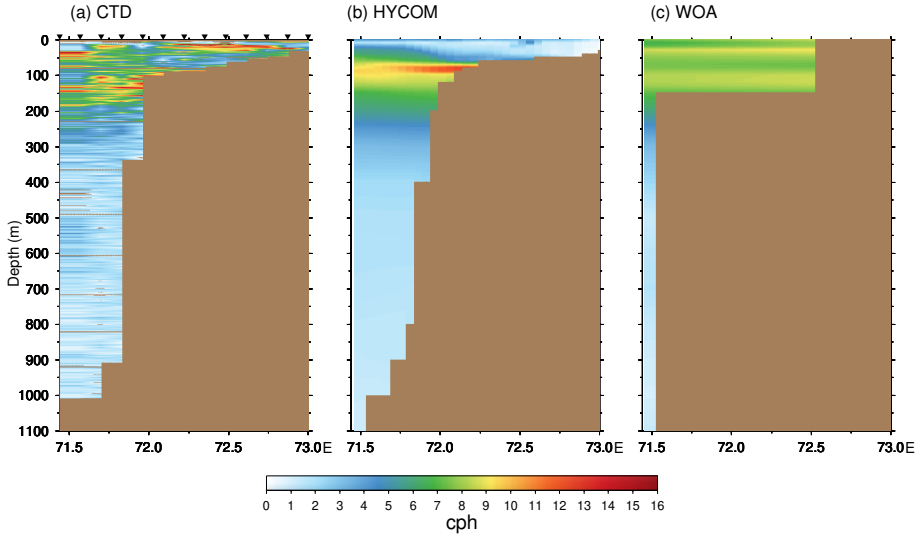

the comparisons.

Time series of internal tides

Time evolution of M_2 and K_1 ITs from both observations and model are shown in Figs. 6.7 and 6.8 respectively. Model simulations with climatology stratification and reanalysis stratification show differences in IT amplitude and vertical structure. Off Mumbai (20° N), ROMS-CLM run shows weak ITs on the shelf. Model ITs are stronger in ROMS-HYC run. Off Mumbai, both simulations underestimate the observations, where RMS error (Equation 6.1) of M_2 IT at the surface waters is about 3-4 cm s^{-1} in ROMS-CLM. In the same location, RMS error is reduced to 1-2 cm s^{-1} in ROMS-HYC. However, off Jaigarh, ROMS-HYC overestimates the M_2 ITs (Fig. 6.7). Off Jaigarh, M_2 IT shows a standing mode vertical structure in observations and ROMS-HYC model. Off Goa, ROMS-CLM shows surface enhanced ITs and ROMS-HYC shows bottom intensified ITs. ROMS-HYC results show comparable vertical structure with the observations. Off Bhatkal, ITs clearly show a downward phase propagation (upward energy propagation) in both observations and the two model experiments. Observations and model simulations indicate that the Bhatkal mooring

Figure 6.7 Observed (left panel) and simulated (middle panel indicates ROMS-CLM and right panel indicates ROMS-HYC) cross-isobath M_2 ITs on the shelf and slope mooring locations for July. Observed ITs are the harmonic analysis results of July data for corresponding years (See Table 3.1). Model IT is obtained from harmonic analysis of 2008 July data. For the other years predicted tides are used for the comparison. Barotropic tides are not removed from the slope data. The panels (a), (b), (c), (d), (e) show the data on the shelf, while (f) and (g) show the data on the slope. Blank regions in (f) and (g) indicate the absence of data.

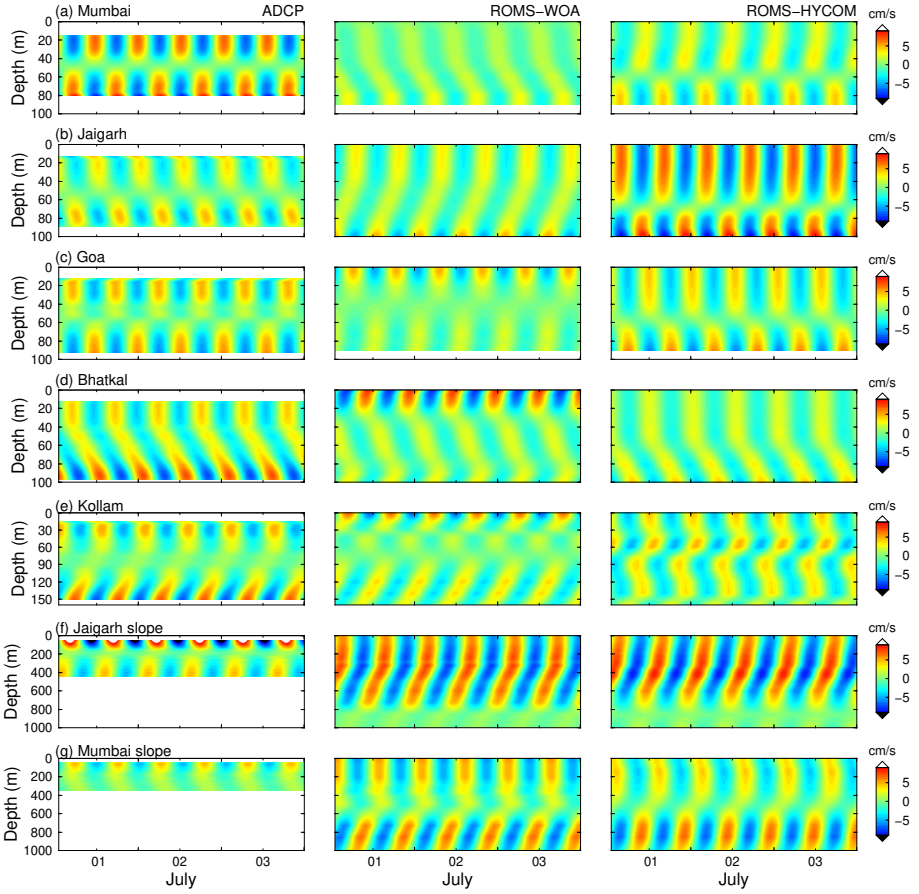

location is close to the generation site. In general, bottom intensification on the shelf is better resolved in ROMS-HYC simulation. Off Kollam, observations show downward propagating ITs. It is clearly found in ROMS-CLM, however, not found in ROMS-HYC run. The mooring location off Kollam is located towards the offshore side of the shelf break, at about 170 m depth, and showed the presence of downward propagating ITs from the onshore side of the shelf break. The detailed description of ITs generation and propagation across the mooring locations is given in

Figure 6.8 Same as in Fig. 6.7, but for K_1.

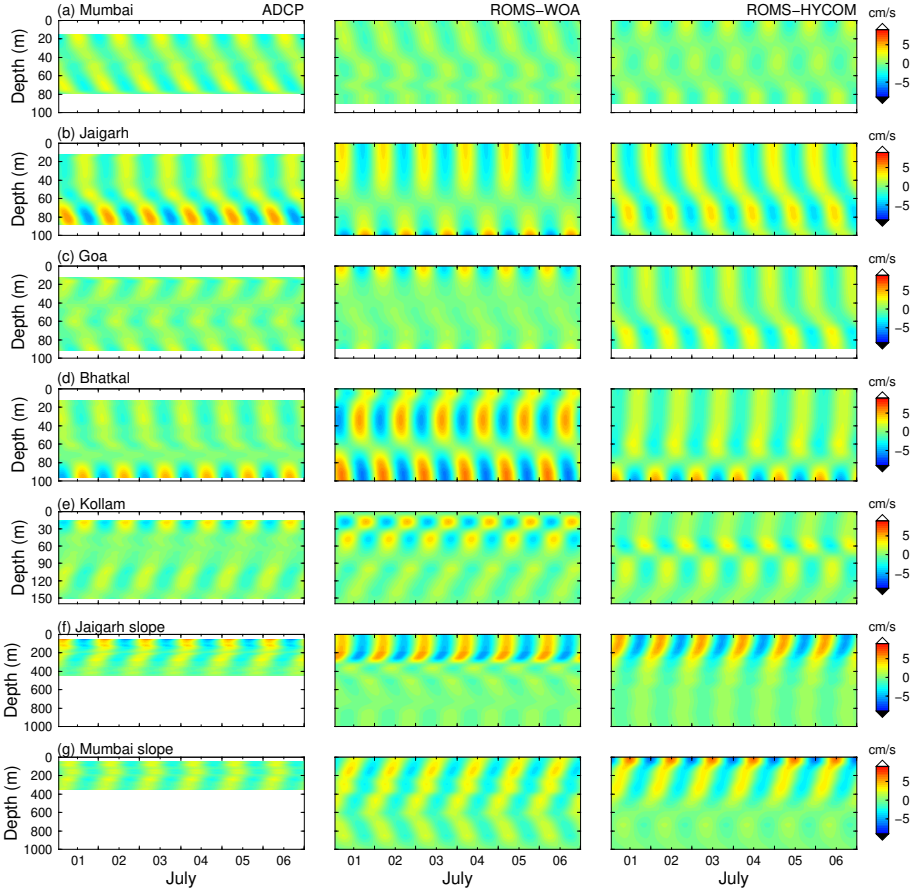

the section 6.3.1. The differences in amplitudes of ITs in the model could mainly be due to the difference between climatology/reanalysis stratification and realistic stratification. On the slope, ROMS-CLM and ROMS-HYC simulations do not show a significant difference in magnitudes of simulated ITs. On the slope locations, M_2 and K_1 ITs show downward energy propagation consistent with the downward propagating ITs from shelf break. All the analysis after this section is made using ROMS-HYC run, as the results of this experiment are better than those obtained in ROMS-CLM run.

Vertical structure of internal tides

The study used the Empirical Orthogonal Function (EOF) analysis to compare the vertical modal structure of model IT with those of observations. EOF analysis was carried out for the cross-shore

and alongshore baroclinic tidal currents from observations and model simulations for the shelf ADCP locations. First, harmonic analysis of total baroclinic currents was carried out by keeping 28 tidal constituents and baroclinic tidal currents were extracted. Then EOF analysis was carried out on the baroclinic tidal currents. Fig. 6.9 shows the first three normalized spatial modes for both observed and simulated tidal currents. The results show that first three modes together explain about 90% of the variance in both observations and the model. The first three modes resemble to the first three baroclinic mode vertical structure, except in the southernmost location off Kollam. Off Kollam, the second EOF mode shows three zero crossings in observations and simulations. The model could reproduce vertical structures very well.

6.3 Energetics of internal tides

Fig. 6.10 shows the snapshot of surface velocity of M_2 and K_1 ITs over the entire model domain. On the central and northern parts of the shelf, ITs are generated from shelf-slope region, which propagate offshore. This is consistent with satellite observations, where IT amplitudes are found to be decreasing towards offshore (Fig. 5.11). The first mode wavelength of M_2 ITs is about 125 km and 270 km for K_1 (See section 5.3.1) in the central Arabian Sea (17° N). The wavelength of ITs for M_2 and K_1 in deep ocean matches with these values, consistent with observations. In the southern part of the domain, ITs mainly generate from the northern part of the Chagos-Laccadive ridge system and propagate southward (Fig. 6.10).

In order to understand the characteristics of generation and propagation of IT in detail, baroclinic tidal energy flux, barotropic to baroclinic conversion rates, dissipation and radiation terms were estimated (See Section 3.3.5 for equations). Table 6.3 shows the area integrated baroclinic energy for five major tidal constituents M_2, S_2, N_2, K_1 and O_1. The total energy conversion from these five constituents is 3.63 GW. Most of the barotropic to baroclinic energy conversion is taking place via M_2 in the domain (66%), followed by K_1 (17%), S_2 (10%), O_1 (3%) and N_2 (3%). Magnitude of area-integrated dissipation term is almost same as that of conversion, indicating that nearly entire baroclinic tide is dissipated inside the model domain. The area integrated value of radiation term is negligible compared with the dissipation term. The area-integrated value of

Figure 6.9 Normalized first three EOF spatial modes for ITs (black represents observed and red represents simulated). ITs were obtained from one-month harmonic analysis of baroclinic currents for July. The percentage of variance of each mode for the model (red) and observation (black) is also shown.

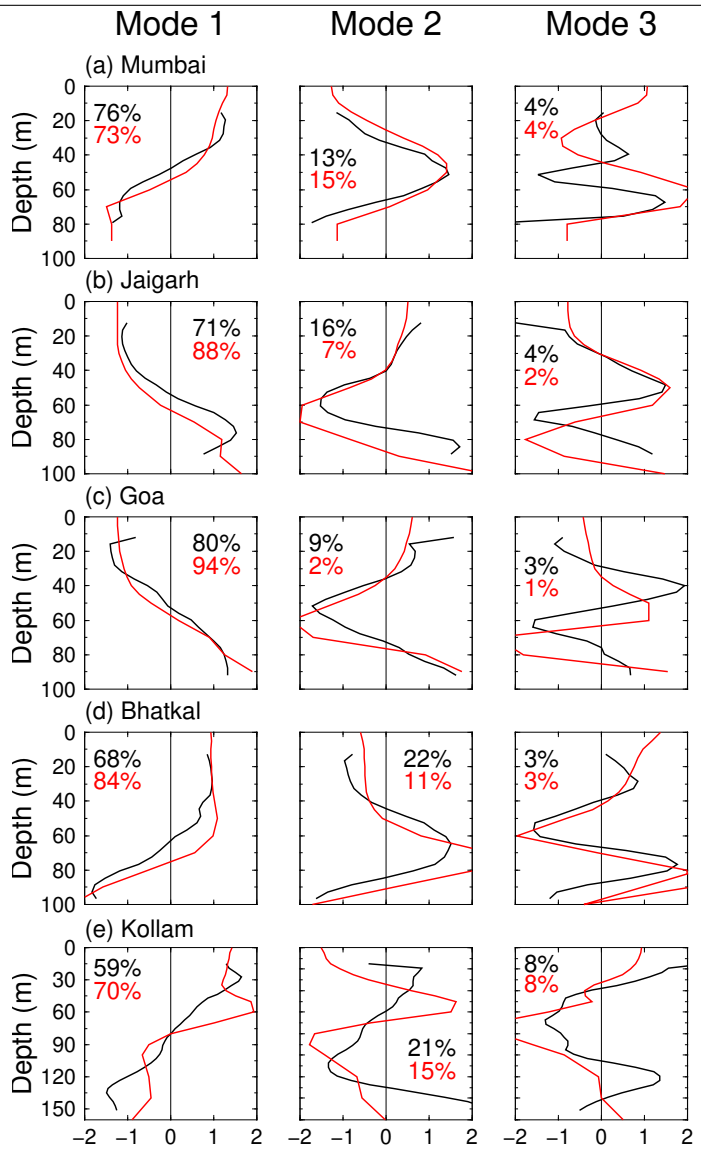

conversion in ROMS-HYC run is 2.4 GW and same in ROMS-CLM run is 2 GW for M_2. The difference is due to the higher IT magnitudes in ROMS-HYC. The discussion hereafter will be restricted to M_2 ITs, as it has the largest magnitudes among various constituents in the region.

Spatial distribution of energy flux, conversion (Fig. 6.11), and dissipation, radiation (Fig.

Figure 6.10 Snapshot of surface M_2 baroclinic velocity on 01st July 2008. Left panel shows snapshot of U velocity and right panel shows the V velocity. The region less than 40 m depth is not considered. 100 m and 1000 m depth contours are also shown.

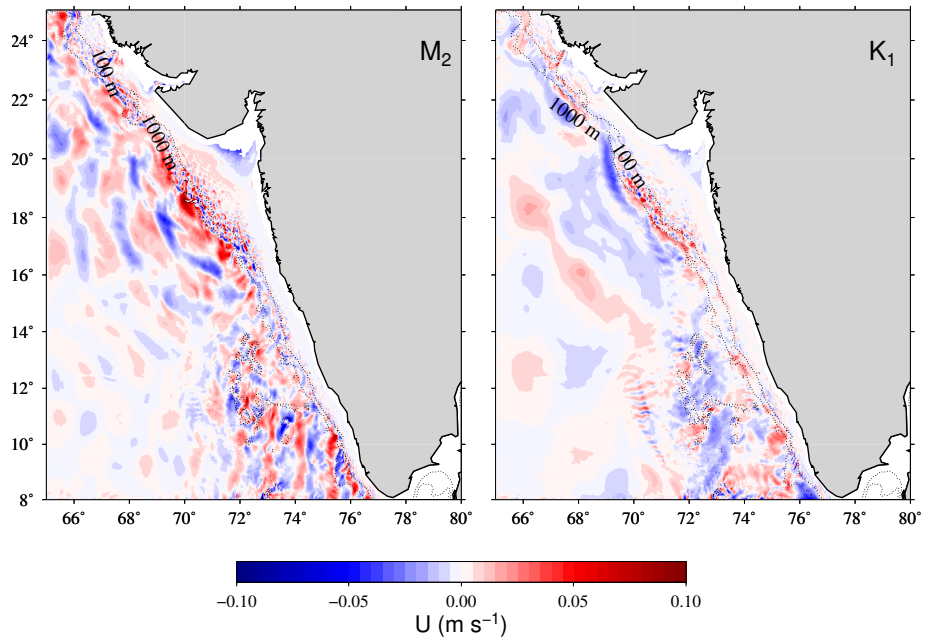

Table 6.3 The area integrated values of conversion, dissipation and radiation terms for major five constituents over the model domain. The units are in GW (Gigawatt).

Tidal constituents	Conversion (GW)	Dissipation (GW)	Radiation (GW)
M_2	2.4	2.4	-.05
S_2	.37	.38	-.01
N_2	.12	.12	-.002
K_1	.62	.67	-.05
O_1	.12	.13	-.01

6.12) for M_2 are shown. The model estimates show that there are two potential regions of strong barotropic energy conversion off the WCI. One is the continental shelf-slope region around 16°-18.5° N in the central part off the WCI (Box-1 in Fig. 6.11). These shelf and slope regions show a clear positive conversion indicating local IT generation. The total barotropic to baroclinic conversion for M_2 is 1.15 GW for this box.

The second strongest energy conversion occurs along the Chagos-Laccadive ridge system extending from 8° N to 14° N (Box-2 in Fig. 6.11). Unlike the generation site off the central WCI, both positive and negative energy conversion rates can be seen in this region. Negative energy

Figure 6.11 (a) Baroclinic energy conversion rate and (b) RMS value of depth-integrated baroclinic energy flux for M_2 is shaded and overlaid with energy-flux vectors. Scale of the vectors is given. Rectangular boxes indicate the two major IT generation regions off the WCI. 100 m and 1000 m bathymetry contours are shown.

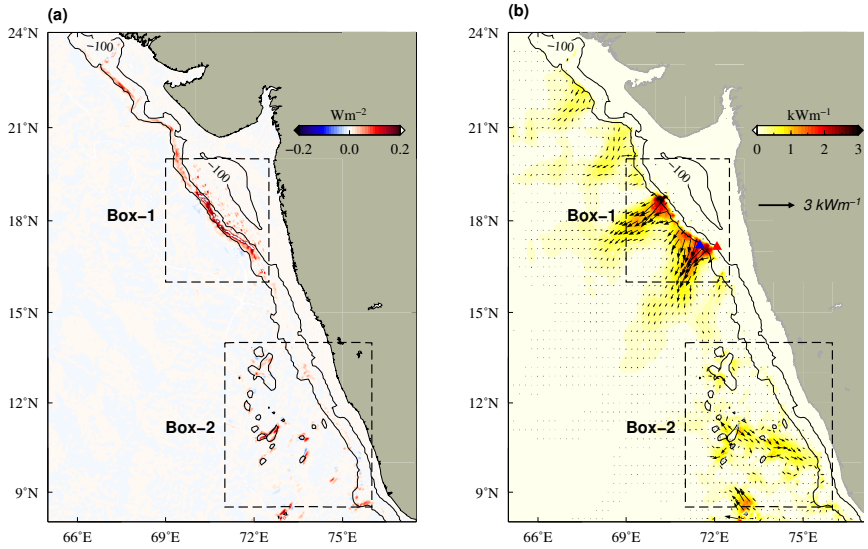

conversion is due to the phase difference between local barotropic tidal currents (Ub) and baroclinic bottom pressure anomaly ($p\prime_{bot}$), which arises due to the propagation of ITs generated from other sources [Carter et al., 2012]. The Chagos-Laccadive ridge system consists of many isolated Islands, in which IT generation occurs in multiple locations. Therefore, the negative conversion rates in some areas could be due to the propagation of IT from different sources. The total M_2 conversion in the Chagos-Laccadive ridge system is about 0.62 GW (Box-2 in Fig. 6.11). The two other important generation sites are found to be in the shelf-slope region around 20° N and 22° N.

Further, the spatial distribution of depth-integrated energy flux is examined (6.11b). Large energy flux is found over the central shelf-slope region and near the Chagos-Laccadives ridge. Offshore propagating ITs dominate the central WCI, particularly between 16°-18.5° N. Depth-integrated energy flux is found to be maximum over the shelf break and the slope regions, and the magnitude decreases towards the deep region. Depth-integrated M_2 energy flux has the amplitude of 1-3 kW/m on the slope region. It is important to note that most of the IT generated along the continental margins radiates into the offshore regions and only a small part is propagating towards

Figure 6.12 Spatial distribution of baroclinic M_2 (a) dissipation and (b) radiation.

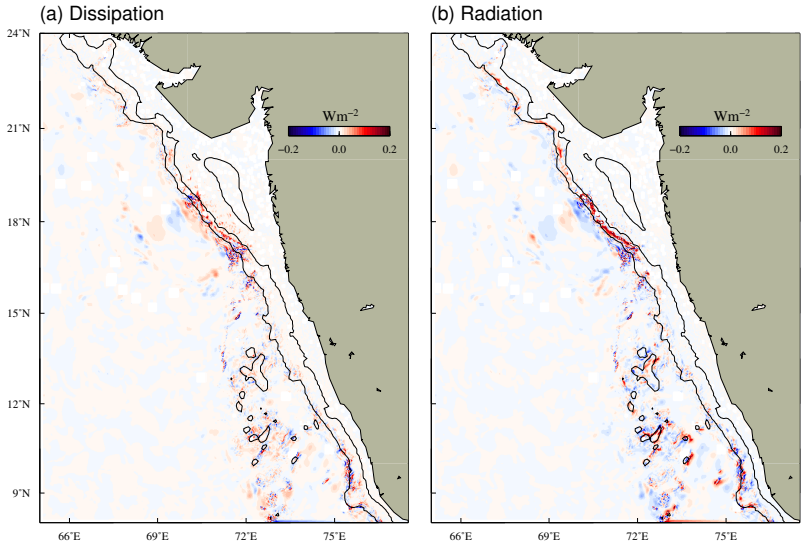

the coast. Near the Chagos-Laccadive ridge system, energy flux value exceeds 2 kW/m. The direction of flux vectors shows that IT generated in these regions radiate southward (8°-11° N 72°-75° E). It is possible that IT radiating from multiple generation sites interact with each other and cause constructive and destructive interference patterns. Depth-integrated M_2 energy flux shows enhancement in the IT energy in the deep region (around 20° N), which possibly resulted from the interference of IT. Further, the spatial distribution of depth-integrated K_1 energy flux is similar to that of M_2 on the central and northern shelf with values ranging between 0.3 and 1 kW/m, which is about half of the M_2 energy flux. However, on the southernmost shelf region (near 9° N), K_1 IT energy flux is also found to be large with the comparable magnitude of M_2 energy flux. The magnitude is about 0.5-0.7 kW/m for both M_2 and K_1. In observations also, K_1 ITs are strong on the shelf off Kollam (9° N), indicating the importance of diurnal ITs on the southern part of the shelf.

Fig. 6.12 shows the spatial distribution of dissipation and radiation of M_2 ITs. Fig. 6.11 and 6.12 show that a part of ITs dissipates at the conversion region and the remaining is radiated out. Dissipation is strong on the shelf break and slope regions and getting weak towards the deep regions. Radiation and dissipation of ITs at the generation source depends upon the type of topog-

raphy. If the topography is critical, i.e., slope of topography (ΔH/ΔX) matches the characteristic slope of ITs C=$(\frac{\omega^2-f^2}{N^2-\omega^2})^{\frac{1}{2}}$, an enhanced dissipation can be expected [Kang et al., 2000]. Estimates (Fig. 6.13) show that slope of IT characteristics and bottom topography match at the continental slope region. The large dissipation taking place on the continental slope could be due to this. In this region, most of the radiation occurs towards offshore side of the shelf break. This is because the shelf breaks off five ADCP locations are supercritical (ΔH/ΔX $> C$) to IT, which do not allow much shoreward propagation onto the shelf.

6.3.1 Cross-shore and along-shore variability of internal tide energetics

Internal tide characteristics across 5 ADCP moorings

Fig. 6.13 shows M_2 ITs emanating from the shelf-slope region off the five ADCP mooring locations on the shelf. Depth-integrated energy flux in x and y directions, depth-integrated barotropic to baroclinic conversion, potential energy, kinetic energy, dissipation and radiation are shown in the figure. IT energy flux, potential energy and kinetic energy are maximum at the upper slope, which weakens towards the deep ocean. Over the deeper part of the of slope region, IT energy is surface intensified and becomes weak with depth owing to the weak stratification in deeper depths. The surface intensification of IT is also visible in ADCP observations on the slope locations (section 5.3).

I estimated two parameters, which are useful to understand the generation of ITs. They are the criticality parameter and the Baines barotropic forcing term. Criticality parameter is the ratio between topographic slope and IT slope ($\gamma = \frac{\Delta H/\Delta X}{C}$). Slope of IT for a particular frequency is given by C=$(\frac{\omega^2-f^2}{N^2-\omega^2})^{\frac{1}{2}}$, where ω is the frequency of IT, f is Coriolis frequency and N is the buoyancy frequency. Maximum energy conversion is expected to take place when topographic slope matches with characteristic slope. Body force [Da Silva et al., 2009] was calculated from the equation. F=z$N^2(z)\int_0^T Qdt.(1/h)$; Where z is the upward vertical direction, Q=(uh, vh) the barotropic mass flux vector and u and v are barotropic velocities from model output and h is the water depth. Stratification was derived using monthly averaged temperature and salinity fields from HYCOM. The Baines forcing term was integrated over a tidal period (Figs. 6.4b, 6.5b).

Criticality parameters across ADCP locations (Fig. 6.13) show that the shelf breaks are su-

Figure 6.13 M_2 ITs across five ADCP mooring. The panels (a), (b), (c), (d) and (e) represent each shelf ADCP location. For each location, there are four panels, the top panel shows potential energy (black) and kinetic energy (red). The second panel indicates radiation (black) and dissipation (red) across the locations. The third panel shows, depth-integrated energy flux in x (black) and y (red) directions, and barotropic to baroclinic conversion (blue). Values of flux are given in left axis and conversion in right axis. The fourth indicates amplitude of M_2 IT across the shelf. The calculations were done for July month. The M_2 IT is constructed from the amplitude and phase value obtained from harmonic analysis of baroclinic currents. Criticality parameter (Ratio of topography and IT slope) is also shown in the fourth panel of each figure. The values are given at the right axis.

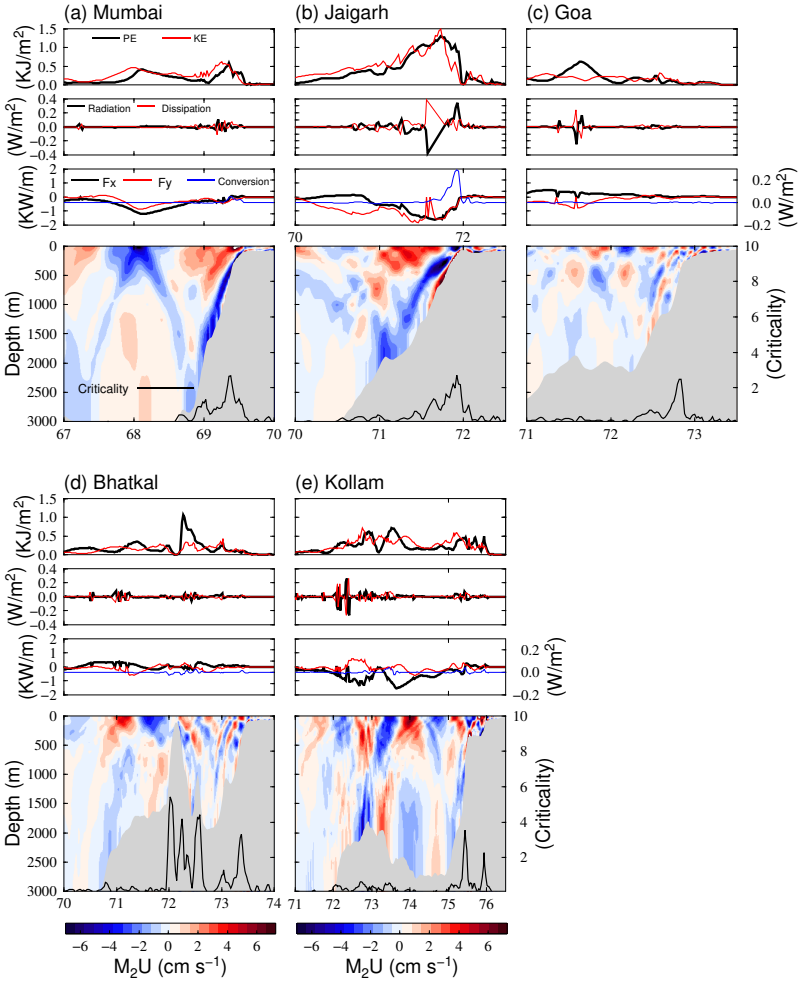

percritical to M_2 ITs. This restricts ITs propagating from deep regions onto the inner shelf. The criticality parameter decreases towards onshore and offshore directions and becomes close to one

Figure 6.14 Conversion and dissipation integrated over each 100 m depths across the shelf over the model domain. The depth-integrated values are shown for both March and July, which are taken as the representative months of pre-monsoon and SW monsoon. The cumulative fraction is the percentage of the ratio of integrated values between each section and the total (Thin black and red lines). The values of the cumulative fraction are given on the right axis. The blue dashed line is the criticality averaged over the same depth intervals. Criticality values vary from 0 to 3. Right axis of the plot (without percentage) indicates criticality values.

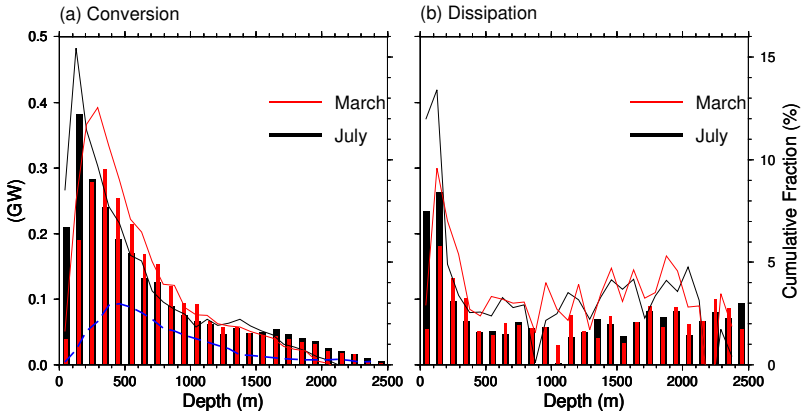

over upper slope regions, middle-slope and onshore side of the shelf breaks. For instance, off Jaigarh, the shelf ADCP mooring was located offshore side a topographic structure having a height of about 60 m. This topographic structure separates dynamics of IT on the shelf from that on the slope region. The two sides of the topographic structure are potential IT generation sites for both semi-diurnal and diurnal frequencies. ITs propagate onshore from the onshore side of the structure and offshore from the offshore side of the topography. Large offshore propagating energy fluxes reaching approximately 2-3 kW/m are noted in this region with a positive barotropic to baroclinic energy conversion. Barotropic to baroclinic energy conversion rate in this region is about 0.2-0.4 W/m^2. Towards the shelf, the depth-integrated energy flux reduced upto 200-300 W/m, which propagates in an onshore direction. Off Mumbai, the estimated depth-integrated energy flux propagating to onshore direction is about 120-160 W/m. Off Goa, IT energy is relatively weaker on the shelf than those on other locations in the model with a value of 50-80 W/m. Off Goa, the deep region experiences large southward propagating ITs (See Fig. 6.13c) indicating that ITs off Goa in deep regions are generated from north of the site (Fig. 6.11 b).

Figure 6.15 Conversion, dissipation, and radiation for M_2 ITs integrated between shelf (0-100 m), shelf-break (100-200 m), upper slope (200-1000 m) and deep slope (1000-3000 m) regions. Three terms were estimated for the month of July. The dotted lines indicate the latitudes of ADCP mooring locations.

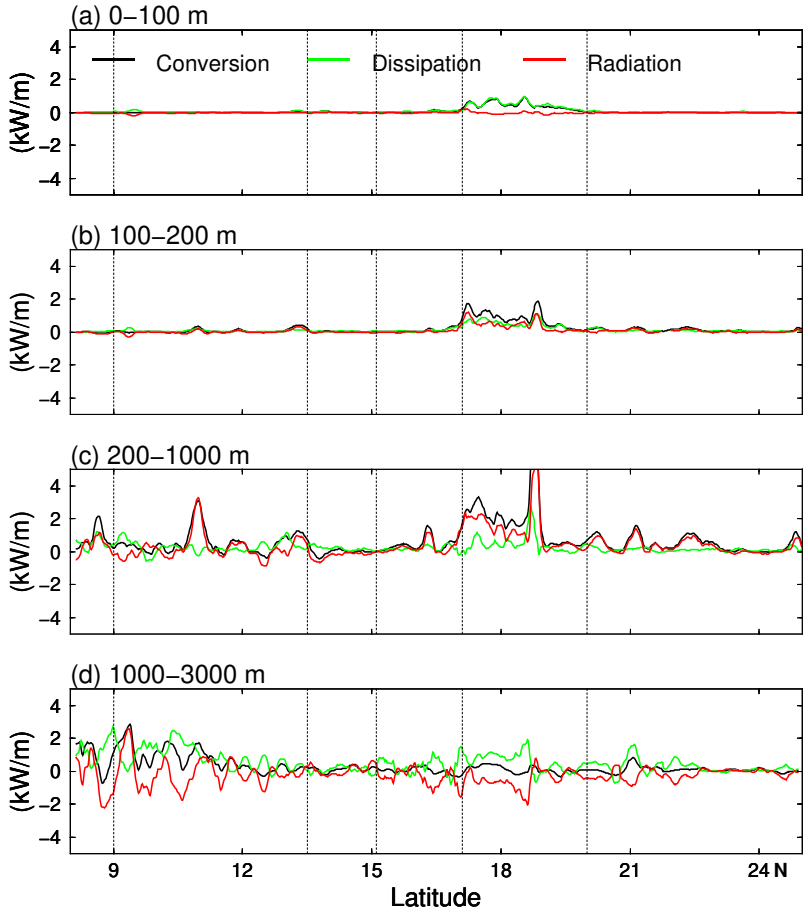

6.3.2 Seasonal variations of internal tides on the shelf off west coast off India

The previous chapters (Chapters 4 and 5), based on ADCP observations, showed marked seasonal variations in the amplitudes of ITs on the shelf showing enhanced ITs mostly during the south-west (SW) monsoon period, when the stratification is increased, and relatively weaker ITs during the pre-monsoon period. Simulated ITs on the shelf also show seasonal variations, with weak ITs found in March and strong ITs in July. The strengthening of ITs during July is attributed to the increased stratification on the shelf during the southwest monsoon. For instance, the depth-integrated energy flux of M_2 ITs on the shelf off Jaigarh is about 0-50 W/m in March, which

increased up to 200-250 W/m in July. Off Mumbai, it is increased from 20-40 W/m to 80-100 W/m. However, no significant increase in IT energy is found on the shelf off Goa during July. Bottom intensification of ITs during the month of July was noted off Jaigarh, Bhatkal, and Mumbai. Bottom intensification occurs at the region, where the slope of IT beam becomes close to the topographic slope. During the month of July, the shelf region becomes more favourable for the generation of ITs. The increase in stratification helped to turn the flat shelf area to become critical for IT generation. The Barotropic body force is also increased on the shelf during July due to the increase in stratification.

Off Jaigarh, seasonal variations on the slope is opposite to that on the shelf region, where IT is strong during March than that in July. The depth-integrated Baines forcing is found to be slightly enhanced on the slope during the pre-monsoon period, opposite to that on the shelf region. In slope region, pre-monsoon stratification is slightly enhanced below 200 m depth. The barotropic forcing gets strengthened due to the increased stratification and ITs also get enhanced. This suggests that the seasonal variation on the slope off Jaigarh is also controlled by the deep pycnocline stratification.

6.3.3 Conversion and dissipation of energy on the shelf

Conversion and dissipation values integrated for each 100 m depth interval (Fig. 6.14) along the latitude and plotted across the shelf to understand the shelf-slope variation of IT energy in detail. The maximum energy conversion is taking place within 100-300 m depths, i.e., at the shelf breaks and the upper slope regions. Conversion decreases towards the deeper depths and becomes nearly zero below 2500 m depth. The averaged criticality parameter is also shown in the figure. Maximum barotropic to baroclinic conversion occurs in the region, where criticality parameter becomes close to one. Though barotropic to baroclinic conversion is largely taking place on shelf break and upper slope regions, the dissipation is distributed to deep ocean, where a large part of the baroclinic tide gets dissipated between 500-2500 m. A large part of ITs generated on the shelf break and upper slope radiate offshore and dissipate within a distance of about 100 km.

Seasonality of ITs is significant on the shelf and upper slope, but weak on the mid-slope and deep regions. On the shelf, maximum conversion takes place in July. Though seasonality is not

significant on the lower slope, a slight increase in the conversion and dissipation is found during March. This is consistent with the observations described in Chapter 5.

6.3.4 Latitudinal variations

Latitudinal variation of conversion, dissipation and radiation was also assessed. The three terms were integrated over the shelf (0-100 m), shelf break (100-200 m), upper slope (200-1000 m), and deep regions (1000-3000 m) (Fig. 6.15) for July. The maximum energy conversion of ITs takes place between 16°-18.5° N. Barotropic to baroclinic conversion is weak on the shelf compared to the shelf break and slope regions, and most of the energy is dissipated inside the shelf region. Weak radiation values on the shelf show that ITs on the shelf are well separated from the slope region, because of the supercriticality of the shelf break.

6.4 Realistic simulations

6.4.1 Introduction

This section mainly involves a description of the results from a model run using realistic forcing. The previous section assessed the capability of the model, with barotropic tidal forcing and monthly-averaged temperature and salinity fields, to simulate ITs, for studying generation, propagation and dissipation of ITs on the shelf and slope off the WCI. The model could reproduce IT variability on the shelf and slope. In the third numerical experiment, realistic atmospheric forcings along with tidal forcing were given and boundary and initial conditions of temperature and salinity were given from a coarse resolution (1/12°) ROMS model output. Tides were prescribed from global tidal model OTIS, as in experiments 1 and 2. The details of coarse resolution model for the Indian Ocean are given in Francis et al. [2013]. I intend to study the model performance in runs, in which temperature and salinity fields evolve in time. It is important to assess the capability of the model to capture ITs in a realistic simulation for operational oceanographic applications. The description is given in Chapters 4 and 5 show that tidal currents on the shelf and slope off the WCI, particularly on the northern part, have comparable magnitudes with those of low-frequency currents, thereby operational models for this region require inclusion of tidal currents. Table 6.4

gives the percentage of contribution of tidal currents in total currents on the shelf. Also, the studies in other ocean basins show that BTs and ITs play an important role in the shelf, slope and deep ocean dynamics [Kurapov et al., 2003; Leichter et al., 2003; Arbic et al., 2012]. ITs are well known for interacting with low-frequency currents [Pereira and Castro, 2007], mesoscale eddies [Dunphy and Lamb, 2014], near-inertial waves [Aucan and Merrifield, 2008] etc. Incorporation of tidal forcings in the model is found to improve the model performance in the simulation of distribution of water masses [Lee et al., 2011] and low-frequency variabilities. Finally, to improve tidal mixing parameterisation in models, it is important to know the spatial and temporal pattern of energy budget in the realistic ocean. The motivation for realistic simulation is twofold. The first is to study the variation of ITs in the presence of other low-frequency variabilities. The second aim is to understand the role of ITs on the background low-frequency variabilities due to the mixing induced by ITs. However, in this thesis, I will not be addressing the second part. The present study attempts to address the first motivation and try to make a strong platform for addressing the second motivation.

Table 6.4 Percentage of variance of tidal currents in observed total currents on the shelf. Total currents are band passed between 4-30 hours band to obtain tidal currents. This band excludes inertial signals in all locations, where inertial period varies from 35-76 hours from 9° N to 20° N. Depth and time-averaged variance ($< u^2 + v^2 >$) were estimated for both tidal currents and raw currents, and the ratios were estimated. One year data were used to estimate the variance. The ADCP data used to calculate variance is described in Chapter 4. (Table 3.1 gives the details of the moorings and the data period).

ADCP Location	Barotropic tidal currents (%)	Baroclinic tidal currrents (%)	Total tidal currents (%)
Mumbai	39.4	8.6	48
Jaigarh	46.6	9.3	55.9
Goa	5.5	8.7	14.3
Bhatkal	9.5	7.6	17.1
Kollam	11.2	8.6	19.8

In this section, I determined the capability of the model to reproduce ITs on the shelf and slope off WCI by comparing model output with ADCP data. The comparison of BTs with observations is not done in detail in this section, as practically no difference between the results of earlier runs and the present runs has been found in simulated barotropic currents.

Figure 6.16 Locations of ADCP moorings, whose data were used for comparison with the results of realistic model experiments. The model run was carried for the year 2014. Red triangles represent shelf ADCP mooring locations. Slope mooring locations are shown in black triangle. The model domain is shown in rectangle. The red dots indicate locations of Argo floats, whose data are available for the month of January 2014.

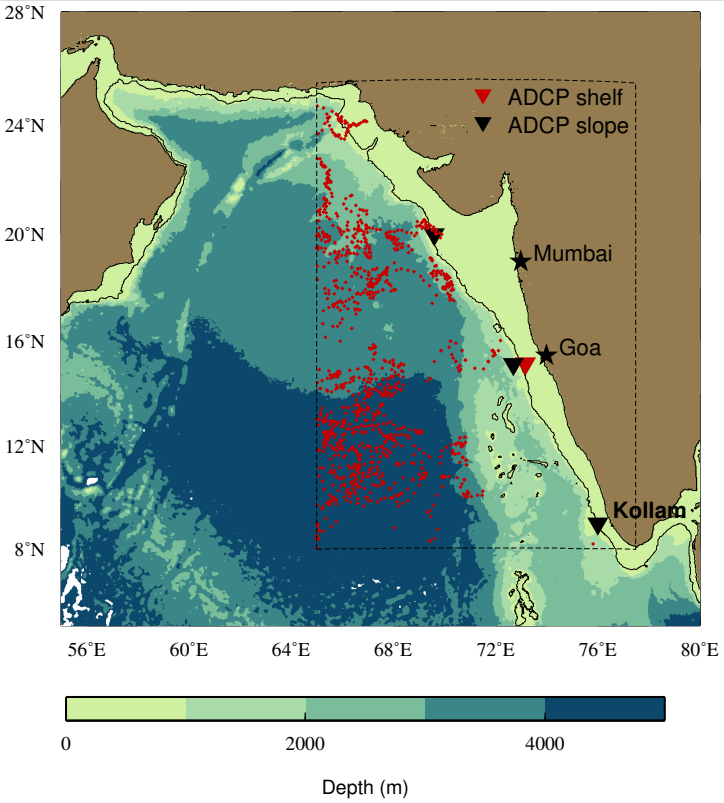

6.4.2 Stratification

It is important to simulate temperature and salinity accurately, as stratification causes considerable variability in ITs. To understand the performance of the model in reproducing stratification, buoyancy frequency obtained from the model was compared with values estimated from Argo observations (Fig. 6.17). There are about 1200 Argo profiles available in the model domain in the month of January in the year 2014 (Fig. 6.16). Argo floats data are not available on the shelf and slope regions. To compare the model stratification in shallow shelf and slope regions, CTD data off Goa were used. The temperature and salinity profiles from each Argo data were used to

Figure 6.17 Buoyancy frequencies (cph) from Argo data and the model simulations. Standard deviation of model (Argo) stratification is given in red (black) colour. The gray line indicates the bias of the model with observation. Root-mean-square error (RMSE) is given in green colour. The unit of x-axis is cycle/hour.

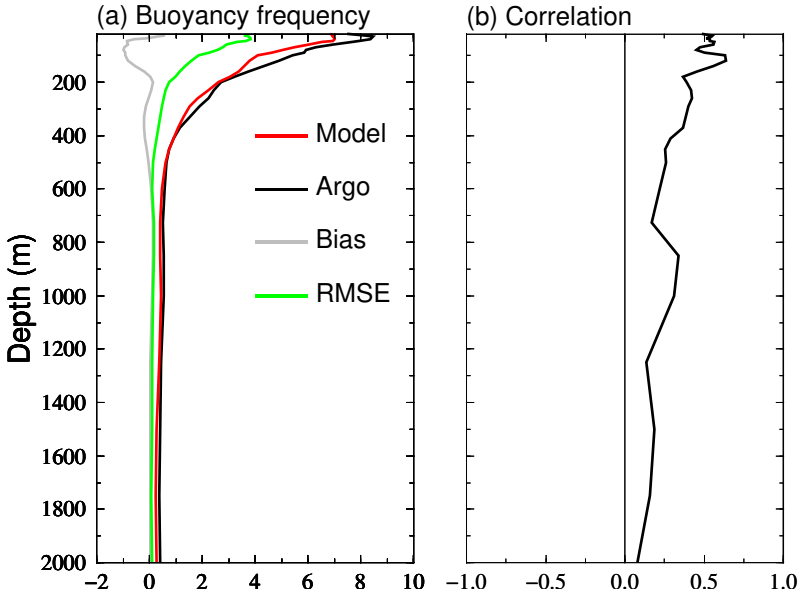

calculate buoyancy frequency and the corresponding values from the model were estimated for the same grid point for comparison. Before doing the calculation, Argo data were re-gridded to the model grid. Standard deviation, bias and RMSE were calculated at each point and spatially averaged. The standard deviation of the model and observed stratification and the correlation between the two shows that the model could capture stratification fairly well (Fig. 6.17). The negative bias and root-mean-square values indicate that the model overestimates stratification in the subsurface. Comparison of stratification in the model with CTD data off Goa is shown in Fig. 6.18. 5 CTD casts were taken in a cross-shore section off Goa on 19 and 20 September 2014. The casts were made at depths of 100, 200, 300, 800 and 1000 m. Buoyancy frequency was estimated for each profile averaged across the shelf and compared with that estimated from the model simulation.

6.4.3 Spectra

Rotary spectra of horizontal currents were computed to determine the dominant internal wave frequency present in the ADCP current data. For shelf data, the rotary spectrum was calculated

Figure 6.18 Temperature and buoyancy frequency from observations off Goa (15° N) and the model simulations. Temperature and buoyancy data were averaged across the shelf. Prior to averaging, CTD temperature data was re-gridded to the model grid.

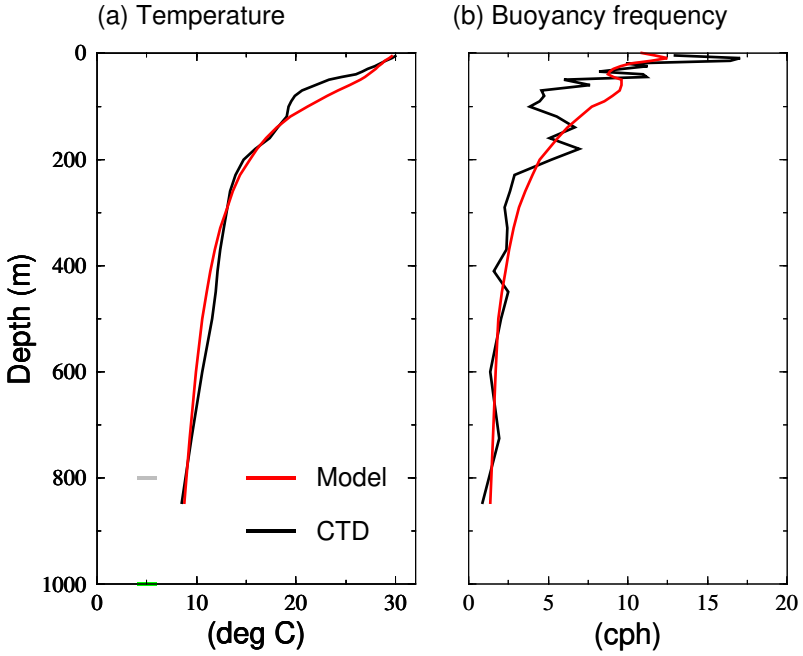

on baroclinic currents and for the slope data, the calculation was carried out on the raw data. As the barotropic tidal currents could not be removed from the slope observations, all the analysis was carried out on the total tidal currents. Model barotropic tidal currents show small values on the slope locations (1-2 cm s^{-1}). Rotary spectra were computed for the month of January 2014. The vertically averaged clockwise and anticlockwise spectra of horizontal currents are shown in Figs. 6.19 and 6.20 respectively. Internal tidal energy peaks are found at semidiurnal, diurnal and at higher harmonics like quarter-diurnal frequencies. On the shelf and slope off Goa, diurnal ITs are found be weak in the observations. However, the model shows elevated energy at the diurnal frequency. The time series (Fig. 6.22) shows surface intensified diurnal ITs in the model. ADCP data were missing over the first 20 m water column for making a comparison. Model also overestimates quarter-diurnal frequencies on the slope off Goa and Kollam, and on the shelf break off Goa. Though not strong, elevated clockwise energy is found in the near-inertial wave (NIW) peak in the shelf data. However, near-inertial waves are weak in the model. The NIW peak is

Figure 6.19 Clockwise component of rotary spectra for observed (blue) and model (red) currents. On the shelf off Goa the spectra were averaged over the entire water column. On the slope locations, the spectra were averaged over the upper water column. The depth range used for averaging is given on the top of the figures. The frequencies of tidal constituents are shown in dotted vertical lines. The Coriolis frequency (f) for each location is also marked. The dotted black line is $\omega^{-1.5}$ where ω is the frequency.

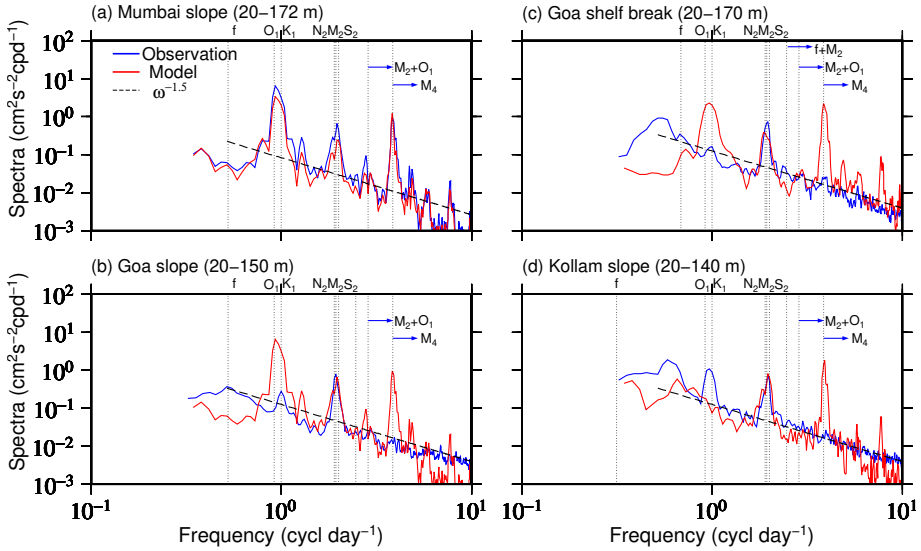

absent in the slope location. There was no cyclone reported in the Arabian sea during January 2014. The elevated energy may be due to the local high-frequency strong winds during the period. The model could not simulate these events probably due to the inadequate accuracies in wind fields. The spectral slope of both observations and simulations are smooth ($\omega^{-1.5}$), less steep than that of GM spectra (ω^{-2}).

6.4.4 Time series

The barotropic tidal currents are of moderate strength on the shelf break off Goa (4-8 cm s^{-1}), however, ITs are found to be strong (18-24 cm s^{-1}). The maximum velocity of barotropic tidal currents is aligned across the shelf break (Fig. 4.6). This triggers large ITs in the region. On the slope, ITs are surface intensified (Figs. 6.21 and 6.22). On the shelf, ITs are bottom intensified. This shows that large barotropic to baroclinic energy conversion takes place on the shelf break and nearby regions. It can be further understood by looking at the vertical structure of ITs. The M_2

Figure 6.20 Same as in Fig. 6.19, but for counterclockwise component of rotary spectra for the model and observations.

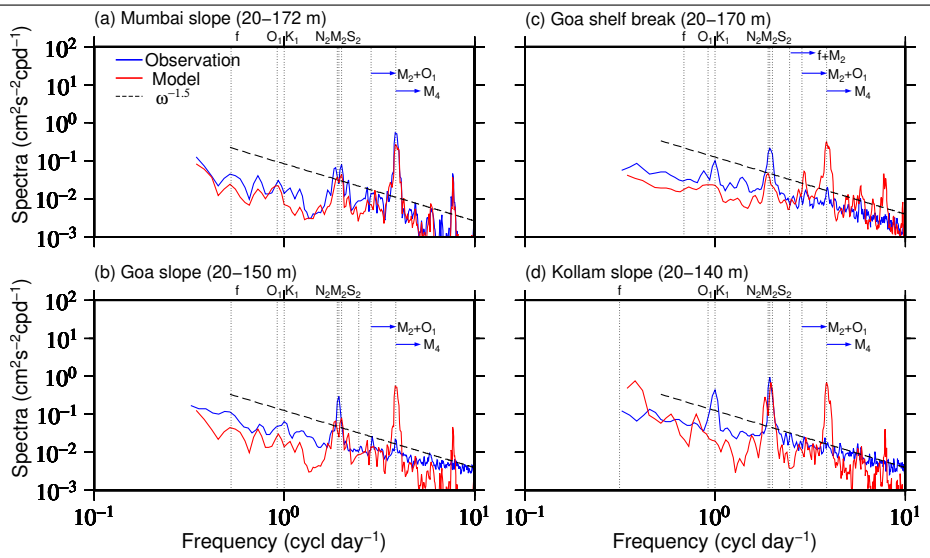

ITs show a clear upward energy propagation on the shelf break. The model results also show the upward energy propagation (Fig 6.21b). This shows that the mooring is located along the path of the upward ray, or near to the generation site. Slope ITs over mid-depth and towards bottom show downward energy propagation. This is consistent with the downward propagating IT ray from the shelf break. Off Mumbai, slope IT data show downward energy propagation. This also shows that the slope is experiencing downward propagating ITs from the shelf. The model is found to be overestimating the magnitudes of ITs off Mumbai.

6.4.5 Internal tide energetics in the realistic model

Barotropic to baroclinic conversion rate, dissipation and radiation terms for M_2 and K_1 were estimated using realistic model outputs (Table 6.5). The values given in the bracket are those estimated from the ROMS-CLM run. Barotropic to baroclinic conversion is increased in the realistic run compared to the climatology run by about 0.2 GW for M_2. Most of the energy dissipates inside the domain and a little is radiating out (Table 6.5), similar to other runs. The spatial distribution of energy flux does not appreciably vary from that in the previous experiment (not shown).

Figure 6.21 M_2 ITs from observations and model simulations.

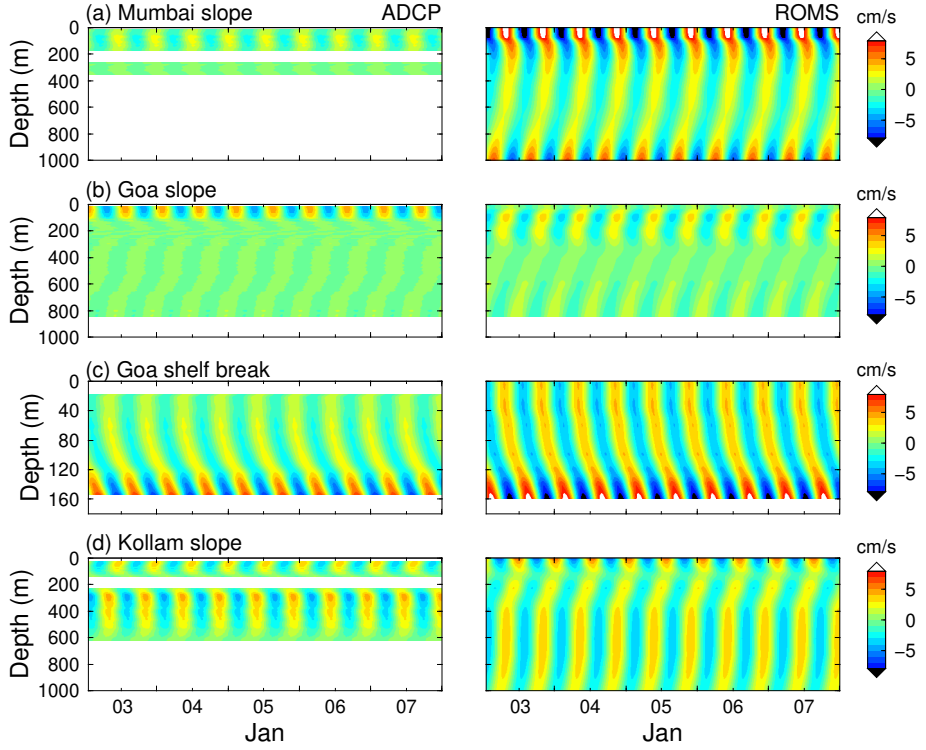

Table 6.5 The area integrated values of conversion, dissipation and radiation for M_2 and K_1 constituents. Calculation is carried out for the month of July. The values given in the bracket are from the climatology run (ROMS- CLM) for the same month.

Tidal constituents	Conversion (GW)	Dissipation (GW)	Radiation (GW)
M_2	2.2 (2)	2.2 (2)	0.02 (.02)
K_1	.68 (.62)	.67 (.6)	.02 (.09)

6.4.6 Coherent and incoherent internal tides

ITs vary with variations in background stratification, low-frequency currents, mesoscale eddies etc. In addition, shoaling of remotely generated ITs can also result in intermittent variability in the IT field. Total IT field at a particular location can be decomposed into two parts, the coherent and the incoherent parts. Here, coherent ITs are defined as the ITs that retain constant phase and amplitude for a given period of time. The coherent signals can be separated by applying harmonic analysis on bandpassed ITs. The ITs, that are retaining after the harmonic analysis can be considered as the 'stationary' component of the ITs at that location. The remaining unresolved part of

Figure 6.22 K_1 ITs from observations and model simulations.

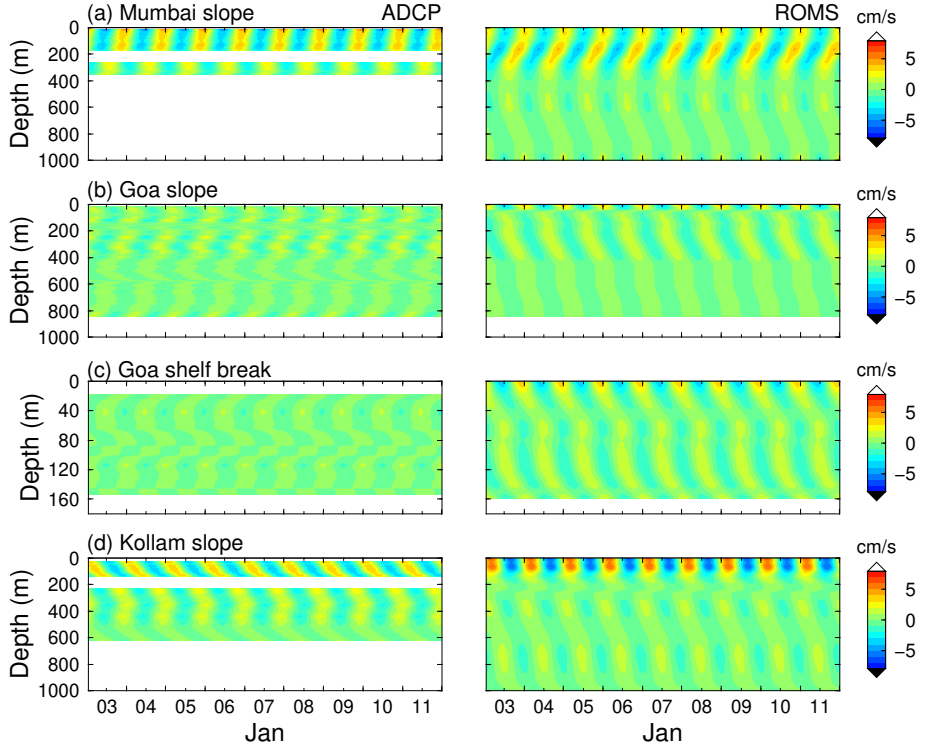

bandpassed ITs can be considered as incoherent ITs, those do not retain constant phase and amplitude for that 'particular' period. Nash et al. [2012] showed that the capability of harmonic analysis to resolve ITs largely varies with time window used in the analysis. This implies that to extract the stationary ITs at a particular location, I need quite a long time series which should include all the above variabilities in the location. The same exercise was done using ADCP observations on the shelf and slope. For instance, off Jaigarh, harmonic analysis on a 15-day time window could resolve 76% (59%) of ITs on the slope (shelf). Harmonic analysis using a 1-month window resolved 70% (50%) on the slope (shelf) and 8-month window harmonic analysis could only resolve 56% (29%). Analysis on 8-month window on the remaining four shelf locations shows that the capability of harmonic analysis to resolve ITs is less than 30%. Two inferences from the above results can be made. First, ITs are varying in different time scales on the continental shelf and slope off the WCI. Second, the shelf off WCI experiences relatively large part of incoherent ITs compared to those on continental slopes.

Figure 6.23 Percentage of coherent semidiurnal ITs across the shelf. The percentage of coherent IT was estimated for each grid point and averaged over each 100 m depth intervals along the latitude.

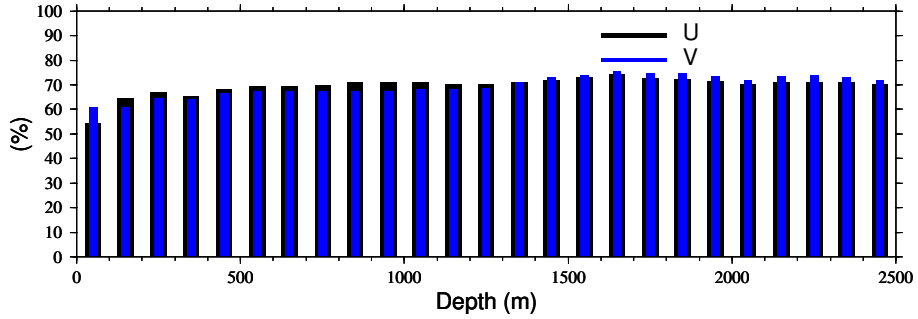

Figure 6.24 Percentage of coherent semidiurnal ITs along the shelf averaged between 0-100 m (black), 100-200 m (blue), 200-300 m (red) and 300-1000 m (green). Thin lines denote U component. The dashed line denotes the V component. Lines with different colours indicate percentage of coherent tides at different depths. V component is only plotted for 0-100 m.

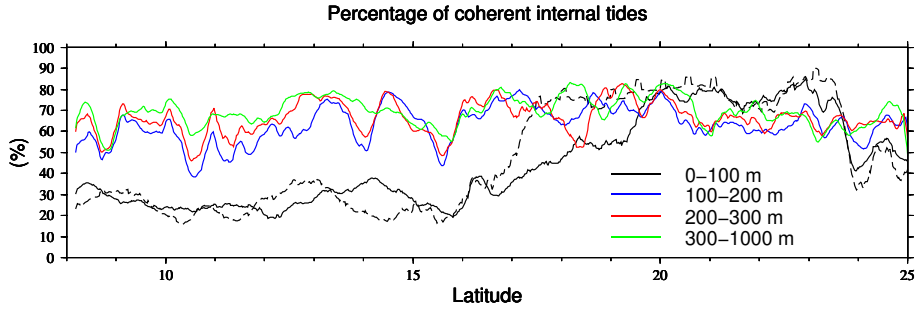

To understand coherent and incoherent ITs in detail, the model output was used. As the ROMS-CLM and ROMS-HYC runs lack the background variations, except on monthly scales, it was not adequate to study the coherent and incoherent ITs. I took model output of realistic run for one month (July) to separate coherent and incoherent ITs. The values of coherent and incoherent ITs largely vary with the time window selected for the harmonic analysis. Here the coherent signal is defined as the part of ITs retained after harmonic analysis of one-month data. The main interest is to understand the difference in coherency across and along the shelf. As the semidiurnal ITs are prominent in this region, the analysis was carried out in semidiurnal bandpassed ITs. First, baroclinic currents were bandpassed (10-14 hours) for semidiurnal ITs at each grid point. Harmonic analysis was carried out on the bandpassed ITs by keeping three prominent semidiurnal

constituents (M_2, S_2 and N_2) in the control files of the TTTB. The harmonic analysis output is considered as coherent ITs and the remainder is considered as incoherent ITs Nash et al. [2012]. Variance of coherent and incoherent ITs was estimated and averaged over the vertical ($< u^2 >$).

The predictive capability (See Equation 4.1 in Chapter 4) of harmonic analysis was estimated. This gives the percentage of contribution of coherent ITs on total bandpassed ITs. Fig. 6.23 shows the latitudinally averaged percentage of coherent ITs. On the shelf, the average value of percentage of coherent ITs is about 55% for U and 60% for V. On the slope and for deep slope regions, the value is more than 60%. These values are consistent with observations, where harmonic analysis of Jaigarh data showed 70% of coherent ITs on the slope and 50% on the shelf (see section 5.3.10). Fig. 6.24 shows the latitudinal variation of coherent ITs. On the slope, the percentages of coherent ITs are more or less constant from south to north. However, on the shelf, the coherent ITs are weak up to 15.5° N (Fig. 6.24), and gradually increase towards north. It is interesting to note that the percentage of coherence of V component (Dashed line in Fig. 6.24) shows 20-30% increase than for the coherency of U around 17°-20° N. The loss of coherency of U compared to V could be due to the presence of shoaling ITs in U. V component could be mainly controlled by local barotropic forcing.

In the observations and model, it is evident that the coherent ITs on the shelf are relatively smaller than those on the slope. One reason for the loss of coherency on the shelf compared to slope region could be the presence of IT generated from different sites. A part of IT generated from the shelf edge can propagate onshore and distort the ITs on the shelf. Moreover, the coherency of IT may also be lost due to the background variability such as low-frequency currents and mesoscale eddies. However, more analysis is needed to confirm this, which is beyond the scope of the present study.

6.4.7 Coherent and incoherent internal tide energy flux

Coherent and incoherent energy fluxes were estimated for semidiurnal ITs using the model output. The study used July month output to calculate energy flux. First, the broadband semidiurnal ITs using a third order Butterworth filter were analysed harmonically. Isopycnal oscillations were computed using density fields from the model. Energy flux was estimated using both broadband

Figure 6.25 Coherent (black) and incoherent (red) depth-integrated IT energy flux at ADCP locations. The simulations were made for the year 2014. The locations where the ADCP data available are chosen for calculating coherent and incoherent ITs. Semidiurnal barotropic tidal current (U) is shown for Mumbai location. Spring-neap variability follows nearly same phase in all other locations, hence not shown.

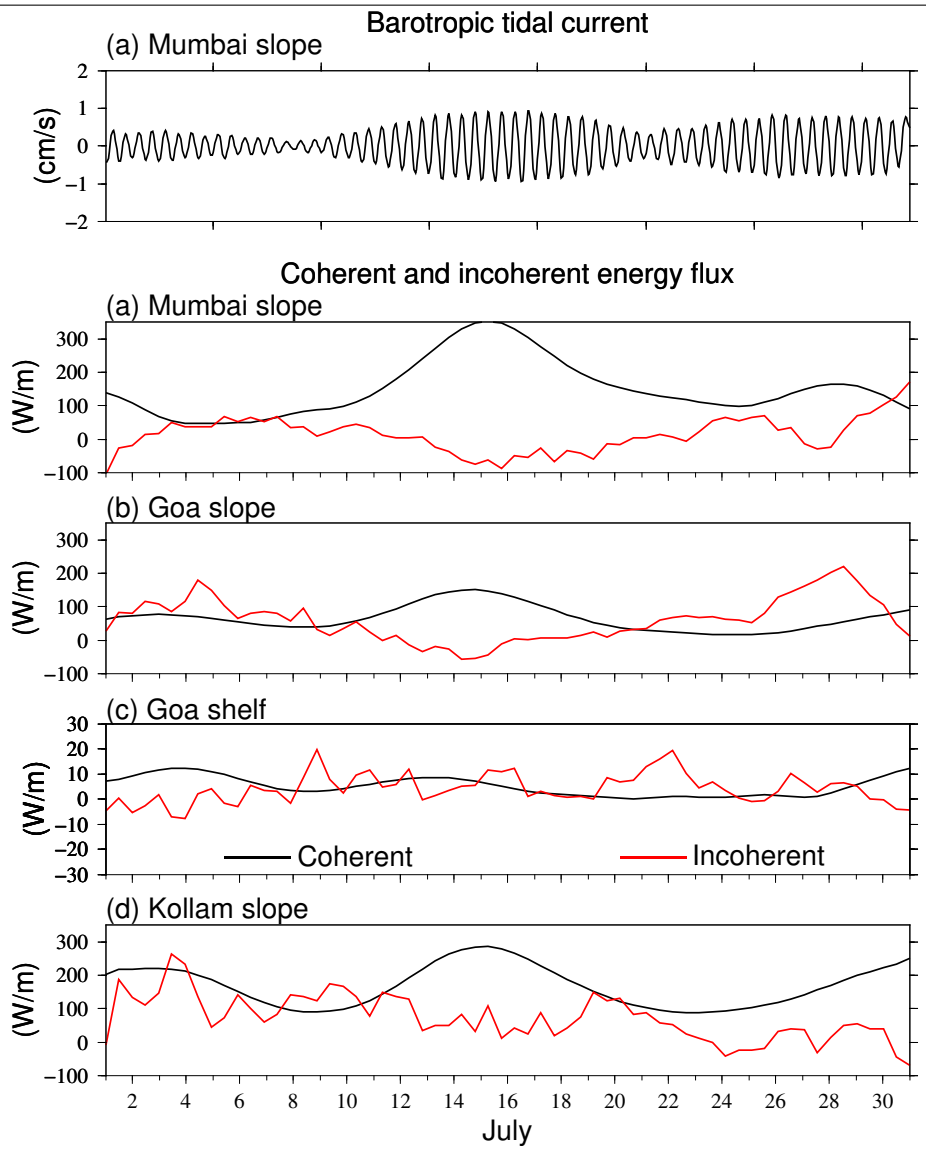

ITs and coherent ITs for each time step. The difference of coherent IT flux from broadband IT flux was considered as the incoherent IT energy flux. The energy flux was averaged over the tidal period.

Figure 6.26 Depth-integrated coherent and incoherent energy flux over the model domain. Note that the scale of two figures are different with (a) showing a larger range than (b).

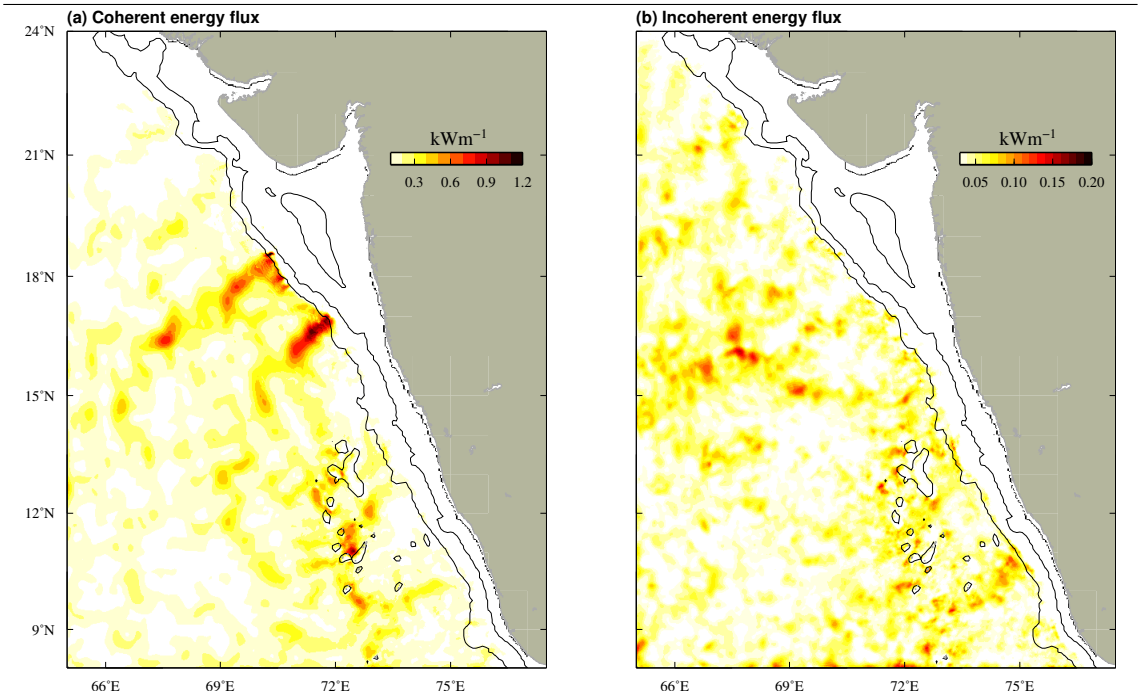

Time evolution of depth-integrated energy flux at ADCP locations is shown in Fig. 6.25. Spring-neap variability is clearly visible in the coherent ITs. As expected, incoherent ITs are intermittent in nature, which do not show any regular oscillations. Over slope regions, during spring, coherent ITs exceed incoherent ITs. Variation in incoherent IT energy does not follow spring-neap variation of BTs. The depth-integrated monthly-averaged IT energy flux for coherent and incoherent ITs is shown in Fig. 6.26. Strong coherent IT energy is found in regions close to the generation sites. Coherency is decreasing towards the deep regions away from the generation sites.

6.5 Summary and Conclusions

Chapters 4 and 5 provided evidence of efficient IT generation on the shelf and slope off the WCI. In this chapter, a three-dimensional, nonlinear, primitive equation numerical model Regional Ocean Modelling System (ROMS) with a grid resolution of 1/48 degree was set up for the eastern Arabian

Sea for simulating BTs and ITs on the shelf and slope.

Three numerical modelling experiments were carried out for this purpose. First two experiments consisted of using temperature and salinity fields from monthly climatology and HYCOM reanalysis data. In the two experiments, tides were forced from open boundaries using the output of the global tidal model, OTIS. A similar approach, using constant stratification over a time period in the presence of tidal forcing at the boundaries had been used in many past studies [Rayson et al., 2011; Jan and Chen, 2009]. A third experiment, consisted of a realistic simulation by including atmospheric forcing was performed. Initial and boundary conditions were given from the coarse resolution Indian Ocean model output available for 2013-2014 periods. The model was run for the year 2008 in the first two experiments, while in the third experiment, the model was run for 2014. Model results were compared with ADCP data available for different years.

The performance of the model to simulate BT is very good in all three experiments. The model also could resolve IT variability on the shelf and slope to a good extent. As ITs are sensitive to small variations in stratification and model's limitations in simulating these variations make an exact comparison of IT amplitude and phase with observation difficult. The model could simulate the bottom amplification of IT, their seasonal variations and identify the possible generation sites of IT on the shelf and slope region. HYCOM reanalysis stratification is found to be more realistic on the shelf and shelf break compared to climatology stratification and it is reflected in IT simulation as well, particularly on the shelf region. ITs are found to be sensitive to the spatial variations in stratification on the shelf break. In deeper regions, ITs show no significant difference between the simulations.

As there is no simultaneous measurement of temperature and salinity along with velocity data, it is not possible to estimate IT energy flux from the observations. As the model reproduced IT velocities reasonably well, it is considered that density fields from the model can be used for calculating internal tidal energy flux. More focus is given to the characteristics of M_2 constituent, as it is the most important IT constituent in the region (Table 6.3). The estimated energy flux values on the southern shelf (8°-12° N) off WCI are 50-100 W/m, and those on the northern shelf (16°-18.5° N) are 200-300 W/m. The estimates of IT energy flux are found to be comparable to those values reported for the other shelf regions around the world. For instance, the depth-integrated

energy flux noted off Oregon is 70 W/m [Torgrimson and Hickey, 1979], 104 W/m on the Malin Shelf [Sherwin, 1988], 400-500 W/m on the NW Australian shelves [Holloway et al., 2001]. On the slope off WCI, they vary from 0.5 to 3.0 kW/m. The values of same at near Hawaiian Ridge is 1-40 kW/m [Rudnick, 2003], Luzon strait is 5.5 kW/m [Klymak et al., 2011], submarine canyon is 1-2 kW/m [Kang and Fringer, 2012].

The model results show that about 2.4 GW of barotropic M_2 tidal energy is converted to baroclinic tides over the domain. The major conversion occurs between 100-300 m depth, where the topography slope matches with IT slope (Fig. 6.13). The observations in earlier chapters and the model study in the present chapter show that ITs on the shelf and slope are mostly locally forced. Shelf and slope do not experience much IT coming from deep ocean. This also points out that regional modelling is adequate for simulating ITs on the shelf and slope off WCI because of the prominence of local IT generation sources. It is found that most of the IT generation sites are inside the model domain.

The northern shelf of the eastern Arabian Sea experiences relatively strong coherent ITs compared to elsewhere in the world. Nash et al. [2012] showed that fraction of ITs resolved by harmonic analysis attains 30-60% when considering a one-month window. The shelf off WCI also shows similar values especially south of 15° N. However, towards northern part of the shelf, the coherent ITs are much larger compared to those in the south. Compared to shelf, slope regions experience large coherent ITs.

Chapter 7

Summary and Future perspectives

7.1 Summary

The present thesis describes barotropic and baroclinic tides on the continental shelf and slope off the west coast of India (WCI) using observations from ADCP moorings and a numerical model. In 2008, CSIR-National Institute of Oceanography (NIO) moored five pairs of ADCPs on the shelf and slope off the WCI for long-term measurements of currents on the shelf-slope region. My thesis gives a comprehensive description of tidal currents on the shelf and slope off the WCI using these observations and a numerical model. A fully nonlinear, high-resolution (1/48°), numerical model, Regional Ocean Modelling System (ROMS), developed for the eastern Arabian Sea was used to simulate tidal currents in the region. The simulations were used to describe the characteristics, generation, propagation and dissipation of ITs in the region. The model simulations were also used to estimate tidal energy flux, conversion and dissipation of IT and study energetics.

Tidal currents on the shelf off west coast of India

ADCP data in five locations on the shelf were analysed to understand the characteristics of tidal currents. The magnitude of barotropic tidal currents on the shelf exceeds 30 cm s^{-1} on the northern locations (Mumbai (20° N), Jaigarh (17° N)) and lie between 10-20 cm s^{-1} on the central and southern shelf locations (Goa (15° N), Bhatkal (13° N) and Kollam (9° N)). The analysis shows that the northern part of the shelf off the west coast is tidally dominant, where the percentage of

contribution of tidal currents to the total current is about 45-55%. Towards the south, it decreases to about 10-20%. The percentage of barotropic tidal current in total current is 40-45% in northern locations and 5-10% in central and southern locations. About 10% of the total currents is contributed by IT, where the percentage of contribution almost remains unchanged from south to north of the shelf. IT's amplitude ranges from 10-20 cm s^{-1} on the shelf, with dominant semidiurnal variability, followed by diurnal variability. ITs on the shelf show strong seasonal variations, with relatively weak currents during the pre-monsoon, which become strong during SW monsoon. The difference is attributed to the increased stratification during SW monsoon. ITs are highly intermittent on the shelf, where the percentage of coherent IT is found to be 10-30% in total ITs. The vertical structure of ITs show a dominance in first three modes with the three modes explaining more than 80% of the variability of total ITs.

Tidal currents on the slope off WCI

I further looked into the ADCP measurements on the continental slope off the WCI. The main focus is given to the ITs off Jaigarh, a typical site of large ITs generated because of strong cross-shore BTs and associated favourable conditions. CTD time series and satellite altimeter data were also used to describe ITs on the slope off Jaigarh. ITs on the slope off Jaigarh are strongly coupled with BT forcing. The coherent IT represents more than 50% in this location. At the same time, the percentage of coherency on the shelf is below 30%. Shelf and slope regions off Jaigarh also show a contrast in seasonal variations in IT, where IT on the shelf gets strengthened during SW monsoon period, and IT on the slope gets strengthened during pre-monsoon (March), owing to the difference in stratification between shelf and slope. Shelf-slope IT dynamics off Jaigarh is well separated by the presence of a super-critical shelf break. Calculation of Baines barotropic forcing and criticality parameter showed that the shelf-break and slope regions are the potential IT generating sites. The analysis of data at other slope locations also showed IT activity, however the activity was weaker as compared to that off Jaigarh. In all slope locations, similar to those on shelf, ITs are dominant in semidiurnal frequencies and exhibit low-mode baroclinic vertical structures.

Numerical modelling of tidal currents off the WCI

Generation, propagation, dissipation and energetics of BTs and ITs on the shelf and slope of WCI are described using simulations from a three-dimensional, high-resolution numerical model (ROMS). The model was forced by tides, extracted from the global tidal model, at open boundaries. To understand the sensitivity of ITs to the background stratification and low-frequency variabilities, different model experiments involving (i) using monthly mean climatology of temperature (T) and salinity (S) restored every month (ii) using monthly mean of T and S from HYCOM reanalysis data restored every month (iii) realistic run, using atmospheric forcing, and boundary and initial conditions from a coarse resolution Indian Ocean model were carried out. Model simulations of barotropic tidal currents agree well with observations on the shelf and slope regions. As far as the simulations of IT are concerned, model captures the spring-neap variability and seasonal variations very well. Moreover, the vertical structures and the propagation characteristics of simulated ITs agree well with the observations. Barotropic to baroclinic tide energy conversion and energy flux show that shelf breaks and upper slope regions around 16°-18.5° N and the northern part of the Chagos-Laccadive island chain are the potential internal tide generation sites. These two areas together contribute to more than 50% of total area-integrated conversion over the domain. About 2.3 GW of M_2 energy is found to be converted from barotropic to baroclinic and almost the entire energy is found to be dissipated inside the model domain.

Highlights of the thesis are given as follows:

1. First comprehensive description of barotropic and baroclinic tidal currents is made on the shelf and slope off WCI using long-term ADCP data.

2. The major generation sites of baroclinic tides off the WCI are identified and their energetics and propagation are further explained using a numerical model. This study gives an insight into the importance of incorporation of tidal currents in ocean models to get improved simulation of currents.

3. The model-based descriptions of ITs off the WCI given in this thesis are novel. The estimates showed that about 3.6 GW of barotropic tidal energy is being converted to baroclinic tidal energy and is readily available for mixing on the shelf-slope regions off WCI.

7.2 Future perspectives

Several studies in many oceanic regions showed the importance of tidal mixing on distribution of biogeochemical variables, water-mass distribution, sediment resuspension, etc. in shelf-slope regions. Similar experiments need to be carried out in the Arabian Sea. This thesis gives a first attempt of giving a comprehensive description of ITs off the WCI, including their magnitudes, vertical structure and possible generation sites. The next step is to understand the impact and interaction of ITs and their effects on mixing of other ocean parameters like temperature, salinity, chlorophyll, etc. This calls for detailed observations of ocean parameters in the shelf-slope regions and numerical modelling studies in this direction. The main caveat of the present observation is the lack of temperature and salinity data along with the velocity data, which restricts the computation of IT energy flux.

In recent years, many efforts have been made to estimate small-scale turbulence in the Bay of Bengal by making use of the state-of-the-art instruments like microstructure profilers [Mahadevan et al., 2016]. However, as per my best knowledge so far, no efforts have been carried in this direction in the Arabian Sea. This present work shows that a total 3.6 GW of barotropic tides gets converted baroclinic tides over the region with large IT activity on the shelf, slope and deep ocean, which in fact causes increased vertical mixing in the water column. The small-scale vertical mixing observations in the eastern Arabian Sea will give new insights to tidal mixing over the region. A combination of mixing measurements, full water column observations of currents, temperature and salinity, and numerical modelling efforts can address the questions on contribution of mixing by internal waves in shelf and slope circulations and water mass distribution. To what extent that mixing induced by IT can increase the biological productivity on the shelf and shelf break off WCI. In fact, studies show that 300-400 W/m of IT flux on the shelf is enough to bring nutrients up [Sharples et al., 2001] and it is interesting to note that the IT energy flux in the continental shelf off Jaigarh reaches up to this value.

The present thesis also highlights the importance of Near-Inertial Wave (NIW) studies off the WCI. The ADCP data off Jaigarh shows NIW activity on the shelf and slope. A detailed study with the help of observations and numerical modelling will be required for the understanding of relative contribution of tides and NIW to mixing off the WCI.

One of the major challenges in Oceanography is to represent the tidal mixing in ocean circulation models, hence demanding a good parameterisation scheme representing the spatiotemporal variation of tidal mixing. Though there have been efforts to develop tidal mixing parameterisations [Laurent and Garrett, 2002; Polzin, 2004], there still requires a lot of improvements especially in the area of "far-field" tidal mixing [MacKinnon et al., 2017]. For example, the mixing efficiency in the present tidal mixing parameterisation scheme is given as a constant, however, in reality, it has significant spatiotemporal variations [Nagai and Hibiya, 2015]. High-resolution numerical model is a good tool to understand controlling parameters of IT, thereby improving parameterisation schemes.

Appendix A

Internal tides: Dispersion relation

To understand the basic internal tide dynamics, I describe the evolution of dispersion relation for internal waves by solving Navier-Stokes equations under the following assumptions i) linearization (Advection terms are removed) ii) incompressibility iii) f-plane (Coriolis force varying with latitude is neglected) iv) horizontal component of Coriolis force is neglected;

$$\frac{\partial u'}{\partial t} - fv = \frac{-1}{\rho_0}\frac{\partial p'}{\partial x} \tag{A.1}$$

$$\frac{\partial v'}{\partial t} + fu = \frac{-1}{\rho_0}\frac{\partial p'}{\partial y} \tag{A.2}$$

$$\frac{\partial w'}{\partial t} = \frac{-1}{\rho_0}\frac{\partial p'}{\partial z} - g\frac{\rho'}{\rho_0} \tag{A.3}$$

$$\frac{\partial u'}{\partial x} + \frac{\partial v'}{\partial y} + \frac{\partial w'}{\partial z} = 0 \tag{A.4}$$

$$\frac{\partial p'}{\partial t} + w\frac{\partial \rho}{\partial z} = 0 \tag{A.5}$$

Where u and v are horizontal velocities, w is vertical velocity, p pressure and ρ is the density, '$prime$' denotes the perturbations from the mean value (for instance, $u = u_b + u', v = v_b + v'$, etc. where u_b and v_b are the background velocities and, u' and v' are the perturbation velocities), f is the coriolis frequency and g is the gravity. Now we have five unknowns and five equations. After doing some manipulations and rearrangements a single equation for vertical velocity perturbation (In similar way we can derive a single equations for each unknowns in above equations, however,

we use equation for vertical velocity as giving boundary condition is easy for this variable.) can be constructed.

$$\frac{\partial^2}{\partial t^2}\nabla^2 w + (f.\nabla)^2 w + N^2\nabla_h^2 w = 0 \tag{A.6}$$

Where, $\nabla^2 = \frac{\partial^2}{\partial x^2} + \frac{\partial^2}{\partial y^2} + \frac{\partial^2}{\partial z^2}$

Assuming w is sinusoidal wave varying in time at a frequency ω, $w \sim e^{-i\omega t}$

Substituting for w in equation A.6,

$$(N^2 - \omega^2)\nabla_h^2 w - (\omega^2 - f^2)w_{zz} = 0 \tag{A.7}$$

Considering wave propagation in x direction ($\partial/\partial y = 0$), the equation A.7 become,

$$(N^2 - \omega^2)w_{xx} - (\omega^2 - f^2)w_{zz} = 0 \tag{A.8}$$

Substituting for$w$ in the form of travelling plane wave in x-z cordinate, w=$e^{i(kx+mz)}$ (Where k and m are the wavenumbers in x and z directions) in equation A.8 will give the relation between wave frequency and wave numbers called dispersion relation,

$$\omega^2 = \frac{N^2k^2 + f^2m^2}{k^2 + m^2} \tag{A.9}$$

To simplify the above equation wave vectors in polar form $\vec{k} = (k, m) = K(cos\theta, sin\theta)$ (where θ is the angle of wave vector with respect to the horizontal plane and $K = \sqrt{k^2 + m^2}$ is the length of the wave vector.) can be substituted in equation A.9. The equation A.9 become,

$$\omega^2 = N^2 cos^2\theta + f^2 sin^2\theta \tag{A.10}$$

The dispersion relation shows that the frequency of internal tides is only dependent on the direction of wave vector and independent on the wave vector length. This results in propagation of internal tide energy perpendicular to the lines of constant phase. (Detailed derivation is given in Gerkema and Zimmerman [2008]).

Besides the dispersion relation, two sets of analytical solutions can be developed based on the equation A.8.

i) If the coefficients of the w_{xx} and w_{zz} are fixed, the general solution of the equation A.8 in two-dimension can be written as

$$w = F(\mu + x - z) + G(\mu - x - z) \tag{A.11}$$

Where $\mu_{\pm} = \pm\sqrt{\frac{\omega^2 - f^2}{N^2 - \omega^2}}$ the ray slope, and F and G are arbitrary functions. $\mu_{\pm}x - z$ is known as as the characteristic coordinate. The resulting solution consists of internal tide beam propagating along the characteristic slope. This framework is applicable to study the propagation of internal tides along the topographic features like shelf-slope and ridges. The linear solution breaks when the ray slope of incident wave (characteristic slope) matches the slope of bottom topography. Non linearity comes into play. If the topographic slope is steeper than the characteristic slope, internal tide is reflected back. If topographic slope less than internal tide slope the energy get reflected forward without disturbance.

ii) Substituting the form $w = W(z)e^{i(kx-\omega t)}$ in equation will give,

$$\frac{\partial^2 W}{\partial z^2} + k^2 \frac{N^2(z) - \omega^2}{\omega^2 - f^2} W = 0 \tag{A.12}$$

For low-frequency internal tides, buoyancy frequency is much larger than internal tide frequency. Including that case, the equation can be written in general way,

$$\frac{\partial^2}{\partial z^2} + \alpha_n^2 N^2(z) G_n(z) = 0 \tag{A.13}$$

Where $\alpha^2 = \frac{k^2}{(\omega^2 - f^2)}$. Imposing the boundary condition based on rigid layer approximation $W = 0$ at $h = 0$ (surface) and H (bottom) equation A.8 form a Sturm-Liouville problem. G_n is the eigenfunction, α_n the eigenvalue for n$^{\text{th}}$ mode.

For a constant stratification, the equation can be solved analytically. For varying stratification, the equation must be solved numerically. Once a solution is obtained, the phase speed (c_p), group speed (c_g) and horizontal wavenumber (k_x) of internal tides with frequency can be derived from the relations as follows,

$$C_p = \frac{\omega}{(\omega^2 - f^2)^{1/2}} C_n \tag{A.14}$$

$$C_g = \frac{(\omega^2 - f^2)^{1/2}}{\omega} C_n \tag{A.15}$$

$$k_x = \frac{(\omega^2 - f^2)^{1/2}}{C_n} \tag{A.16}$$

The two above stated analytical solutions, ray, and modes, are two useful dynamical frameworks to understand basic characteristics of internal tides at a location based on the background oceanography information like stratification and bottom slope etc. The method of normal mode decomposition is valid for a flat horizontal topography for vertically standing waves.

Bibliography

Aguirre, C., Pizarro, O. and Sobarzo, M. [2010], 'Observations of semidiurnal internal tidal currents off central Chile (36.6 S)', *Continental Shelf Research* **30**(14), 1562–1574. 6, 45, 70

Alford, M. H. [2003], 'Improved global maps and 54-year history of wind-work on ocean inertial motions', *Geophysical Research Letters* **30**(8). 5

Alford, M. H., Gregg, M. C. and Merrifield, M. A. [2006], 'Structure, propagation, and mixing of energetic baroclinic tides in Mamala Bay, Oahug, Hawaii', *Journal of Physical Oceanography* **36**(6), 997–1018. 21

Alford, M. H., Gregg, M. C., Zervakis, V. and Kontoyiannis, H. [2012], 'Internal wave measurements on the Cycladic Plateau of the Aegean Sea', *Journal of Geophysical Research* **117**(C1). 88

Alford, M. H. and Zhao, Z. [2007], 'Global patterns of low-mode internal-wave propagation. part-1 : Energy and energy flux', *Journal of Physical Oceanography* **37**(7), 1829–1848. 33, 34

Allain, D. [2016], 'TUGOm Tidal Toolbox'.
URL: *ftp://ftp.legos.obsmip.fr/pub/ecola/tools/ttb.pdf* 32

Amol, P., Shankar, D., Aparna, S. G., Shenoi, S. S. C., Fernando, V., Shetye, S. R., Mukherjee, A., Agarvadekar, Y., Khalap, S. and Satelkar, N. P. [2012], 'Observational evidence from direct current measurements for propagation of remotely forced waves on the shelf off the west coast of India', *Journal of Geophysical Research* **117**(C5). 25

Andersen, O. B. [1999], 'Shallow water tides in the northwest European shelf region from TOPEX/POSEIDON altimetry', *Journal of Geophysical Research: Oceans* **104**(C4), 7729–7741. 113

Andersen, O. B., Egbert, G. D., Erofeeva, S. Y. and Ray, R. D. [2006], 'Mapping nonlinear shallow-water tides: a look at the past and future', *Ocean Dynamics* **56**(5-6), 416–429. 113

Andersen, O. B., Woodworth, P. L. and Flather, R. A. [1995], 'Intercomparison of recent ocean tide models', *Journal of Geophysical Research* **100**(C12), 25261. 17

Antony, M. K. and Shenoi, S. S. C. [1993], 'On the flow, thermal field and winds along the western continental shelf of India', *Continental Shelf Research* **13**(4), 425–439. 8

Antony, M. K. and Unnikrishnan, A. S. [1993], 'On an upwelling front, propagation of upwelling and vertical velocity in the eastern arabian sea during monsoon,1987', *Proceedings of the PORSEC 92 in Okinawa, Conference for Pacific Ocean Environments and Probing* **1**(4), 527–532. 48, 70

Aparna, M., Shetye, S. R., Shankar, D., Shenoi, S. S. C., Mehra, P. and Desai, R. G. P. [2005], 'Estimating the seaward extent of sea breeze from QuikSCAT scatterometry', *Geophysical Research Letters* **32**(13). 62

Arakawa, A. and Lamb, V. R. [1977], Computational design of the basic dynamical processes of the UCLA general circulation model, *in* 'Methods in Computational Physics: Advances in Research and Applications', Elsevier, pp. 173–265. 37

Arbic, B. K., Garner, S. T., Hallberg, R. W. and Simmons, H. L. [2004], 'The accuracy of surface elevations in forward global barotropic and baroclinic tide models', *Deep Sea Research Part II: Topical Studies in Oceanography* **51**(25-26), 3069–3101. 20

Arbic, B. K., Wallcraft, A. J. and Metzger, E. J. [2010], 'Concurrent simulation of the eddying general circulation and tides in a global ocean model', *Ocean Modelling* **32**(3-4), 175–187. 20, 37

Arbic, B., Richman, J., Shriver, J., Timko, P., Metzger, J. and Wallcraft, A. [2012], 'Global modeling of internal tides within an eddying ocean general circulation model', *Oceanography* **25**(2), 20–29. 137

Aucan, J. and Merrifield, M. [2008], 'Boundary mixing associated with tidal and near-inertial internal waves', *Journal of Physical Oceanography* **38**(6), 1238–1252. 137

Azevedo, A., Da Silva, J. and New, A. L. [2006], 'On the generation and propagation of internal solitary waves in the southern Bay of Biscay', *Deep Sea Research Part I: Oceanographic Research Papers* **53**(6), 927–941. 103

Baines, P. G. [1973], 'The generation of internal tides by flat-bump topography', *Deep Sea Research and Oceanographic Abstracts* **20**(2), 179–205. 20

Baines, P. G. [1974], 'The generation of internal tides over steep continental slopes', *Philosophical Transactions of the Royal Society A: Mathematical, Physical and Engineering Sciences* **277**(1263), 27–58. 20

Baines, P. G. [1982*a*], 'On internal tide generation models', *Deep Sea Research Part A. Oceanographic Research Papers* **29**(3), 307–338. 5, 20, 101

Baines, P. G. [1982*b*], 'On internal tide generation models', *Deep Sea Research Part A. Oceanographic Research Papers* **29**(3), 307–338. 79

Baines, P. G. [1986], 'Internal tides, internal waves and near-inertial motions', *Baroclinic processes on continental shelves* pp. 19–31. 100

Becker, J. J., Sandwell, D. T., Smith, W. H. F., Braud, J., Binder, B., Depner, J., Fabre, D., Factor, J., Ingalls, S., Kim, S.-H., Ladner, R., Marks, K., Nelson, S., Pharaoh, A., Trimmer, R., Rosenberg, J. V., Wallace, G. and Weatherall, P. [2009], 'Global bathymetry and elevation data at 30 arc seconds resolution: SRTM30_PLUS', *Marine Geodesy* **32**(4), 355–371. 40, 100

Bell, C., Vassie, J. and Woodworth, P. [1999], 'POL/PSMSL tidal analysis software kit 2000 (TASK-2000)', *Permanent Service for Mean Sea Level, CCMS Proudman Oceanographic Laboratory, Bidston Observatory, Birkenhead, UK* **20**. 32, 46, 116

Bernoulli, D. [1740], *Traite sur le flux et reflux de la mer*, Acadmie Royale des Sciences. 14

Blanton, B. O., Werner, F. E., Seim, H. E., Luettich, R. A., Lynch, D. R., Smith, K. W., Voulgaris, G., Bingham, F. M. and Way, F. [2004], 'Barotropic tides in the south Atlantic bight', *Journal of Geophysical Research* **109**(C12). 119, 120

Bogdanov, K. and Magarik, V. [1967], 'Numerical solutions for the world's semi-diurnal (M2 and S2) tides', *Proceedings of the USSR Academy of Sciences* **172**, 1315–1317. 15, 16

Bratkovich, A. [1985], 'Aspects of the tidal variability observed on the southern California continental shelf', *Journal of Physical Oceanography* **15**(3), 225–239. 19

Bravo, L., Ramos, M., Sobarzo, M., Pizarro, O. and Valle-Levinson, A. [2013], 'Barotropic and baroclinic semidiurnal tidal currents in two contrasting coastal upwelling zones of Chile', *Journal of Geophysical Research: Oceans* **118**(3), 1226–1238. 6

Briscoe, M. G. [1975], 'Internal waves in the ocean', *Reviews of Geophysics* **13**(3), 591. 18

Bryan, F. [1987], 'Parameter sensitivity of primitive equation ocean general circulation models', *Journal of Physical Oceanography* **17**(7), 970–985. 2

Buijsman, M. C., Uchiyama, Y., McWilliams, J. C. and Hill-Lindsay, C. R. [2012], 'Modeling semidiurnal internal tide variability in the southern California Bight', *Journal of Physical Oceanography* **42**(1), 62–77. 20

Cairns, J. L. and LaFond, E. C. [1966], 'Periodic motions of the seasonal thermocline along the southern California coast', *Journal of Geophysical Research* **71**(16), 3903–3915. 18

Cairns, J. L. and Williams, G. O. [1976], 'Internal wave observations from a midwater float, 2', *Journal of Geophysical Research* **81**(12), 1943–1950. 18

Carrère, L., Lyard, F., Cancet, M., Guillot, A. and Roblou, L. [2012], FES2012: A new global tidal model taking advantage of nearly 20 years of altimetry, Vol. 20. 81

Carter, G., Fringer, O. and Zaron, E. [2012], 'Regional models of internal tides', *Oceanography* **25**(2), 56–65. 129

Carter, G. S. [2010], 'Barotropic and BaroclinicM2 tides in the Monterey Bay region', *Journal of Physical Oceanography* **40**(8), 1766–1783. 20

Carter, G. S., Merrifield, M. A., Becker, J. M., Katsumata, K., Gregg, M. C., Luther, D. S., Levine, M. D., Boyd, T. J. and Firing, Y. L. [2008], 'Energetics of M2 barotropic-to-baroclinic tidal conversion at the Hawaiian islands', *Journal of Physical Oceanography* **38**(10), 2205–2223. 37

Cartwright, D. E. [1967], 'Some further results of the "response method" of tidal analysis.', *Report on the Symposium on Tides* . 15

Cartwright, D. E. [1999], *Tides : a scientific history*, Cambridge University Press. 13

Cartwright, D. E. and Ray, R. D. [1990], 'Oceanic tides from geosat altimetry', *Journal of Geophysical Research* **95**(C3), 3069. 16, 17

Cartwright, D. E. and Ray, R. D. [1991], 'Energetics of global ocean tides from geosat altimetry', *Journal of Geophysical Research* **96**(C9), 16897. 16, 17

Chapman, D. C. [1985], 'Numerical treatment of cross-shelf open boundaries in a barotropic coastal ocean model', *Journal of Physical Oceanography* **15**(8), 1060–1075. 41

Chatterjee, A., Shankar, D., McCreary, J. and Vinayachandran, P. N. [2013], 'Yanai waves in the western equatorial Indian Ocean', *Journal of Geophysical Research* **118**(3), 1556–1570. 97, 98, 106

Chatterjee, A., Shankar, D., Shenoi, S. S. C., Reddy, G. V., Michael, G. S., Ravichandran, M., Gopalkrishna, V. V., Rao, E. P. R., Bhaskar, T. V. S. U. and Sanjeevan, V. N. [2012], 'A new atlas of temperature and salinity for the north Indian Ocean', *Journal of Earth System Science* **121**(3), 559–593. 42, 48, 51

Chelton, D. B., Deszoeke, R. A., Schlax, M. G., El Naggar, K. and Siwertz, N. [1998], 'Geographical variability of the first baroclinic rossby radius of deformation', *Journal of Physical Oceanography* **28**(3), 433–460. 83, 85

Chuang, W.-S. and Wang, D.-P. [1981], 'Effects of density front on the generation and propagation of internal tides', *Journal of Physical Oceanography* **11**(10), 1357–1374. 20

Clarke, A. J. and Battisti, D. S. [1981], 'The effect of continental shelves on tides', *Deep Sea Research Part A. Oceanographic Research Papers* **28**(7), 665–682. 1, 118

Cummins, P. F. and Oey, L.-Y. [1997], 'Simulation of barotropic and baroclinic tides off northern British Columbia', *Journal of Physical Oceanography* **27**(5), 762–781. 20, 116

Da Silva, J. C. B., New, A. L. and Magalhaes, J. M. [2009], 'Internal solitary waves in the Mozambique channel: Observations and interpretation', *Journal of Geophysical Research (1978–2012)* **114**(C5). 101, 131

Dalan, F., Stone, P. H., Kamenkovich, I. V. and Scott, J. R. [2005], 'Sensitivity of the ocean's climate to diapycnal diffusivity in an EMIC. part i: Equilibrium state', *Journal of Climate* **18**(13), 2460–2481. 3

D'Asaro, E. A. [1985], 'The energy flux from the wind to near-inertial motions in the surface mixed layer', *Journal of Physical Oceanography* **15**(8), 1043–1059. 5, 108

Doodson, A. T. [1921], 'The harmonic development of the tide-generating potential', *Proceedings of the Royal Society A: Mathematical, Physical and Engineering Sciences* **100**(704), 305–329. 15

Dunne, J. P., John, J. G., Adcroft, A. J., Griffies, S. M., Hallberg, R. W., Shevliakova, E., Stouffer, R. J., Cooke, W., Dunne, K. A., Harrison, M. J., Krasting, J. P., Malyshev, S. L., Milly, P. C. D., Phillipps, P. J., Sentman, L. T., Samuels, B. L., Spelman, M. J., Winton, M., Wittenberg, A. T. and Zadeh, N. [2012], 'GFDL's ESM2 global coupled climate–carbon earth system models. part i: Physical formulation and baseline simulation characteristics', *Journal of Climate* **25**(19), 6646–6665. 21

Dunphy, M. and Lamb, K. G. [2014], 'Focusing and vertical mode scattering of the first mode internal tide by mesoscale eddy interaction', *Journal of Geophysical Research: Oceans* **119**(1), 523–536. 137

Eanes, R. and Bettadpur, S. [1996], *The CSR 3.0 Global Ocean Tide Model: Diurnal and Semidiurnal Tides from TOPEX/POSEIDON Altimetry*, Technical memorandum/Center for Space Research, the University of Texas at Austin, Center for Space Research. 17

Eckart, C. [1960], *Hydrodynamics of Oceans and Atmospheres*, Elsevier. 20

Egbert, G. D. and Erofeeva, S. Y. [2002], 'Efficient inverse modeling of barotropic ocean tides', *Journal of Atmospheric and Oceanic Technology* **19**(2), 183–204. 17, 41

Egbert, G. D. and Ray, R. D. [2000], 'Significant dissipation of tidal energy in the deep ocean inferred from satellite altimeter data', *Nature* **405**(6788), 775–778. 4, 5, 21

Ekman, V. W. [1945], 'Internal waves in the sea', *Nature* **155**(3944), 669–669.
URL: *https://doi.org/10.1038/155669b0* 18

Emery, K. O. [1956], 'Deep standing internal waves in California basins1', *Limnology and Oceanography* **1**(1), 35–41. 18

Euler, L. [1740], *Inquisitio physica in causam fluxus ac refluxus maris*, Acadmie Royale des Sciences. 14

Fairall, C. W., Bradley, E. F., Godfrey, J. S., Wick, G. A., Edson, J. B. and Young, G. S. [1996], 'Cool-skin and warm-layer effects on sea surface temperature', *Journal of Geophysical Research: Oceans* **101**(C1), 1295–1308. 42

Fairall, C. W., Bradley, E. F., Rogers, D. P., Edson, J. B. and Young, G. S. [1996], 'Bulk parameterization of air-sea fluxes for tropical ocean-global atmosphere coupled-ocean atmosphere response experiment', *Journal of Geophysical Research: Oceans* **101**(C2), 3747–3764. 42

Fernandes, A. A., Chandramohan, P. and Nayak, B. U. [1993], 'Observed currents at Bombay High during a winter', *Mahasagar* **26**(2), 95–104. 8

Fjeldstad, J. E. [1933], 'Windstrom in einem eisbedeckten meere', *ZAMM - Zeitschrift für Angewandte Mathematik und Mechanik* **13**(5), 348–355. 18

Flather, R. A. [1976], 'A tidal model of the northwest European continental shelf', *Memoires de la Societe Royale des Sciences de Liege* **10**(6), 141–164. 41

Foreman, M. [2004], *Manual for Tidal Currents Analysis and Prediction*, Institute of Ocean Sciences, Patricia Bay, Sidney, B.C. 15

Francis, P. A., Vinayachandran, P. N. and Shenoi, S. S. C. [2013], 'The Indian ocean forecast system', *Current Science* **104**(10), 1354–1368. 42, 136

Furuichi, N., Hibiya, T. and Niwa, Y. [2008], 'Model-predicted distribution of wind-induced internal wave energy in the world's oceans', *Journal of Geophysical Research* **113**(C9). 5

Ganju, N. K., Lentz, S. J., Kirincich, A. R. and Farrar, J. T. [2011], 'Complex mean circulation over the inner shelf south of Martha's Vineyard revealed by observations and a high-resolution model', *Journal of Geophysical Research* **116**(C10). 2

Garrett, C. [2001], 'What is the "near-inertial" band and why is it different from the rest of the internal wave spectrum?', *Journal of Physical Oceanography* **31**(4), 962–971. 48

Garrett, C. and Kunze, E. [2007], 'Internal tide generation in the deep ocean', *Annual Review of Fluid Mechanics* **39**(1), 57–87. 5

Garrett, C. and Munk, W. [1972], 'Space-time scales of internal waves', *Geophysical Fluid Dynamics* **3**(1), 225–264. 18

Garrett, C. and Munk, W. [1975], 'Space-time scales of internal waves: A progress report', *Journal of Geophysical Research* **80**(3), 291–297. 18

Garrett, C. and Munk, W. [1979], 'Internal waves in the ocean', *Annual Review of Fluid Mechanics* **11**(1), 339–369. 18

George, P. C., Raja, B. T. A. and George., K. C. [1977], 'Fishery resources of the Indian Economic Zone', *Souvenir. Silver Jubilee, Integrated Fisheries Project, Cochin. India* pp. 79–116. 9

Gerkema, T., Lam, F.-P. A. and Maas, L. R. [2004], 'Internal tides in the Bay of Biscay: conversion rates and seasonal effects', *Deep Sea Research Part II: Topical Studies in Oceanography* **51**(25), 2995–3008. 111

Gerkema, T., Maas, L. R. and van Haren, H. [2013], 'A note on the role of mean flows in doppler-shifted frequencies', *Journal of Physical Oceanography* **43**(2), 432–441. 6

Gerkema, T. and Zimmerman, J. T. F. [2008], 'An introduction to internal waves: Lecture notes', *NIOZ Royal Netherlands Institute for Sea Research. Den Burg* . 157

Godin, G. [1972], *The analysis of tides*, University of Toronto press. 15

Gonella, J. [1972], A rotary-component method for analysing meteorological and oceanographic vector time series, Vol. 19, Elsevier, pp. 833–846. 32, 88

Green, J. A. M., Simpson, J. H., Thorpe, S. A. and Rippeth, T. P. [2010], 'Observations of internal tidal waves in the isolated seasonally stratified region of the western Irish Sea', *Continental Shelf Research* **30**(2), 214–225. 6

Gregg, M. C., D'Asaro, E. A., Riley, J. J. and Kunze, E. [2018], 'Mixing efficiency in the ocean', *Annual Review of Marine Science* **10**(1), 443–473. 22

Griffies, S. M., Böning, C., Bryan, F. O., Chassignet, E. P., Gerdes, R., Hasumi, H., Hirst, A., Treguier, A.-M. and Webb, D. [2000], 'Developments in ocean climate modelling', *Ocean Modelling* **2**(3-4), 123–192. 41

Haidvogel, D., Arango, H., Budgell, W., Cornuelle, B., Curchitser, E., Lorenzo, E. D., Fennel, K., Geyer, W., Hermann, A., Lanerolle, L., Levin, J., McWilliams, J., Miller, A., Moore, A., Powell, T., Shchepetkin, A., Sherwood, C., Signell, R., Warner, J. and Wilkin, J. [2008], 'Ocean forecasting in terrain-following coordinates: Formulation and skill assessment of the regional ocean modeling system', *Journal of Computational Physics* **227**(7), 3595–3624. 37

Haidvogel, D. B., Arango, H. G., Hedstrom, K., Beckmann, A., Malanotte-Rizzoli, P. and Shchepetkin, A. F. [2000], 'Model evaluation experiments in the north Atlantic basin: simulations in nonlinear terrain-following coordinates', *Dynamics of Atmospheres and Oceans* **32**(3-4), 239–281. 38

Haidvogel, D. B., Wilkin, J. L. and Young, R. [1991], 'A semi-spectral primitive equation ocean circulation model using vertical sigma and orthogonal curvilinear horizontal coordinates', *Journal of Computational Physics* **94**(1), 151–185. 37

Haidvogel, D. and Beckmann, A. [1999], *Numerical Ocean Circulation Modeling*, Imperial College Press. 37, 38

Halpern, D. [1971], 'Semidiurnal internal tides in Massachusetts Bay', *Journal of Geophysical Research* **76**(27), 6573–6584. 18

Hayes, S. and Helpern, D. [1976], 'Variability of the semidiurnal internal tide during coastal upwelling', *Mmoires of Socit Royale des Sciences de Lige* **6**, 175–186. 19

Hendry, R. M. [1975], *The generation, energetics and propagation of internal tides in the western North Atlantic Ocean*, Massachusetts Institute of Technology and Woods Hole Oceanographic Institution. 18

Holloway, P. E. [1983], 'Internal tides on the Australian north-west shelf: A preliminary investigation', *Journal of Physical Oceanography* **13**(8), 1357–1370. 71

Holloway, P. E. [1984], 'On the semidiurnal internal tide at a shelf-break region on the Australian north west shelf', *Journal of Physical Oceanography* **14**(11), 1787–1799. 19, 70, 71

Holloway, P. E. [1996], 'A numerical model of internal tides with application to the Australian north west shelf', *Journal of Physical Oceanography* **26**(1), 21–37. 20

Holloway, P. E., Chatwin, P. G. and Craig, P. [2001], 'Internal tide observations from the Australian north west shelf in summer 1995', *Journal of Physical Oceanography* **31**(5), 1182–1199. 20, 150

Holloway, P. E. and Merrifield, M. A. [1999], 'Internal tide generation by seamounts, ridges, and islands', *Journal of Geophysical Research: Oceans* **104**(C11), 25937–25951. 20

Holloway, P. E., Pelinovsky, E., Talipova, T. and Barnes, B. [1997], 'A nonlinear model of internal tide transformation on the Australian north west shelf', *Journal of Physical Oceanography* **27**(6), 871–896. 37

Horn, W. and Meincke, J. [1976], 'Note on the tidal current field in the continental slope area off northwest Africa', *Mmoires of Socit Royale des Sciences de Lige* **10**, 31–42. 19

Huthnance, J. M. [1989], 'Internal tides and waves near the continental shelf edge', *Geophysical & Astrophysical Fluid Dynamics* **48**(1-3), 81–106. 19

Huthnance, J. M. and Baines, P. G. [1982], 'Tidal currents in the northwest African upwelling region', *Deep Sea Research Part A. Oceanographic Research Papers* **29**(3), 285–306. 19, 70

Jachec, S. M., Fringer, O. B., Gerritsen, M. G. and Street, R. L. [2006], 'Numerical simulation of internal tides and the resulting energetics within Monterey Bay and the surrounding area', *Geophysical Research Letters* **33**(12). 20

Jan, S. and Chen, C.-T. A. [2009], 'Potential biogeochemical effects from vigorous internal tides generated in luzon strait: A case study at the southernmost coast of taiwan', *Journal of Geophysical Research* **114**(C4). 122, 149

Jiang, J. [2005], 'Estimating the energy flux from the wind to ocean inertial motions: The sensitivity to surface wind fields', *Geophysical Research Letters* **32**(15). 5

Jithin, A. K., Unnikrishnan, A. S., Fernando, V., Subeesh, M. P., Fernandes, R., Khalap, S., Narayan, S., Agarvadekar, Y., Gaonkar, M., Tari, P., Kankonkar, A. and Vernekar, S. [2017a], 'Observed tidal currents on the continental shelf off the east coast of India', *Continental Shelf Research* **141**, 51 – 67. 19

Johnston, T. M. S. [2003], 'Internal tide scattering at the Line Islands ridge', *Journal of Geophysical Research* **108**(C11). 6

Joseph, A., Vijay Kumar, K., Mehra, P., Unnikrishnan, A. S., Sundar, D. and Desai, R. G. P. [2009], 'Observed tides at Mumbai High offshore region, near the continental shelf break in the eastern Arabian Sea', *Current science* **96**(9), 1233–1235. 7

Kang, D. and Fringer, O. [2012], 'Energetics of barotropic and baroclinic tides in the Monterey Bay area', *Journal of Physical Oceanography* **42**(2), 272–290. 150

Kang, S. K., Foreman, M. G. G., Crawford, W. R. and Cherniawsky, J. Y. [2000], 'Numerical modeling of internal tide generation along the Hawaiian ridge', *Journal of Physical Oceanography* **30**(5), 1083–1098. 131

Kantha, L. H., Tierney, C., Lopez, J. W., Desai, S. D., Parke, M. E. and Drexler, L. [1995], 'Barotropic tides in the global oceans from a nonlinear tidal model assimilating altimetric tides: 2. altimetric and geophysical implications', *Journal of Geophysical Research* **100**(C12), 25309. 119

Kelly, S. M., Jones, N. L., Nash, J. D. and Waterhouse, A. F. [2013], 'The geography of semidiurnal mode-1 internal-tide energy loss', *Geophysical Research Letters* **40**(17), 4689–4693. 6

Kelly, S. M. and Nash, J. D. [2010], 'Internal-tide generation and destruction by shoaling internal tides', *Geophysical Research Letters* **37**(23). 34, 40

Killworth, P. [1998], 'Something stirs in the deep', *Nature* **396**(6713), 720–721.
URL: *https://doi.org/10.1038/25444* 5

Killworth, P. D., Webb, D. J., Stainforth, D. and Paterson, S. M. [1991], 'The development of a free-surface bryan–cox–semtner ocean model', *Journal of Physical Oceanography* **21**(9), 1333–1348. 37

Klymak, J. M., Alford, M. H., Pinkel, R., Lien, R.-C., Yang, Y. J. and Tang, T.-Y. [2011], 'The breaking and scattering of the internal tide on a continental slope', *Journal of Physical Oceanography* **41**(5), 926–945. 19, 85, 150

Klymak, J. M., Moum, J. N., Nash, J. D., Kunze, E., Girton, J. B., Carter, G. S., Lee, C. M., Sanford, T. B. and Gregg, M. C. [2006], 'An estimate of tidal energy lost to turbulence at the Hawaiian ridge', *Journal of Physical Oceanography* **36**(6), 1148–1164. 21

Koch-Larrouy, A., Madec, G., Bouruet-Aubertot, P., Gerkema, T., Bessières, L. and Molcard, R. [2007], 'On the transformation of Pacific water into Indonesian throughflow water by internal tidal mixing', *Geophysical Research Letters* **34**(4). 21

Kumar, P. V. H., Kumar, T. P., Sunil, T. and Gopakumar, M. [2005], 'Observations on the relationship between scattering layer and mixed layer', *Current Science* **88**(11), 1799–1802. 70

Kumar, P. V. H., Lekshmi, S., Jagadeesh, P., Anilkumar, K., Krishnakumar, G. V. and Rao, A. D. [2010], 'Internal tides in the coastal waters of ne Arabian Sea: observations and simulations', *Marine Geodesy* **33**(2-3), 232–244. 8, 45, 70

Kumar, P. V. H., Sanilkumar, K. V. and Panchalai, V. N. [2006], 'Shallow water internal waves and associated acoustic intensity fluctuations', *Defence Science Journal* **56**, 485–493. 8, 70

Kumar, S. P., Ramaiah, N., Gauns, M., Sarma, V. V. S. S., Muraleedharan, P. M., Raghukumar, S., Kumar, M. D. and Madhupratap, M. [2001], 'Physical forcing of biological productivity in the northern Arabian Sea during the northeast monsoon', *Deep Sea Research Part II: Topical Studies in Oceanography* **48**(6-7), 1115–1126. 9

Kundu, P. K., Allen, J. S. and Smith, R. L. [1975], 'Modal decomposition of the velocity field near the Oregon coast', *Journal of Physical Oceanography* **5**(4), 683–704. 32

Kundu, P. K. and Cohen, L. M. [1990], 'Fluid mechanics', *Academic, Calif* . 83

Kunze, E. [1985], 'Near-inertial wave propagation in geostrophic shear', *Journal of Physical Oceanography* **15**(5), 544–565. 107

Kurapov, A. L., Egbert, G. D., Allen, J., Miller, R. N., Erofeeva, S. Y. and Kosro, P. [2003], 'The M2 internal tide off Oregon: Inferences from data assimilation', *Journal of Physical Oceanography* **33**(8), 1733–1757. 137

LaFond, E. [1961], 'Isotherm follower', *Journal of Marine Research* **19**, 33–39. 18

LaFond, E. and Rao, C. B. [1954], 'Rotary currents in the Bay of Bengal', *Andhra University memmo in Oceanography* **1**, 102–108. 18

Laplace, P. [1776], 'Recherches sur plusieurs points du systeme du monte', *Mémoire de l'Acadmie Royale des Sciences de Paris* **89**, 177–264. 14

Large, W. G. and Crawford, G. B. [1995], 'Observations and simulations of upper-ocean response to wind events during the ocean storms experiment', *Journal of Physical Oceanography* **25**(11), 2831–2852. 5

Large, W. G. and Gent, P. R. [1999], 'Validation of vertical mixing in an equatorial ocean model using large eddy simulations and observations', *Journal of Physical Oceanography* **29**(3), 449–464. 38

Large, W. G., McWilliams, J. C. and Doney, S. C. [1994], 'Oceanic vertical mixing: A review and a model with a nonlocal boundary layer parameterization', *Reviews of Geophysics* **32**(4), 363. 41, 42

Laurent, L. S. and Garrett, C. [2002], 'The role of internal tides in mixing the deep ocean', *Journal of Physical Oceanography* **32**(10), 2882–2899. 7, 21, 71, 155

Le Provost, C. [2001], Chapter 6 ocean tides, Elsevier, pp. 267–303. 16

Le Provost, C., Genco, M. L., Lyard, F., Vincent, P. and Canceil, P. [1994], 'Spectroscopy of the world ocean tides from a finite element hydrodynamic model', *Journal of Geophysical Research* **99**(C12), 24777. 17

Leaman, K. D. [1980], 'Some observations of baroclinic diurnal tides over a near-critical bottom slope', *Journal of Physical Oceanography* **10**(10), 1540–1551. 19

Lee, C. M., Sanford, T. B., Kunze, E., Nash, J. D., Merrifield, M. A. and Holloway, P. E. [2006], 'Internal tides and turbulence along the 3000-m isobath of the Hawaiian ridge', *Journal of Physical Oceanography* **36**(6), 1165–1183. 21

Lee, H.-I., Wang, Y.-H., Yang, Y. and Wang, D.-P. [2012], 'Temporal variability of internal tides in the northeast South China Sea', *Journal of Geophysical Research (1978–2012)* **117**(C2). 85, 95

Lee, H. J., Park, J.-H., Wimbush, M., Jung, K. T., Jang, C. J., Cho, Y.-K., Seo, Y.-K. and Nam, J. H. [2011], 'Tidal effects on intermediate waters: A case study in the East/Japan Sea', *Journal of Physical Oceanography* **41**(1), 234–240. 137

Lee, W. and Cox, C. [1966], 'Time variation of ocean temperature and its relation to internal wave and oceanic heat flow measurements', *Journal of Geophysical Research* **259**, 533–581. 18

Leichter, J. J., Stewart, H. L. and Miller, S. L. [2003], 'Episodic nutrient transport to Florida coral reefs', *Limnology and Oceanography* **48**(4), 1394–1407. 137

Lerczak, J. A., Hendershott, M. C. and Winant, C. D. [2001], 'Observations and modeling of coastal internal waves driven by a diurnal sea breeze', *Journal of Geophysical Research: Oceans* **106**(C9), 19715–19729. 19

Levine, M. D., Padman, L., Muench, R. D. and Morison, J. H. [1997], 'Internal waves and tides in the western Weddell Sea: Observations from ice station Weddell', *Journal of Geophysical Research (1978–2012)* **102**(C1), 1073–1089. 88

Lien, R.-C., Sanford, T. B., Jan, S., Chang, M.-H. and Ma, B. B. [2013], 'Internal tides on the East China Sea continental slope', *Journal of Marine Research* **71**(1-2), 151–185. 89

Lueck, R. and Reid, R. [1984], 'On the production and dissipation of mechanical energy in the ocean', *Journal of Geophysical Research* **89**(C3), 3439. 5

Lyard, F., Lefevre, F., Letellier, T. and Francis, O. [2006], 'Modelling the global ocean tides: modern insights from FES2004', *Ocean Dynamics* **56**(5-6), 394–415. 7, 17

MacKinnon, J. A., Zhao, Z., Whalen, C. B., Waterhouse, A. F., Trossman, D. S., Sun, O. M., Laurent, L. C. S., Simmons, H. L., Polzin, K., Pinkel, R., Pickering, A., Norton, N. J., Nash, J. D., Musgrave, R., Merchant, L. M., Melet, A. V., Mater, B., Legg, S., Large, W. G., Kunze, E., Klymak, J. M., Jochum, M., Jayne, S. R., Hallberg, R. W., Griffies, S. M., Diggs, S., Danabasoglu, G., Chassignet, E. P., Buijsman, M. C., Bryan, F. O., Briegleb, B. P., Barna, A., Arbic, B. K., Ansong, J. K. and Alford, M. H. [2017], 'Climate process team on internal wave–driven ocean mixing', *Bulletin of the American Meteorological Society* **98**(11), 2429–2454. 21, 22, 155

Magaard, L. and McKee, W. D. [1973], 'Semi-diurnal tidal currents at 'site D'', *Deep Sea Research and Oceanographic Abstracts* **20**(11), 997–1009. 8, 18

Magalhaes, J. and da Silva, J. [2012], 'Sar observations of internal solitary waves generated at the Estremadura Promontory off the west Iberian coast', *Deep Sea Research Part I: Oceanographic Research Papers* **69**, 12–24. 103

Mahadevan, A., Paluszkiewicz, T., Ravichandran, M., Sengupta, D. and Tandon, A. [2016], 'Introduction to the special issue on the Bay of Bengal: From monsoons to mixing', *Oceanography* **29**(2), 14–17. 154

Marchesiello, P., McWilliams, J. C. and Shchepetkin, A. [2001], 'Open boundary conditions for long-term integration of regional oceanic models', *Ocean Modelling* **3**(1-2), 1–20. 41

Martini, K. I., Alford, M. H., Nash, J. D., Kunze, E. and Merrifield, M. A. [2007], 'Diagnosing a partly standing internal wave in Mamala Bay, Oahug', *Geophysical Research Letters* **34**(17). 20

Melet, A., Legg, S. and Hallberg, R. [2016], 'Climatic impacts of parameterized local and remote tidal mixing', *Journal of Climate* **29**(10), 3473–3500. 21

Merrifield, M. A. and Holloway, P. E. [2002], 'Model estimates of M2 internal tide energetics at the Hawaiian ridge', *Journal of Geophysical Research: Oceans (1978–2012)* **107**(C8), 5–1. 20, 37, 101, 103, 122

Merrifield, M. A., Holloway, P. E. and Johnston, T. [2001], 'The generation of internal tides at the Hawaiian ridge', *Geophysical Research Letters* **28**(4), 559–562. 28

Mitchum, G. T. and Chiswell, S. M. [2000], 'Coherence of internal tide modulations along the Hawaiian ridge', *Journal of Geophysical Research: Oceans* **105**(C12), 28653–28661. 36

Mohanty, S., Rao, A. D. and Latha, G. [2018], 'Energetics of semidiurnal internal tides in the andaman sea', *Journal of Geophysical Research: Oceans* **123**(9), 6224–6240.
URL: *https://doi.org/10.1029/2018jc013852* 20

Mohanty, S., Rao, A. and Pradhan, H. K. [2017], 'Estimates of internal tide energetics in the western Bay of Bengal', *IEEE Journal of Oceanic Engineering* . 19

Muacho, S., da Silva, J., Brotas, V., Oliveira, P. and Magalhaes, J. [2014], 'Chlorophyll enhancement in the central region of the Bay of Biscay as a result of internal tidal wave interaction', *Journal of Marine Systems* **136**, 22–30. 103

Mukherjee, A., Shankar, D., Aparna, S. G., Amol, P., Fernando, V., Fernandes, R., Khalap, S., Narayan, S., Agarvadekar, Y., Gaonkar, M., Tari, P., Kankonkar and Vernekar, S. [2013], 'Near-inertial currents off the east coast of India', *Continental Shelf Research* **55**, 29–39. 108

Müller, P., Olbers, D. J. and Willebrand, J. [1978], 'The IWEX spectrum', *Journal of Geophysical Research (1978–2012)* **83**(C1), 479–500. 89

Munk, W. [1981], 'Internal waves and small-scale processes', *Evolution of physical oceanography* pp. 264–291. 87

Munk, W. H. [1966], 'Abyssal recipes', *Deep Sea Research and Oceanographic Abstracts* **13**(4), 707–730. 4

Munk, W. and Wunsch, C. [1998], 'Abyssal recipes II: energetics of tidal and wind mixing', *Deep Sea Research Part I: Oceanographic Research Papers* **45**(12), 1977–2010. 4, 21

Murphy, A. H. [1988], 'Skill scores based on the mean square error and their relationships to the correlation coefficient', *Monthly weather review* **116**(12), 2417–2424. 66, 98

Murthy, P. G. K. and Kumar, P. V. H. [1991], 'Response of coastal waters off karwar to a deep depression', *Continental Shelf Research* **11**(3), 239–250. 8

Muschinski, A. [1996], 'Possible effect of Kelvin-Helmholtz instability on VHF radar observations of the mean vertical wind', *Journal of Applied Meteorology* **35**(12), 2210–2217. 41, 42

Nagai, T. and Hibiya, T. [2015], 'Internal tides and associated vertical mixing in the Indonesian Archipelago', *Journal of Geophysical Research: Oceans* **120**(5), 3373–3390. 7, 21, 155

Nansen, F. [1902], *Oceanography of the North Pole Basin: Norwegian North Polar Expedition, 1893-1896: Scientific Results*, Vol. 3, Fridtjof Nansen Fund for the Advancement of Science. 18

Naqvi, S. W. A. [1991], 'Geographical extent of denitrification in the Arabian Sea in relation to some physical processes', *Oceanologica Acta* **14**(3), 281–290. 83

Nash, J. D., Kunze, E., Lee, C. M. and Sanford, T. B. [2006], 'Structure of the baroclinic tide generated at Kaena Ridge, Hawaii', *Journal of Physical Oceanography* **36**(6), 1123–1135. 21

Nash, J. D., Kunze, E., Toole, J. M. and Schmitt, R. W. [2004], 'Internal tide reflection and turbulent mixing on the continental slope', *Journal of Physical Oceanography* **34**(5), 1117–1134. 6, 19

Nash, J., Shroyer, E., Kelly, S., Inall, M., Duda, T., Levine, M., Jones, N. and Musgrave, R. [2012], 'Are any coastal internal tides predictable?', *oceanography* **25**(2), 80–95. 66, 98, 144, 146, 150

New, A. L. [1988], 'Internal tidal mixing in the Bay of Biscay', *Deep Sea Research Part A. Oceanographic Research Papers* **35**(5), 691–709. 20

Newton, S. I. [1687], *Philosophae Naturalis Principia Mathematica*, The Royal Society, London. 14

Niwa, Y. and Hibiya, T. [2004], 'Three-dimensional numerical simulation of M2 internal tides in the East China Sea', *Journal of Geophysical Research: Oceans* **109**(C4). 35, 37

Niwa, Y. and Hibiya, T. [2011], 'Estimation of baroclinic tide energy available for deep ocean mixing based on three-dimensional global numerical simulations', *Journal of Oceanography* **67**(4), 493–502. 20

Nycander, J. [2005], 'Generation of internal waves in the deep ocean by tides', *Journal of Geophysical Research* **110**(C10). 5

Park, J.-H. and Watts, D. R. [2006], 'Internal tides in the southwestern Japan/East Sea', *Journal of Physical Oceanography* **36**(1), 22–34. 36

Parke, M. E. and Hendershott, M. C. [1980], 'M2, S2, K1 models of the global ocean tide on an elastic earth', *Marine Geodesy* **3**(1-4), 379–408. n/a. 16

Pauly, D., Christensen, V., Guénette, S., Pitcher, T. J., Sumaila, U. R., Walters, C. J., Watson, R. and Zeller, D. [2002], 'Towards sustainability in world fisheries', *Nature* **418**(6898), 689–695. 7

Pekeris, C. L. and Accad, Y. [1969], 'Solution of Laplace's equations for the MFormula tide in the world oceans', *Philosophical Transactions of the Royal Society A: Mathematical, Physical and Engineering Sciences* **265**(1165), 413–436. 15, 16

Pereira, A. F. and Castro, B. M. [2007], 'Internal tides in the southwestern Atlantic off Brazil: Observations and numerical modeling', *Journal of Physical Oceanography* **37**(6), 1512–1526. 137

Petruncio, E. T., Rosenfeld, L. K. and Paduan, J. D. [1998], 'Observations of the internal tide in Monterey Canyon', *Journal of Physical Oceanography* **28**(10), 1873–1903. 94

Phillips, O. M. [1966], *Dynamics of the Upper Ocean*, Cambridge University Press. 20

Pingree, R. D. [1984], Some applications of remote sensing to studies in the Bay of Biscay, Celtic Sea and English Channel, Elsevier, pp. 287–315. 9

Pingree, R. and New, A. [1989], 'Downward propagation of internal tidal energy into the Bay of Biscay', *Deep Sea Research Part A. Oceanographic Research Papers* **36**(5), 735–758. 19

Plueddemann, A. and Farrar, J. [2006], 'Observations and models of the energy flux from the wind to mixed-layer inertial currents', *Deep Sea Research Part II: Topical Studies in Oceanography* **53**(1-2), 5–30. 5

Polzin, K. [2004], 'A heuristic description of internal wave dynamics', *Journal of Physical Oceanography* **34**(1), 214–230. 7, 155

Powell, B. S., Janeković, I., Carter, G. S. and Merrifield, M. A. [2012], 'Sensitivity of internal tide generation in Hawaii', *Geophysical Research Letters* **39**(10), n/a–n/a. 37

Prinsenberg, S. J. and Rattray, M. [1975], 'Effects of continental slope and variable brunt-väisälä frequency on the coastal generation of internal tides', *Deep Sea Research and Oceanographic Abstracts* **22**(4), 251–263. 20

Prinsenberg, S. J., Wilmot, W. L. and Rattray, M. [1974], 'Generation and dissipation of coastal internal tides', *Deep Sea Research and Oceanographic Abstracts* **21**(4), 263–281. 20

Rainville, L., Johnston, T. M. S., Carter, G. S., Merrifield, M. A., Pinkel, R., Worcester, P. F. and Dushaw,

B. D. [2010], 'Interference pattern and propagation of theM2 internal tide south of the Hawaiian ridge', *Journal of Physical Oceanography* **40**(2), 311–325. 20

Rainville, L. and Pinkel, R. [2006], 'Propagation of low-mode internal waves through the ocean', *Journal of Physical Oceanography* **36**(6), 1220–1236. 21, 36

Ramp, S., Tang, T., Duda, T., Lynch, J., Liu, A., Chiu, C.-S., Bahr, F., Kim, H.-R. and Yang, Y.-J. [2004], 'Internal solitons in the northeastern South China Sea part i: Sources and deep water propagation', *IEEE Journal of Oceanic Engineering* **29**(4), 1157–1181. 37

Rao, A. D., Babu, S. V., Murty, P. L. N. and Pandey, S. [2011], 'Impact of stratification on internal waves and differential wearing of thermal inversions on the east coast of India', *Natural hazards* **57**(3), 577–595. 19

Rao, A. D., Joshi, M. and Ravichandran, M. [2008], 'Oceanic upwelling and downwelling processes in waters off the west coast of India', *Ocean Dynamics* **58**(3-4), 213–226. 48, 73

Rao, D. G., Paropkari, A. L., Krishna, K. S., Chaubey, A. K., Ajay, K. K. and Kodagali, V. N. [2010], 'Bathymetric highs in the mid-slope region of the western continental margin of India— structure and mode of origin', *Marine Geology* **276**(1-4), 58–70. 40

Rattray, M. [1960], 'On the coastal generation of internal tides', *Tellus* **12**, 54–62. 20

Rattray, M., Dworski, J. G. and Kovala, P. E. [1969], 'Generation of long internal waves at a continental slope', *Deep Sea Research* **16**, 179–195. 20

Ray, R. D. [2001], Internal tides, Elsevier, pp. 258–265. 6

Ray, R. D. and Cartwright, D. E. [2001], 'Estimates of internal tide energy fluxes from Topex/Poseidon altimetry: Central North Pacific', *Geophysical Research Letters* **28**(7), 1259–1262. 28

Rayleigh [1882], 'Investigation of the character of the equilibrium of an incompressible heavy fluid of variable density', *Proceedings of the London Mathematical Society* **s1-14**(1), 170–177. 19

Rayson, M. D., Ivey, G. N., Jones, N. L., Meuleners, M. J. and Wake, G. W. [2011], 'Internal tide dynamics in a topographically complex region: Browse basin, Australian north west shelf', *Journal of Geophysical Research: Oceans* **116**(C1). 122, 149

Reid, J. L. [1956], 'Reviews and abstracts', *Transactions, American Geophysical Union* **37**(4), 502. 18

Rimac, A., von Storch, J.-S., Eden, C. and Haak, H. [2013], 'The influence of high-resolution wind stress field on the power input to near-inertial motions in the ocean', *Geophysical Research Letters* **40**(18), 4882–4886. 5

Robertson, R. [2006], 'Modeling internal tides over Fieberling Guyot: resolution, parameterization, performance', *Ocean Dynamics* **56**(5-6), 430–444. 38

Rooth, C. and Düing, W. [1971], 'On the detection of "inertial" waves with pycnocline followers', *Journal of Physical Oceanography* **1**(1), 12–16. 18

Rosenfeld, L. K. [1990], 'Baroclinic semidiurnal tidal currents over the continental shelf off northern California', *Journal of Geophysical Research* **95**(C12), 22153. 6, 19, 45, 70

Rudnick, D. L. [2003], 'From tides to mixing along the Hawaiian ridge', *Science* **301**(5631), 355–357. 21, 150

Rudnick, P. and Cochrane, J. [1951], 'Diurnal fluctuations in bathythermograms', *Journal of Marine Research* **10**, 257–262. 18

Sandstrom, H. and Elliott, J. A. [1984], 'Internal tide and solitons on the scotian shelf: A nutrient pump at work', *Journal of Geophysical Research* **89**(C4), 6415. 7

Schiermeier, Q. [2007], 'Oceanography: Churn, churn, churn', *Nature* **447**(7144), 522–524. 3

Schott, F. [1971], 'On horizontal coherence and internal wave propagation in the North Sea', *Deep Sea Research and Oceanographic Abstracts* **18**(3), 291–307. 18

Schott, F. [1977], 'On the energetics of baroclinic tides in the North Atlantic', *Annales Geophysicae* **33**, 41–62. 19

Schwiderski, E. W. [1980*a*], 'Ocean tides, part II: A hydrodynamical interpolation model', *Marine Geodesy* **3**(1-4), 219–255. 16, 17

Schwiderski, E. W. [1980*b*], 'On charting global ocean tides', *Reviews of Geophysics* **18**(1), 243. 16, 17

Scotti, A., Beardsley, R. C. and Butman, B. [2007], 'Generation and propagation of nonlinear internal waves in Massachusetts Bay', *Journal of Geophysical Research* **112**(C10). 37

Serpette, A. and Mazé, R. [1989], 'Internal tides in the Bay of Biscay: a two-dimensional model', *Continental Shelf Research* **9**(9), 795–821. 20

Shankar, D., Shenoi, S. S. C., Nayak, R. K., Vinayachandran, P. N., Nampoothiri, G., Almeida, A. M., Michael, G. S., Ramesh Kumar, M. R., Sundar, D. and Sreejith, O. P. [2005], 'Hydrography of the eastern Arabian Sea during summer monsoon 2002', *Journal of earth system science* **114**(5), 459–474. 8, 29, 73, 81, 86

Shankar, D. and Shetye, S. R. [1997], 'On the dynamics of the lakshadweep high and low in the southeastern Arabian Sea', *Journal of Geophysical Research: Oceans* **102**(C6), 12551–12562. 45

Sharples, J., Moore, C. M. and Abraham, E. R. [2001], 'Internal tide dissipation, mixing, and vertical nitrate flux at the shelf edge of NE New Zealand', *Journal of Geophysical Research: Oceans* **106**(C7), 14069–14081. 3, 7, 9, 154

Sharples, J., Moore, C. M., Hickman, A. E., Holligan, P. M., Tweddle, J. F., Palmer, M. R. and Simpson, J. H. [2009], 'Internal tidal mixing as a control on continental margin ecosystems', *Geophysical Research Letters* **36**(23). 3, 7, 9

Shchepetkin, A. F. and McWilliams, J. C. [2003], 'A method for computing horizontal pressure-gradient force in an oceanic model with a nonaligned vertical coordinate', *Journal of Geophysical Research* **108**(C3). 37, 38

Shchepetkin, A. F. and McWilliams, J. C. [2005], 'The regional oceanic modeling system (roms): a split-explicit, free-surface, topography-following-coordinate oceanic model', *Ocean modelling* **9**(4), 347–404. 37

Shchepetkin, A. F. and McWilliams, J. C. [2009], 'Correction and commentary for "ocean forecasting in terrain-following coordinates: Formulation and skill assessment of the regional ocean modeling system" by Haidvogel et al., J. Comp. Phys. 227, pp. 3595–3624', *Journal of Computational Physics* **228**(24), 8985–9000. 37

Shenoi, S. C., Gouveia and A. D., Shetye, S. R. [1992], 'Diurnal and semidiurnal tidal currents in the deep mid-Arabian sea', *Proceedings of the Indian Academy of Science (Earth and planetary sciences)* **101**, 177–189. 8

Shenoi, S. C., Gouveia and A. D., Shetye, S. R. [1994], 'M2 tidal currents on the shelf off Goa, west coast of India', *Ocean Technology perspectives* pp. 415–427. 8, 19

Shenoi, S. S. C., Antony, M. K. and Sundar, D. [1988], 'Nature of the observed oscillatory flows in shelf waters of the western continental shelf of India', *Journal of Coastal Research* pp. 617–626. 8, 71

Shenoi, S. S. C., Shankar, D., Michael, G. S., Kurian, J., Varma, K. K., Kumar, M. R. R., Almeida, A. M., Unnikrishnan, A. S., Fernandes, W., Barreto, N., Gnanaseelan, C., Mathew, R., Praju, K. V. and Mahale, V. [2005], 'Hydrography and water masses in the southeastern Arabian Sea during march–june 2003', *Journal of earth system science* **114**(5), 475–491. 45, 73

Sherwin, T. J. [1988], 'Analysis of an internal tide observed on the Malin shelf, north of Ireland', *Journal of Physical Oceanography* **18**(7), 1035–1050. 19, 71, 150

Sherwin, T. J. and Taylor, N. K. [1990], 'Numerical investigations of linear internal tide generation in the Rockall trough', *Deep Sea Research Part A. Oceanographic Research Papers* **37**(10), 1595–1618. 20

Shetye, S. R. [1999], 'Propagation of tides in the Mandovi and Zuari estuaries', *Sadhana* **24**(1-2), 5–16. 7

Shetye, S. R., Gouveia, A. D., Shenoi, S. S. C., Michael, G. S., Sundar, D., Almeida, A. M. and Santanam, K. [1991], 'The coastal current off western India during the northeast monsoon', *Deep Sea Research Part A. Oceanographic Research Papers* **38**(12), 1517–1529. 8, 72

Shetye, S. R., Gouveia, A. D., Shenoi, S. S. C., Sundar, D., Michael, G. S., Almeida, A. M. and Santanam, K. [1990], 'Hydrography and circulation off the west coast of India during the southwest monsoon 1987', *Journal of Marine Research* **48**(2), 359–378. 8, 45, 48, 72

Shetye, S. R. and Shenoi, S. C. C. [1988], 'Seasonal cycle of surface circulation in the coastal north Indian Ocean', *Proceedings of the Indian Academy of Science (Earth and Planetary Sciences)* **97**, 53–62. 48

Shetye, S. R., Suresh, I., Shankar, D., Sundar, D., Jayakumar, S., Mehra, P., Prabhudesai, R. G. and Pednekar, P. S. [2008], 'Observational evidence for remote forcing of the west India coastal current', *Journal of Geophysical Research* **113**(C11). 8

Simmons, H. L., Jayne, S. R., Laurent, L. C. and Weaver, A. J. [2004], 'Tidally driven mixing in a numerical model of the ocean general circulation', *Ocean Modelling* **6**(3-4), 245–263. 20, 21, 37

Simpson, J. H. and Hunter, J. R. [1974], 'Fronts in the Irish Sea', *Nature* **250**(5465), 404–406. 2

Sindhu, B., Suresh, I., Unnikrishnan, A. S., Bhatkar, N. V., Neetu, S. and Michael, G. S. [2007], 'Improved bathymetric datasets for the shallow water regions in the Indian Ocean', *Journal of Earth System Science* **116**(3), 261–274. 40

Sjöberg, B. and Stigebrandt, A. [1992], 'Computations of the geographical distribution of the energy flux to mixing processes via internal tides and the associated vertical circulation in the ocean', *Deep Sea Research Part A. Oceanographic Research Papers* **39**(2), 269–291. 5

Song, Y. and Haidvogel, D. [1994], 'A semi-implicit ocean circulation model using a generalized topography-following coordinate system', *Journal of Computational Physics* **115**(1), 228–244. 37

Stokes, G. G. [1847], 'On the theory of oscillatory waves', *Transactions of the Cambridge Philosophical Society* . 19

Suanda, S. H., Feddersen, F. and Kumar, N. [2017], 'The effect of barotropic and baroclinic tides on coastal stratification and mixing', *Journal of Geophysical Research: Oceans* **122**(12), 10156–10173. 2, 7

Subeesh, M. P. and Unnikrishnan, A. S. [2016], 'Observed internal tides and near-inertial waves on the continental shelf and slope off Jaigarh, central west coast of India', *Journal of Marine Systems* **157**, 1–19. 12

Subeesh, M. P., Unnikrishnan, A. S., Fernando, V., Agarwadekar, Y., Khalap, S. T., Satelkar, N. P. and Shenoi, S. S. C. [2013], 'Observed tidal currents on the continental shelf off the west coast of India', *Continental Shelf Research* **69**, 123–140. 12, 81

Sundar, D. and Shetye, S. R. [2005], 'Tides in the Mandovi and Zuari estuaries, Goa, west coast of India', *Journal of Earth System Science* **114**(5), 493–503. 7

Taylor, G. I. [1919], 'Tidal friction in the Irish Sea', *Philosophical Transactions of the Royal Society of London* **A 220**, 1–93. 121

Testut, L. and Unnikrishnan, A. S. [2016], 'Improving modeling of tides on the continental shelf off the west coast of India', *Journal of Coastal Research* **317**, 105–115. 7, 117

Torgrimson, G. M. and Hickey, B. M. [1979], 'Barotropic and baroclinic tides over the continental slope and shelf off Oregon', *Journal of Physical Oceanography* **9**(5), 945–961. 150

Turner, J. S. [1973], *Buoyancy Effects in Fluids*, Cambridge University Press. 20

Unnikrishnan, A. S. and Antony, M. K. [1990], 'On vertical velocity fluctuations and internal tides in an upwelling region off the west coast of India', *Estuarine, Coastal and Shelf Science* **31**(6), 865–873. 8

Unnikrishnan, A. S. and Luick, J. L. [2003], 'A finite element simulation of tidal circulation in the Gulf of Kutch, India', *Estuarine, Coastal and Shelf Science* **56**(1), 131–138. 7

Unnikrishnan, A. S., Shetye, S. R. and Michael, G. S. [1999], 'Tidal propagation in the Gulf of Khambhat, Bombay High, and surrounding areas', *Proceedings of the Indian Academy of Sciences-Earth and Planetary Sciences* **108**(3), 155–177. 7, 8, 79

Varkey, M. J. [1980], 'Power spectra of currents off Bombay', *Indian Journal of Marine Sciences* **9**, 278–280. 8

Vipin, P., Sarkar, K., Aparna, S. G., Shankar, D., Sarma, V. V. S. S., Gracias, D. G., Krishna, M. S., Srikanth, G., Mandal, R., Rao, E. P. R. and Rao, N. S. [2015], 'Evolution and sub-surface characteristics of a sea-surface temperature filament and front in the northeastern Arabian Sea during november–december 2012', *Journal of Marine Systems* **150**, 1–11. 9

Vitousek, S. and Fringer, O. B. [2011], 'Physical vs. numerical dispersion in nonhydrostatic ocean modeling', *Ocean Modelling* **40**(1), 72–86. 37

Watanabe, M. and Hibiya, T. [2002], 'Global estimates of the wind-induced energy flux to inertial motions in the surface mixed layer', *Geophysical Research Letters* **29**(8), 64–1–64–3. 5

Waterhouse, A. F., MacKinnon, J. A., Nash, J. D., Alford, M. H., Kunze, E., Simmons, H. L., Polzin, K. L., Laurent, L. C. S., Sun, O. M., Pinkel, R., Talley, L. D., Whalen, C. B., Huussen, T. N., Carter, G. S., Fer, I., Waterman, S., Garabato, A. C. N., Sanford, T. B. and Lee, C. M. [2014], 'Global patterns of diapycnal mixing from measurements of the turbulent dissipation rate', *Journal of Physical Oceanography* **44**(7), 1854–1872. 5, 6

Weigand, J. G., Farmer, H. G., Prinsenberg, S. J. and Rattray., M. [1969], 'Effects of friction and surface tide angle of incidence on the coastal generation of internal waves.', *Journal of Marine Research* **27**(2), 241–259. 20

Weisberg, R. H., Halpern, D., Tang, T. Y. and Hwang, S. M. [1987], 'M2 tidal currents in the eastern equatorial Pacific Ocean', *Journal of Geophysical Research* **92**(C4), 3821. 8

Weston, D. and Reay, W. [1969], 'Tidal-period internal waves in a tidal stream', *Deep Sea Research and Oceanographic Abstracts* **16**(5), 473–478. 18

Wunsch, C. [1975], 'Internal tides in the ocean', *Reviews of Geophysics* **13**(1), 167. 18, 19

Wunsch, C. and Dahlen, J. [1974], 'A moored temperature and pressure recorder', *Deep Sea Research and Oceanographic Abstracts* **21**(2), 145–154. 18

Wunsch, C. and Ferrari, R. [2004], 'Vertical mixing energy and the general circulation of the oceans', *Annual Review of Fluid Mechanics* **36**(1), 281–314. 2

Wunsch, C. and Hendry, R. [1972], 'Array measurements of the bottom boundary layer and the internal wave field on the continental slope', *Geophsical Fluid Dynamics* **4**, 101. 18

Wunsch, C. and Webb, S. [1979], 'The climatology of deep ocean internal waves', *Journal of Physical Oceanography* **9**(2), 235–243. 18

Xing, J. and Davies, A. M. [1998], 'A three-dimensional model of internal tides on the Malin-Hebrides shelf and shelf edge', *Journal of Geophysical Research: Oceans* **103**(C12), 27821–27847. 20

Xu, Z., Yin, B., Hou, Y. and Xu, Y. [2013], 'Variability of internal tides and near-inertial waves on the continental slope of the northwestern South China Sea', *Journal of Geophysical Research* **118**(1), 197–211. 56, 88

Zahel, W. [1977], 'A global hydrodynamicnumerical 1- model of the ocean tides; the oscillation system of the M2-tide and its distribution of energy dissipation', *Annales Geophysicae* **33**, 31–40. 16

Zeilon, N. [1912], *On Tidal Boundary-waves and Related Hydrodynamical Problems*, number pt. 1911 *in* 'Kungl. Svenska vetenskapsakademiens handlingar', Almqvist & Wiksells. 19

Zhao, Z., Alford, M. H. and Girton, J. B. [2012], 'Mapping low-mode internal tides from multisatellite altimetry', *Oceanography-Oceanography Society* **25**(2), 42. 28